Analysis of Instabilities in Microelectromechanical Systems, and of Local Water Slamming

Kaushik Das

Dissertation submitted to the faculty of the Virginia Polytechnic Institute
and State University in partial fulfillment of the requirements for
the degree of

Doctor of Philosophy
in
Engineering Mechanics

Romesh C. Batra, Chair
Mark S. Cramer
Mark R. Paul
Norman E. Dowling
Scott L. Hendricks

August 24, 2009

Blacksburg, Virginia

Key words: Symmetry breaking, pull-in instability, snap-through instability, local water slamming, fluid-structure interaction.

Analysis of Instabilities in Microelectromechanical Systems, and of Local Water Slamming

Kaushik Das

ABSTRACT

Arch-shaped microelectromechanical systems (MEMS) have been used as mechanical memories, micro-sensors, micro-actuators, and micro-valves. A bi-stable structure, such as an arch, is characterized by a multivalued load deflection curve. Here we study the symmetry breaking, the snap-through instability, and the pull-in instability of bi-stable arch shaped MEMS under steady and transient electric loads. We analyze transient finite electroelastodynamic deformations of perfect electrically conducting clamped-clamped beams and arches suspended over a flat rigid semi-infinite perfect conductor. The coupled nonlinear partial differential equations (PDEs) for mechanical deformations are solved numerically by the finite element method (FEM) and those for the electrical problem by the boundary element method.

The coupled nonlinear PDE governing transient deformations of the arch based on the Euler-Bernoulli beam theory is solved numerically using the Galerkin method, mode shapes for a beam as basis functions, and integrated numerically with respect to time. For the static problem, the displacement control and the pseudo-arc length continuation (PALC) methods are used to obtain the bifurcation curve of arch's deflection versus the electric potential. The displacement control method fails to compute arch's asymmetric deformations that are found by the PALC method. For the dynamic problem, two distinct mechanisms of the snap-through instability are found. It is shown that critical loads and geometric parameters for instabilities of an arch with and without the consideration of mechanical inertia effects are quite different. A phase diagram between a critical load parameter and the arch height is constructed to delineate different regions of instabilities.

The local water slamming refers to the impact of a part of a ship hull on stationary water for a short duration during which high local pressures occur. We simulate slamming impact of rigid and deformable hull bottom panels by using the coupled Lagrangian and Eulerian formulation in the commercial FE software LS-DYNA. The Lagrangian formulation is used to describe plane-strain deformations of the wedge and the Eulerian description of motion for deformations of the water. A penalty contact algorithm couples the wedge with the water surface. Damage and delamination induced, respectively, in a fiber reinforced composite panel and a sandwich composite panel and due to hydroelastic pressure are studied.

Acknowledgments

I would like to thank my PhD adviser Prof. Romesh C. Batra for his support and guidance during my doctoral program. His meticulous research is an inspiration for me. I am also thankful to my committee members for their valuable time and suggestions in improving upon my research work.

For all the helpful suggestions and encouragements, I thank my friends and fellow students of the Computational Mechanics Lab at Virginia Tech, Alejandro Pacheco, Anoop Varghese, Davide Spinello, Filippo Bosco, Gautam Gopinath, Haowen Fang, Mou Zhang, Shakti Gupta, and Wen Jiang. I truly appreciate the friendship and encouragements I received from my friends Attilio Arcari, Carmine Senatore, Fang Fang, Mohammed Rabius Sunny, and Pankaj Joshi. It was great knowing them and I had a wonderful time with them at Blacksburg.

I express my deepest gratitude to my parents and my brother, Shaunak, for their sacrifices and constant encouragements.

This work was partially supported by the Office of Naval Research Grant No. N00014-98-06-0567 to Virginia Polytechnic Institute and State University with Dr. Y. D. S. Rajapakse as the program manager. Partial financial support from Virginia Tech's Institute of Critical Technologies and Sciences is gratefully acknowledged. Views expressed herein are those of the author, and neither of the funding agencies nor of VPI&SU.

The author alone is responsible for errors, if any, in the dissertation.

Contents

List of Figures

List of Tables

Chapter 1

Symmetry breaking, snap-through, and pull-in instabilities under dynamic loading of microelectromechanical shallow arch

1.1. Introduction

Microelectromechanical systems (MEMS) having components of dimensions in the range of a few to a hundred micrometers are used as radio frequency (RF) switches, varactors and inductors [78], accelerometers [79], pressure sensors, controllers for micro-mirrors [96], micro-pumps [10], and bio-MEMS [3]. A number of different actuation properties, such as piezoresistive, piezoelectric, electrostatic, electromagnetic, thermal, and optical have been exploited in MEMS. Of these, the electric actuation is widely used because of the low power consumption and potential for integration in a standard integrated circuit environment. An electrically actuated MEMS consists of a deformable electrode made of a conductive material suspended above a rigid conductive electrode with a dielectric medium, generally air, between them. An electric potential difference applied between the two electrodes induces the Coulomb pressure on the electrodes, which deflects the deformable electrode towards the rigid one. The elastic restoring force induced in the deformed electrode restricts its motion. Electric charges redistribute on the deformable electrode's surface and the gap between it and the rigid electrode decreases, which in turn increases the Coulomb force and deforms the deformable electrode more until the elastic restoring force is balanced by the Coulomb force.

1.1.1 The pull-in instability in MEMS

For electrically actuated MEMS, the applied electric potential has an upper limit, beyond which the corresponding Coulomb force is not balanced by the elastic restoring force, resulting in sudden collapse of the deformable electrode on the rigid one. This phenomenon, called the pull-in instability, was observed experimentally by Taylor [92] and Nathanson et al. [62]. The corresponding values of the potential difference and the peak displacement of the deformable

electrode are called the pull-in voltage and the pull-in displacement, respectively; collectively the two are called pull-in parameters.

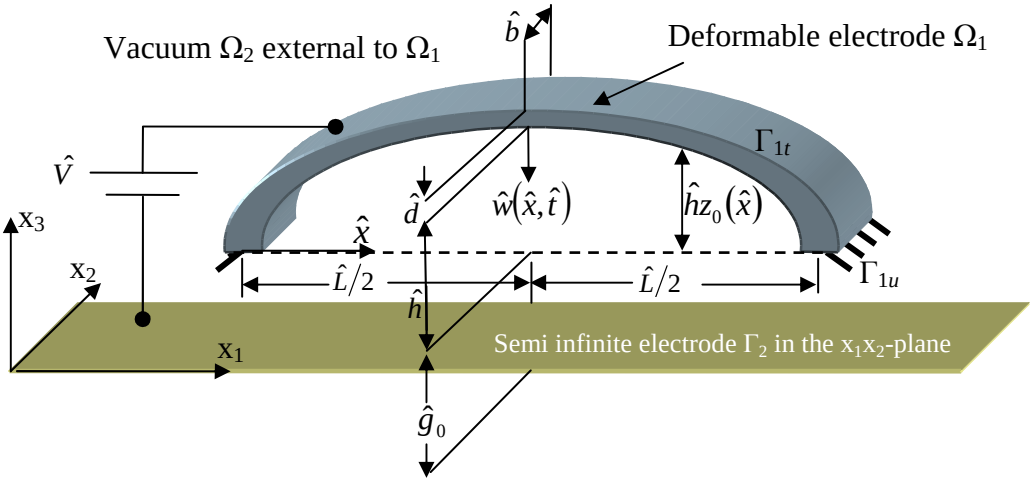

Figure 1. Schematic sketch of the problem studied.

Accurate estimates of pull-in parameters are crucial for designing electrically actuated MEMS. In switching applications [67], the pull-in instability is necessary for the switch to operate. However, for micro-mirrors [47] and micro-resonators [54] the pull-in instability restricts the range of operational displacement of the device.

1.1.2 The snap-through instability in an arch shaped MEMS

In an arch shaped deformable electrode (e.g., see figure 1), in addition to the pull-in instability, the snap-through instability can occur under the Coulomb pressure; these two instabilities have been studied in [51, 49] with a one degree of freedom system. Figure 2 shows a bifurcation diagram between the nondimensional peak displacement $w = \hat{w}/\hat{g}_0$ of an arch shaped MEM electrode and the electric potential difference parameter β defined as $\varepsilon_0 \hat{b}\hat{L}^4\hat{V}^2/2\hat{E}\hat{I}\hat{g}_0^3$. Here ε_0 is the vacuum permittivity, $\hat{b}$ the width, $\hat{L}$ the length, $\hat{g}_0$ the initial gap, $\hat{V}$ the electric potential difference between the two electrodes, $\hat{E}$ Young's modulus, and $\hat{I}$ the second moment of the cross-section of the deformable electrode about the neutral axis. The bifurcation diagram has two stable branches AC and DF. Initially, with the increase in β, w increases gradually from point A to point C, the arch maintains its initial curved shape, and the resultant elastic restoring force

balances the Coulomb force. At point C, the deflection increases suddenly, and the arch is inverted to a new equilibrium position corresponding to point E. This sudden jump in the deflection is called the snap-through instability, and the corresponding voltage the snap-through voltage. From point E to point F, the elastic restoring force induced in the arch again balances the Coulomb force. However, just after point F the deformable electrode collapses on to the rigid one, and the pull-in happens. The portions CD and FG of the curve are unstable. During the loading process, the arch follows the path ACEFL, and it follows the path FDBA during unloading.

Advantages of the snap-through instability have been exploited in actuators [97, 98, 80, 69], microvalves [40], and transducers [53]. The snap-through instability of an arch shaped MEMS under slowly applied electric loads has been observed experimentally and studied through reduced order models in [105, 51, 52, 49].

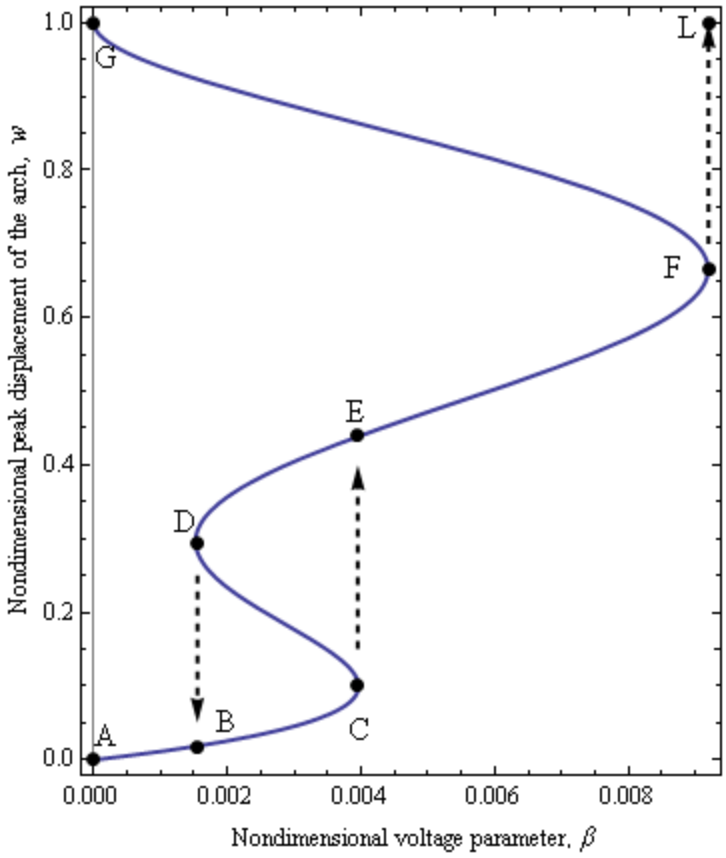

Figure 2. Bifurcation diagram for the snap-through and the pull-in instabilities of arch shaped MEMS (from [49]).

The snap-through instability of an arch is not guaranteed. Various conditions such as the arch rise $\hat{h}$ (see figure 1) for different arches (parabolic, circular or sinusoidal), arch thickness $\hat{d}$, type of loads (step or ramp), and the gap $\hat{g}_0$ between the electrodes determine whether or not the snap-through will occur. Pippard [73] and Patricio et al. [70] have presented a phase diagram between the arch length and the initial arch angle at the clamped end, showing conditions for which the snap-through can occur due to a quasistatic mechanical point load, which is not dependent on arch deflection; they studied different arch configurations either experimentally or numerically and joined the points to get the phase plot. Zhang et al. [105] and Krylov et al. [52] have studied static problems involving the snap-through and the pull-in instabilities in circular and bell shaped arches, respectively. Krylov et al. [49] have presented a phase diagram between $\hat{h}$ and $\hat{d}$ showing conditions for which the snap-through can occur in static deflections of a bell shaped MEMS. Zhang et al. [105] explained that the snap-through and the pull-in instabilities

can only be distinguished by the physical criterion of whether or not the collision between the deformable and the rigid electrodes occurs. Depending on the arch shape and the load type the following three scenarios arise: either only the pull-in instability occurs, or the arch undergoes the snap-through and then the pull-in instability, or the snap-through and the pull-in happen simultaneously. In each case, the pull-in instability occurs.

1.1.3 The dynamic pull-in and snap-through instabilities

In dynamic loading, transient effects may trigger either the snap-through or the pull-in instability first. The pull-in instability in a MEMS under a transient electric load has been studied in [63, 74, 36, 30, 5, 50], and the snap-through of arches and shells during their transient deformations under mechanical loads has been reported in [46, 25]. The snap-through of laminated composite spherical caps during their transient deformations under mechanical loads has been studied in [38, 41]. Identifying pull-in instability is easy because of the physical phenomenon of the deformable electrode touching the rigid one. The "dynamic snap-through" generally means a large increase in response, resulting from a small increase in a load parameter [46]. Simitses [84] has proposed that for static deformations under a distributed mechanical load, the arch rise parameter, $e_{arch} = 2\sqrt{3}\hat{h}/\hat{d}$, must be greater than 5.0 for the snap-through instability to occur in a shallow arch defined as one for which $(dz_0(x_1)/dx_1)^2 < 0.05$, where $z_0(x_1)$ is the shape of the bottom surface of the arch; see figure 1. However, e_{arch} must be greater than 5.86 and 9.73, respectively, for a step load described by a Heaviside function and an impulsive load given by a Dirac delta function. Thus, conditions for the dynamic snap-through to occur depend not only on geometric parameters of the arch, but also on the type of loads. As far as we can determine, the combined snap-through and pull-in instabilities in transient deformations of arch shaped MEMS have not been analyzed.

1.1.4 Modeling of electrically actuated MEMS

The modeling of electrically actuated MEMS has been reviewed in [16]. In most cases, the Coulomb pressure on the electrodes has been computed by using the parallel plate approximation (PPA) which assumes that the two electrodes are locally parallel to each other. In order to

alleviate computational difficulties of a 3-D analysis a number of reduced order models approximating the deformable electrode as a beam [94, 4, 104, 55, 14, 19] have been developed. If the aspect ratio of the deformable electrode is large, approximation of the electrode as a plate is more appropriate [107, 64, 57, 99, 17, 18, 66, 61, 93, 28, 48]. Many MEMS devices, such as micro-pumps made of thin glassy polymers, and grating light valves comprised of stretched ribbons can be approximated as membranes, e. g. see [36, 71, 12, 72].

Reduced order models estimate global quantities, such as the natural frequency or the deflected shape of the deformable electrode with reasonable accuracy; they cannot predict accurately local quantities such as the stress and the strain in a MEMS electrode of arbitrary geometry. Therefore, for analysis, design, optimization, and product development of MEMS devices, continuum mechanics based simulations are necessary.

Nishiguchi and Sasaki [68] have presented a large deformation theory for solids subjected to electromagnetic loads but did not solve any engineering problem. Gilbert et al. [39] developed the software CoSolve-EM to solve 3-D quasi electro-mechanical problems; it couples the FE code ABAQUS and the BE code FASTCAP; the former for analyzing mechanical problems and the latter for electrical problems. They did not solve a transient problem. The commercial software COMSOL can be used to study MEMS problems using the FEM with the Eulerian description of motion for the electric field in the medium surrounding the electrodes and the Lagrangian description of motion for deformations of the electrode. It needs frequent re-meshing of the region exterior to the MEM electrodes for analyzing both static and transient problems, which require considerable computational resources. Shapoorabadi and Andrew [82] have compared three different methods available in the commercial FE software ANSYS, namely, (1) ESSOLV: a sequentially coupled electrostatic and structural field tool, (2) TRANS126: a directly coupled electrostatic and structural field tool employing 1-D transducer element, and (3) ROM144: a directly coupled electrostatic and structural reduced order model. They studied static infinitesimal deformations of a torsional and a flexural-torsional micromirror, and concluded that predictions from the ROM144 and the ESSOLV compare well with analytical and experimental results. However, for problems involving large deformations, the TRANS126

should be used instead of the ROM144 and the ESSOLV. They too did not consider transient problems.

De and Aluru [32] used the coupled finite cloud and the boundary cloud methods to convert partial differential equations (PDEs) describing the balance of linear momentum and the charge conservation to ordinary differential equations (ODEs) in time and solved them using Newton's and the relaxation schemes. They employed the Lagrangian description of motion, computed exactly the Jacobian matrix in Newton's method, modeled the MEM electrodes as 2-D bodies, and neglected effects of fringing fields and material nonlinearities.

From the literature review given above, it can be concluded that transient deformations of arch shaped MEMS considering both material and geometric nonlinearities have not been studied. Here, we describe a mathematical model for studying 2-D problems, and develop the needed software to analyze the mechanical problem by the FEM and the electrical problem by the BEM. The two are coupled with information exchanged between them after every time step. After validating the mathematical model, we study the pull-in and the snap-through instabilities in arch shaped MEMS under time-dependent potential difference.

Apart from the coupled FE-BE method, we also study the snap-through and the pull-in instabilities using a reduced order model (ROM) based on the Euler-Bernoulli beam theory, which takes into account the von Kármán nonlinearity. The ROM is computationally more efficient than the coupled FE-BE method and effects of a number of design parameter on instabilities can be studied in less time using ROM. Arches under static and dynamic displacement-independent mechanical loads have been studied using a ROM by various researchers; e.g. see [46, 56, 44, 45 , 70, 73]. However, only recently, the response of arch shaped MEMS under a slowly varying electrostatic pressure is reported in [52, 105]. However, neither a detailed analysis of symmetry breaking, nor the response of arches under transient electric loads has been reported. In the present work, using a ROM, a detailed study of the dynamic response including the symmetry breaking, the snap-through, and the pull-in instabilities of arches over a range of values of the arch height and the stretching parameter is provided.

The rest of the chapter is organized as follows. Section 2 presents governing equations for MEMS using continuum balance laws and Maxwell's equations, and the numerical technique to solve the system of governing equations. In Section 3, results for flat and arch shaped MEMS are described and discussed. Section 4 presents the ROM and numerical techniques to solve the governing equation of the ROM. In Section 5, two different mechanisms of the snap-through instability, namely the direct and the indirect snap-through, are described. Effects of various parameters such as arch height, damping, rate of loading, and different arch shapes (e.g. parabolic, sinusoidal and bell shaped) on the instability parameters are studied using the ROM in Section 5. We summarize conclusions from the present work in Section 6.

1.2. Mathematical model based on continuum mechanics

1.2.1. Balance laws for MEMS

A schematic sketch of the problem studied is shown in figure 1 that also exhibits the rectangular Cartesian coordinate axes used to describe deformations of the bodies. The deformable electrode is modeled as a perfectly conductive solid body undergoing finite deformations and the rigid electrode as a semi-infinite plate in the x_1x_2-plane. Let $\Omega_1 \subset \Re^3$ and $\Gamma_2 \subset \Re^2$ be regions occupied by the deformable electrode and the rigid semi-infinite electrode, respectively; $\Omega_2 \subset \Re^3$ is the semi-infinite region surrounding Ω_1 and situated above the electrode Γ_2, and is vacuum. Γ_1 is the boundary of Ω_1 with disjoint parts Γ_{1u} and Γ_{1t}. The kinematic and the traction boundary conditions are prescribed, respectively, on Γ_{1u} and Γ_{1t}. The reference configurations Ω_1 and Ω_2 are deformed into the current configurations $\omega_1 \subset \Re^3$ and $\omega_2 \subset \Re^3$, respectively; γ_1 is the boundary of ω_1, and γ_2 the image of Γ_2 in the current configuration. We note that $\Gamma_2 = \gamma_2$ since the bottom electrode is rigid. We denote position vectors of a point with X_i and x_i (i = 1, 2, 3) in the reference and in the current configurations, respectively.

The electric field vanishes in a perfect conductor. Thus, no net charge is present inside the body. The motion of the deformable electrode Ω_1 is governed by the balance of mass, the balance of linear momentum, and the balance of moment of momentum given, respectively, by equations (1), (2) and (3) in the referential description:

$$\rho\, J = \rho_0 \tag{1}$$

$$\rho_0 \dot{v}_i = \frac{\partial \hat{T}_{ji}}{\partial X_j} + \rho_0 f_i \text{ in } \Omega_1 \tag{2}$$

$$\hat{T}_{ik} F_{kj} = \hat{T}_{jk} F_{ki} \text{ in } \Omega_1. \tag{3}$$

The coupling between the mechanical and the electrical effects is through the Coulomb pressure which acts as tractions on the surface Γ_{1t} of the electrode. Deformations of Γ_1 influence the electric field in Ω_2 since Γ_1 is also a boundary surface of Ω_2. In equations (1) – (3) ρ_0 and ρ are mass densities in the reference and the current configurations, respectively; J the determinant of the deformation gradient $F_{ij} = \frac{\partial x_i}{\partial X_j}$, v_i the velocity field defined as $v_i = \dot{x}_i$, a superimposed dot denotes the material time derivative, $\hat{T}_{ij}$ the first Piola-Kirchhoff stress tensor, f_i the body force per unit mass and a repeated index implies summation over the range of the index. The first Piola-Kirchhoff stress tensor is related to the Cauchy stress tensor T_{pj} by

$$\hat{T}_{ij} = J \frac{\partial X_i}{\partial x_p} T_{pj}\,. \tag{4}$$

1.2.2. Electrostatic approximations

The electric and the magnetic fields in Ω_2 are governed by Maxwell's equations [65]. Since the characteristic time scale of mechanical deformations is much larger than that of inertia effects in Maxwell's equations, therefore we neglect time dependence of electric and magnetic fields there by eliminating coupling between magnetic and electric fields. Henceforth we consider electric fields only, and assume that a scalar potential $\phi(x_i, t)$ exists. The electric field E_i^{elec} is given by

$$E_i^{elec} = -\frac{\partial \phi}{\partial x_i} \tag{5}$$

1.2.3. Constitutive relations

Even though the problem formulation and the analysis technique are applicable to a general material, for simplicity we presume that the deformable electrode is comprised of a neo-Hookean material for which

$$T_{ij} = \lambda E_{ll}\delta_{ij} + 2\mu E_{ij} \tag{6}$$

where λ and μ are elastic constants for the material of the body Ω_1, and E_{ij} is the Almansi-Hamel strain tensor defined as

$$E_{ij} = \frac{1}{2}\left(\delta_{ij} - \left(F^{-1}\right)_{li}\left(F^{-1}\right)_{lj}\right). \tag{7}$$

Note that equation (7) considers all geometric nonlinearities, including the von Kármán nonlinearity. With the constitutive assumption (6), the balance of moment of momentum equation (3) is identically satisfied; and only geometric nonlinearities are considered. Material damping due to viscous effects can be incorporated by modifying the constitutive relation (6).

1.2.4. Simplified governing equations

Assuming that there are no free charges in ω_2 the electric potential distribution in the current configuration is governed by the Laplace equation

$$\frac{\partial^2 \phi}{\partial x_i \partial x_i} = 0 \text{ in } \omega_2. \tag{8}$$

Therefore, equations (2) and (8) constitute governing equations for the MEMS. Substitution for E_{ij} from equation (7) into equation (6) and the result into equation (4) gives the first Piola-Kirchhoff stress tensor in terms of displacement field u_i defined as

$$u_i(X_l, t) = x_i - X_i(X_l, t). \tag{9}$$

Substitution from equations (6) and (9) into equation (4) and the result into equation (2) gives a set of coupled nonlinear PDEs for the determination of the displacement field. Knowing the displacement field, the present mass density can be found from equation (1).

1.2.5. Initial and boundary conditions

We assume that initially the deformable electrode is at rest, and occupies the reference configuration at time *t=0*. That is

$$u_i(X_l,0)=0 \tag{10}$$

and

$$v_i(X_l,0)=0. \tag{11}$$

For equation (8)

$$\phi \text{ is specified as non-zero on } \gamma_1 \tag{12}$$

$$\text{and } \phi = 0 \text{ on } \gamma_2. \tag{13}$$

For equation (2)

$u_i(X_l, t)$ is specified on Γ_{1u} for all t and

$$\hat{T}_{ji} N_j = T^0_i \text{ on } \Gamma_{1t} \text{ for all } t. \tag{14}$$

Here N_i is an outward unit normal vector on Γ_{1t} and T_i^0 is the electrostatic traction given by

$$T_i^{\,0} = \frac{(\sigma_{sur})^2}{2\varepsilon_0} J(F^{-1})_{ji} N_j \tag{15}$$

$$\sigma_{sur} = -\varepsilon_0 \frac{\partial \phi}{\partial x_i} n_i . \tag{16}$$

In equations (15) and (16) σ_{sur} is the charge density on the surface of the deformed electrode and n_i is an outward unit normal vector on γ_{1t}. Note that the coupling between equations (2) and (8) is through equations (14), (15) and (16)**.**

1.2.6. Numerical solution of the initial-boundary-value problem

We seek an approximate solution of the nonlinear coupled initial-boundary-value problem defined by equations (2) and (8) - (16). The FEM is employed to solve the linear momentum equation (2), because previous research [11] has shown that, at least at the present time for transient problems, the FEM is computationally more efficient than a meshless method. To solve Laplace's equation the BEM is used because it can easily consider the semi-infinite domain ω_2. The FEM and the BEM are described in [108, 75].

We take the inner product of both sides of equation (2) with a test function V_i which vanishes on Γ_{1u}, and integrate both sides of the resulting equation over the domain Ω_1 to obtain

$$\int_{\Omega_1}\left(\frac{\partial \hat{T}_{ji}}{\partial X_j}+\rho_0 f_i\right)V_i d\Omega=\int_{\Omega_1}\rho_0\ddot{u}_i V_i d\Omega. \tag{17}$$

Using the chain rule of calculus, the divergence theorem, and the natural boundary condition (14), we get

$$\int_{\Omega_1}\rho_0\ddot{u}_i V_i d\Omega=\int_{\Gamma_{1t}}T_i^0 V_i d\Gamma-\int_{\Omega_1}\left(\hat{T}_{ji}\frac{\partial V_i}{\partial X_j}-\rho_0 f_i V_i\right)d\Omega. \tag{18}$$

We express the test function and the trial displacement in terms of basis functions $\psi_a(X_l)$, a = *1,2, …* as $V_i(X_l)=\overline{V}_{ai}\psi_a(X_l)$, $u_i(X_l,t)=\bar{u}_{bi}(t)\psi_b(X_l)$, *a, b = 1,2, …,*

where $\bar{u}_{bi}$ is the value of u_i at node *b*, and conclude from equation (18) the following

$$M_{ab}\ddot{\bar{u}}_{bi}=\hat{F}_{ai}\ , i=1, 2, 3 \tag{19}$$

where

$$M_{ab}=\int_{\Omega_1}\rho_0\psi_b\psi_a d\Omega \tag{20}$$

and

$$\hat{F}_{ai}=\int_{\Gamma_{1t}}T_i^0\psi_a d\Gamma-\int_{\Omega_1}\left(\hat{T}_{ji}\frac{\partial\psi_a}{\partial X_j}-\rho_0 f_i\psi_a\right)d\Omega\ . \tag{21}$$

Note that $\hat{F}_{ai}$ depends on $\hat{T}_{ij}$, which is related to u_i through the constitutive relation (6) and the strain displacement relation (7), and T^0_i, which depends on the charge distribution on the surface of the electrode through equations (15) and (16).

Using the identity

$$[M]\frac{d}{dt}\{\bar{u}\}-[M]\{\dot{\bar{u}}\}=\{0\} \tag{22}$$

equation (19) can be written in the matrix (or the state space) form as

$$\begin{bmatrix} [M] & 0 \\ 0 & -[M] \end{bmatrix} \frac{d}{dt} \begin{Bmatrix} \{\dot{\bar{u}}\} \\ \{\bar{u}\} \end{Bmatrix} + \begin{bmatrix} 0 & 0 \\ [M] & 0 \end{bmatrix} \begin{Bmatrix} \{\dot{\bar{u}}\} \\ \{\bar{u}\} \end{Bmatrix} = \begin{Bmatrix} \{\hat{F}\} \\ \{0\} \end{Bmatrix}. \tag{23}$$

Equation (23) is integrated with respect to time by using the subroutine LSODE (Livermore Solver for ODEs) [77].

The salient feature of our FE formulation is that no assumption has been made with regard to the constitutive relation, which relates the first Piola-Kirchhoff stress tensor to the displacement gradient and/or the velocity gradient. Therefore, a wide class of materials, such as linear and nonlinear elastic, viscoelastic, and viscoplastic, can be considered for the MEM electrode of arbitrary geometry.

The solution of equation (8) in ω_2 is [75]

$$\phi(\mathbf{x_0}) = -\frac{4\pi}{\alpha} \int_{\gamma_1} G(\mathbf{x},\mathbf{x_0}) [n(\mathbf{x}).\nabla\phi(\mathbf{x})] d\Gamma_1(\mathbf{x}) + \frac{4\pi}{\alpha} \overset{PV}{\int_{\gamma_1}} \phi(\mathbf{x}) [n(\mathbf{x}).\nabla G(\mathbf{x},\mathbf{x_0})] d\Gamma_1(\mathbf{x}). \tag{24}$$

where $\mathbf{x}$ and $\mathbf{x_0}$ are the field point and the source point respectively, α the external angle at $\mathbf{x_0}$, ∇ the gradient operator with respect to $\mathbf{x}$, *PV* over the integration sign indicates the Cauchy principal value of the integral, and $G(\mathbf{x},\mathbf{x}_0)$ is Green's function of the first kind.

When analyzing a plane strain problem in the x_1x_3 - plane, we set $x_2=X_2$ and solve the mechanical problem for u_1 and u_3. For studying a plane stress problem in the x_1x_3 - plane, we set $T_{22} = 0$ in equation (6), solve the resulting equation for E_{22}, substitute for E_{22} in equations for T_{11}, T_{33} and T_{13}, and solve the mechanical problem for displacements u_1 and u_3. For both plane stress and plane strain problems we solve the electrical problem in the x_1x_3 – plane and use the following Green's function

$$G(\mathbf{x},\mathbf{x_0}) = -\frac{1}{2\pi}\ln(r_{dis}) + \frac{1}{2\pi}\ln(r_{dis}^{\mathrm{Im}}) \tag{25}$$

where $r_{dis} = |\mathbf{x}-\mathbf{x_0}|$, $r_{dis}^{\mathrm{Im}} = |\mathbf{x}-\mathbf{x}_0^{\mathrm{Im}}|$ with $\mathbf{x_0} = (x_1^0, x_3^0)$ and $\mathbf{x}_0^{\mathrm{Im}} = (x_1^0, -x_3^0)$. The first term on the right hand side of equation (25) is the free space Green's function for the source point $\mathbf{x_0}$, and the second term is Green's function for the source point $\mathbf{x}_0^{\mathrm{Im}}$ which is the image of $\mathbf{x_0}$ with respect to the plane $x_3=0$. Therefore, $G(\mathbf{x}, \mathbf{x_0})$ vanishes on Γ_2 and satisfies boundary condition (13). The boundary integral equation (24) holds only on γ_1.

In the aforementioned problem formulation, the linear momentum equation is written in the Lagrangian description of motion, and Laplace's equation for the electric field in the Eulerian description of motion. De and Aluru [32] have written both equations in the Lagrangian description of motion, employed Newton's method to solve ODEs arising from the weak formulation of the problem, and computed analytically the Jacobian matrix. This makes the resulting numerical algorithm computationally less intensive. However, one of our goals is to keep the FE formulation general enough to include a wide class of materials for the deformable electrode that makes the analytical evaluation of the Jacobian matrix impractical. We use LSODE with the Adam-Moulton method [77] to integrate the coupled nonlinear ODEs (23) that does not require the evaluation of the Jacobian matrix, and adjusts the time step adaptively to compute the solution within the prescribed absolute and relative tolerances.

1.3. Results from continuum mechanics approach

Based on the formulation given above, we have developed a computer code to find an approximate solution of the coupled nonlinear initial-boundary-value problem. It uses 8-node serendipity quadrilateral elements with 3 x 3 Gauss points for studying 2-D structural problems and uses 2-node line elements with one collocation point at the centroid of the element and 12 Gauss points for computing the electric flux $n(\mathbf{x}).\nabla\phi(\mathbf{x})$ on the boundary of the deformable electrode. Since, the BE has only one collocation point, the electric flux is constant over the element and is discontinuous across the inter element boundary. Therefore, discontinuities in the electric flux at sharp corners of the deformable electrode can be easily captured, as the variation of the electric flux over elements on both sides of a corner need not be continuous at the corner. Boundary elements with linear or quadratic variation of the electric flux need special treatment to capture discontinuities at a corner [95, 60]; e.g. see discontinuous elements and corner problems in [20].

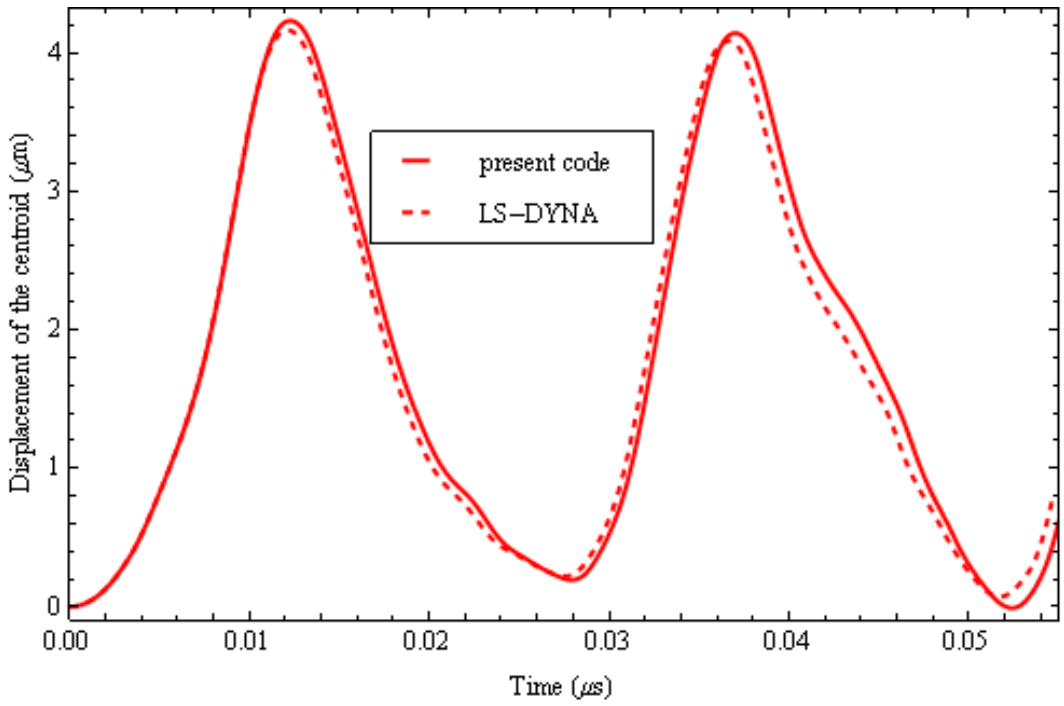

Figure 3. Time histories of the displacement u_3 of the centroid of the fixed-fixed beam under a body force f_3 = 150 kN/mm^3.

The mass matrix is lumped by using the special lumping technique. In LSODE, the relative and the absolute tolerances are set equal to 10^{-6}. Results for each problem are computed with at least two meshes to assess the order of error in the numerical solution. After every time step coordinates of nodes for the BE mesh are updated, boundary integral equation (24) is solved for the electric flux $n(\mathbf{x}).\nabla\phi(\mathbf{x})$ along the boundary of the deformable electrode, and surface tractions (15) due to the Coulomb pressure are computed and applied to surfaces of the deformable electrode. The FE and the BE codes are fully integrated into one software and no human intervention is needed.

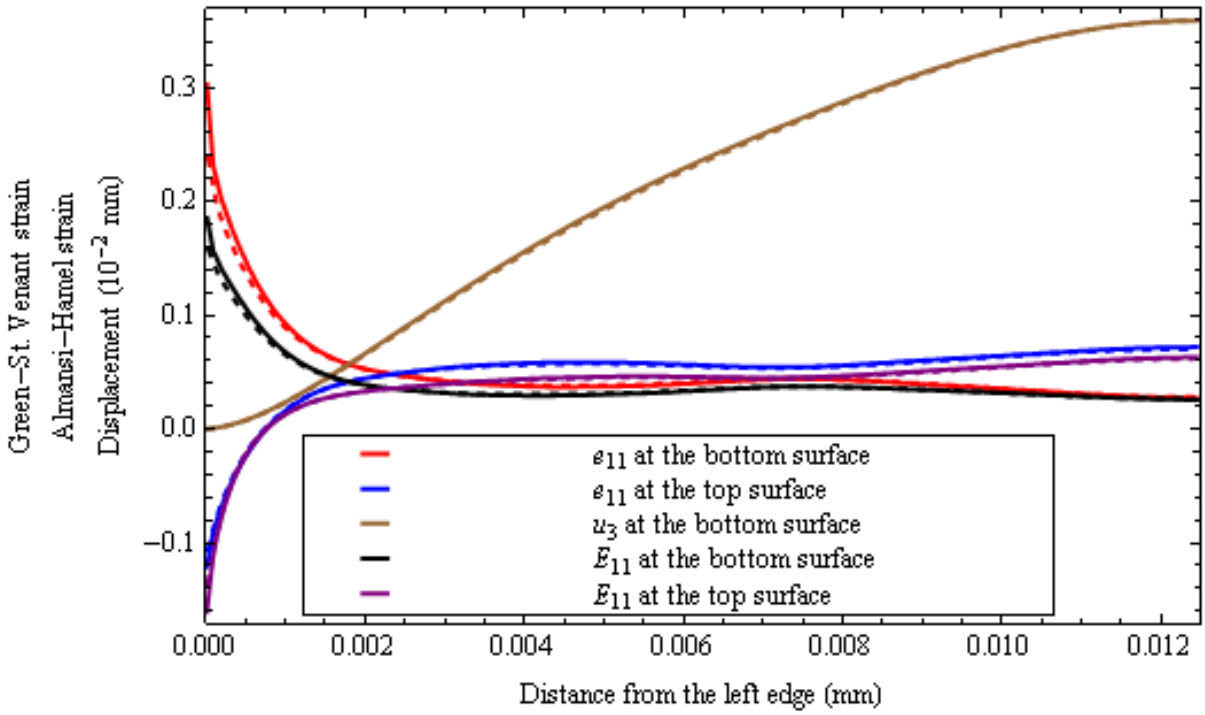

Figure 4. Variation of the Green-St. Venant strain e_{11} and the Almansi-Hamel strain E_{11} along the top and the bottom surfaces of the beam, and of the displacement u_3 along the bottom surface of the beam at $t = 0.0102\ \mu s$; results for only the left half of the beam are shown. Solid lines: Present code, dashed lines: LS-DYNA.

1.3.1. Code verification

The code has been verified by comparing computed results for three problems with those obtained by numerically analyzing the same problems with commercial codes. The first problem studied is a 25 μm long, 10 μm wide, and 0.5 μm thick fixed-fixed beam made of an isotropic neo-Hookean material with ρ_0 = 2231 kg/m^3, λ = 12.05 GPa and μ = 79.27 GPa. The magnitude 150 kN/mm^3 of the body force in x_3 direction is unusually high to induce large deformations in the beam so that effects of nonlinear strain-displacement relation (7) can be delineated. The computed results are compared with those derived by using the commercial FE software LS-DYNA by implementing in it the constitutive relation (6) through the user supplied subroutine option. Deformations of one-half of the beam have been studied due to the symmetry of the

problem. The FE mesh for the plane strain problem has 60 x 10 8-node serendipity elements along half of the length and the thickness of the beam. The element dimension along the beam length is varied gradually and the element length at the fixed end of the beam is 1/5 of that at the mid-span. A similarly graded 120 x 20 4-node FE mesh is employed to solve the problem with LS-DYNA. The FE mesh was successively refined to obtain converged solutions and results with only the finest mesh, described above, are given here. As can be seen from results plotted in figure 3, time histories of the centroidal deflection computed with our code agree very well with that obtained by using LS-DYNA. The variation of the E_{11} component of the Almansi-Hamel strain tensor, the e_{11} component of the Green-St. Venant strain tensor defined by

$$e_{ij} = \frac{1}{2}\left(F_{li}F_{lj} - \delta_{ij}\right) \tag{26}$$

and the displacement u_3 along the beam span at t = 0.0102 μs are exhibited in figure 4. It is clear that results computed with our code agree very well with those obtained with LS-DYNA. At points near the supports E_{11} and e_{11} exceed 0.2. However, along most of the beam span the axial strain is about 0.01. Results from the Euler-Bernoulli beam theory will significantly under estimate the axial strain at points near the clamped edges.

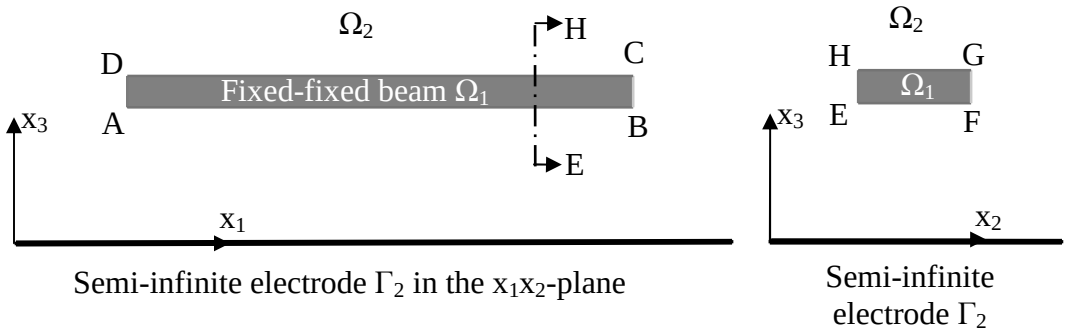

Figure 5. The long-section (a) and the cross-section (b) of the deformable electrode suspended over the rigid semi-infinite electrode.

The second problem analyzed is also a fixed-fixed 1000 μm x 2.4 μm x 30 μm (L x b x h) beam (cf. figure 5) suspended 10.1 μm above a rigid electrode but we now compute the Coulomb pressure distribution due to the electric potential difference between the rigid electrode and the

beam. For the silicon beam we take ρ_0 = 2231 kg/m^3, λ = 97.5 GPa and μ = 65.0 GPa. The domain Ω_2 is considered as vacuum with ε_0 = 8.854X10^{-12} F/m, and the electric potential difference between the two electrodes equals 10 V. The boundary of the long section of the beam is discretized using two different BE meshes, 60 x 4 and 3000 x 400 (elements along AB and CD x elements along BC and DA). To model the exterior domain Ω_2 in the FE commercial code ANSYS we use PLANE121 and INFIN110 elements (see figure 6). Values of r_0 and l_0 in figure 6 were gradually increased and the FE mesh was refined to obtain converged solutions. We compare in figure 7 the Coulomb pressure on edges AB, DC and BC of the beam. As exhibited in figures 7(a) and 7(b), the electrostatic pressure distribution along AB and DC from our code agrees well with that from ANSYS except near the corners, which could be due to the non-uniqueness of the unit normal at the corners. However, as shown in figure 7(c), mesh 1 failed to compute the Coulomb pressure distribution along the edge BC. Due to the very high aspect ratio (AB/BC = 1000/2.4 $\approx$ 417) a finer BE mesh is required to compute the Coulomb pressure distribution on sides BC and DA of the beam. The distribution of the electrostatic pressure on the bottom surface AB and on the top surface CD of the beam is more important than that on edges BC and AD since it induces the downward electrostatic pressure, which actuates the MEMS. Therefore, the BE meshes used here should suffice to compute the pull-in and the snap-through parameters of the MEMS.

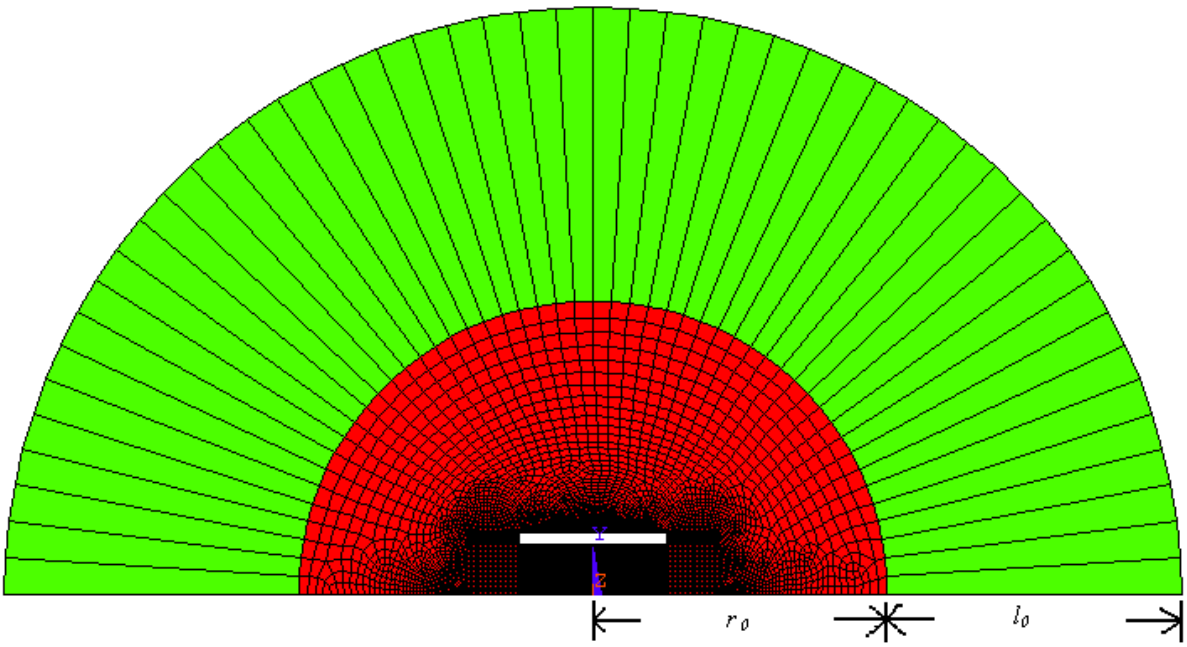

Figure 6. The mesh to study the electrostatic pressure on edges of the cross-section EFGH of the deformable electrode. PLANE121 elements in ANSYS are used to discretize the area (red) around the deformable beam up to radius r_0. Beyond the radius r_0 INFIN110 elements (green) are used up to a length of l_0 to take into account the infinite extent of the domain Ω_2; r_0 = 60 μm and l_0 = 60 μm are used. Similarly, r_0 = 2 mm and l_0 = 2 mm are used in the analysis of the long section ABCD of the beam.

Next, we compare in figure 8 the electrostatic pressure distribution on the boundary of a cross-section of the beam. The boundary of the cross-section of the beam is discretized using BE meshes consisting of 1000 elements along EF and GH and 100 elements along FG and HE. As exhibited in figures 8(a), (b) and (c), the electrostatic pressure distributions on EF, HG and FG from our code agree well with those from ANSYS except near the corners which could be due to the non-uniqueness of the unit normal at a corner. One can see that the electrostatic pressure along EF is not uniform because of the fringing fields due to the finite width and the finite height of the beam. The downward electrostatic pressure p_d per unit length of the beam can be computed by integrating the pressure along EF and HG. That is,

p_d = Total Coulomb pressure along EF – Total Coulomb pressure along HG = *0.151* Pa (27)

If we neglect the fringing fields then the pressure along the width EF of the beam is uniform and the downward pressure per unit length of the beam according to the PPA is given by

$$p_d = \frac{\varepsilon \hat{b} \hat{V}^2}{2\hat{g}_0^{\,2}} = 0.130\ Pa \tag{28}$$

which is 14 % less than the pressure obtained from the BEM solution. Therefore, for this case fringing fields cannot be neglected. The downward pressure/length according to the Mejis-Fokkema formula [13, 49] gives

$$p_d = \frac{\varepsilon \hat{b} \hat{V}^2}{2\hat{g}_0^{\,2}} \left(1 + 0.265 \left(\frac{\hat{g}_0 + \hat{h} z_0(\hat{x}) - \hat{w}(\hat{x})}{\hat{b}} \right)^{3/4} + 0.53 \left(\frac{\hat{d}}{\hat{b}} \sqrt{\frac{\hat{g}_0 + \hat{h} z_0(\hat{x}) - \hat{w}(\hat{x})}{\hat{d}}} \right) \right) = 0.157 \tag{29}$$

which is about 3.7 % more than that from the BE solution. Therefore, the beam problem can be analyzed as a 2-D problem in the $x_1 x_3$ - plane with acceptable errors if the electrostatic pressure found from the PPA is corrected with the Mejis-Fokkema formula.

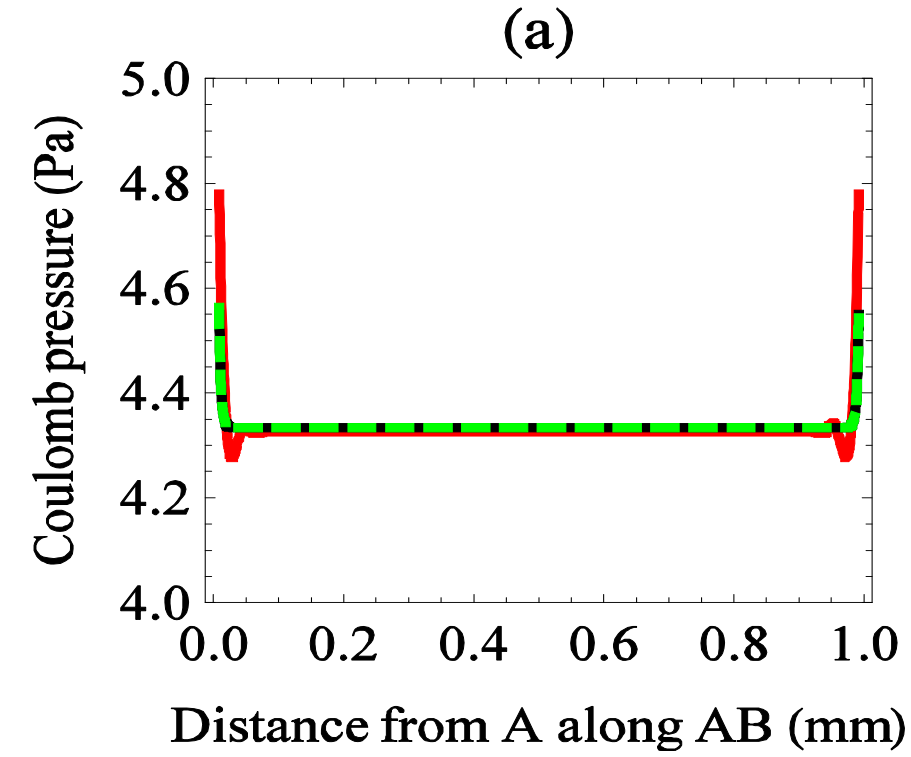
(a)
Coulomb pressure (Pa)
5.0
4.8
4.6
4.4
4.2
4.0
0.0
0.2
0.4
0.6
0.8
1.0
Distance from A along AB (mm)

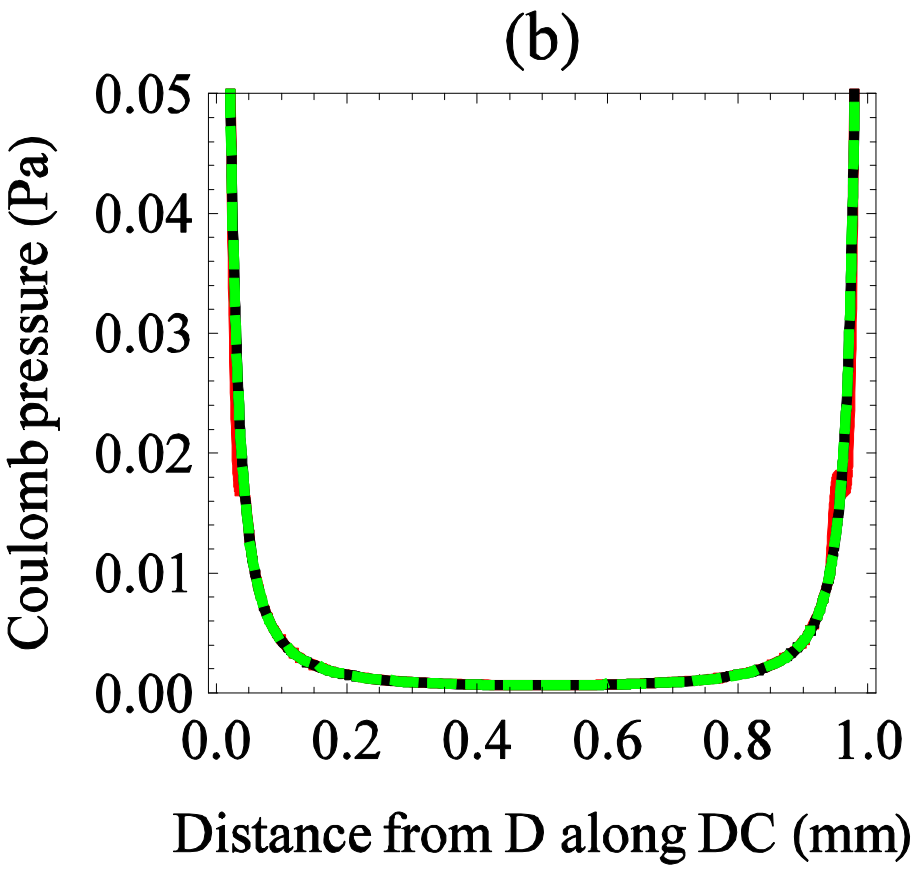
(b)
Coulomb pressure (Pa)
0.05
0.04
0.03
0.02
0.01
0.00
0.0
0.2
0.4
0.6
0.8
1.0
Distance from D along DC (mm)

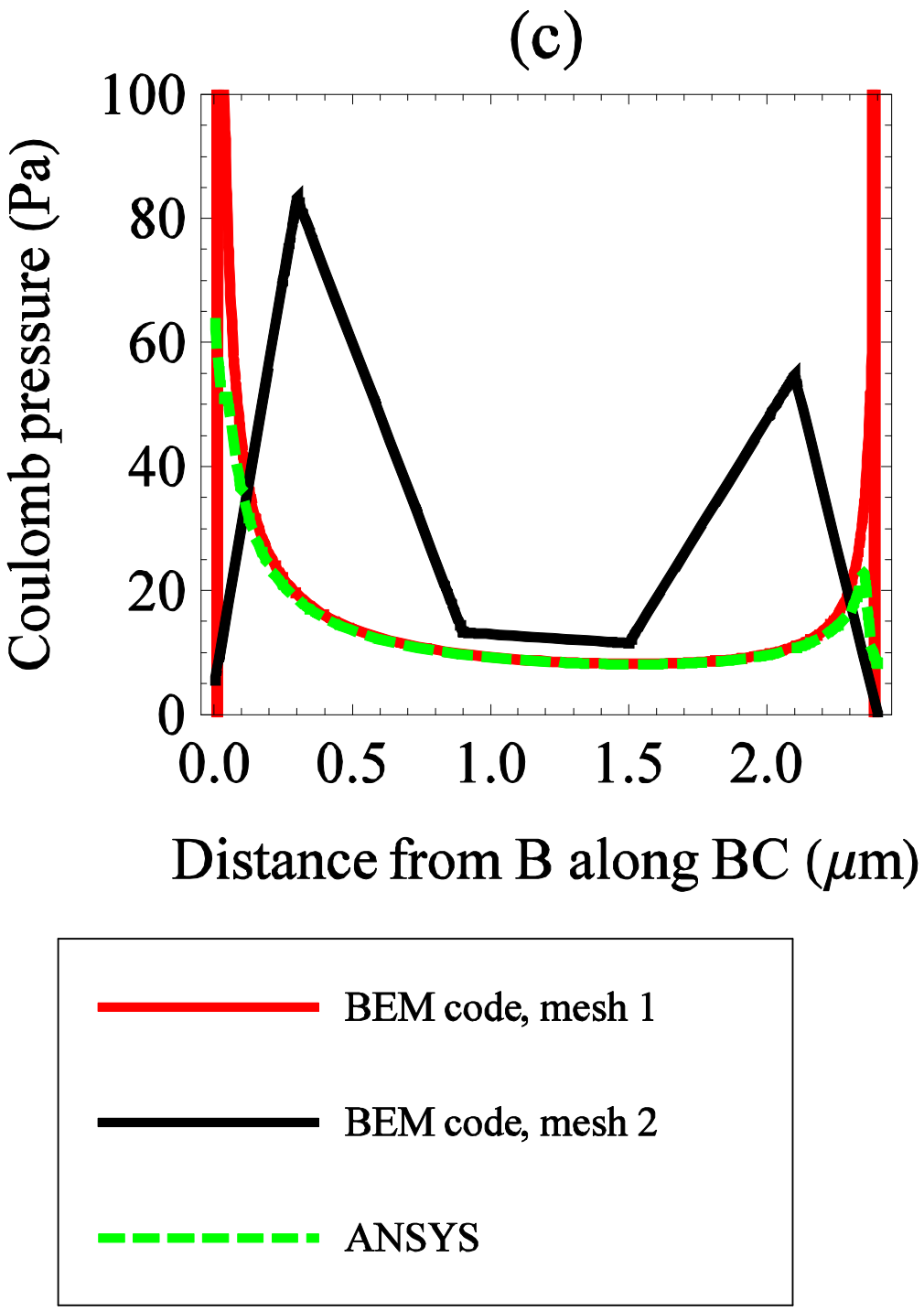

Figure 7. The Coulomb pressure distribution along boundaries AB, DC and BC of the beam (see ABCD in figure 5(a)); due to symmetry the electrostatic pressure distributions along BC and AD are the same.

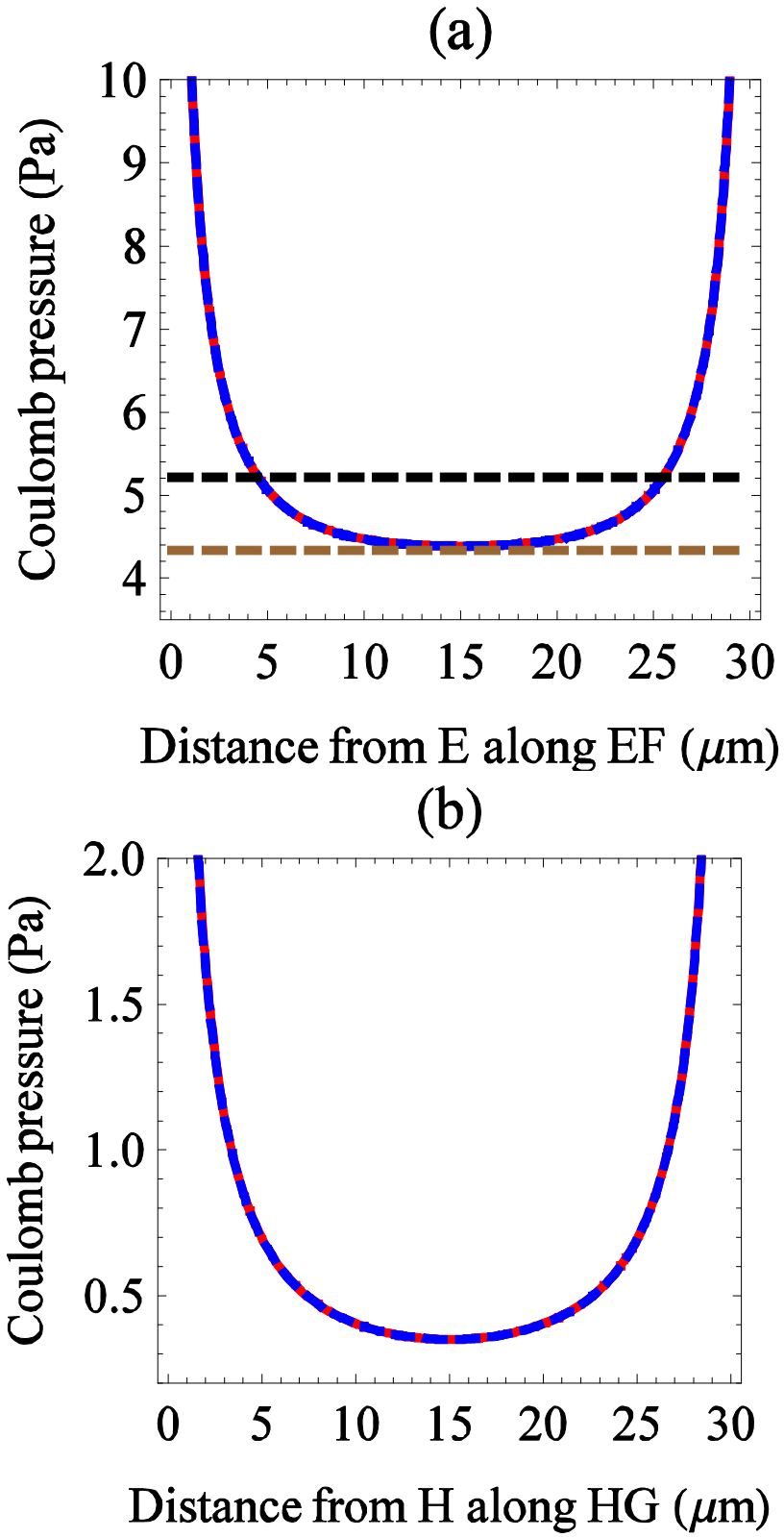
(a)
Coulomb pressure (Pa)
10
9
8
7
6
5
4
0
5
10
15
20
25
30
Distance from E along EF (μm)
(b)
Coulomb pressure (Pa)
2.0
1.5
1.0
0.5
0
5
10
15
20
25
30
Distance from H along HG (μm)

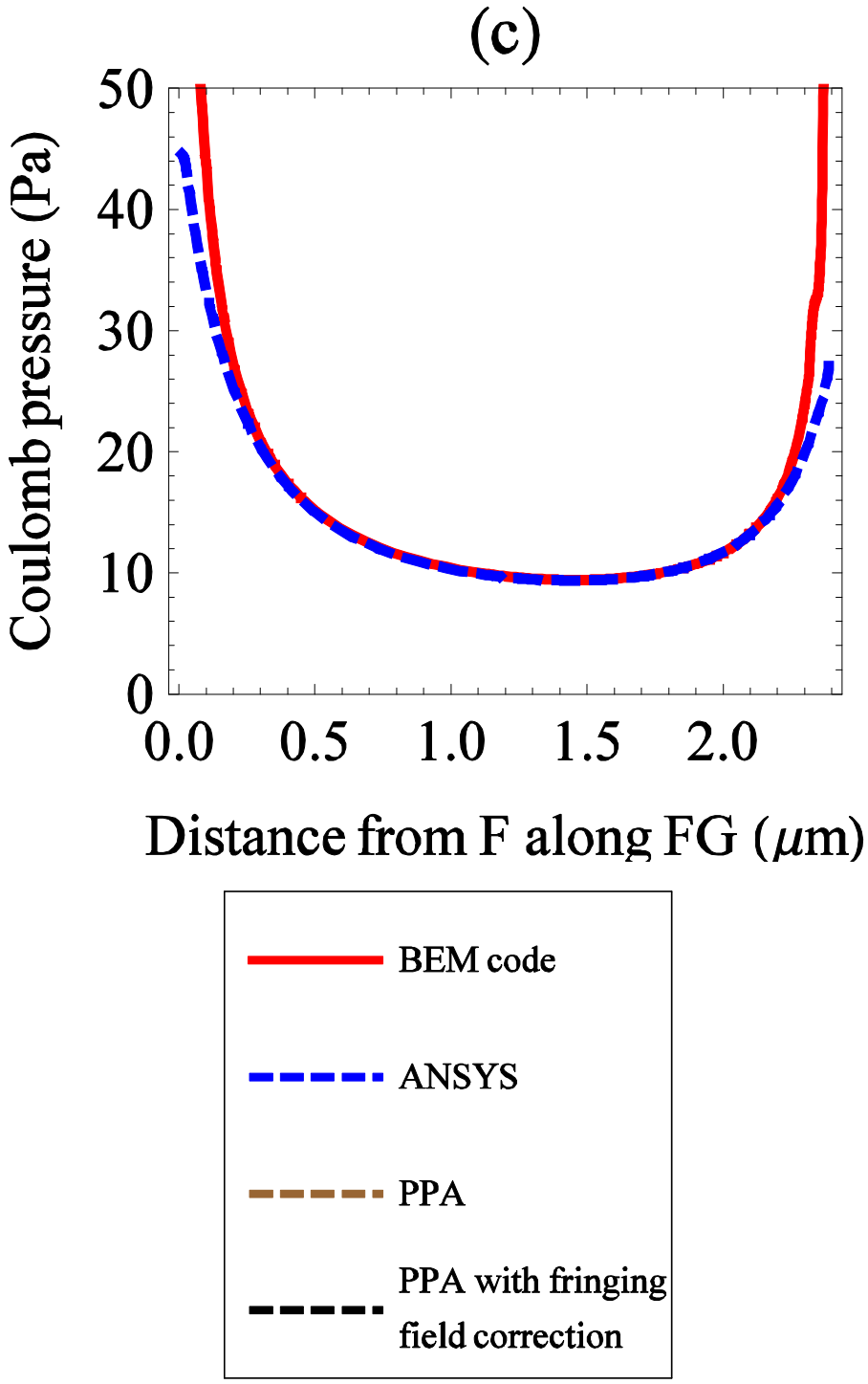

Figure 8. The Coulomb pressure distribution along the boundaries EF, HG and FG of the beam (see EFGH in figure 5(b)); due to symmetry the electrostatic pressure distributions along FG and HE are the same.

Next, we study transient deformations of a fixed-fixed 80 μm x 0.5 μm x 10 μm silicon beam suspended 0.7 μm above a flat rigid electrode due to a step electric potential difference applied to the two electrodes. This problem has been studied in [32] as a plane stress problem. However, as the ratio of the width to the height of the beam is 20, it should be considered as a plane strain problem. Here, we analyze it as both plane stress and plane strain problems to delineate differences between the two sets of results. Since, $\hat{g}_0/\hat{b}$ = 0.07 and $\hat{d}/\hat{b}$ = 0.05, fringing fields can be neglected [14]. To demonstrate the effect of the nonlinearity in the strain displacement relation (7), we also study the problem with the linear strain displacement relation

$$\hat{E}_{ij} = \frac{1}{2}\left(u_{i,j} + u_{j,i}\right) \tag{30}$$

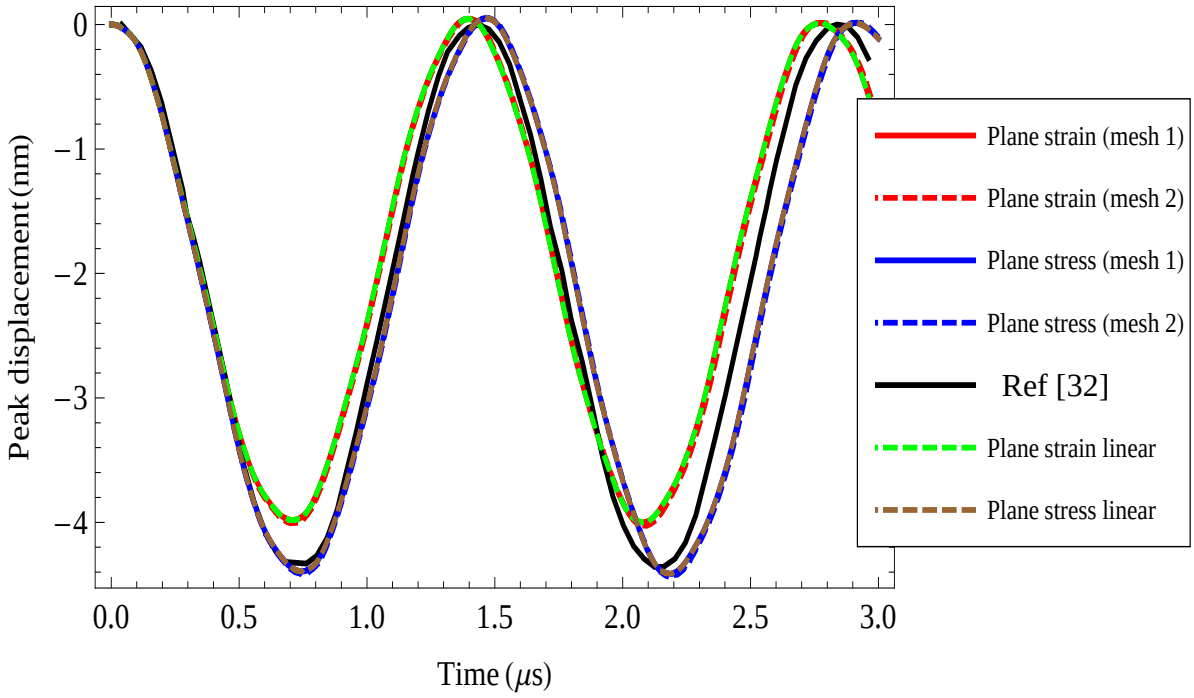

Figure 9. Time histories of the downward displacement of the centroid of the bottom surface of the fixed-fixed beam due to 2 V step potential difference between the rigid and the deformable electrodes. Plots of peak displacements from the linear and the nonlinear problems overlap.

Two FE meshes, 30 x 4 and 60 x 8 (number of elements along the length and the thickness respectively), and 136 and 272 BEs, respectively, are used to solve the 2-D problem. Figure 9 exhibits the time history of the downward displacement of the centroid of the bottom surface of the beam for an applied step electric potential difference of 2 V between the beam and the rigid electrode; results from our code for the plane stress problem agree well with those reported in [32]. Results from the two different meshes overlapped on each other. The maximum transverse displacement and the time period of oscillations from the plane strain analysis are about 10% less than those from the plane stress analysis. The nonlinearity in the strain-displacement relation has a negligible effect on both the amplitude and the time period of oscillations. Figure 10 shows the variation of the Cauchy stress T_{11} along the span of the beam at 0.7 μs. As the two meshes give virtually the same results, for subsequent analyses we use the first mesh. The magnitude of the axial stress near the fixed edges of the beam is more than twice of that at the midsection of the beam.

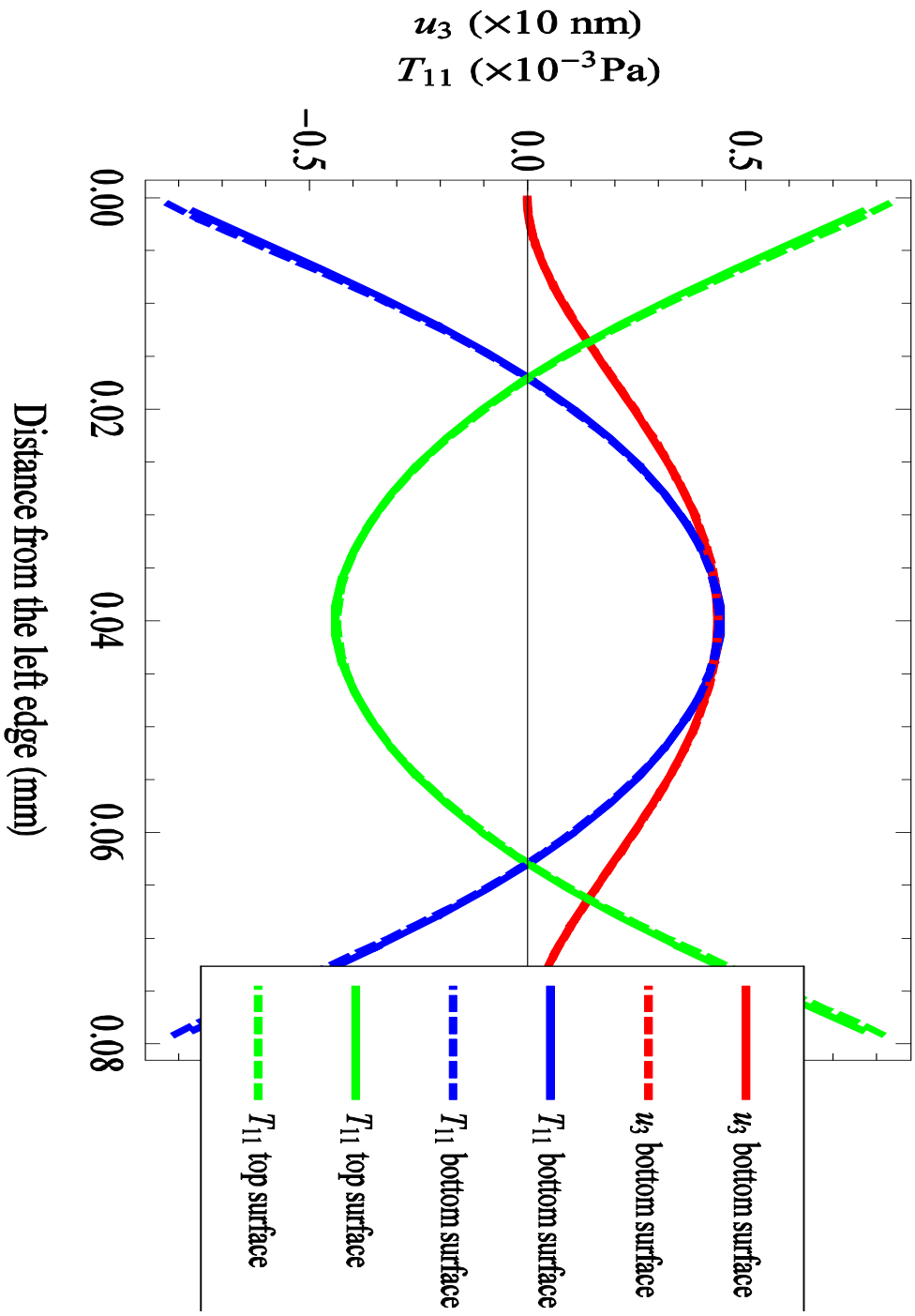

Figure 10. The variation of the Cauchy stress T_{11} and the displacement u_3 along the beam span at time t = 0.7 μs due to 2 V step potential difference between the rigid and the deformable electrodes; solid lines: mesh 1; dashed lines: mesh 2.

Figure 11 depicts the downward displacement of the centroid of the bottom surface of the beam versus time due to different applied step voltages. For the plane strain problem with the nonlinear strain displacement relation, the pull-in voltage is between 16.75 V and 17.0 V, since for the 16.75 V potential difference the peak deflection stays bounded but for the 17.0 V potential difference it becomes unbounded. By solving the problem for several values of the potential difference between 16.75 and 17.0 V, one can compute a better value of the pull-in voltage. For the plane stress approximation with the nonlinear strain displacement relation the pull-in voltage is found to be between 15.75 V and 16.00 V. The pull-in voltage for the plane stress problem reported in [32] is 15.7 V. For the plane strain approximation with the linear strain-displacement relation, the pull-in voltage is between 14.5 V and 14.75 V. The analysis with the linear strain-displacement relation underestimates the pull-in voltage by 13.4%. For the plane strain problem, the consideration of the nonlinear strain displacement relation increases the absolute maximum displacement before the pull-in instability to 0.39 μm (= 0.55 $\hat{g}_0$) from 0.34 μm (= 0.48 $\hat{g}_0$) obtained from the analysis of the linear problem. Using a spring-mass model the maximum pull-in displacement for a statically loaded micro-beam equals $0.33\,\hat{g}_0$ [62]. The spring-mass model accounts for neither the nonlinear strain-displacement relation nor the actual distribution of the Coulomb pressure. Tilmans and Legtenberg [94] accounted for the actual deflection distribution but neglected nonlinear mid-plane stretching of the micro-beam and obtained a pull-in displacement of $0.4\,\hat{g}_0$ in a static problem. Using a reduced order model Abdel-Rahman [4] showed that the pull-in displacement equals $0.39\,\hat{g}_0$ in a static problem if both the mid-plane stretching and the actual distribution of the Coulomb pressure are considered.

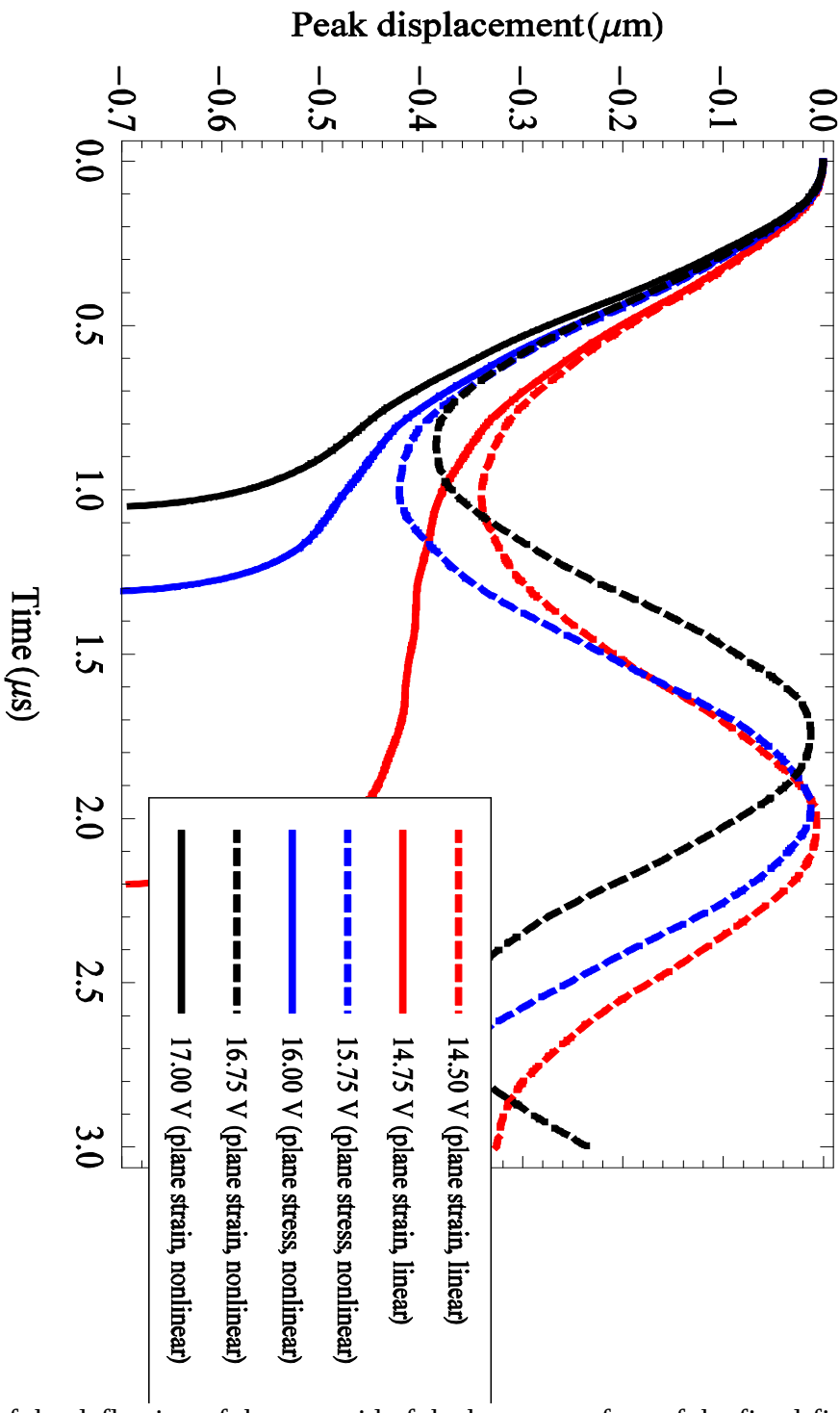

Figure 11. Time histories of the deflection of the centroid of the bottom surface of the fixed-fixed beam for different step applied electric potentials from the nonlinear and the linear strain-displacement relations.

1.3.2. Fixed-fixed beam as MEMS

In order to compare the pull-in parameters of a beam with those of an arch in the next subsection, we study transient deformations of a fixed-fixed silicon beam of length = 1 mm, width = 30 μm and height = 2.4 μm, initial gap = 10.1 μm. For a step potential difference of 90 V, the 30 x 2 and 50 x 4 FE meshes (elements along the length and the thickness directions, respectively) and having 128 and 216 BEs gave maximum downward displacements of the centroid of the bottom surface equal to 6.188 and 6.247 μm, respectively. The variation of the Cauchy stress T_{11} along the span of the beam at time t = 15 μs is exhibited in figure 12. It is clear that the two FE meshes give virtually the same stresses, and for subsequent analyses, we use the first mesh. Whereas the distribution of axial stress T_{11} on the midsurface of the beam is nearly uniform and equals ~ 0.015 MPa, the magnitude of T_{11} at points on the top and the bottom surfaces that are near the clamped edges equal ~ 0.07 and ~ 0.04 MPa respectively. Furthermore, distributions of T_{11} on the top and the bottom surface are not uniform.

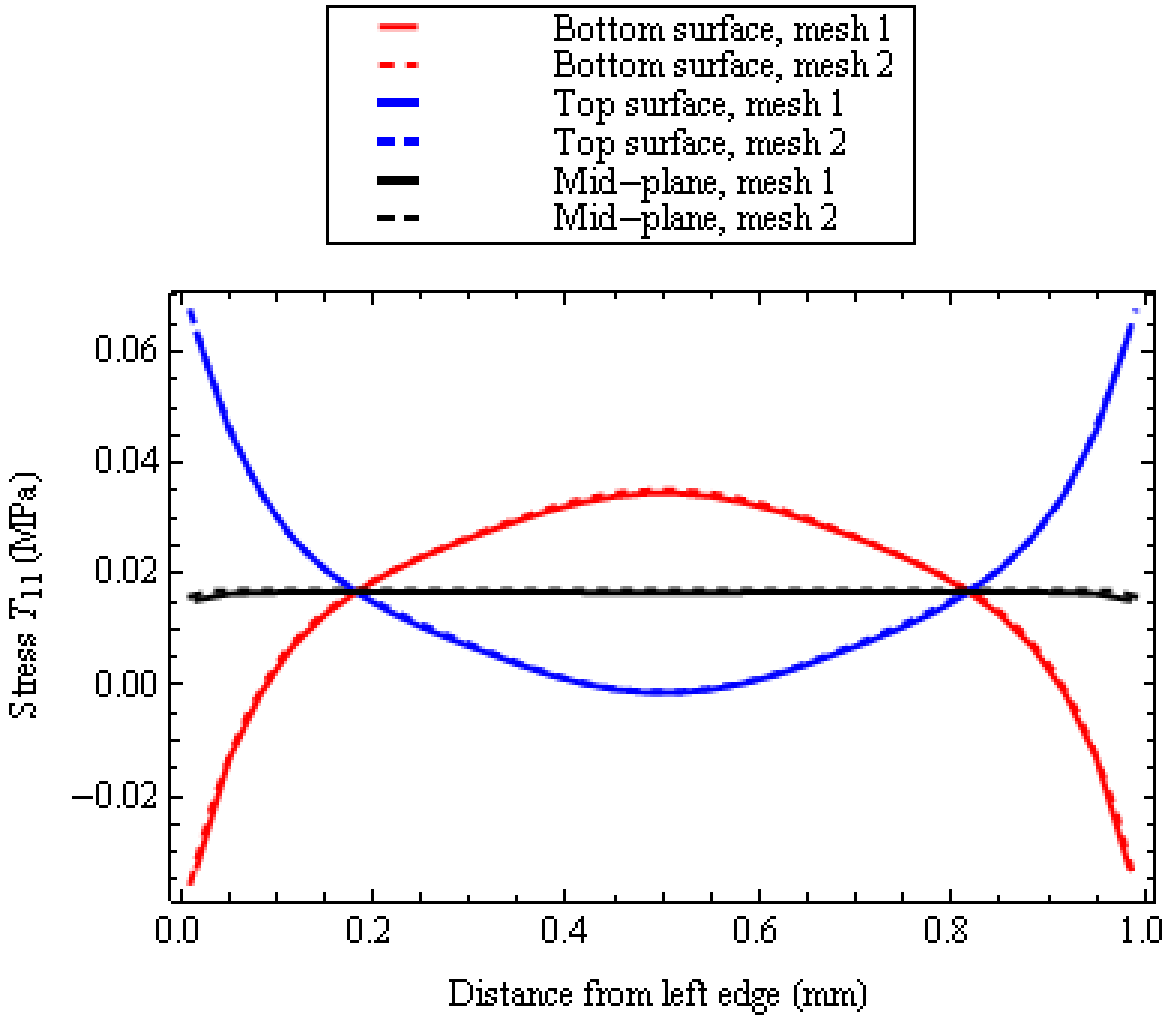

Figure 12. Variation of Cauchy stress T_{11} along the beam span at time $t = 15\ \mu s$ due to 90 V step potential difference between the rigid and the deformable electrodes.

Krylov et al. [52] have studied static deformations of this beam both experimentally and numerically with a reduced order model, and their values of the pull-in voltage are 100.0 V and 118.5 V respectively. Figure 13 exhibits the peak downward deflection of the centroid of the beam bottom surface due to different step potential differences. The pull-in voltage for the dynamic problem is found to be between 99.0 V and 100.0 V since for the 99.0 V potential difference the peak deflection stays bounded but for the 100.0 V potential difference it becomes unbounded. By solving the problem for several values of the potential difference between 99.0 and 100.0 V, one can compute a better value of the pull-in voltage. We note that the presently computed pull-in voltage is very close to Krylov et al.'s [52] experimental value. The pull-in

voltage is found to be between 49.0 V and 50.0 V from the analysis of the linear problem, and is nearly one-half of that for the nonlinear problem. Thus, assumption of the linear strain displacement relation gives the pull-in voltage equal to one-half of that obtained with the nonlinear strain displacement relation. We note that the difference in the pull-in voltage from the linear and the nonlinear strain-displacement relations are problem specific; for the 80 μm x 0.5 μm x 10 μm beam studied above, the difference in the two pull-in voltages was only 12%. The pull-in displacements for the 80 μm x 0.5 μm x 10 μm and the 1000 μm x 2.4 μm x 30 μm beams equal $0.78\,\hat{d}$ and $3.25\,\hat{d}$ respectively.

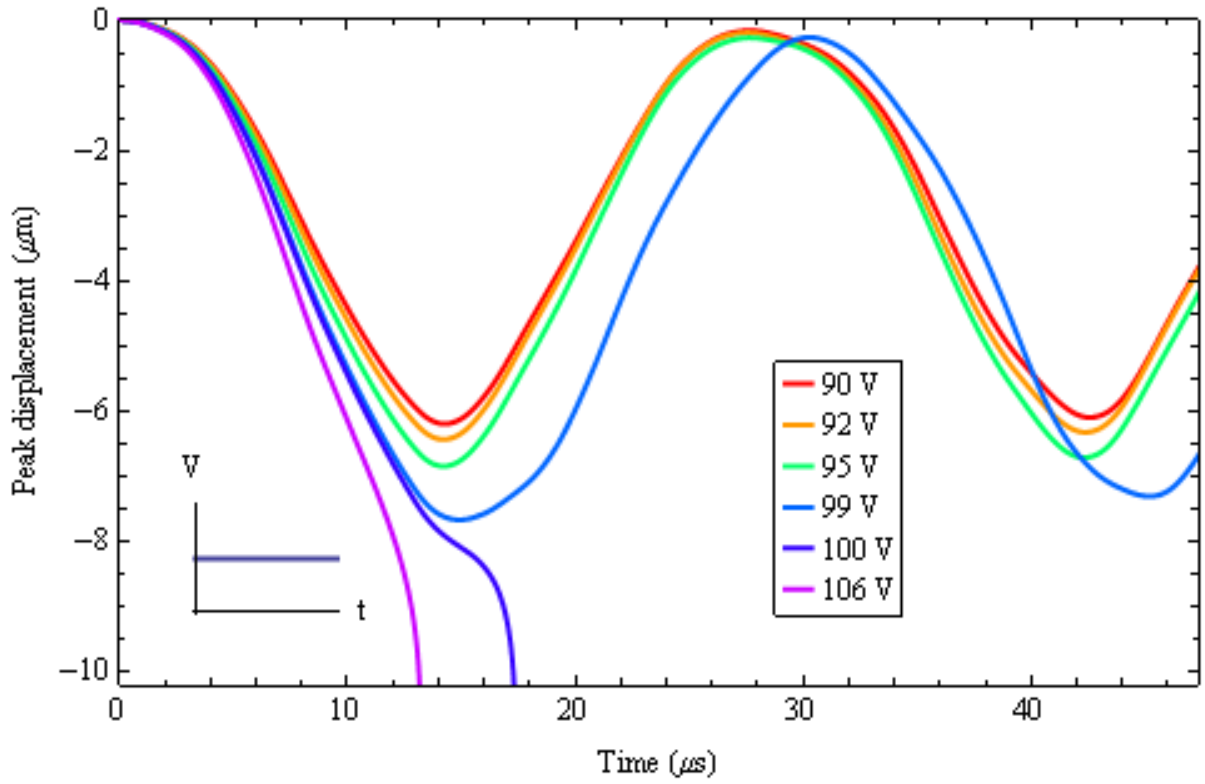

Figure 13. Time histories of the deflection of the centroid of the bottom surface of the fixed-fixed beam for different values of the step electric potentials from analysis of the nonlinear problem.

To delineate the effect of the rate of loading on the pull-in parameters we increase the electric potential difference between the beam and the rigid electrode linearly with time. Figure 14 shows the peak deflection of the centroid of the beam versus the applied voltage for different rates of

increase of the applied voltage. Experimental data and the bifurcation curve derived with a reduced order model [49] are also exhibited. As summarized in Table 1, the pull-in voltage and the pull-in deflection decrease with a decrease in the rate of increase of the potential difference. The pull-in voltage increases by 2.7% with a ten-fold increase in the rate of increase of V from 0.06 V/μs to 0.6 V/μs. However, there is about 16% decrease in the pull-in voltage when the applied potential difference is changed from linearly varying to a step load. The pull-in voltage of 113 V for the slowest loading rate considered is about 13 % more than the experimental static pull-in voltage and about 4.6 % less than the numerical static pull-in voltage reported in [13, 49] with a reduced order model and the Coulomb pressure given by the PPA with the fringing field correction. The present work finds the Coulomb pressure from the charge distribution of the electric field, and applies it along the normal to the bounding surface in the deformed configuration. For both step and linearly increasing potential difference, the use of the linear strain displacement relation underestimates the pull-in voltage by about 50% and the pull-in deflection by as much as 70%.

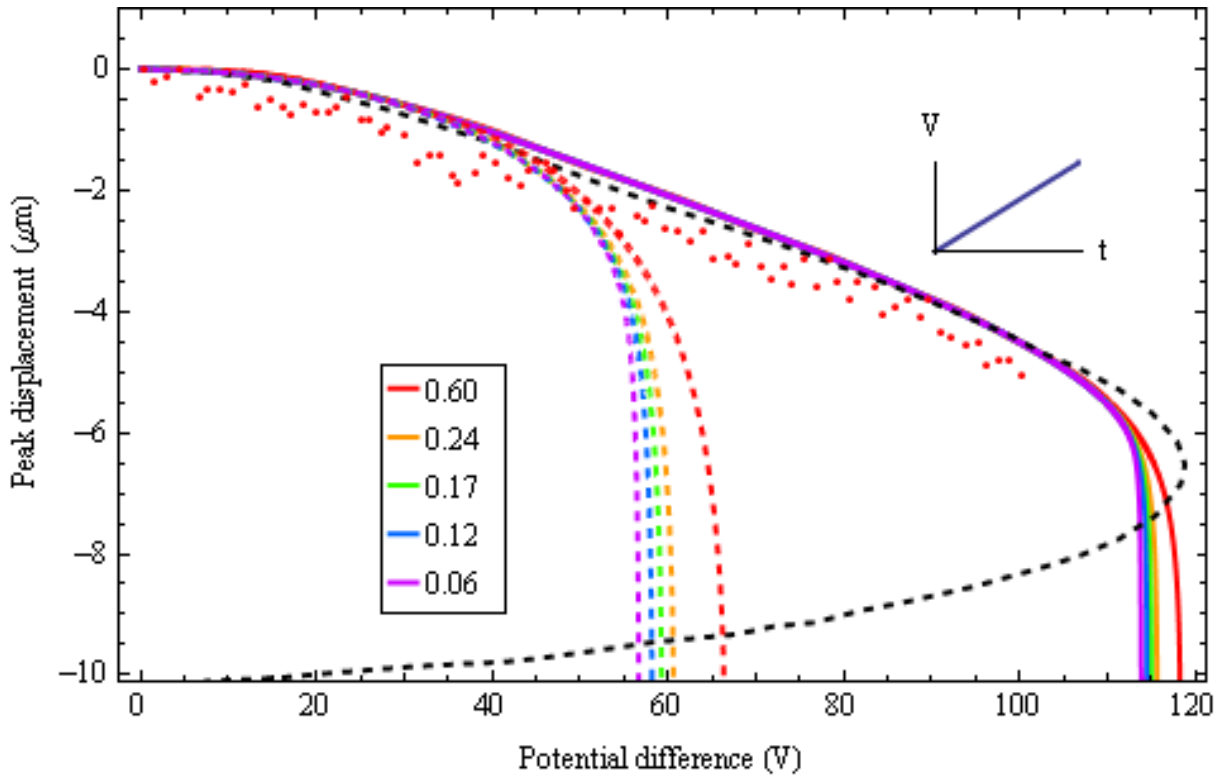

Figure 14. The deflection of the centroid of the bottom surface of the fixed-fixed beam versus the applied voltage for different rates ($V/\mu s$) of increase of the voltage. Red dots represents experimental data from [49] for static deformations of the beam, and the black dashed line is the bifurcation curve reported in [49]. Solid and dashed lines correspond, respectively, to results from analyses of the nonlinear and the linear problems.

Table 1: Pull-in parameters for the fixed-fixed beam for different rates of the applied potential difference

Rate of applied potential difference (V/ μs)	*Nonlinear problem*		*Linear problem*	
	The pull-in voltage (V)	*The pull-in displacement (μm)*	*The pull-in voltage (V)*	*The pull-in displacement (μm)*
Step load	99.50	7.7	49.0	4.5
0.60	116.50	7.0	65.1	7.5
0.24	114.25	6.6	59.0	5.6
0.17	113.75	6.5	58.0	5.5
0.12	113.50	6.4	57.0	5.3
0.06	113.00	6.4	56.0	5.3
Experiment	100.00	5.0		
ROM[1] (static problem)	118.50	6.5		

[1] Reduced order model

1.3.3. Transient deformations of a bell shaped arch MEMS

Referring to figure 1, we consider a bell shaped silicon arch with base length $\hat{L}$ = 1 mm, width $\hat{b}$ = 30 μm, thickness $\hat{d}$ = 2.4 μm, initial gap $\hat{g}_0$ = 10.1 μm, the arch rise $\hat{h}$ = 3.0 μm, and its bottom-surface described by $z_0(\hat{x}) = \hat{h}\ sin^2(\pi\ \hat{x}/\hat{L})$. Values assigned to material parameters are the same as those for the beam of the last section. We analyze it as a plane strain problem, and consider the effect of fringing fields by increasing the traction T^0_i (cf. equation (15)) on the bottom surface of the arch due to the electrostatic force by a factor of

$$\left(1+0.265\left(\frac{z_0(\hat{x})+\hat{g}_0(\hat{x})-\hat{w}(\hat{x})}{\hat{b}}\right)^{3/4}+0.53\left(\frac{\hat{d}}{\hat{b}}\sqrt{\frac{z_0(\hat{x})+\hat{g}_0(\hat{x})-\hat{w}(\hat{x})}{\hat{d}}}\right)\right) \qquad (31)$$

in accordance with the Mejis-Fokkema formula [13, 49].

For a step potential difference of 60 V, the two 30 x 2 and 50 x 4 FE meshes (elements along the length and elements along the thickness directions, respectively) and having 128 and 216 BEs gave maximum downward displacements of the centroid of the bottom surface equal to 1.657 and 1.677 μm. The variations along the span of the arch of the Cauchy stress T_{11} on the top, the middle, and the bottom surfaces at time $t = 20$ μs are exhibited in figure 15. It is clear that the two FE meshes give virtually the same stresses, and for subsequent analyses, we use the first mesh. As for the beam, the maximum values of $|T_{11}|$ occur at points near the clamped edges; whereas T_{11} is essentially uniform on the midsurface of the arch and equals ~ -3 MPa, that at the edges equals ~ -16 MPa on the bottom surface and ~ 10 MPa on the top surface. Because of the curvature of the undeformed arch, maximum magnitudes of the compressive and the tensile axial stress are different.

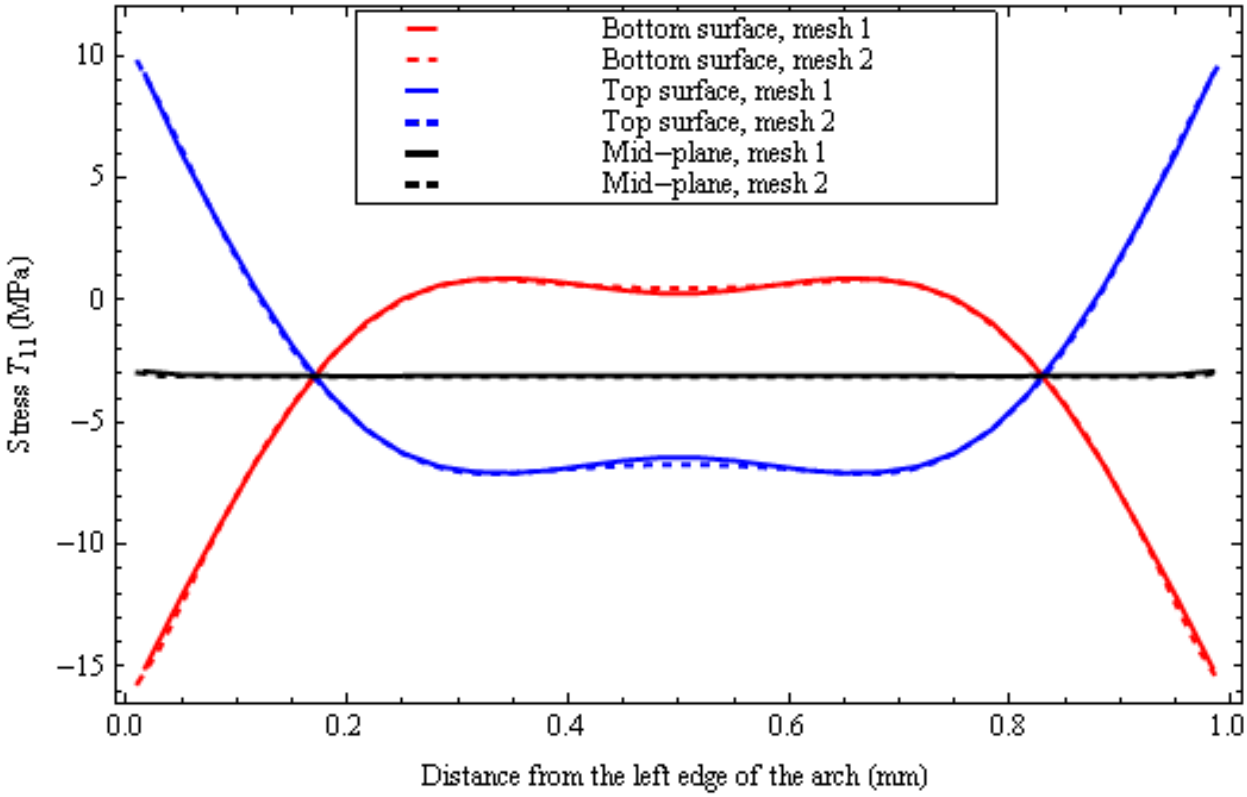

Figure 15. The Cauchy stress T_{11} along the span of the arch at the top, the bottom and the mid-plane at time $t = 20\ \mu s$ due to 60 V potential difference from the analysis of the plane strain nonlinear problem.

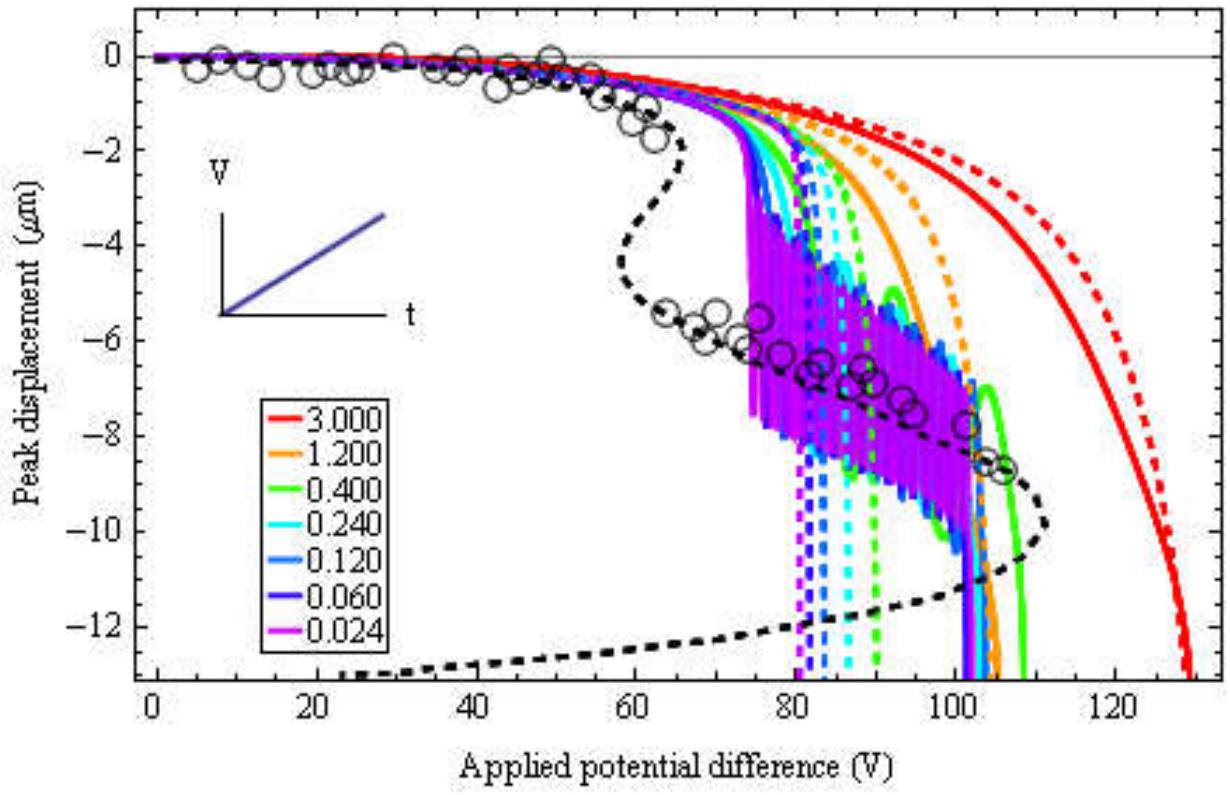

Figure 16. For different rates ($V/\mu s$) of increase of the potential difference, the downward displacement of the centroid of the bottom surface of the fixed-fixed bell shaped arch versus the applied potential difference. Black circles correspond to data from static experiments [49] and the black dashed line is the corresponding bifurcation curve reported in [49]. Solid and dashed lines correspond, respectively, to analysis of the nonlinear and the linear problems.

Figure 16 displays the peak displacement of the centroid of the bottom surface of the arch versus the applied voltage for different uniform rates of increase of the electric potential. Results from the analysis of the linear problem, experimental data [49] and the bifurcation curve derived with a reduced order model in [49] are also exhibited. The first sudden increase in the peak displacement from the analysis of the nonlinear problem at the potential difference of ~ 75 V corresponds to the snap-through instability of the arch. For low to medium rates of increase of the applied potential difference (i.e. ≤ 0.4 $V/\mu s$), the arch vibrates around the snapped through shape till the applied potential difference reaches the pull-in voltage of ~ 102 V. For the loading rates of 1.2 and 3.0 V/μs the snap-through instability is not observed, and only the pull-in instability occurs at ~ 105 V and ~ 129 V, respectively. We have summarized in Table 2 the

snap-through and the pull-in parameters for different rates of loading. As the rate of increase of the potential difference is decreased the snap-through voltage gradually decreases to 73 V monotonically, however the pull-in voltage approaches 111 V non-monotonically. It is evident that the response of the arch approaches that of the statically deformed arch as the rate of loading is decreased. Krylov et al. [49] have studied static deformations of the arch experimentally and numerically by using a reduced order model. Their experimental snap-through voltage of 62.3 V differs by 5% from the presently numerically computed voltage of 65.7 V, and the corresponding pull-in voltages are 106 V and 111 V. We note that the loading rate in experiments cannot be accurately determined. Analyses with the linear strain displacement relation fail to predict the snap-through instability. Therefore, the nonlinearity in the strain displacement relation must be considered for studying the snap-through instability. For subsequent problems, results from analyses with the nonlinear strain displacement relation are reported.

Table 2: The snap-through and the pull-in parameters for the fixed-fixed bell shaped arch for different rates of applied potential difference from the analysis of the nonlinear problem.

Rate of applied potential difference (V/μs)	*The snap-through instability*		*The pull-in instability*	
	Voltage (V)	*Displacement* (μm)	*Voltage* (V)	*Displacement* (μm)
Step load	65.0	2.6	92.0	11.0
3.000	-	-	123.0	11.0
1.200	-	-	100.0	6.0
0.400	77.5	2.0	111.5	9.0
0.240	75.5	1.9	111.0	8.0
0.120	74.0	1.8	113.0	9.0
0.060	73.5	1.7	111.0	8.0
0.024	73.0	1.7	116.0	8.5
Experiment	62.3		106.0	
ROM (static problem)	65.7		111.0	

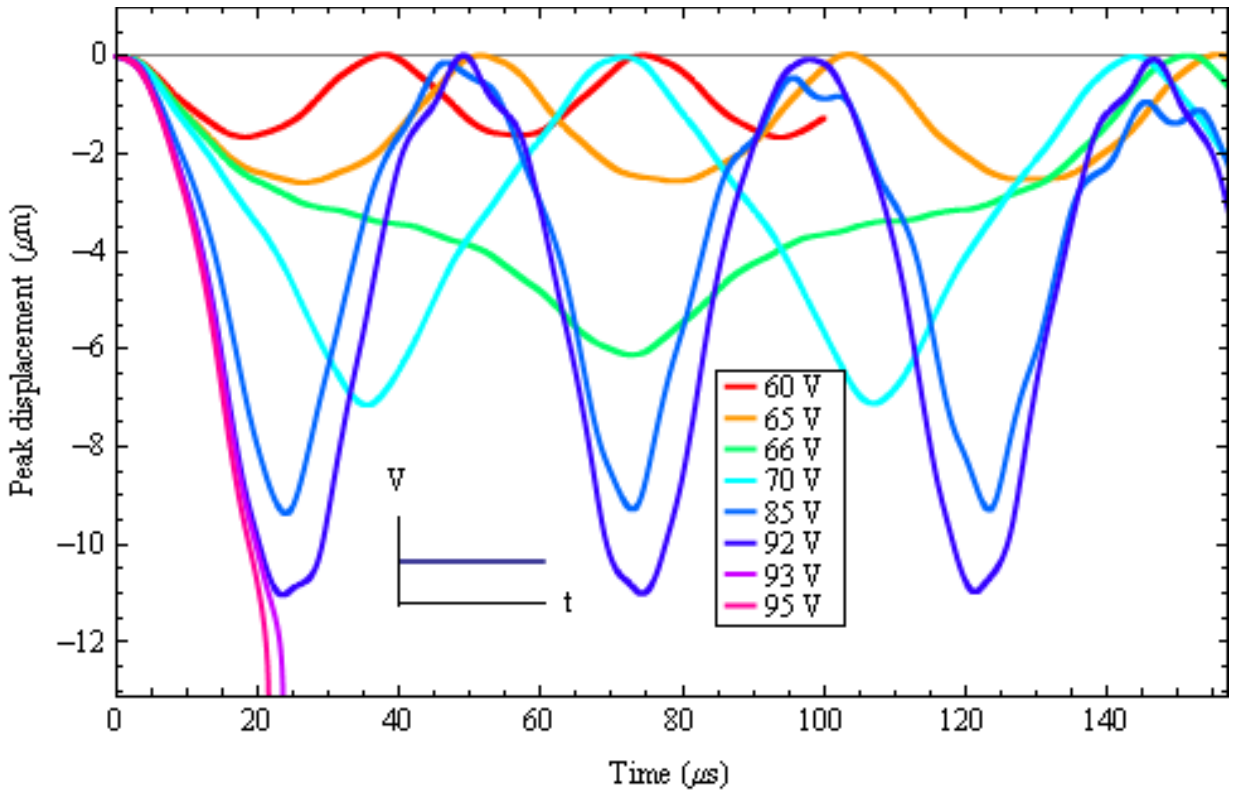

Figure 17. Time histories of the downward displacement of the centroid of the fixed-fixed bell shaped arch for different applied step voltages.

Figure 17 shows time histories of the deflection of the arch for different values of the applied step potential difference. A significant difference in the response of the arch occurs when the applied potential difference is increased from 65 V to 66 V in that the amplitude and the time period of oscillations increase noticeably. This sudden change in the response due to a small change in the applied potential difference indicates the snap-through instability. It should also be evident from the plot of the peak displacement versus the applied step voltage shown by the red curve in the figure 18. The pull-in voltage is found to be 92 V, which is nearly 40% more than the snap-through voltage. The snap-through and the pull-in voltages due to step electric potentials are lower by 15% and 20%, respectively, than those due to a linearly increasing electric potential; we recall that the pull-in voltage for the beam studied above exhibits the same trends.

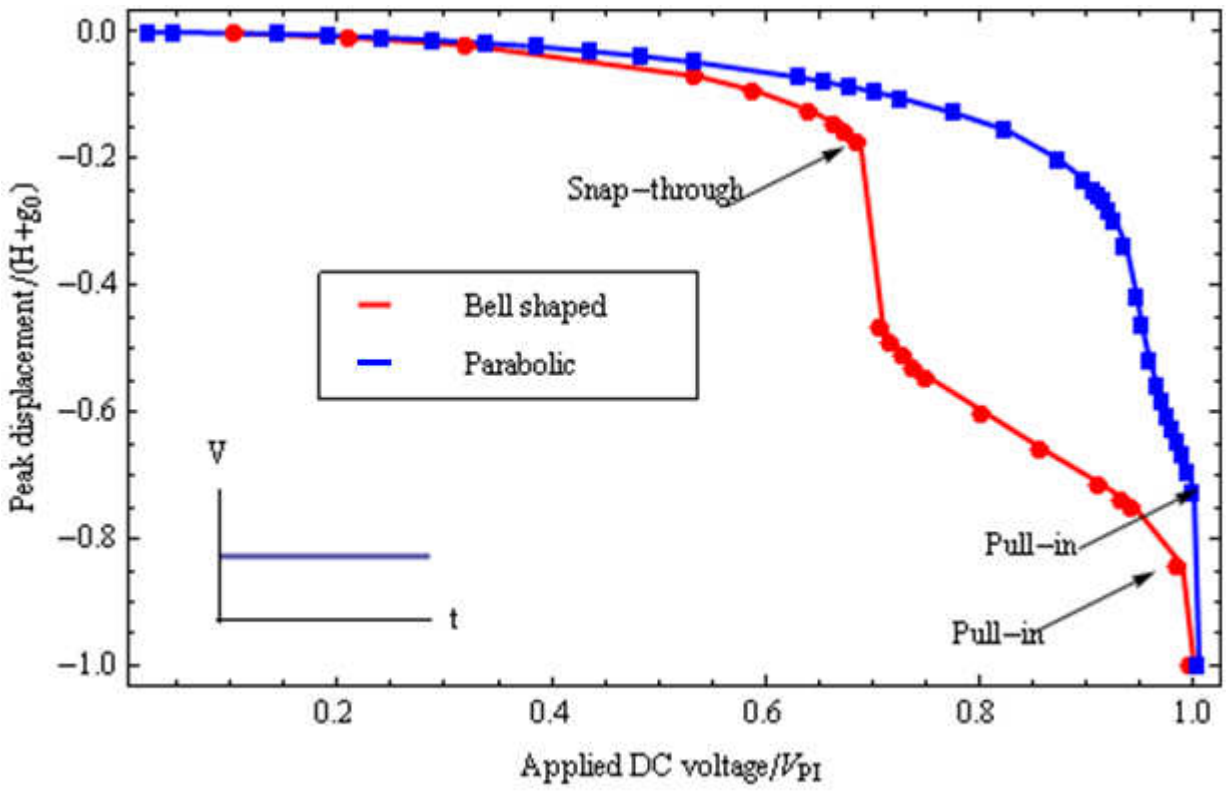

Figure 18. The maximum absolute displacement of the centroid of the bottom surface of the fixed-fixed bell shaped and parabolic arches for different applied step voltages.

Since the rise parameter, e_{arch}, for the shallow arch is 4.33, according to the criterion given in [84], it should not experience a snap-through instability under a deflection-independent distributed static or transient mechanical load. However, under the step electric potential difference, which induces a deflection-dependent distributed force, the arch experiences the snap-through instability. Therefore, the criterion developed with the assumption of displacement-independent loads does not apply for displacement-dependent (or follower type) loads.

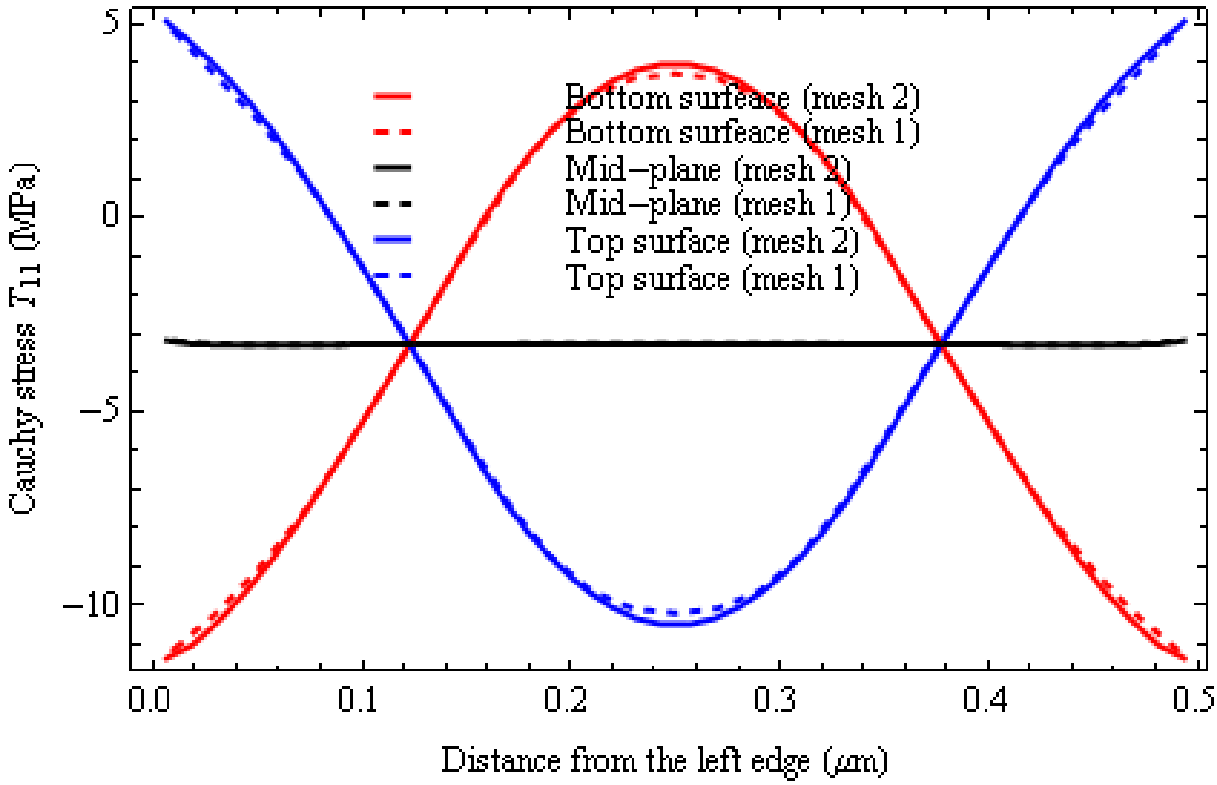

Figure 19. At $t = 4\ \mu s$, the variation of the Cauchy stress tensor T_{11} along the span of the parabolic arch on the top, the bottom and the mid-plane due to 110 V step potential difference.

1.3.4. Transient deformations of a parabolic arch MEMS

The parabolic arch studied in this subsection differs from the bell shaped arch analyzed above primarily in the non-zero slopes of the parabolic arch at the two fixed edges and zero slopes for the bell shaped arch. The geometric and material parameters of the parabolic arch are: $\hat{L}$ = 500 μm, $\hat{b}$ = 50 μm, $\hat{d}$ = 2.6 μm, $\hat{h}$ = 2.9 μm, and $\hat{g}_0$ = 6.4 μm (see figure 1); ρ_0 = 2310 kg/m^3, λ = 73.95 GPa and μ = 63.0 GPa. Since the average gap to the width ratio $(\hat{h}/2 + \hat{g}_0)/\hat{b}$ of 0.157 and $\hat{d}/\hat{b}$ of 0.052 are less than 0.5, effects of fringing fields can be neglected [14]. Even though, in [14] an initially flat beam is considered, for the present problem, the arch height is negligible as compared to its width and length, neglecting fringing fields should not introduce an appreciable error in the pull-in parameters. We analyze it as a plane strain problem. The 20 x 3 and the 40 x 4 FE meshes with 92 and 176 BEs gave the maximum centroidal deflections of 0.442 and 0.444 μm for 110 V step potential difference. Variations of the Cauchy stress T_{11} along the span of the

beam at time $t = 4$ μs are exhibited in figure 19. As results are virtually the same from the two meshes, for the subsequent analyses we use the first mesh.

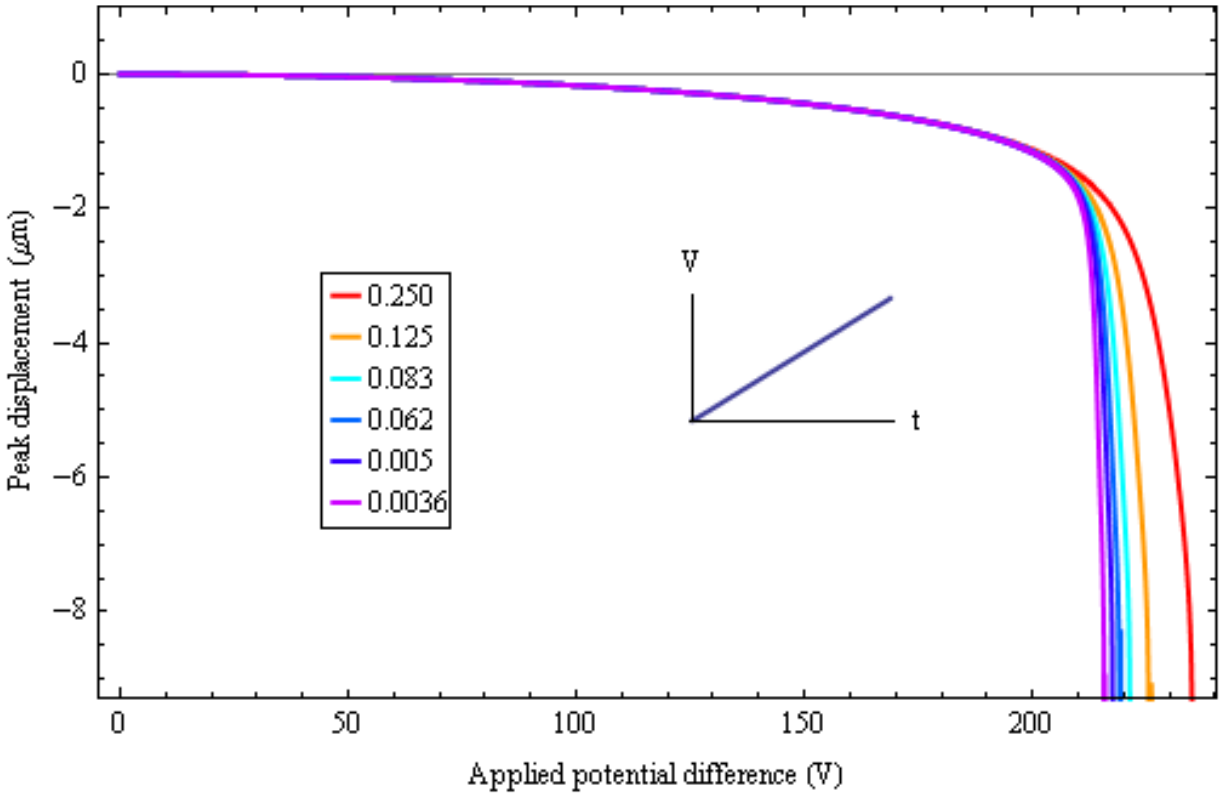

Figure 20. For different rate of increase of the applied potential difference ($V/\mu s$) the downward displacement of the centroid of the bottom surface of the fixed-fixed parabolic arch versus the applied voltage.

Figure 20 evinces time histories of the peak displacement of the centroid of the bottom surface of the arch for different uniform rates of increase of the electric potential. A sudden increase in the peak displacement, observed for a potential difference of 210 V, signifies the pull-in instability. The pull-in voltage depends weakly upon the rate of increase of the applied potential difference. No snap-through instability is observed. Recall that for the bell-shaped arch both instabilities were found.

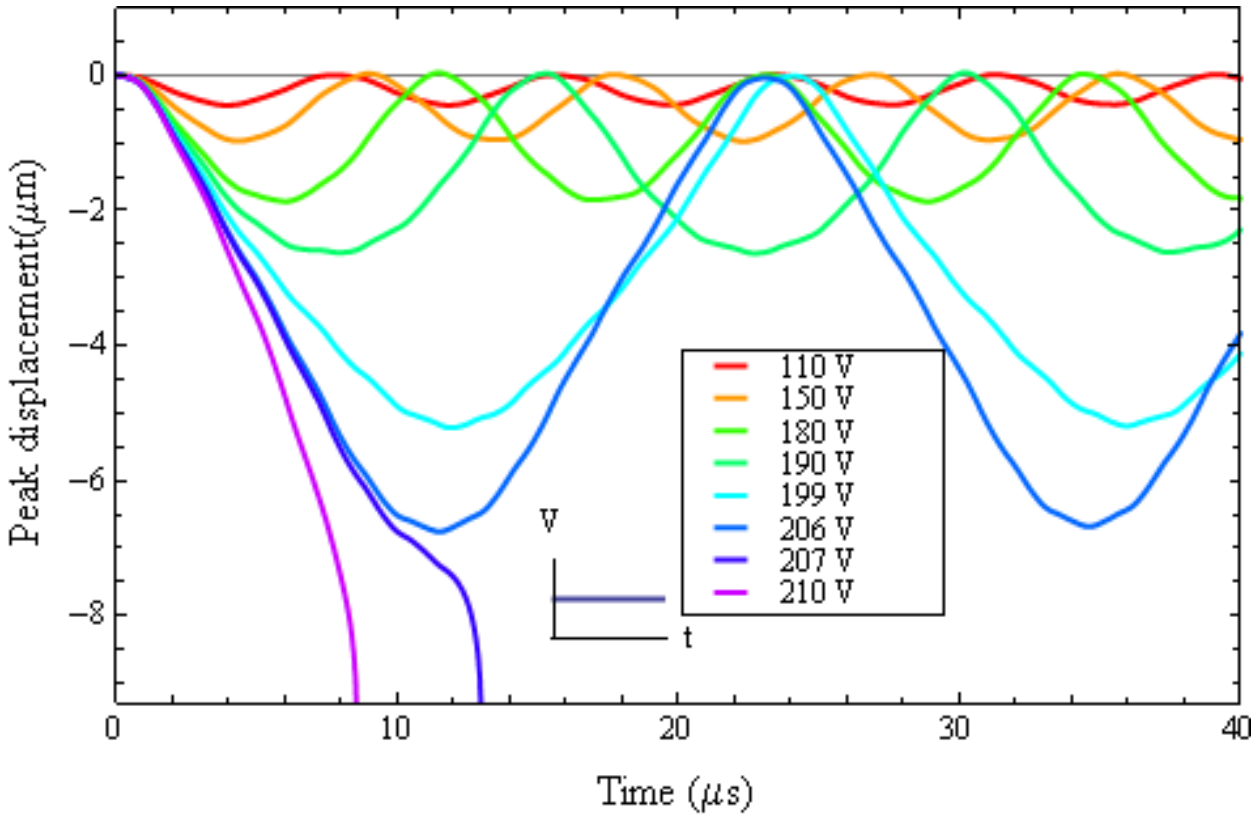

Figure 21. Time histories of the peak downward displacement of the centroid of the fixed-fixed parabolic arch for different applied step voltages.

For different step potential difference, figure 21 exhibits the downward displacement of the centroid of the bottom surface of the arch versus time. Unlike for the bell shaped arch, the amplitude of vibration increases gradually with the increase in the applied step voltage till the potential difference equals 206 V. A sudden change in the response occurs when the applied step voltage is increased to 207 V; thus the dynamic pull-in voltage is between 206 V and 207 V. The blue line in figure 18 shows the variation of the peak displacement with the applied step potential difference. Unlike the bell shaped arch, no sudden change in the peak displacement is seen other than the one at the pull-in voltage. Therefore, the snap-through instability did not occur under step loading also. We note that dimensions of the sinusoidal and the bell-shaped arches are different.

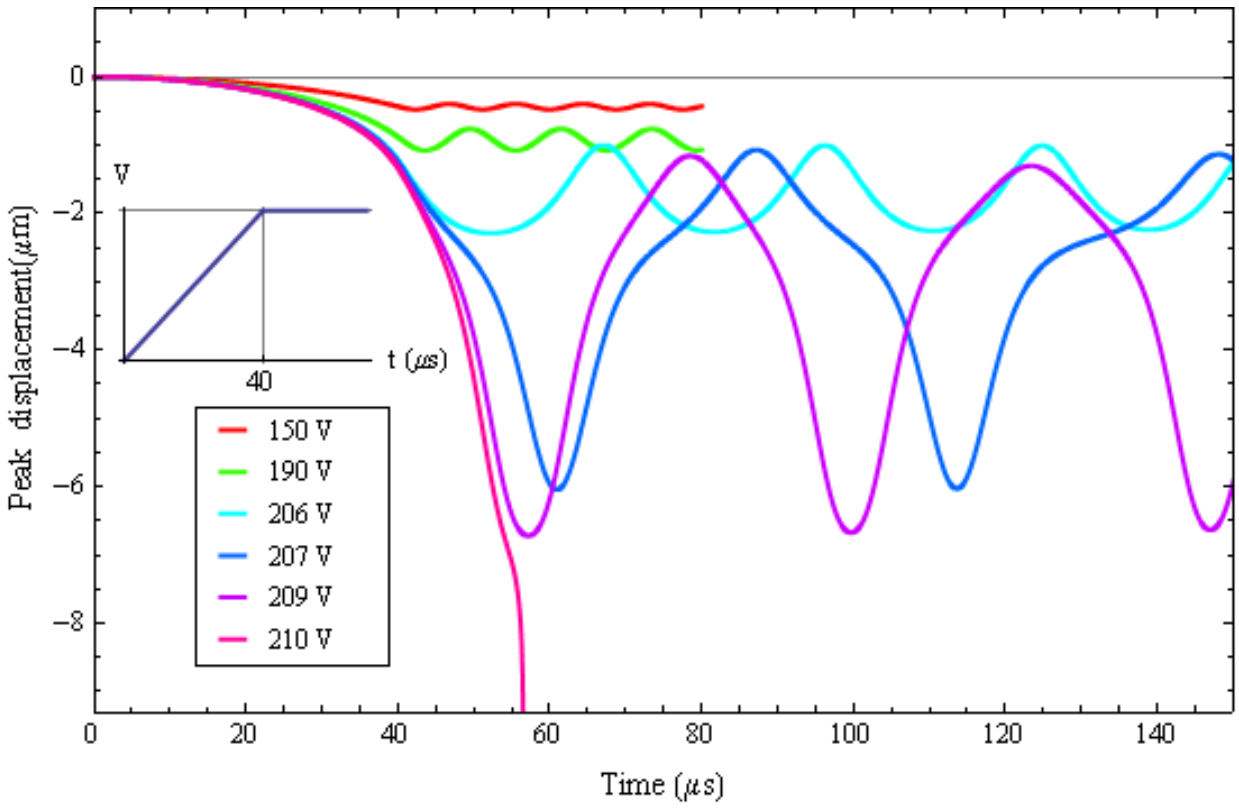

Figure 22. Time histories of the peak downward displacement of the centroid of the parabolic arch for different values of the steady potential difference.

For the applied voltage increased linearly from zero to the desired value in 40 μs and then held there, figure 22 shows time histories of the downward displacement of the centroid of the bottom surface of the arch for various values of the steady voltages. A noticeable difference in responses of the arch for applied steady potential differences of 206 V and 207 V is found. For 207 V the arch oscillates with larger amplitude (see figure 23) and larger time period than those for 206 V. This sudden change in the response of the arch due to a small change in the applied potential difference indicates the snap-through instability. The pull-in voltage is found to be 210 V. We recall that no snap-through instability occurred for this arch under both a step potential difference and a linearly increasing potential difference.

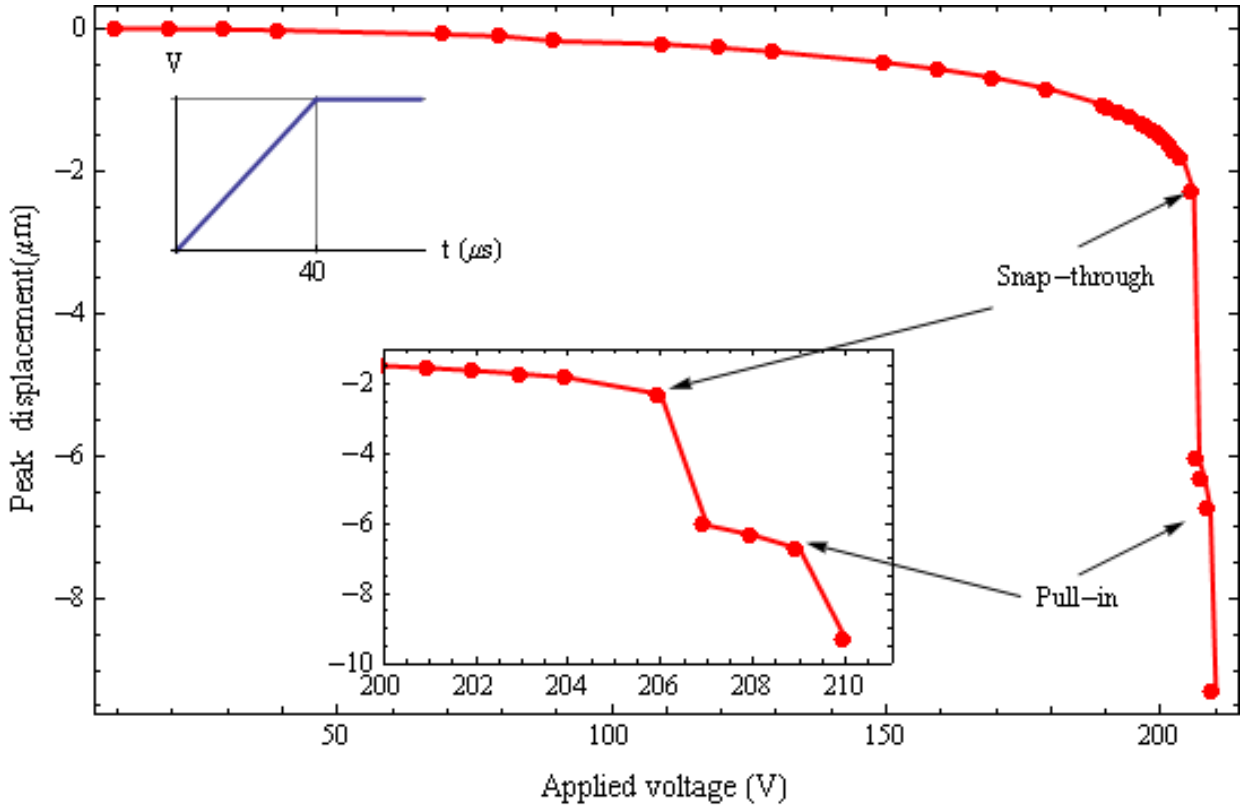

Figure 23. The maximum displacement of the centroid of the bottom surface of the fixed-fixed parabolic arch versus different applied ramp voltages. Two jumps in the displacement are observed. The first jump at 206 V corresponds to the snap-through instability and the second jump at 209 V corresponds to the pull-in instability.

1.3.5. Variation of the lowest natural frequency of arch MEMS with applied voltage

The natural frequency of a MEMS device is an important parameter as it indicates its stiffness, and it affects the quality factor and the switching time. The lowest natural frequencies, ω, 37.9 kHz and 136.8 kHz, of the bell shaped and the parabolic arches, respectively, deformed by a potential difference of 5 V are very close to their natural frequencies, ω_n, 36.0 and 135.5 kHz obtained from a converged modal analysis of the undeformed arches with the commercial FE code ANSYS. Figure 24 shows the variation of the lowest natural frequency (ω/ω_n) with the applied step voltage (V/V_{pi}), where V_{pi} is the pull-in voltage from the analysis of the dynamic problem. With an increase in the deformation of the arches due to an increase in the applied potential difference, the lowest natural frequencies of the deformed arches decrease gradually.

This decrease in the lowest natural frequency can be explained with the Mises truss model [32, 52]. The nondimensional electrostatic force between the deformable and the rigid electrodes with the PPA is given by [49]

$$F_e = \frac{\beta}{(1-w)^2} \tag{32}$$

Here, w is the ratio of the peak displacement of the deformable electrode to the initial gap, and β is the nondimensional potential difference parameter between the two electrodes. For $w < 1$, using the Binomial theorem, we get

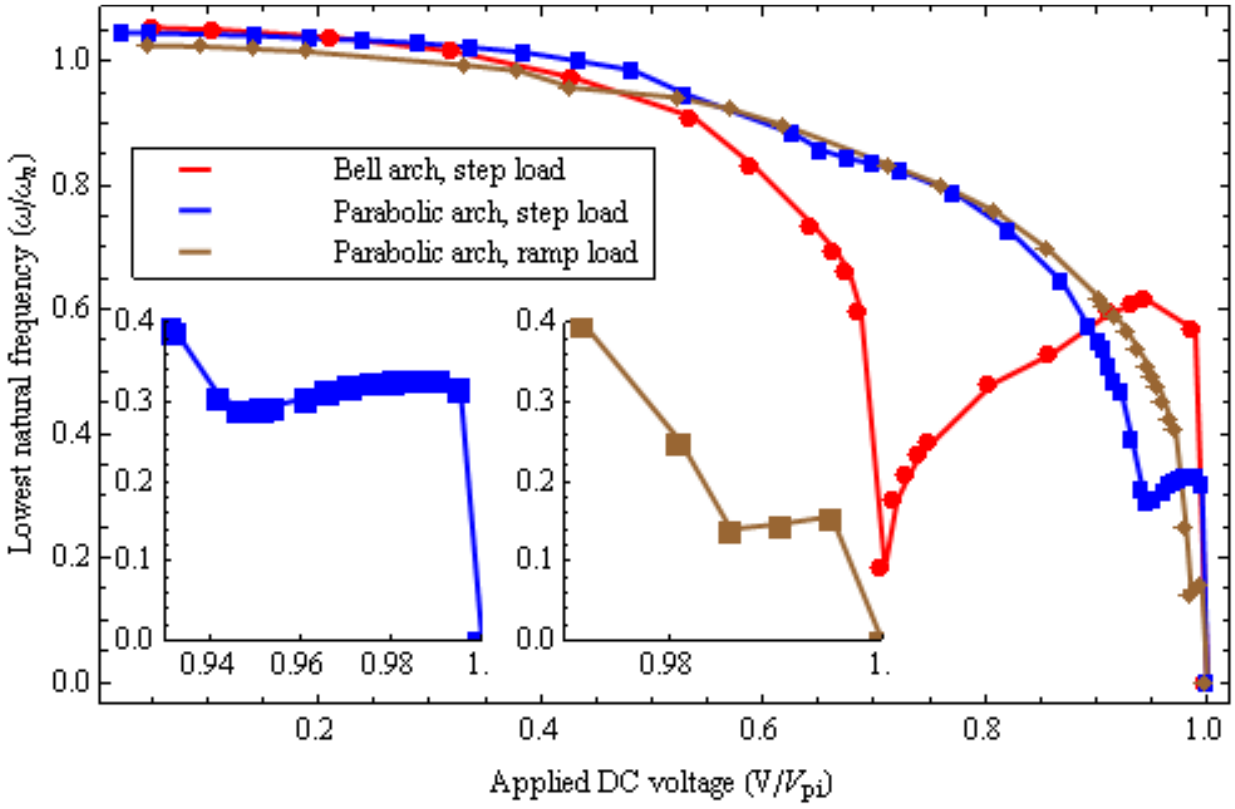

Figure 24. The lowest natural frequency versus the electric potential difference for the fixed-fixed parabolic and bell shaped arches.

$$F_e = \beta\left(1 + 2w + 3w^2 + 4w^3 + \cdots\right) \tag{33}$$

For relatively small voltages and hence small displacements, the electrostatic pressure F_e depends only on β; however, as β increases, w also increases, and F_e depends on w and β. This

makes F_e a negative spring, which decreases the natural frequency, and this effect is known as the electrostatic softening [4]. However, as β increases, so does w, and the strain hardening due to nonlinearities in the strain displacement relation compensates for the electrostatic softening.

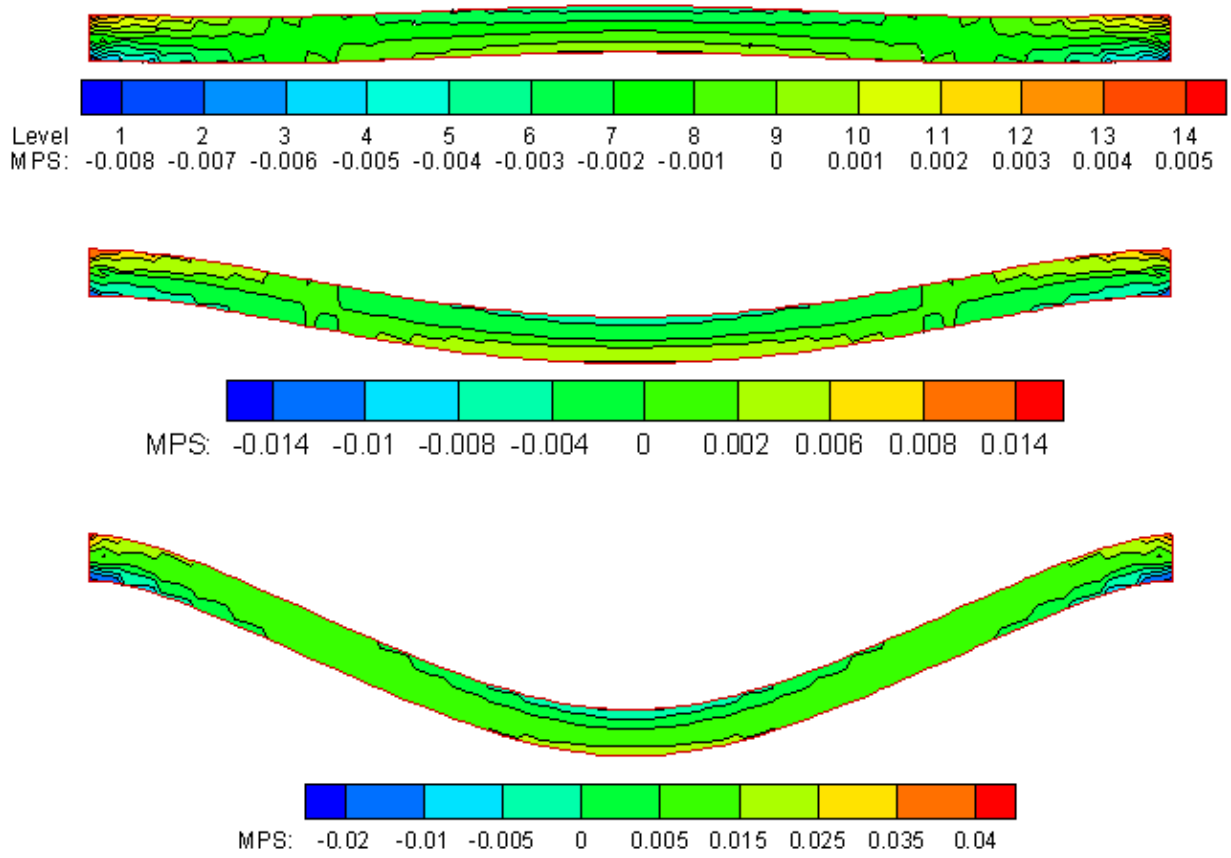

Figure 25. The maximum principal Green – St. Venant strain (MPS in %) on the extreme deformed shapes of the bell shaped arch for the three values of the applied step potential differences; top: 65 V, middle: 66 V, and bottom: 92 V.

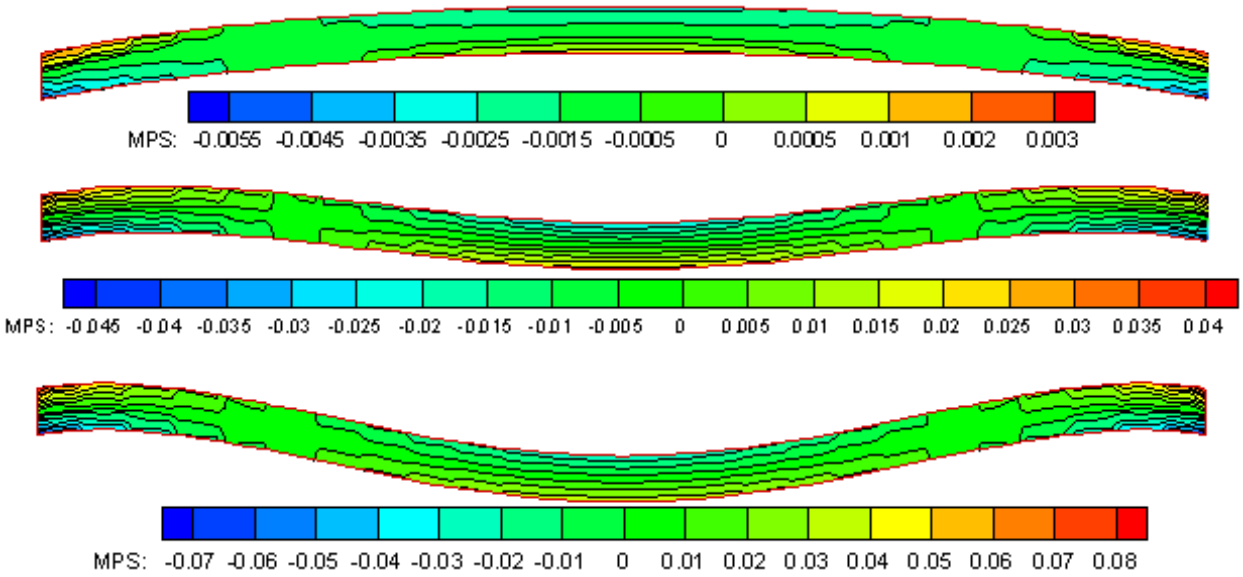

Figure 26. The maximum principal Green – St. Venant strain (MPS in %) on the extreme deformed shapes of the parabolic arch for the three values of the applied step potential differences; top: 130 V, middle: 196 V, and bottom: 205 V.

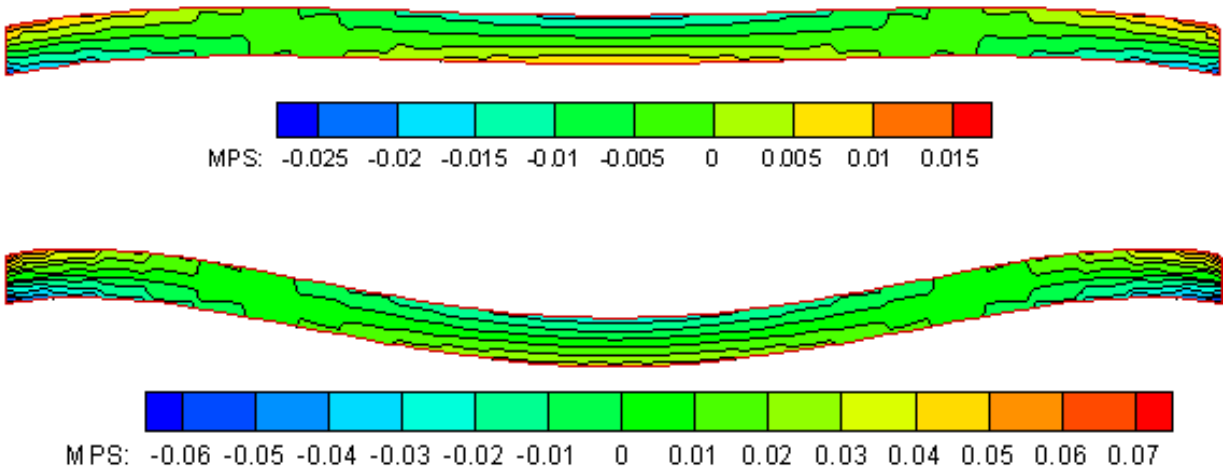

Figure 27. The maximum principal Green – St. Venant strain (MPS in %) on the extreme deformed shapes of the parabolic arch for the two values of the applied ramp potential difference: top: 206 V, and bottom: 207 V

An examination of values of the maximum Green-St. Venant principal strain, E^{pr}, plotted in figures 25-27 on the deformed shapes of the arches at different applied step potential differences provides a qualitative explanation of the strain hardening effect. For the bell shaped arch, as indicated in figure 25, at the potential difference of 65 V (V/Vpi = 0.69), E^{pr} in an extreme shape of the arch equals 0.008 % which is too small for nonlinearities in the strain displacement relation to have a noticeable effect. Therefore, the electrostatic softening effect dominates the strain hardening effect. The natural frequency declines sharply at 66 V due to the snap-through instability. Under a potential difference greater than 65 V, the arch oscillates with E^{pr} = 0.014 % and 0.02 % at 66 V and 92 V, respectively. Hence, after the snap-through the lowest natural frequency increases because hardening due to stretching of the arch compensates for the electrostatic softening. However, the lowest natural frequency again suddenly falls to zero at the pull-in voltage of 92 V when the softening and the hardening effects cancel each other.

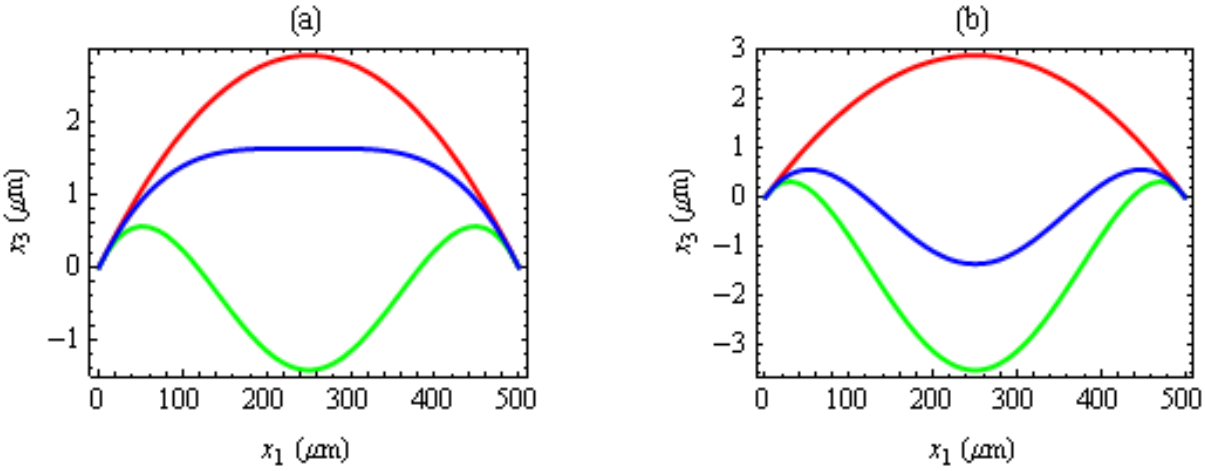

Figure 28. Two extreme and one intermediate shapes of the parabolic arch for the two values of the potential difference; (a) 196 V, and (b) 205 V.

For the parabolic arch deformed by a step potential difference, the lowest natural frequency also decreases initially. As the snap-through instability does not occur in this arch under a step electric potential difference, the lowest natural frequency does not drop sharply; cf. figure 24. Instead, as the arch oscillates with increasing amplitude the strain hardening effect gradually compensates the electrostatic softening and the lowest natural frequency starts to increase. The E^{pr} for 130 V (V/V_{pi} = 0.62) step electric potential difference equals 0.005 %, which increases to 0.04 % at 196 V (V/V_{pi}= 0.96) (see figure 26). For higher potential differences the arch gets

inverted during its oscillations. By examining shapes of the arch at 196 V (see figure 28(a)), we found that the equilibrium shape of the arch is about to invert, which means that the arch oscillates in the inverted shape only during at most half of the vibration cycle. We define the equilibrium shape of the arch as the one in which the downward velocity of the centroid is the maximum. However, for a potential difference higher than 196 V (see figure 28(b)), the equilibrium shape of the arch also inverts, which indicates that the arch is in the inverted shape during more than half of the vibration cycle. Thus, the arch experiences a higher level of strain during most part of the cycle (see figure 26). Therefore, during deformations of the arch for a step potential difference between 196 V and 206 V, the strain hardening dominates the electrostatic softening and the lowest natural frequency increases. However, the lowest natural frequency again suddenly falls to zero at the pull-in voltage of 207 V.

When the parabolic arch is loaded with the electric potential varying linearly from zero to a steady value in 40 μs, we observe the snap-through instability. In this case, the lowest natural frequency of the arch decreases sharply at 207 V due to the snap-through instability. As indicated in figure 27 the E^{pr} increases from 0.025 % before the snap-through to 0.06% after the snap-through. Hence, after the snap-through the lowest natural frequency increases because hardening due to stretching of the arch exceeds softening due to the Coulomb pressure. However, the lowest natural frequency again suddenly falls to zero at the pull-in voltage when the structural stiffness drops to zero.

The sharp drop in the lowest natural frequency of the arch at the snap-through and the pull-in instabilities agrees with the observation that the lowest natural frequency of the arch becomes zero at bifurcation points C and F in figure 2.

1.3.6. Discussion

Results for the fixed-fixed beam (cf. Section 1.3.2) and the two arches (cf. Sections 1.3.3 and 1.3.4) indicate that for the step loading inertia effects cannot be neglected. The pull-in voltage of the fixed-fixed beam equals 99.5 V under the step load and 113.0 V for the slowest rate of increase of the potential difference. The snap-through and the pull-in voltages of the bell shaped arch equal 65 V and 92 V, respectively, under the step load and 73 V and 116 V, respectively,

for the slowest rate of increase of the potential difference (cf. table 2). The pull-in voltages of the fixed-fixed parabolic arch equal 207 V and 215 V, respectively, under the step load and the slowest rate of increase of the potential difference. The bell shaped arch experiences the snap-through instability under both slowly and rapidly applied potential differences. However, the parabolic arch exhibits the snap-through instability only when the potential difference is increased linearly from zero to a steady value in 40 μs and subsequently held constant. Whether or not an arch exhibits the snap-through instability depends on a number of parameters, such as the ratio of the arch thickness to the arch rise [84], the angle of the arch at the fixed end (for of a circular and a parabolic arch) [70], the ratio of the arch thickness to the maximum distance from the flat rigid electrode, and the rate of increase of the applied potential difference. Finding a phase diagram that shows values of parameters for which the snap-through instability occurs is not easy.

We have neglected the effect of damping. The damping coefficient of a MEMS device is determined by several variables such as the pressure in the surrounding fluid medium, and visco-elastic/plastic behavior of the MEMS material. Most silicon MEMS operate at atmospheric pressure and the damping coefficient is dominated by the squeeze-film damping [6]. Ref. [56] studied snap buckling of a shallow sinusoidal arch under a transient step mechanical pressure load and considered viscous damping. It has been reported in [56] that the critical pressure for the snap-through instability increased by about 3% due to a viscous damping coefficient of 1% of the critical damping and the large-amplitude motions after snap-through instability decay over time and the structure tends to the static snapped configuration.

1.4. The reduced order model

The governing equation for a shallow micro-arch under an electrostatic load in terms of non-dimensional variables is [49]

$$\ddot{w}+c\dot{w}+w^{IV}-\alpha\left(hz_0''-w''\right)\int_0^1\left(2hz_0'w'-\left(w'\right)^2\right)dx=\frac{\beta}{\left(1+hz_0-w\right)^2},\ x\in(0,1). \tag{34}$$

The boundary and initial conditions for a fixed-fixed arch initially at rest are

$$w(0,t)=w(1,t)=w'(0,t)=w'(1,t)=w(x,0)=\dot{w}(x,0)=0. \tag{35}$$

In equations (34) and (35), a super-imposed dot and a prime denote derivative with respect to time *t* and the space coordinate *x*, respectively, $\hat{\varepsilon}_0 = 8.854 \times 10^{-12}\ \mathrm{Fm}^{-1}$ the vacuum permittivity, $\hat{\rho}$ the mass density, $x = \hat{x}/\hat{L}$, $w = \hat{w}/\hat{g}_0$ the transverse displacement, $d = \hat{d}/\hat{g}_0$, $b = \hat{b}/\hat{g}_0$, $h = \hat{h}/\hat{g}_0$, $\alpha = g_0^2 \hat{b}\hat{d}/2\hat{I}$ the stretching ratio, $c = \hat{c}\hat{L}^2/\sqrt{\hat{\rho}\hat{b}\hat{d}\hat{E}\hat{I}}$, $\hat{c}$ the damping coefficient, z_0 the initial shape of the arch, and $t = \hat{t}\sqrt{(\hat{E}\hat{I})/(\hat{\rho}\hat{b}\hat{d}\hat{L}^4)}$, $\hat{t}$ the dimensional time. As discussed in [27] the damping provided by deformations of the air between the two electrodes can also be approximated by the term $c\dot{w}$. We note that equation (34) with *h=0* is the well known governing equation for the microbeam based MEMS [4, 14].

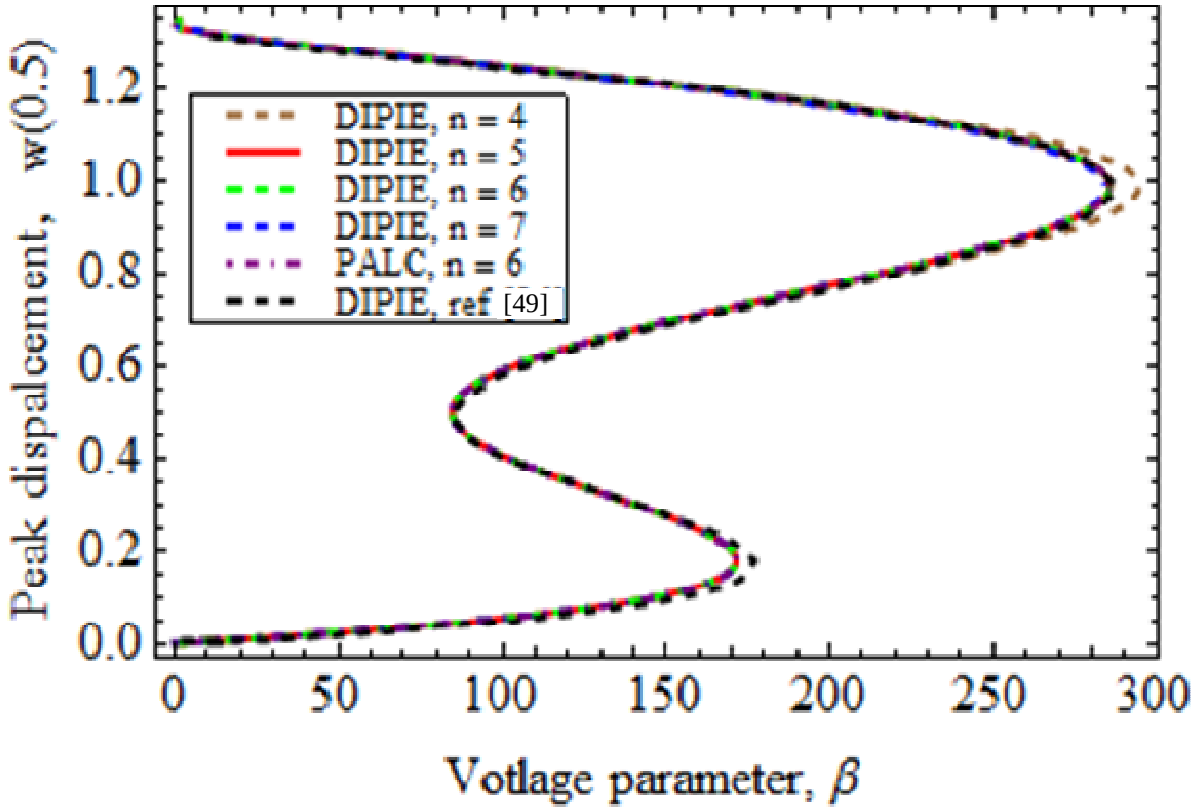

Figure 29. Bifurcation curve of the peak deflection of the mid-span of the arch versus the applied potential difference parameter for the static problem.

We solve equation (34) using the Galerkin method by approximating the transverse displacement *w* by the series

$$w(x,t) \approx \sum_{i=1}^{n} q_i(t)\phi_i(x) \tag{36}$$

where $q_i(t)$ are the generalized coordinates and $\phi_i(x)$ eigenmodes of an undamped fixed-fixed straight beam [49]:

$$\phi_i(x) = J_i\left(\frac{Cos(\lambda_i x) - Cosh(\lambda_i x)}{-Sin(\lambda_i) - Sinh(\lambda_i)} - \frac{Sin(\lambda_i x) - Sinh(\lambda_i x)}{Cos(\lambda_i) - Cosh(\lambda_i)}\right) \tag{37}$$

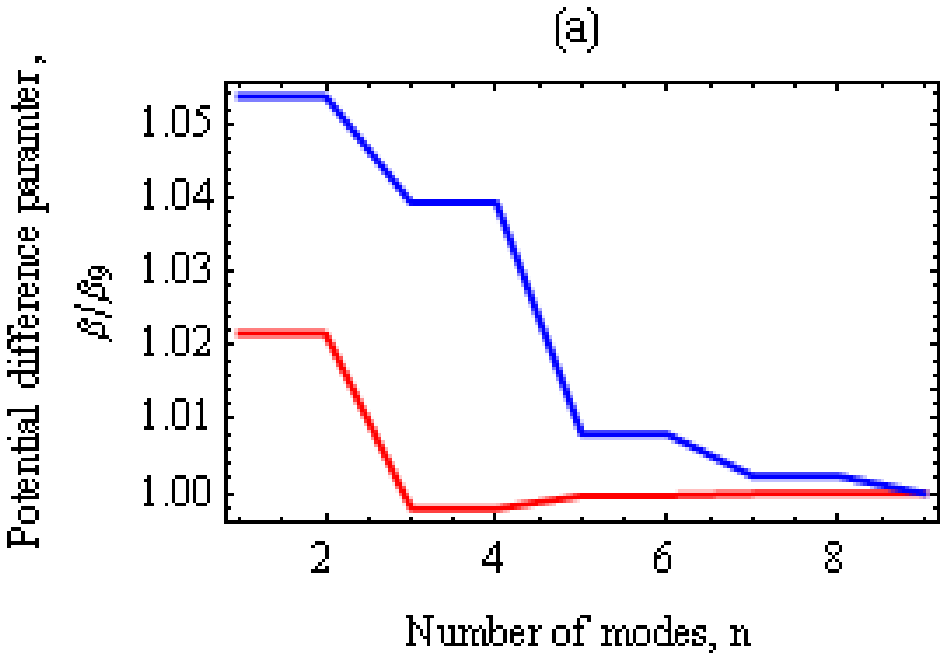

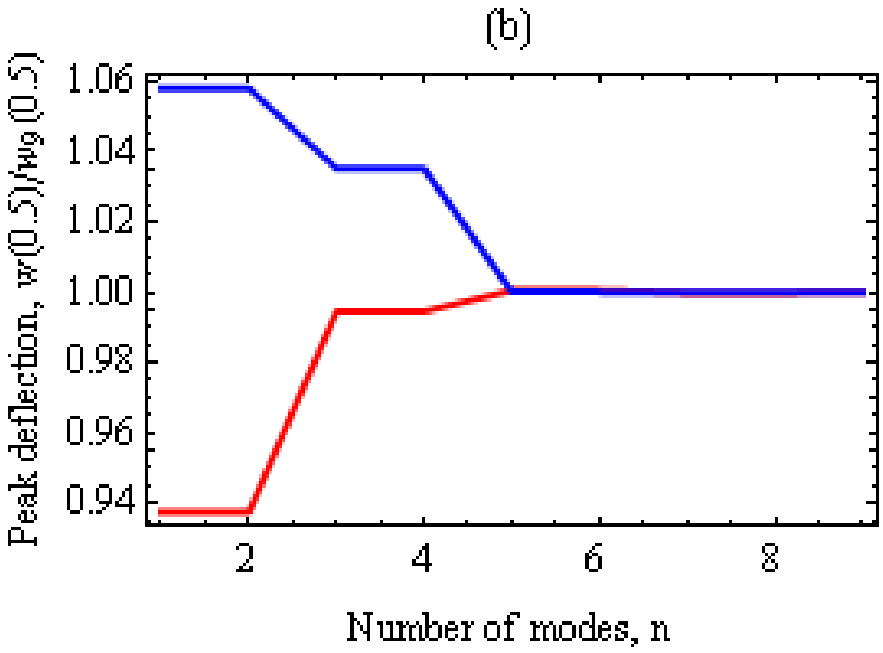

Figure 30. Variation of (a) the critical potential difference parameters and (b) the peak displacements for the snap-through (red curve) and the pull-in (blue curve) instabilities as a function of the number *n* of terms in equation 36. A subscript 9 denotes the value corresponding to $n = 9$.

where λ_i is a solution of the frequency equation

$$Cos(\lambda_i)Cosh(\lambda_i) - 1 = 0\,. \tag{38}$$

The normalization coefficient J_i is such that $\max_{0 \le x \le 1}(\phi_i(x)) = 1$, and n equals the number of modes used in the approximation (36).

Substituting equation (36) into equation (34), multiplying both sides of the resulting equation with $\phi_i(x)$, integrating it over the domain (0, 1), integrating by parts terms involving w^{IV}, z_0'' and w'', and using $\phi(0) = \phi(1) = \phi'(0) = \phi'(1) = 0$ we get

$$\mathbf{M}\ddot{\mathbf{q}} + \mathbf{C}\dot{\mathbf{q}} + \mathbf{B}\mathbf{q} + 2\alpha h^2 \mathbf{z}_0^{\mathrm{T}}\mathbf{q}\mathbf{z}_0 - \alpha h \mathbf{q}^{\mathrm{T}}\mathbf{S}\mathbf{q}\mathbf{z}_0 - 2\alpha h \mathbf{z}_0^{\mathrm{T}}\mathbf{q}\mathbf{S}\mathbf{q} + \alpha \mathbf{q}^{\mathrm{T}}\mathbf{S}\mathbf{q}\mathbf{S}\mathbf{q} = \beta\mathbf{F} \tag{39}$$

where

$$M_{ij} = \int_0^1 \phi_i\, \phi_j\, dx \tag{40}$$

$$C_{ij} = cM_{ij} \tag{41}$$

$$B_{ij} = \int_0^1 \phi_i'' \phi_j'' dx \tag{42}$$

$$z_{0i} = \int_0^1 z_0' \phi_i' dx \tag{43}$$

$$S_{ij} = \int_0^1 \phi_i' \phi_j' dx \tag{44}$$

$$F_i = \int_0^1 \frac{\phi_i}{\left(1 + hz_0(x) - \sum_{i=1}^{n} q_i(t)\phi_i(x)\right)^2} dx\,. \tag{45}$$

Equation (39) is nonlinear in **q** because 5th, 6th and 7th terms on its left-hand side are nonlinear in **q** and the load vector on its right-hand side is a non-linear function of **q**. Boundary conditions in equation (35) are identically satisfied by the assumed form (36) for *w(x,t)*. Initial conditions in equation (35) require that **q**(0) = **0** and $\dot{\mathbf{q}}$= **0**. Non-dimensional variables α, *c*, *h*, β and the initial shape of the arch z_0' affect the arch deformation.

In subsequent sections, unless stated otherwise, the arch shape is described by $z_0 = \sin^2(\pi x)$. Thus, the initial slope of the arch at each clamped end is zero.

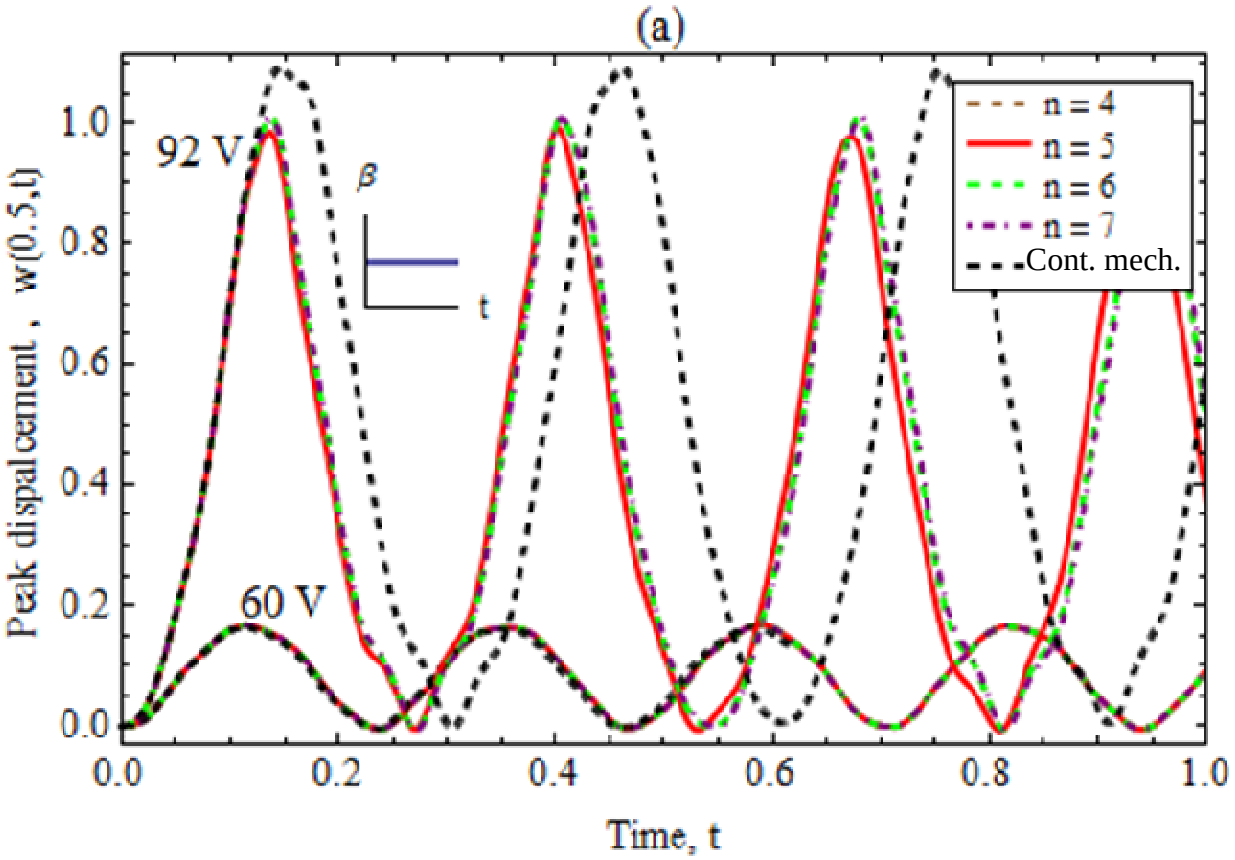
(a)
92 V
60 V
β
t
n = 4
n = 5
n = 6
n = 7
Cont. mech.
Peak displacement , w(0.5,t)
Time, t
0.0
0.2
0.4
0.6
0.8
1.0

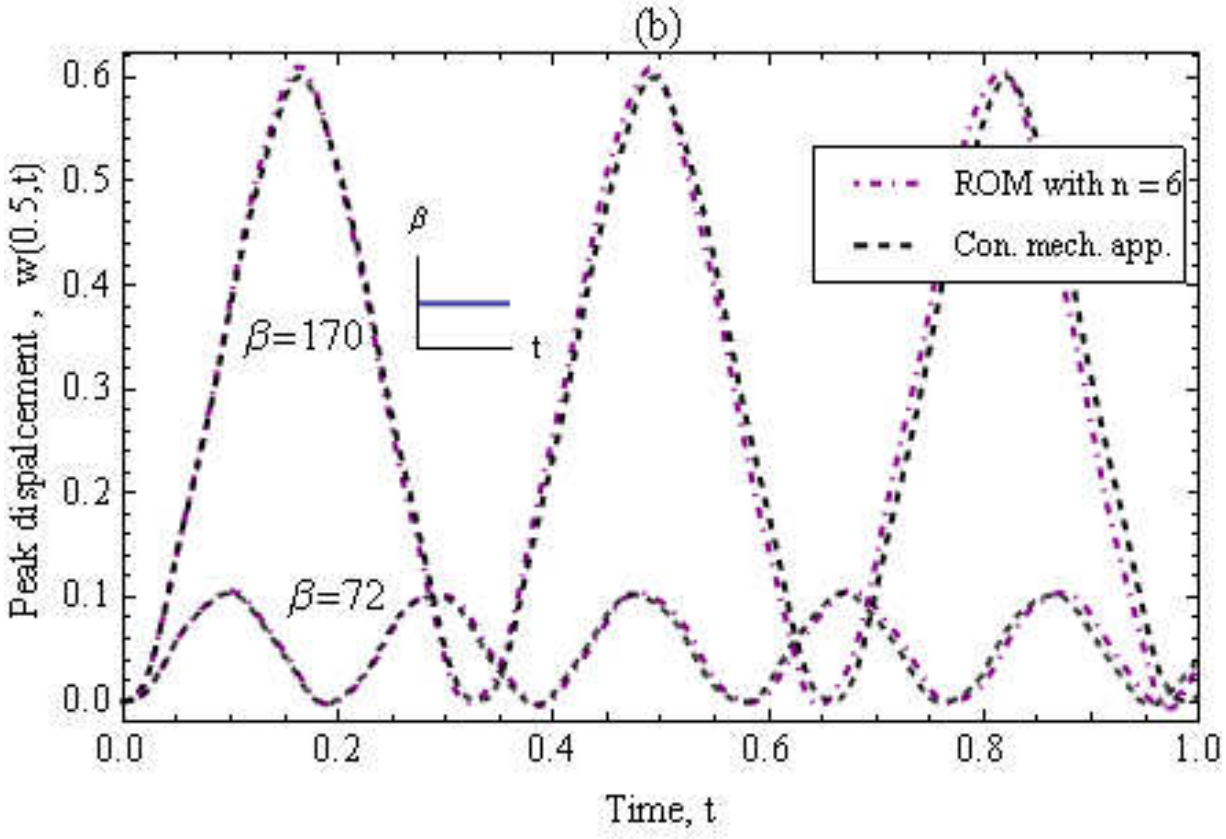

Figure 31. Time histories of the peak deflection of the mid-span of the arch due to (a) 60 V (β = 72) and 92 V (β = 170) step potential difference between the rigid electrode and the arch, and (b) displacement-independent loads β = 72 and β = 170.

1.5. Results from the reduced order model

We have developed a computer code to solve equation (39) numerically by first writing it in the state space form, and using LSODE [77]. The relative and the absolute tolerances in LSODE are set equal to 10^{-6}, and the parameter MF = 22. When solving a static problem we neglect the time dependence of **q** and the first and the second terms on the left-hand side of equation (39), and then solve it using a displacement control approach (displacement iteration pull-in extraction (DIPIE) algorithm [24]) and the pseudo-arc-length continuation (PALC) algorithm [33]. We implement the DIPIE algorithm using the nonlinear equation solver FINDROOT integrated in the commercial computer code MATHEMATICA, and use the freely available software AUTO [1] for the PALC algorithm.

1.5.1. Validation and convergence study

The mathematical model described above has been validated by comparing computed results for four sample problems with those reported in the literature and obtained from the continuum mechanics based approach described in Section 1.3. First, we consider static deformations of an arch with h = 0.3 and α = 121.5. Figure 29 exhibits the bifurcation curve for the arch found with the DIPIE algorithm, the PALC algorithm, and the bifurcation curve for a static problem reported in [49]. Results from the present code agree well with those from [49]. Furthermore, results with the PALC and the DIPIE algorithms coincide with each other, and for the DIPIE algorithm the bifurcation curves computed by taking n = 5, 6 and 7 in equation (36) are nearly indistinguishable from each other. These results agree very well with those in [49] obtained with the DIPIE algorithm. Figure 30 shows the effect of the number n of terms included in the equation (36) upon critical values of β and of the peak displacements at the snap-through and the pull-in instabilities. Critical values of β and of the peak displacements converge as n increases. For $n \geq 6$, the change in the critical values of β and of the peak displacements at the two instabilities is less than 1%. Unless noted otherwise, results presented below are with 6 terms in equation (36).

Referring to figure 1, we consider a bell shaped silicon arch with $\hat{L}$= 1 mm, $\hat{b}$ = 30 μm, $\hat{d}$ = 2.4 μm, $\hat{g}_0$ = 10.1 μm, $\hat{h}$ = 3.0 μm, and its bottom-surface described by $z_0(\hat{x}_1) = \sin^2\left(\pi\hat{x}_1/\hat{L}\right)$. Values assigned to material parameters are $\tilde{E}$ = 169 GPa and the Poisson's ratio ν = 0.3. We analyze it as a plane strain problem by using the effective Young's modulus $\hat{E} = \tilde{E}/(1-\nu^2)$, and consider the effect of fringing fields by increasing the Coulomb pressure F_i (cf. equation (29) on the bottom surface of the arch according to the Mejis-Fokkema formula [13, 49]:

$$F_i = \int_0^1 \frac{\phi_i}{\left(1 + hz_0(x) - w(x)\right)^2} F_g \, dx \tag{46}$$

where

$$F_g = \left(1 + 0.265\left(\frac{1 + z_0(x) - w(x)}{b}\right)^{3/4} + 0.53\left(\frac{d}{b}\sqrt{\frac{1 + z_0(x) - w(x)}{d}}\right)\right). \quad (47)$$

For different number of terms in equation (36), figure 31(a) shows the peak displacement $w(0.5, t)$ versus time t for 60 V and 92 V step potential differences and those reported in Section 1.3. The time histories of the peak displacement for 60 V step electric potential difference agree well with the result reported in Section 1.3. However, for 92 V potential difference, the maximum peak displacement and the time period of oscillation are 8% and 20% lower, respectively, than those reported in Section 1.3. In Section 1.3, the problem is analyzed using the coupled FE and BE methods assuming that the arch is in a plane strain state of deformation, the electric load is computed after every time step accounting for deformations of the arch, and the electric load is applied normal to the deformed surface of the arch. Here the Coulomb pressure is found by using the parallel plate approximation (PPA) [15] and it acts vertically downwards. The effect of the arch curvature on the Coulomb pressure might increase as the arch comes close to the bottom electrode. Thus, the peak deflection for the 92 V step potential difference differs from that in Section 1.3. In Section 1.5.8, a detailed comparison of results from the present method with those from the continuum mechanics based approach is presented.

Next, we analyze an arch of same dimensions as above under a displacement-independent load

$$F_i = \int_0^1 \frac{\phi_i}{(1 + hz_0(x))^2} dx. \quad (48)$$

We get equation (48) by neglecting the term $\sum_{i=1}^{n} q_i(t)\phi_i(x)$ on the right hand side of equation (45). We note that now the Coulomb pressure on the arch in its initial configuration equals βF_i and it does not depend on the arch deflection. Figure 31(b) depicts the peak displacement $w(0.5, t)$ versus time t for $\beta = 72$ and $\beta = 170$ obtained from the present model and from the continuum mechanics based approach described in Section 1.3. Unlike for the displacement-dependent electric load, the time histories of peak displacements for the displacement-independent load agree well with those computed with the continuum mechanics based approach. This further evinces that the disparity in the peak displacement for the 92 V step electric potential difference from the present method and that reported in Section 1.3 is due to the PPA.

As results for the dynamic and the static problems found using n = 5, 6, and 7 are virtually the same, henceforth we take n = 6. Results reported in [56] show no significant changes in displacements and the critical load parameters of an arch under a step mechanical pressure when n is increased from 2 to 5.

We now compare results for a dynamic snap-through instability of a shallow arch with geometric imperfection (shape of the arch $z_0 = (4-4x)x + 0.01d \sum_{i=2,4,6} \phi_i(x)$) under a mechanical pressure load with those reported in [46]. Equation (39) governs deformations of an arch under a mechanical pressure load if the potential difference parameter β is replaced by a load parameter β_m and the generalized force F_i (cf. equation (45)) by $F_i = \int_0^1 \phi_i \, dx$. We use $\hat{h}$ in place of $\hat{g}_0$ to non-dimensionalize the deflection $\hat{w}$ and the arch thickness $\hat{d}$. A different non-dimensional load parameter $p_0 = \beta_m / \left(\hat{d}^2 \hat{L}^2 \hat{b} / \hat{R}^2 \hat{I} \hat{h} \right)$ is used in [46]. $\hat{R}$ is the radius of the circular arch.

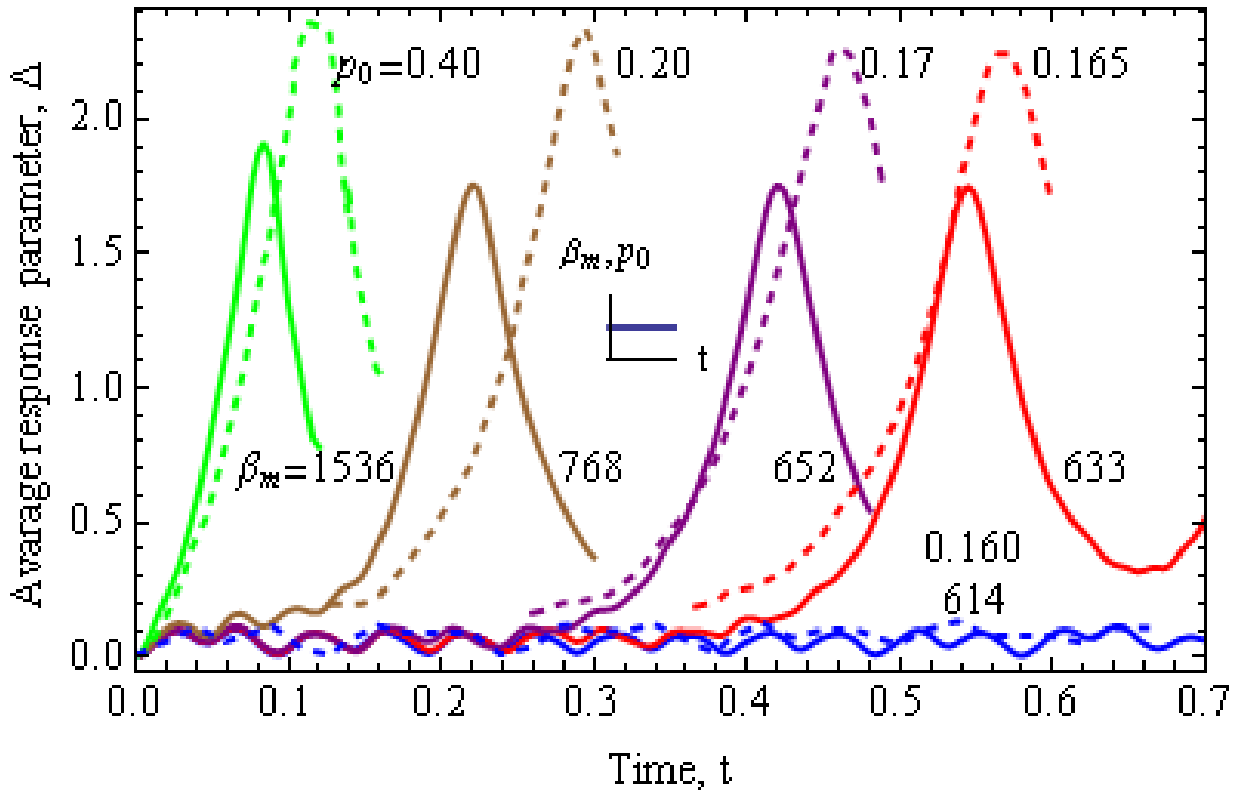

Figure 32. Time histories of the average response parameter for the circular arch ($h = 1.0$) for different values of $\beta_m = \left(\hat{a}^2\hat{L}^2\hat{b}/\hat{R}^2\hat{I}\hat{h}\right)_{p_0}$. Although, value of β_m is different from p_0 in the figure, they represent the same load. Solid curves are computed from the present model and dashed curves are from [46].

Figure 32 exhibits time histories of the average response parameter $\Delta(t) = \int_0^1 w(x,t)dx \Big/ \int_0^1 z_0(x)dx$ for the arch (h = 1.0, α = 150) for different values of β_m. A large change in the response of the arch is observed when the load parameter β_m is increased from 614 (p_0 = 0.159) to 615 (p_0 = 0.160) (not shown in figure). Therefore, the critical load β_m for the snap-through instability according to the present model is between 614 and 615. In [46], the critical load is reported to be between p_0 = 0.160 (β_m = 615) and p_0 = 0.165 (β_m = 633). However, the maximum value of the average response parameter Δ for p_0 = 0.165 (β_m = 633) from the present work is 21.5% lower than that reported in [46]. In [46], equation (39) is solved using an analog computer system with servo-multipliers providing the nonlinear terms. The solutions of frequency equation (38) and the mode shapes (cf. equation (37)) are approximated such that values of different terms in equations

(40) to (45) are accurate only to three significant digits. Here we use the adaptive time integration subroutine LSODE with the double precision arithmetic. We note that the presently computed response of the arch agrees qualitatively with that given in [46] and the two values of the critical load parameter agree well with each other.

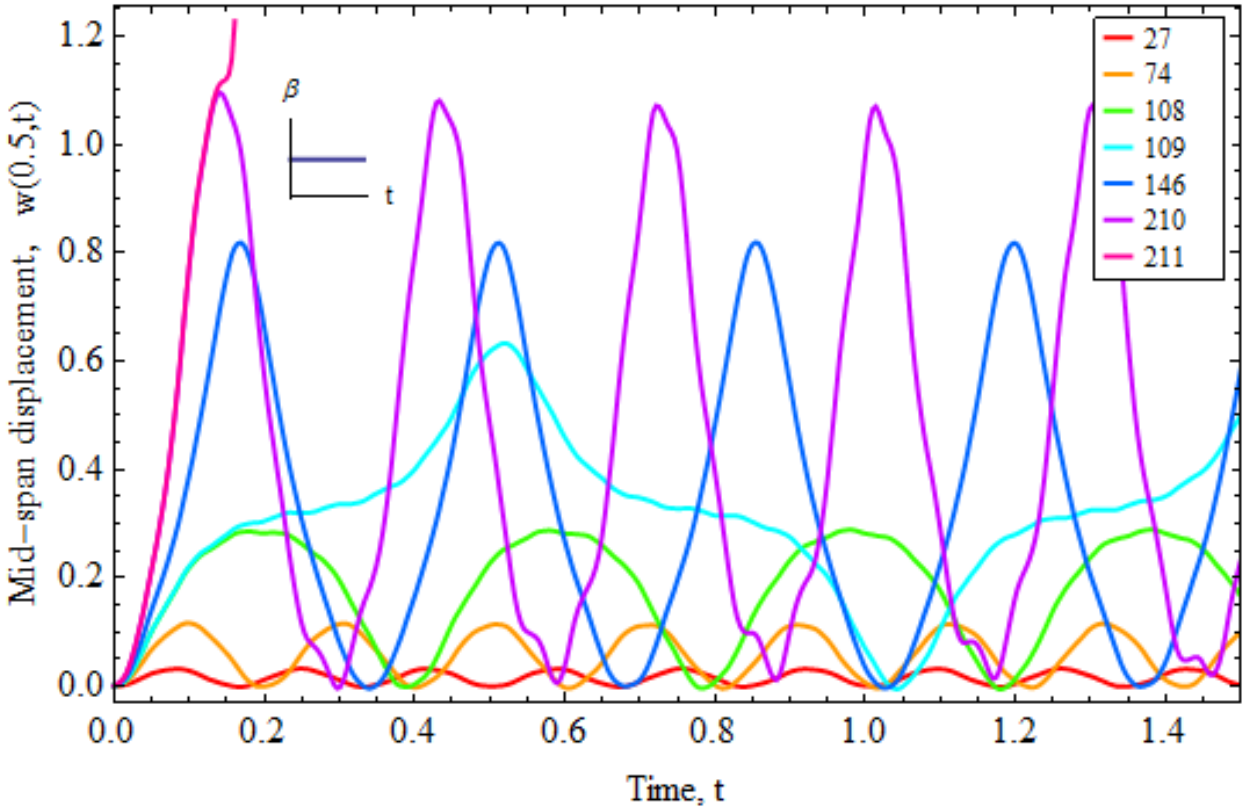

Figure 33. Time histories of the downward displacement of the mid-span of the fixed-fixed bell shaped arch (h = 0.3) for different values of β.

1.5.2. Direct snap-through instability

We consider a bell shaped silicon arch with α = 110, h = 0.3, $z_0(x) = \sin^2(\pi x)$. Figure 33 shows time histories of the deflection of the arch for different values of the applied step potential difference. A significant difference in the response of the arch occurs when β is increased from 108 to 109 in that the amplitude and the time period of oscillation increase noticeably. This sudden change in the response due to a small change in β indicates the snap-through instability. The critical value of β is between 108 and 109. By solving the problem for several values of β

between 108 and 109 (e.g. obtained by the bisection method), one can compute a better value of β for the snap-through instability. The critical value of β for the pull-in instability is found to be between 210 and 211, since for β = 210 the response of the arch remains bounded but for β = 211 it becomes unbounded. By solving the problem for several values of β between 210 and 211, one can compute a better value of β for the pull-in instability.

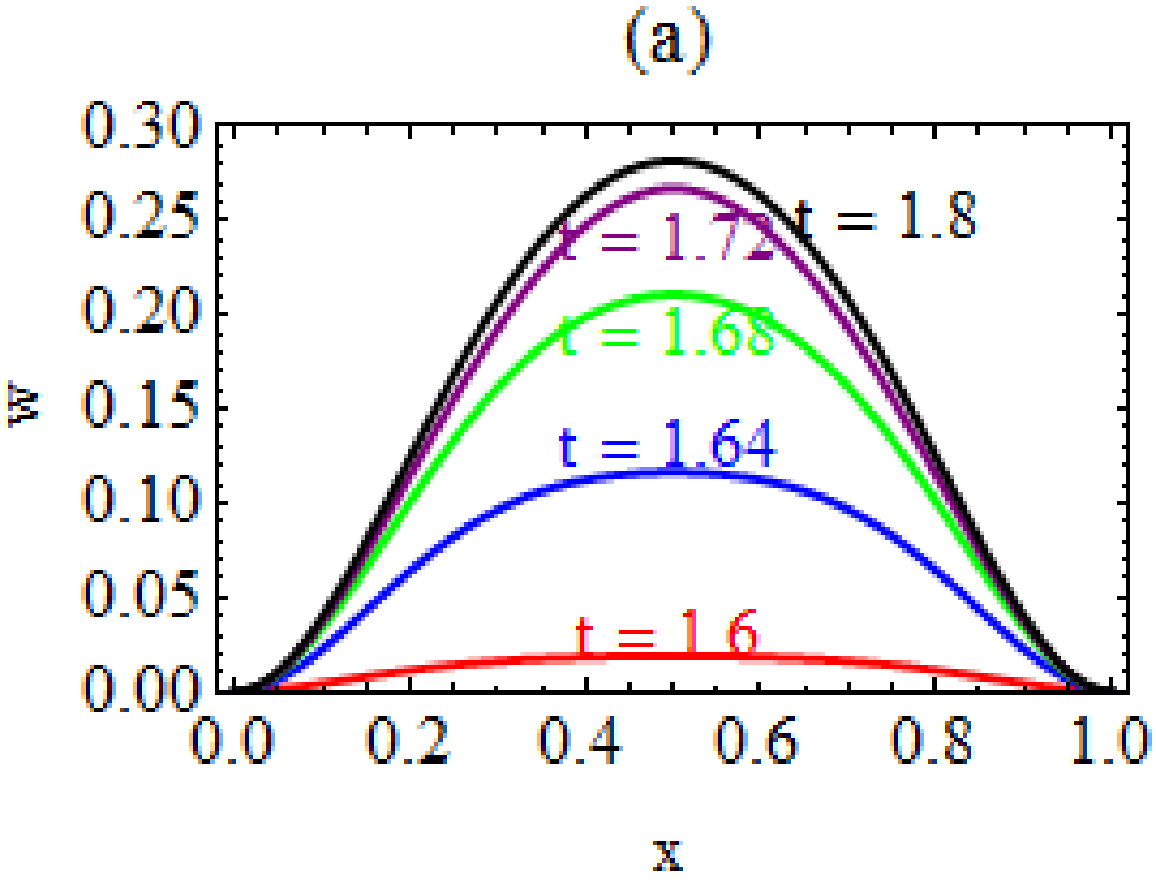

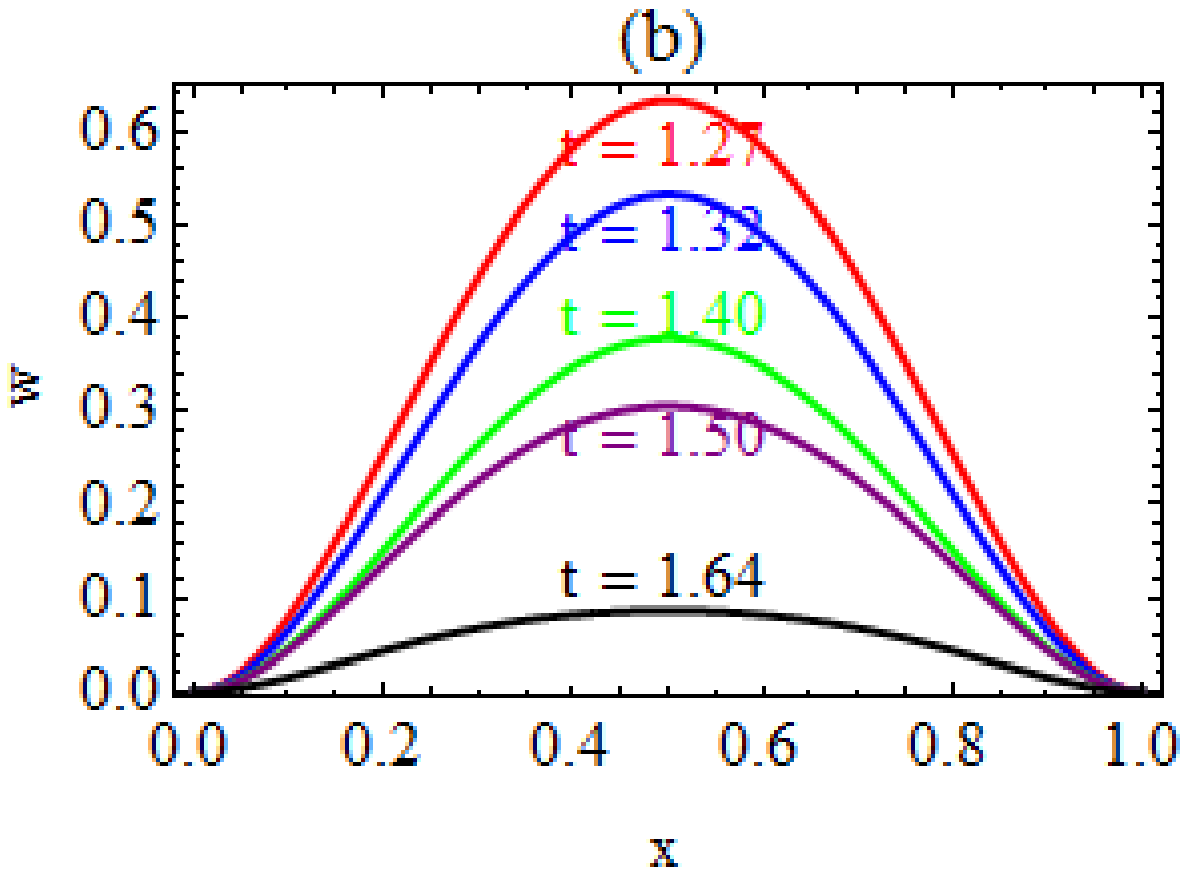

Figure 34. Snap shots of the displacement of the arch (h = 0.3) for (a) β = 108 and (b) β = 109

Figure 34 shows, at different times, snap shots of the variation of the deflection along the arch span for β = 108 (before the snap-through) and 109 (after the snap-through). It is clear that both before and after the snap-through the arch deforms symmetrically about the plane x = 0.5. Figure 35 exhibits time histories of the generalized coordinates for β = 108 and 109; these evince that participations of the asymmetric modes with coefficients q_2, q_4 and q_6 are negligible as compared to those of the symmetric modes with coefficients q_1, q_3 and q_5. Furthermore, a reasonably accurate response of the arch can be computed by considering only the fundamental mode in equation (36).

For several values of the arch height, figure 36 depicts loci of the maximum deflection produced by different step electric potentials with inertia effects, and static bifurcation curves obtained by using the DIPIE and the PALC algorithms. In every case, the bifurcation curve obtained from the DIPIE algorithm coincides with that obtained from the PALC algorithm. We note that the snap-

through due to a step electric potential difference occurs when the locus of the maximum deflection intersects the unstable branch of the static bifurcation curve (e.g., point D for $h = 0.3$ and 0.35 in figures 36a and 36b). A similar observation is reported in [56] due to a displacement-independent mechanical pressure load wherein the snap-through is called the 'direct snap-through' because the external pressure directly induces snapping of the symmetric mode in contrast to the 'indirect snapping' induced due to the parametric excitation of asymmetric modes as reported in the next section.

We note that after the snap-through instability (e.g., point D) arch's deformations are stable (e.g., point K) and the locus of the maximum displacement continues along the path KL until it again intersects the unstable branch of the static bifurcation curve (e.g., point L) when the pull-in instability occurs.

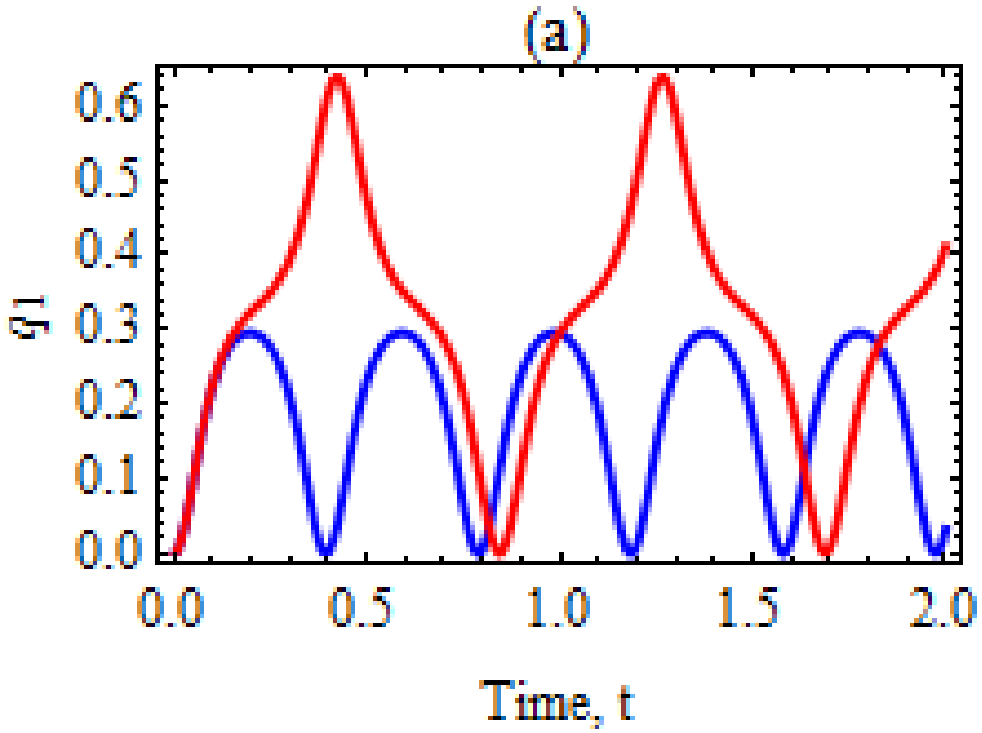

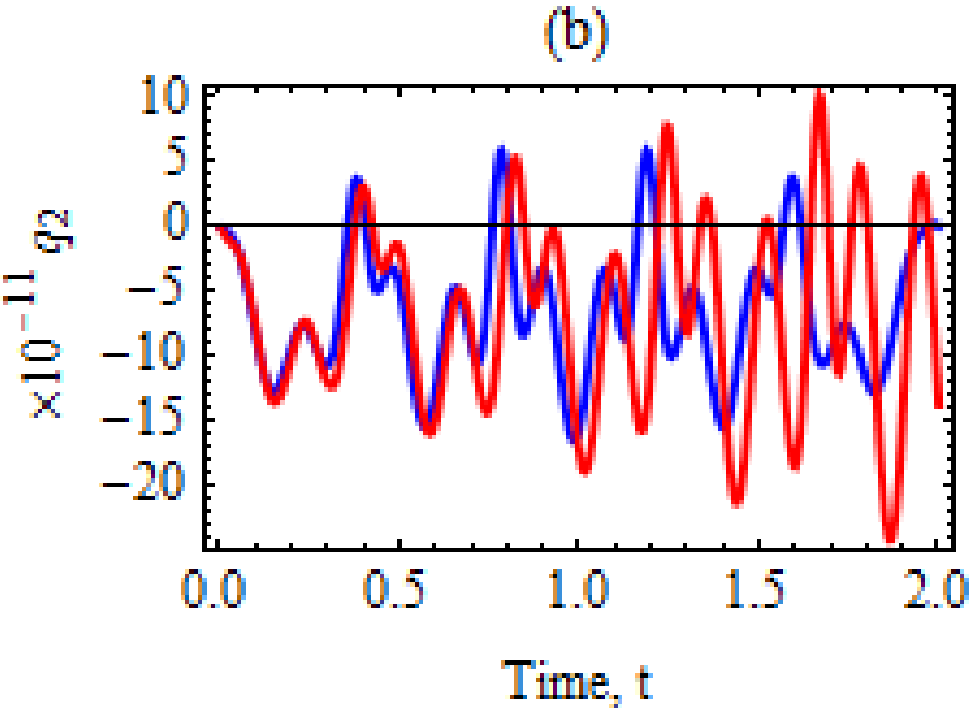
(b)
10
5
0
−5
−10
−15
−20
×10^−11 g2
0.0
0.5
1.0
1.5
2.0
Time, t

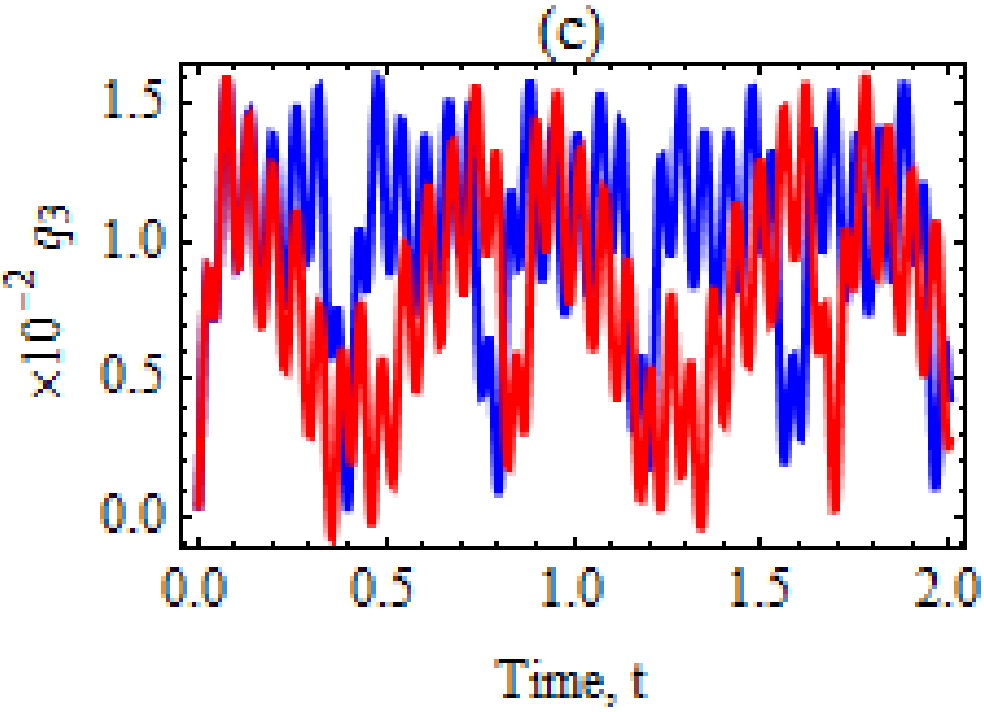
(c)
1.5
1.0
0.5
0.0
×10^−2 g3
0.0
0.5
1.0
1.5
2.0
Time, t

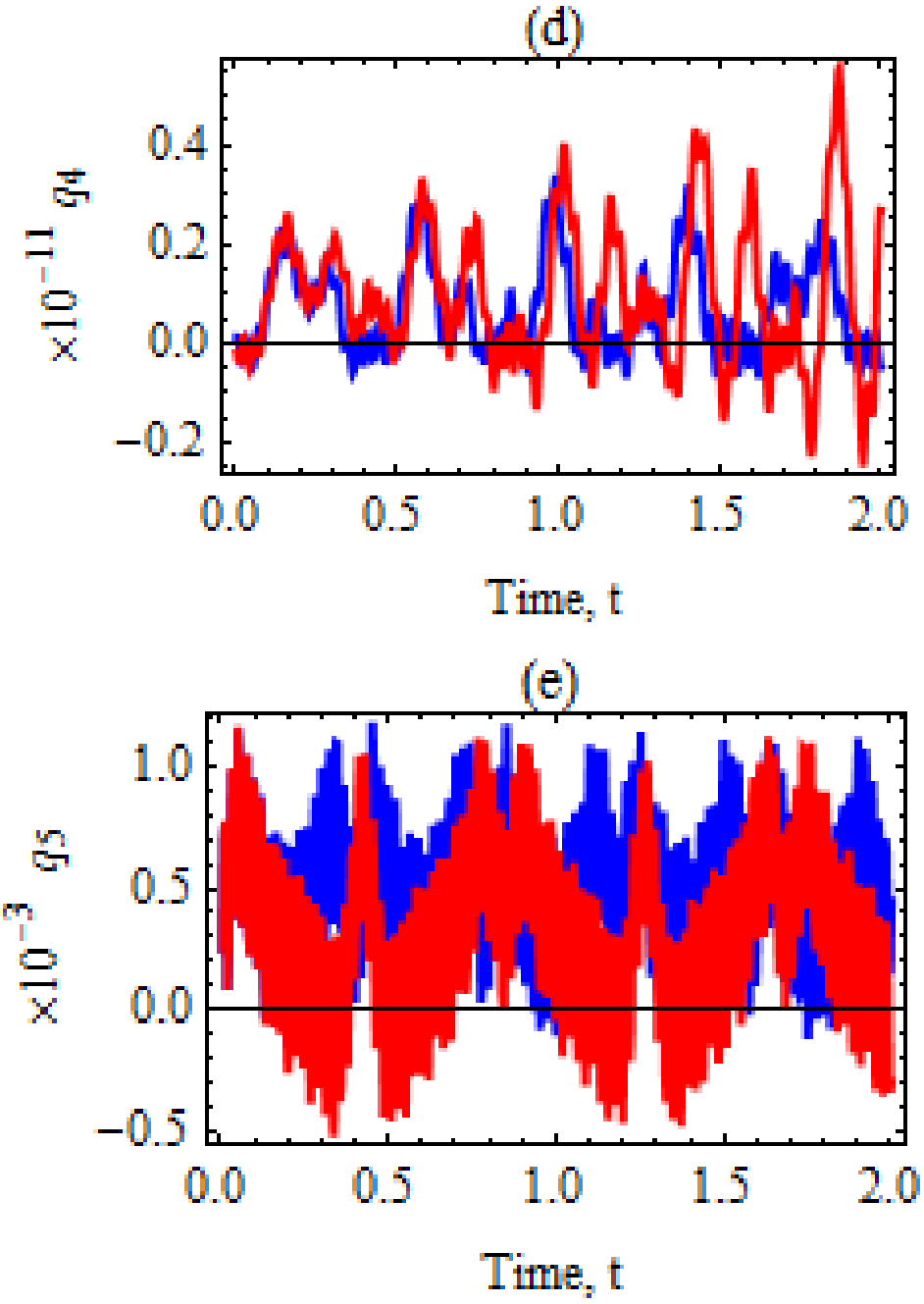
(d)
0.4
0.2
0.0
−0.2
×10^−11 g4
0.0
0.5
1.0
1.5
2.0
Time, t
(e)
1.0
0.5
0.0
−0.5
×10^−3 g5
0.0
0.5
1.0
1.5
2.0
Time, t

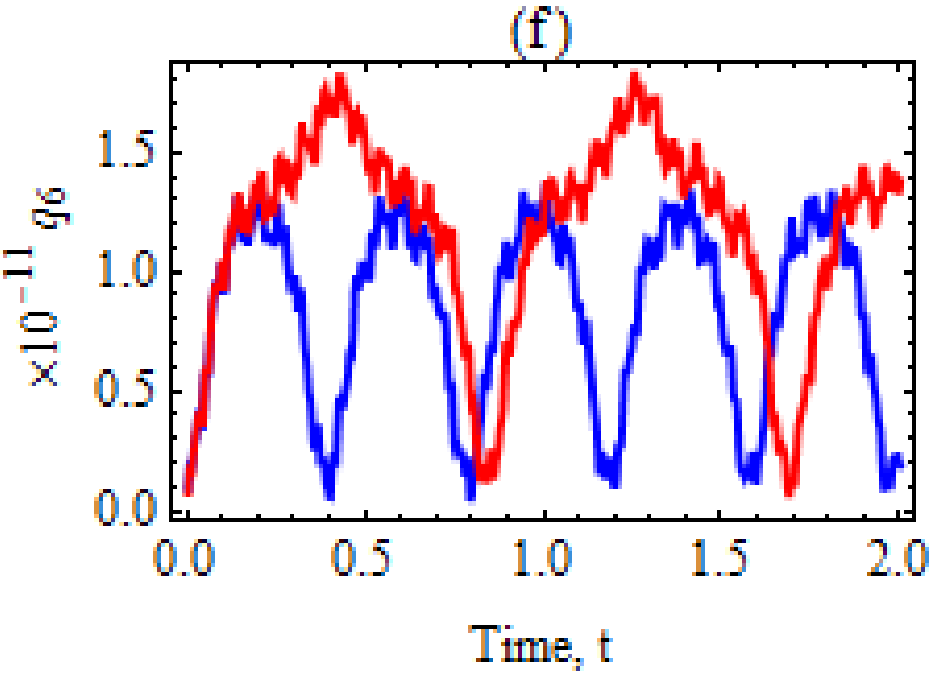

Figure 35. Time histories of q_1, q_2… q_6 for $\beta = 108$ (blue curves) and $\beta = 109$ (red curves).

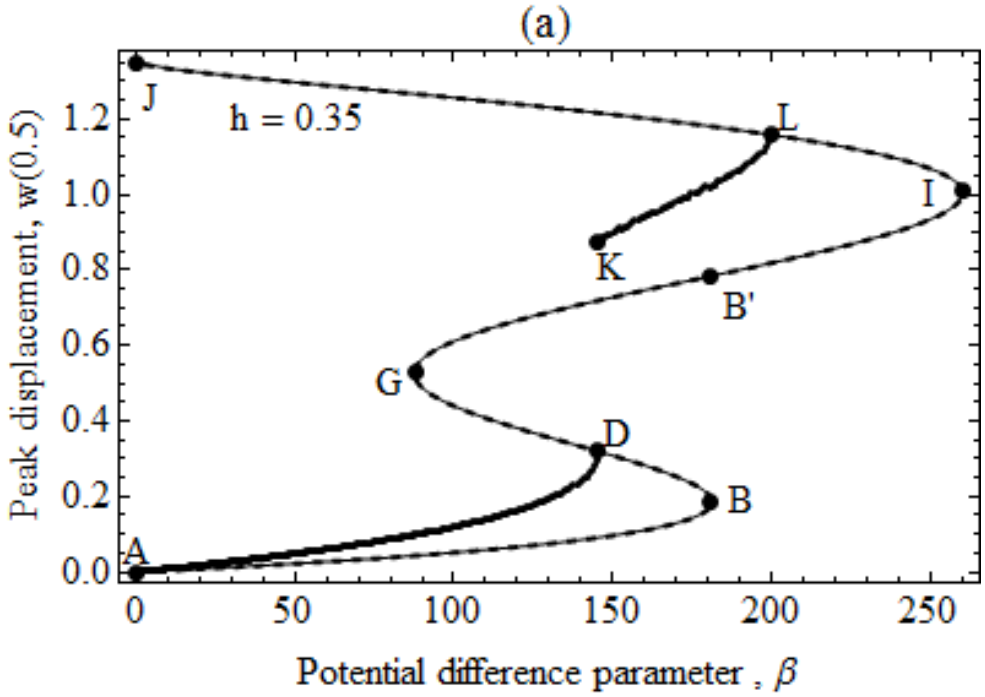

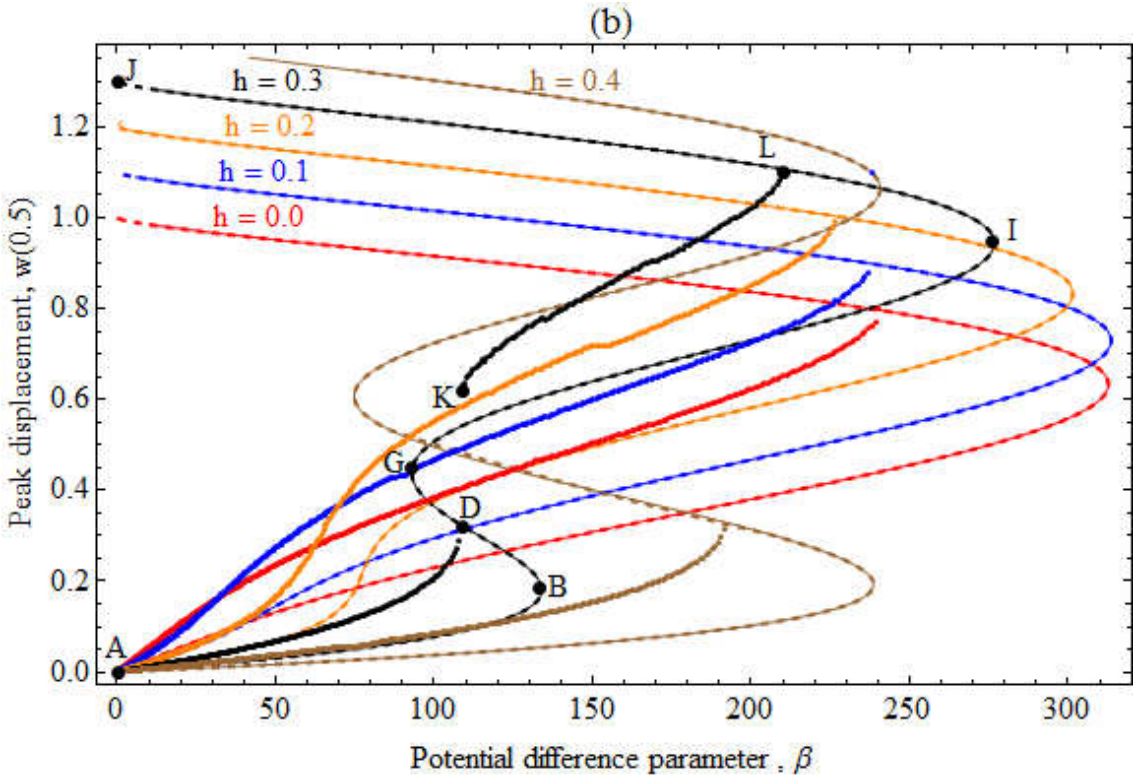

Figure 36. Bifurcation diagrams ($w(0.5)$ vs. β) of the arch for different arch heights for static problems. Dashed curves and light solid curves are results from the DIPIE and the PALC algorithms, respectively. Dark solid curves are the loci of the maximum displacements $\underset{0\le t\le 2}{Max}(w(0.5,t))$ under a step potential difference. Results from the DIPIE and the PALC algorithms overlap each other. Figure 36(a) for $h = 0.35$ clearly shows different curves.

For h = 0.0, 0.2, there is no snap-through instability, and the locus of the maximum deflection continues until the pull-in instability ensues. Therefore, a minimum height is required for the arch to undergo the snap-through instability. In Section 5.4, we report the minimum height required for the snap-through instability to occur for different values of α. For $h = 0.4$ no stable configuration under a step electric potential difference is observed after the snap-through instability as the pull-in instability occurs immediately.

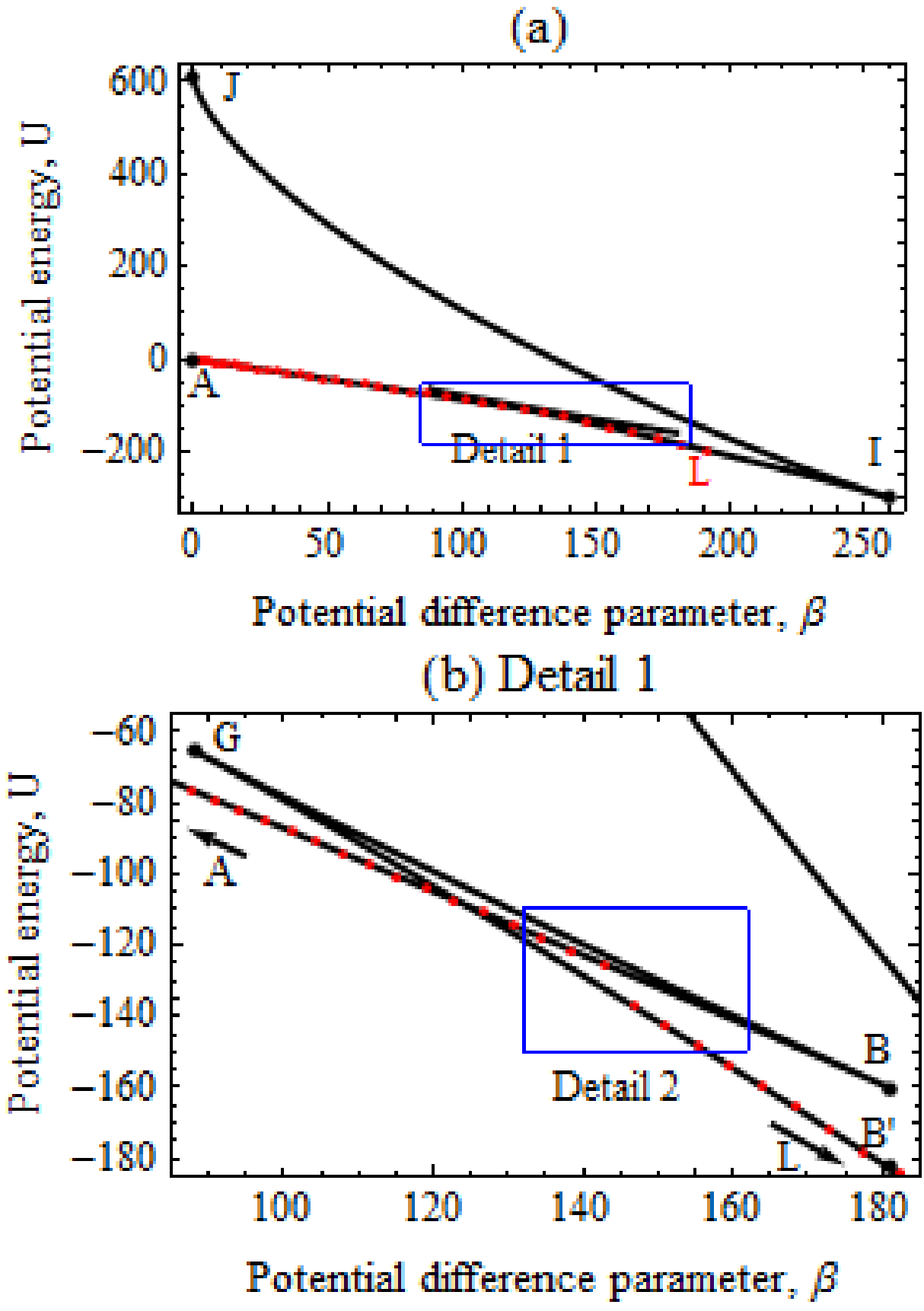
(a)
Potential energy, U
600
400
200
0
−200
J
A
Detail 1
L
I
0
50
100
150
200
250
Potential difference parameter, β
(b) Detail 1
Potential energy, U
−60
−80
−100
−120
−140
−160
−180
G
A
B
Detail 2
B'
L
100
120
140
160
180
Potential difference parameter, β

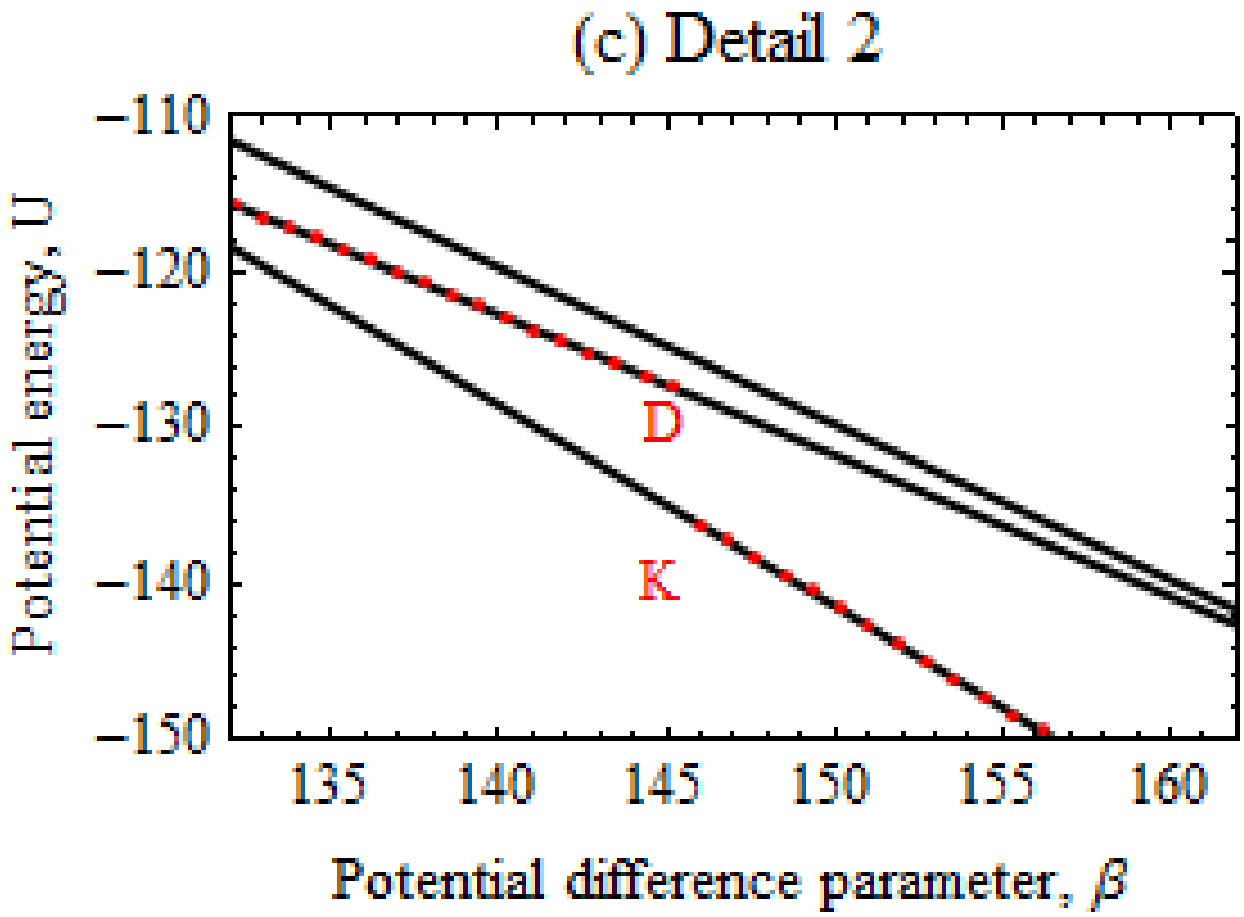

Figure 37. Potential energy *U(β)* versus the potential difference parameter β for $h = 0.35$ for the static problem (black curve), the locus of the minimum potential energy $\underset{0\le t\le 2}{Min}(U(\beta,t))$ as a function of the step potential difference for the dynamic problem (red dots).

At the snap-through instability for $h = 0.3$ and the step potential difference, the potential difference parameter β is *~15%* less and the peak displacement w is *~ 50%* more than their values for the corresponding static problem. At the pull-in instability, β is *~22%* less and the peak displacement *~21%* more than those for the static problem. Thus, the snap-through and the pull-in voltages for the dynamic problem are less than those for the static problem, but the snap-through and the pull-in deflections for the dynamic problem are greater than those for the static problem.

Figure 37 exhibits the variation of the potential energy versus β for a static problem with h = 0.35 and α = 110. The non-dimensional potential energy U is given by [49]

$$U = \frac{1}{2}\int_0^1 \left(w''\right)^2 dx + \frac{\alpha}{4}\left\{\int_0^1 \left(2hz_0'w' - \left(w'\right)^2\right)dx\right\}^2 - \beta\int_0^1 \frac{dx}{\left(1 + hz_0 - w\right)}. \quad (49)$$

For a dynamic problem with β a step function of time, w and U are functions of time. In figure 37, we also plot as red dots the locus of the minimum values of U for given step values of β. Points A, B, D etc. in figure 37 are for the same values of β as those in figure 36(a). For a static problem, the potential energy decreases from point A to point B as the value of β increases. At point B, the arch experiences the snap-through instability and the potential energy suddenly drops from -160 corresponding to point B to -182 for point B′ (see figure 37(b)). After the snap-through, the potential energy gradually decreases from -182 at point B′ to -301 at point I when the pull-in instability happens. For the dynamic problem, the locus of the minimum potential energy (red dots in figure 37) follows the curve of U versus β for the static problem from point A to point D. At point D, with a small increase in β, the minimum potential energy drops from -130 at point D to -138 at point K, this indicates the snap-through instability. After the snap-through instability at point K, the locus of the minimum potential energy follows the curve of U versus β for the static problem from point K to point L where the pull-in instability happens (figure 37(a)).

1.5.3. Indirect snap-through instability

For arch height h = 0.5, figure 38 shows time histories of the maximum deflection of the arch for different values of the step potential differences β. At β = 293 the arch undergoes several cycles of moderate-amplitude oscillations before snapping. The pull-in instability occurs immediately after the snap-through instability. The critical value of β is between 292 and 293. This behavior is significantly different from that observed for h = 0.3 and h = 0.35 for which the snap-through instability ensued without the arch undergoing oscillations.

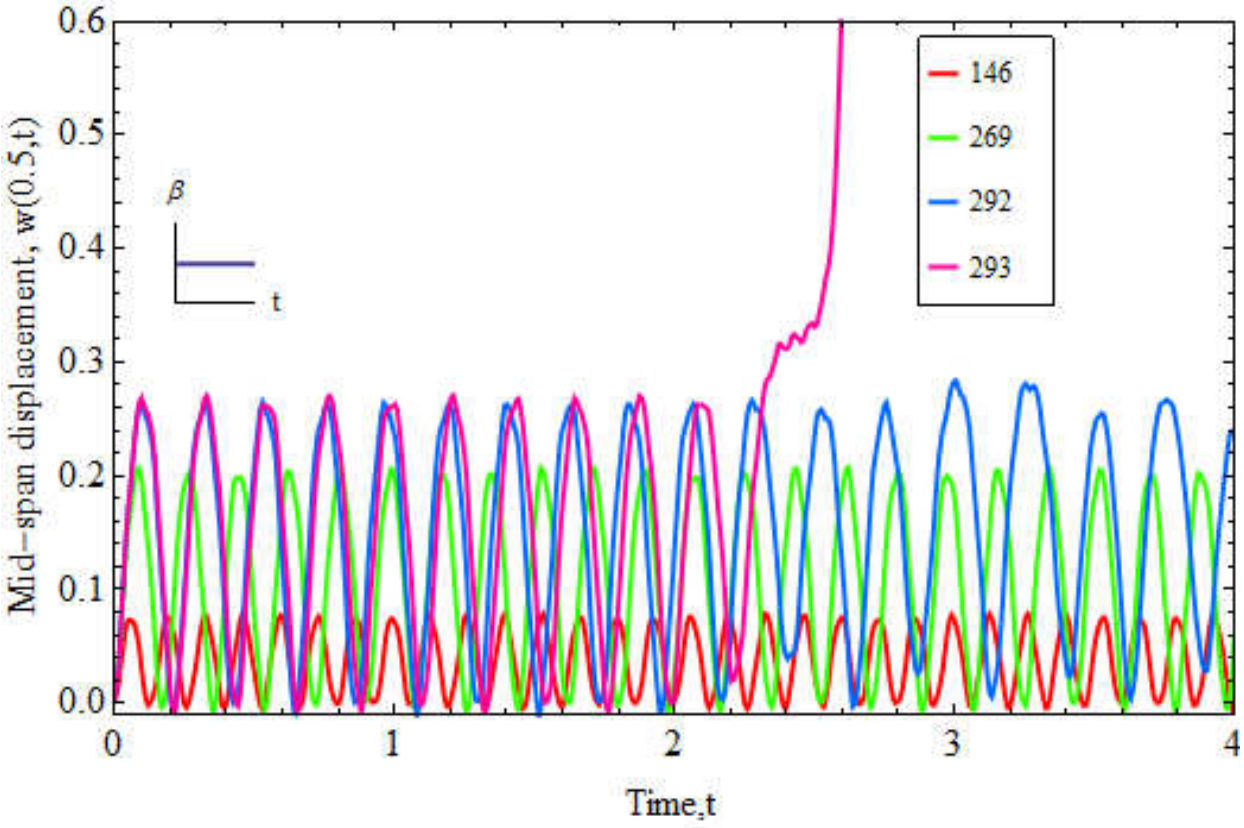

Figure 38. For different applied step voltages time histories of the downward displacement of the mid-span of the fixed-fixed bell shaped arch with $h = 0.5$.

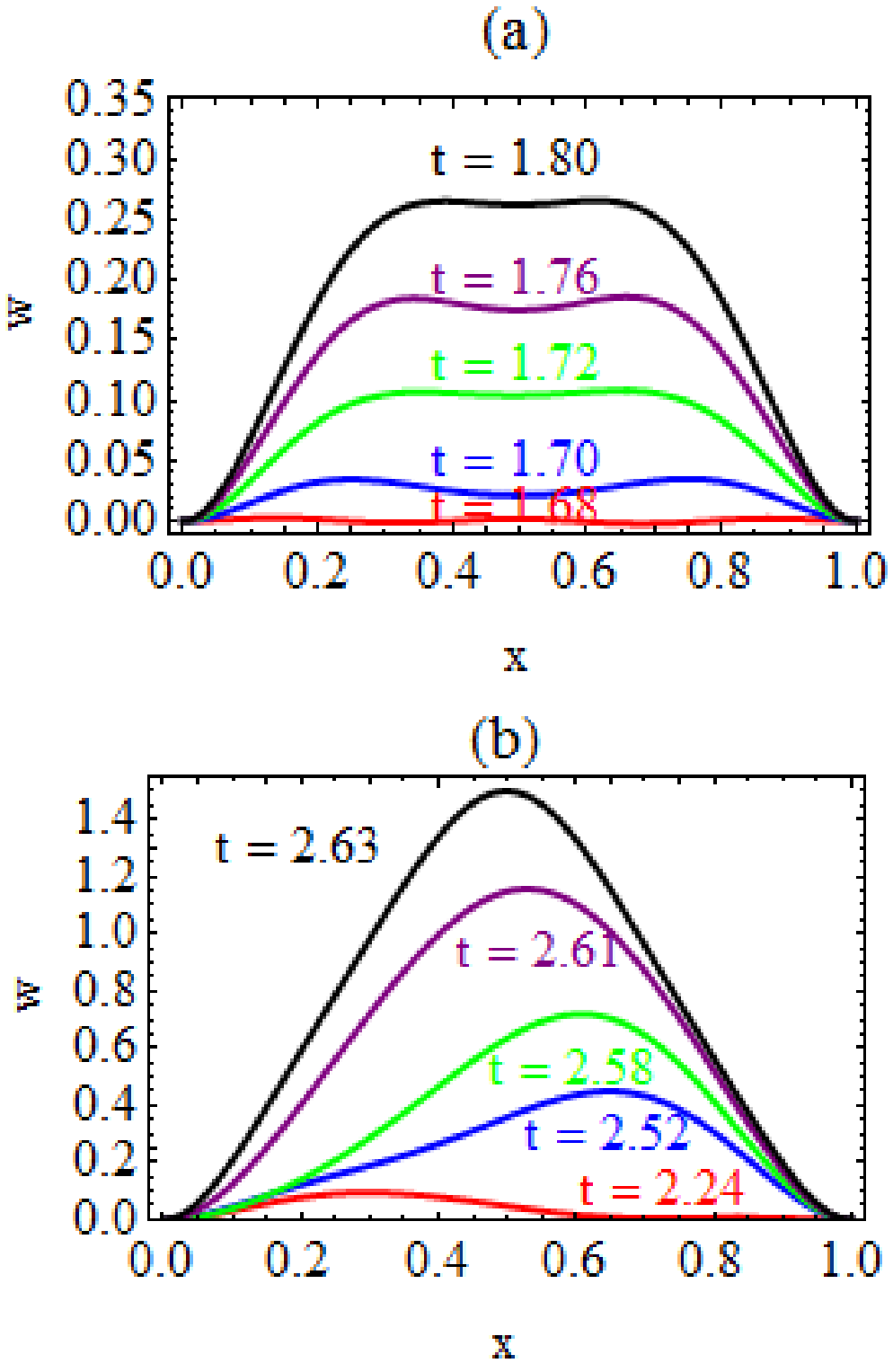

Figure 39. Snap shots of the displacement of the arch ($h = 0.5$) for (a) $\beta = 292$ and (b) $\beta = 293$.

Figure 39 exhibits snap shots of the variation of the deflection along the span of the arch at different non-dimensional times for β = 292 (before the snap-through) and 293 (after the snap-through). It is clear that the arch deforms symmetrically about x = 0.5 before the snap-through instability but asymmetrically after the snap-through. However, we observe that just before the arch touches the bottom electrode at t = 2.63, its deflections are again symmetric about x = 0.5. Figure 40 exhibits time histories of the generalized coordinates for β = 292 and 293. These evince that the participation of the asymmetric modes (q_2, q_4 and q_6) grows considerably after t = 2.2 when the snap-through instability occurs. Whereas values of q_2, q_4 and q_6 in figure 35 were of the order of 10^{-11}, those in figure 40 are of the order of 10^{-1}, 10^{-2} and 10^{-3} respectively. These suggest that the participation of mode 2 is more than that of modes 4 and 6 in making deformations of the arch asymmetric about x = 0.5. Asymmetric modes starts to participate in deformation of the arch for β = 292 after t = 2.2. However, the participations of the asymmetric modes remain bounded and do not cause either the snap-through or the pull-in instability. On the other hand, for β = 293, the displacement of the arch becomes unbounded at about t = 2.2 and the pull-in instability occurs.

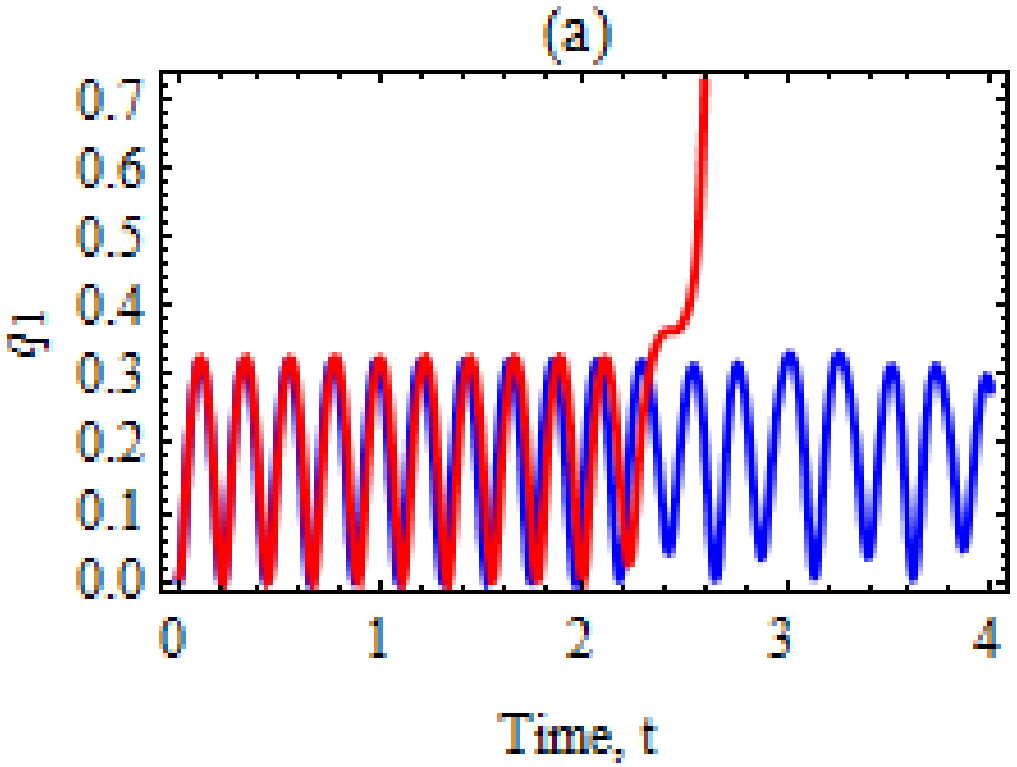

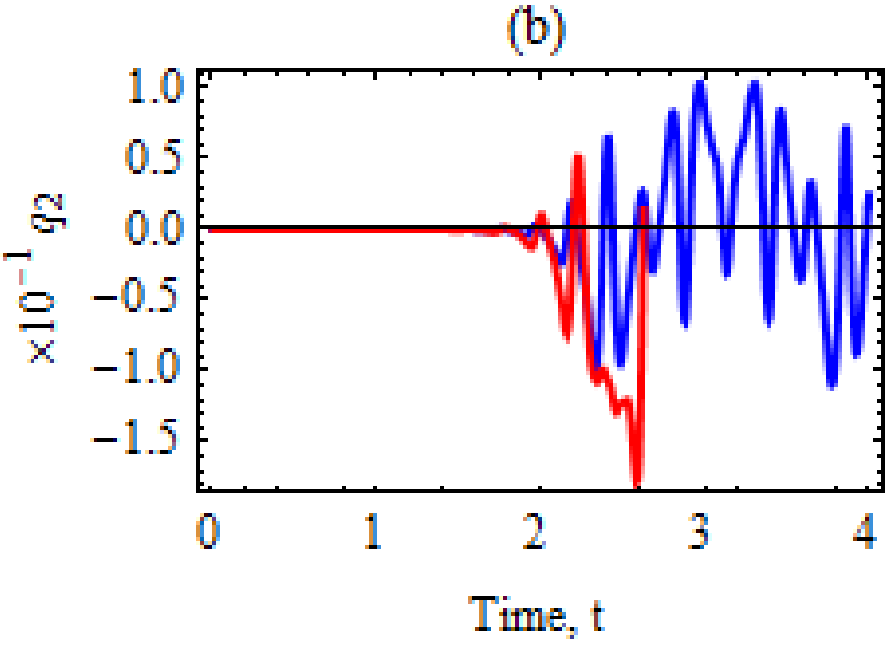
(b)
1.0
0.5
0.0
−0.5
−1.0
−1.5
×10⁻¹ q2
0
1
2
3
4
Time, t

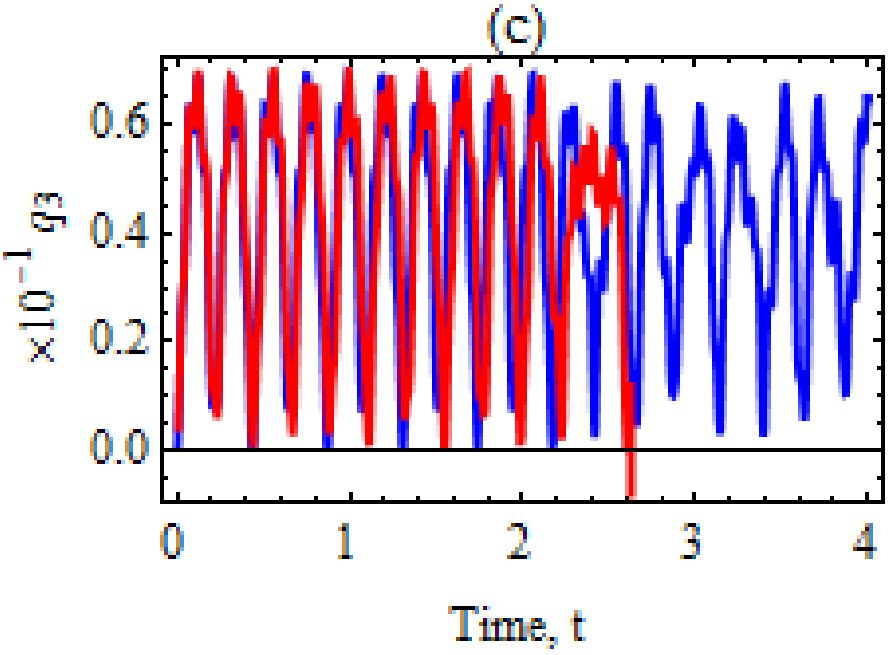
(c)
0.6
0.4
0.2
0.0
×10⁻¹ q3
0
1
2
3
4
Time, t

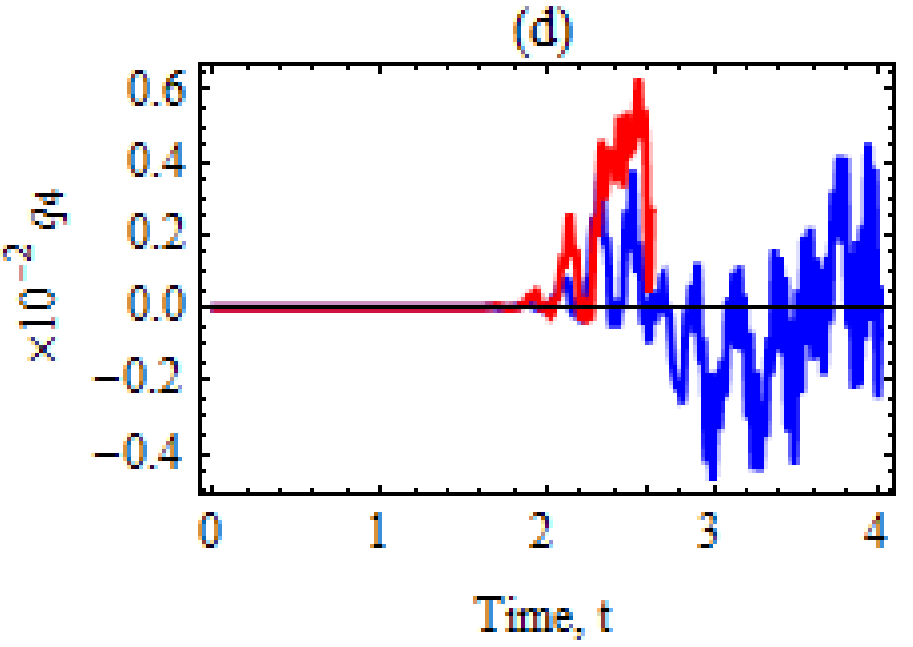
(d)
0.6
0.4
0.2
0.0
−0.2
−0.4
×10^−2 q4
0
1
2
3
4
Time, t

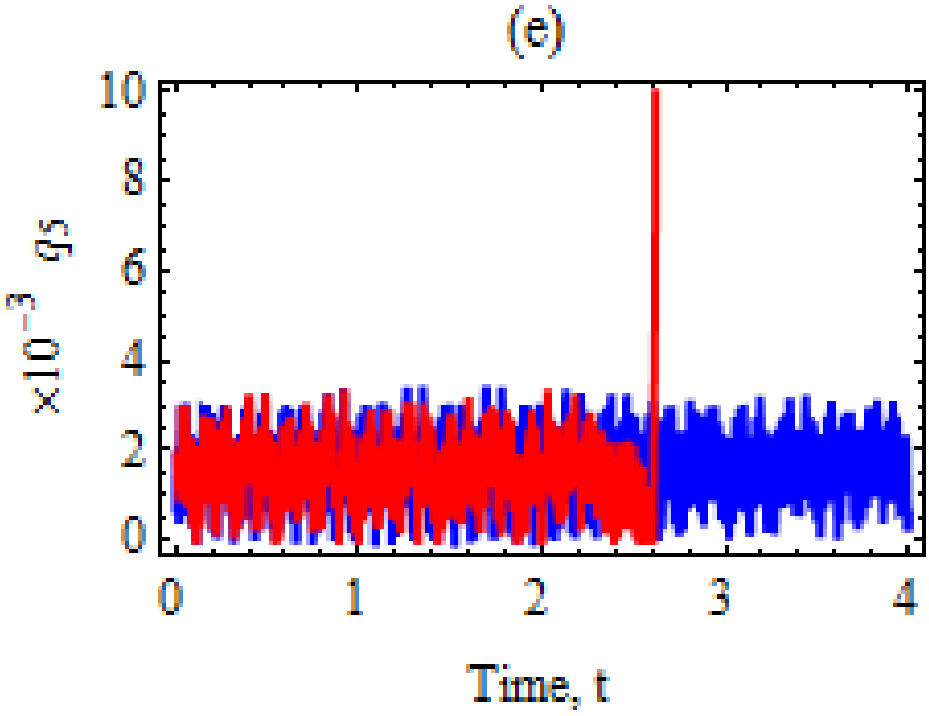
(e)
10
8
6
4
2
0
×10^−3 q5
0
1
2
3
4
Time, t

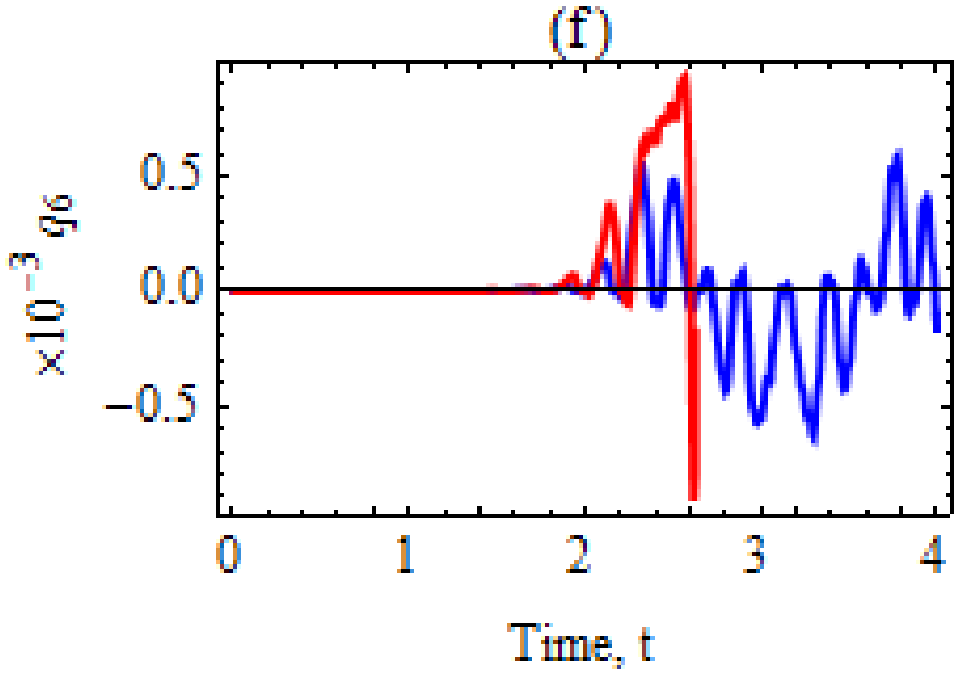

Figure 40. Time histories of q_1, q_2… q_6 for β = 292 (blue curves) and β = 293 (red curves).

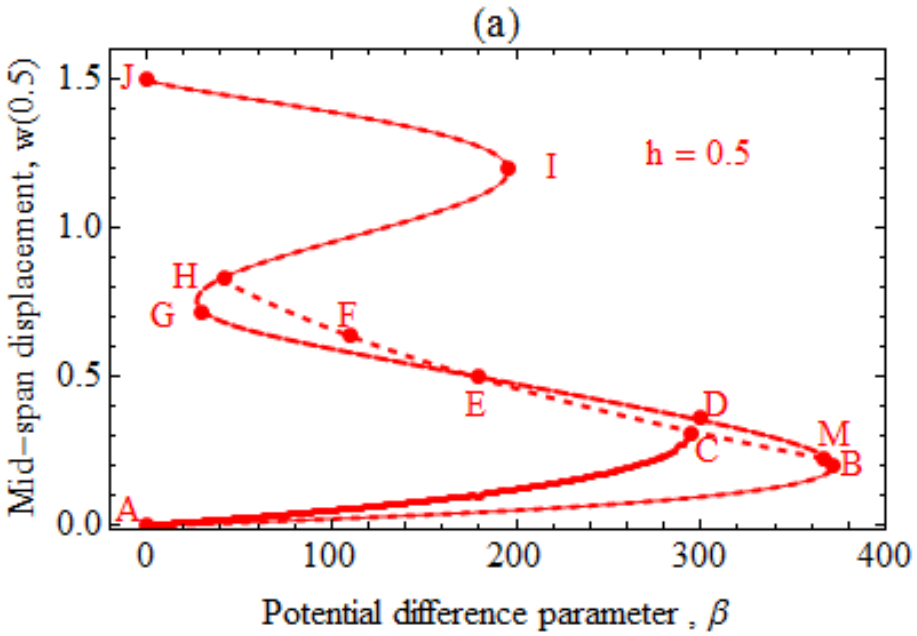

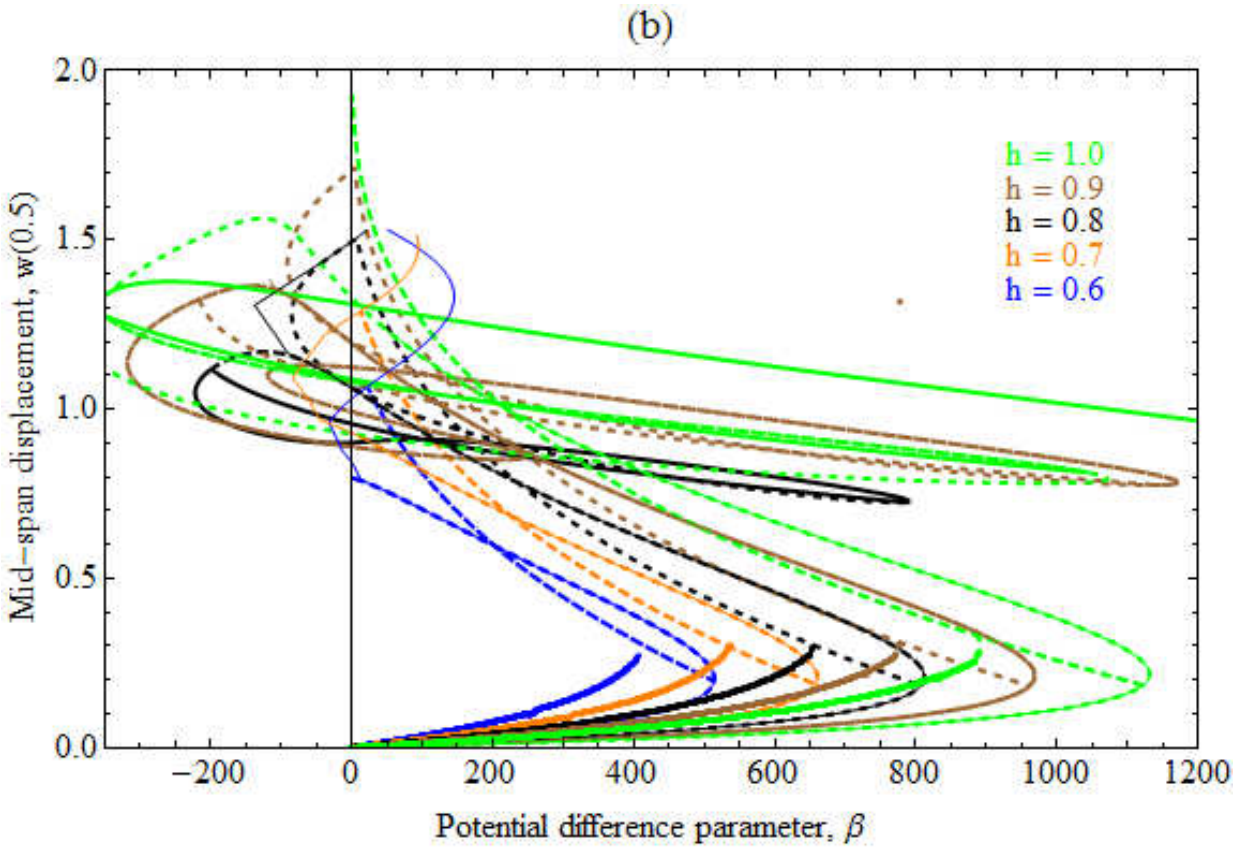

Figure 41. Bifurcation diagrams ($w(0.5)$ vs. β) of the arch for different arch heights for static problems. Dashed curves and light solid curve are results from the DIPIE and the PALC algorithms, respectively. Dark solid curves are the loci of the maximum displacements $\underset{0\le t\le 4}{Max}(w(0.5,t))$ under the step load. Results of the DIPIE and the PALC algorithms overlap only when arch's deformations are symmetric about $x = 0.5$.

The reason of the snap-through instability with asymmetric deformations is the parametric excitation of the anti-symmetric modes arising through coupling terms such as $q_i q_{i+1}$ (with i = 1 ... n-1) in equation (39). These terms act as an effective load whose magnitude increases as the amplitude of the anti-symmetric motion grows under the parametric excitation. If the amplitude of anti-symmetric motion becomes sufficiently large, a critical effective load is reached, and the snap-through instability occurs. This second kind of snapping is called 'indirect snap-through' or 'parametrically induced snap-through' in [56] where snapping of a shallow arch under a displacement-independent step pressure load is studied. Note that for the electric loading F_i in equation (39) also depends on deformations of the arch, unlike the displacement-independent

pressure load where F_i is independent of q_i; thus, there are more coupled terms in the MEMS problem than those in the mechanical problem analyzed in [56]. Results for a problem reported in the next section show that under an electric load an arch is more prone to snap through asymmetrically than under displacement-independent mechanical loads.

Figure 41 depicts loci of the maximum deflection produced by a step electric potential for the transient problem, and bifurcation curves for static problems obtained with the DIPIE and the PALC algorithms for h = 0.5, 0.6, 0.7, 0.8, 0.9, and 1.0. In every case, the bifurcation curve for symmetric deformations computed with the DIPIE algorithm overlaps on that obtained with the PALC algorithm (e.g., the curve ABMDEGHIJ for $h = 0.5$ in figure 41(a)). The DIPIE algorithm does not give asymmetric solutions [12, 72] (e.g., the dashed curve MCEFH for $h = 0.5$ in figure 41(a)), which are obtained by the PALC algorithm. We note that, for all values of h, the snap-through due to the step load occurs when the locus of the maximum deflection intersects the unstable branch of the static bifurcation curve (e.g., point C for $h = 0.5$ in figure 41(a)) corresponding to the asymmetric solution. The pull-in instability happens immediately after the snap-through instability. Values of β and the peak deflection w at the snap-through instability due to a step potential difference (e.g., point C for $h = 0.5$) for the dynamic problem are ~20% lower and ~25% higher, respectively, than those for the corresponding static problem (e.g., point B for $h = 0.5$). For $h \geq 0.8$, complex branches of the bifurcation diagram corresponding to unstable deformations of the arch are found from the PALC algorithm. A similar behavior, known as the looping behavior of an arch, is reported in [37, 102] due to a displacement-independent mechanical pressure load. Results in figure 41(b) for $\beta < 0$ do not have physical meaning since β cannot be less than zero in reality. For asymmetric deformations of the arch corresponding to a point on the dashed curve BCEFH for h = 0.5 in figure 41(a), the PALC algorithm gives two solutions displayed in figure 42.

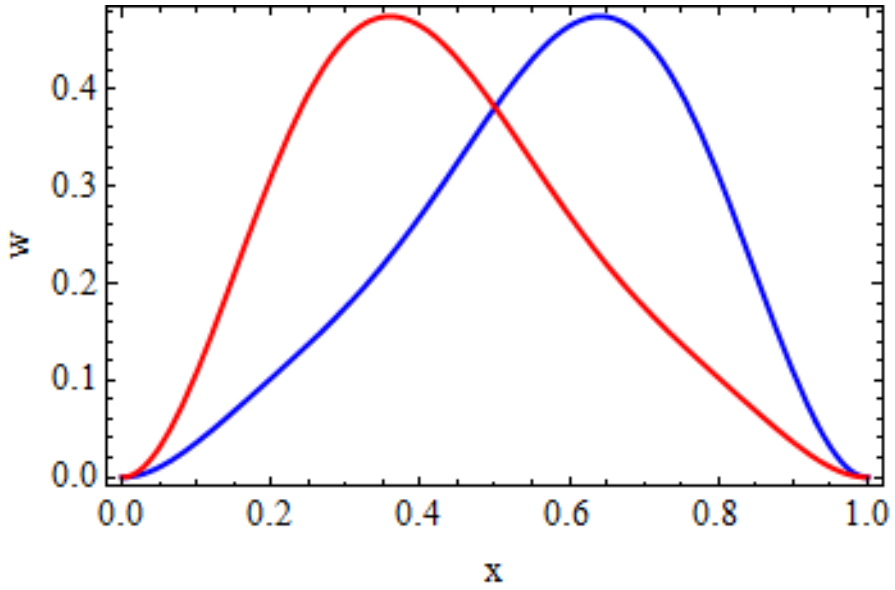

Figure 42. The two asymmetric solutions for $h = 0.5$ and $\beta = 250$.

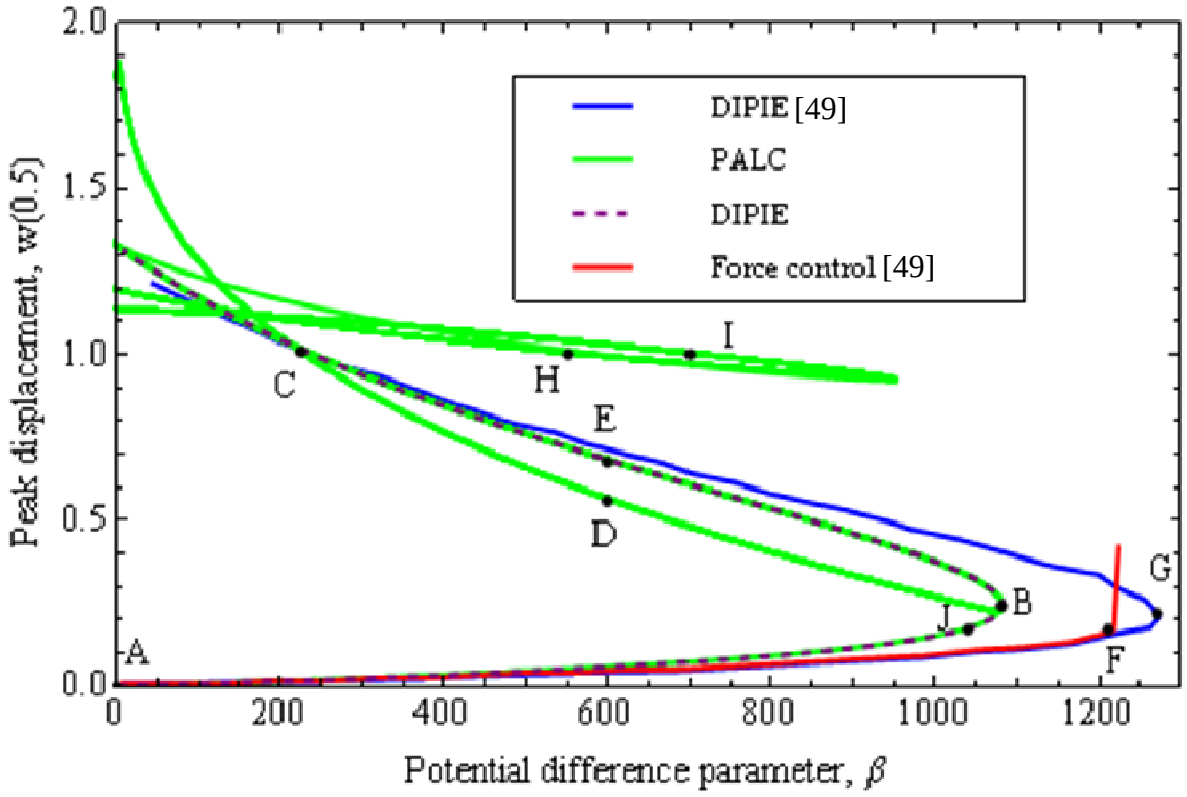

Figure 43. Bifurcation diagrams ($w(0.5)$ vs. β) of the arch for different arch heights for static problems ($h = 1.0, \alpha = 250$).

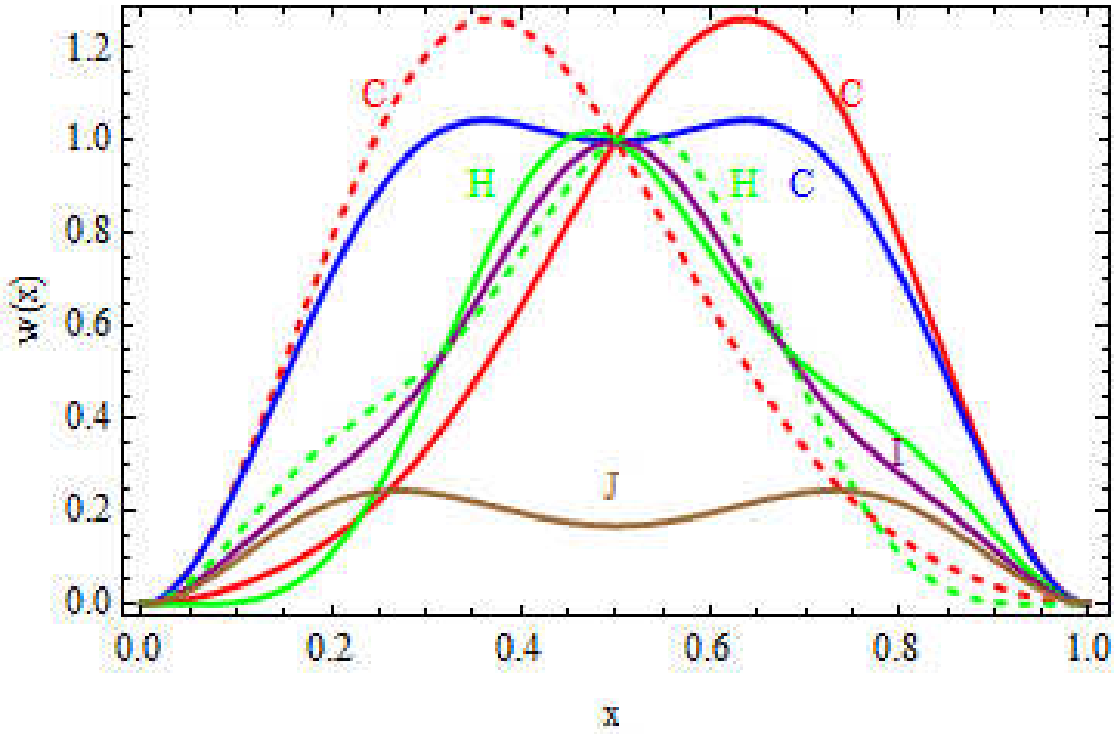

Figure 44. Deformations at different points of the bifurcation diagram for $h = 1.0$ and $\alpha = 110$.

In [49], the symmetry breaking of arches under electric loads in static problems is studied using a force control method and taking $n = 15$ in equation (36). Figure 43 compares the presently computed bifurcation curve for an arch with $h = 0.5, \alpha = 250$ and $n = 6$ with that reported in [49]. The bifurcation curve (ABEC from our code and AFGEC from [49]) from the DIPIE algorithm fails to show the asymmetric deformations of the arch. Asymmetric deformations (BDC) and the looping behavior are observed in the solution from the PALC algorithm. In [49], the symmetry breaking is found with the force control method. The critical value of β at the snap-through instability computed with our code is 16.7% less than that reported in [49]. We found that increasing n from 6 to 10 does not change the results appreciably and including mode shapes for $n > 10$ increases numerical inaccuracies because for large λ_i, $cos(\lambda_i x)$ is very small as compared to values of $sinh(\lambda_i x)$ and $cosh(\lambda_i x)$.

Figure 44 shows different unstable and one stable solution for the arch corresponding to different points on the bifurcation curve in figure 43. Deformations corresponding to points C, H and I are unstable, which means the arch may have those equilibrium configurations under a static load of $\beta = \sim 230$, ~ 550 and ~ 700, respectively. However, a small perturbation will cause the arch to

experience the pull-in instability. Points C and H represent multiple symmetric and asymmetric deformations of the arch.

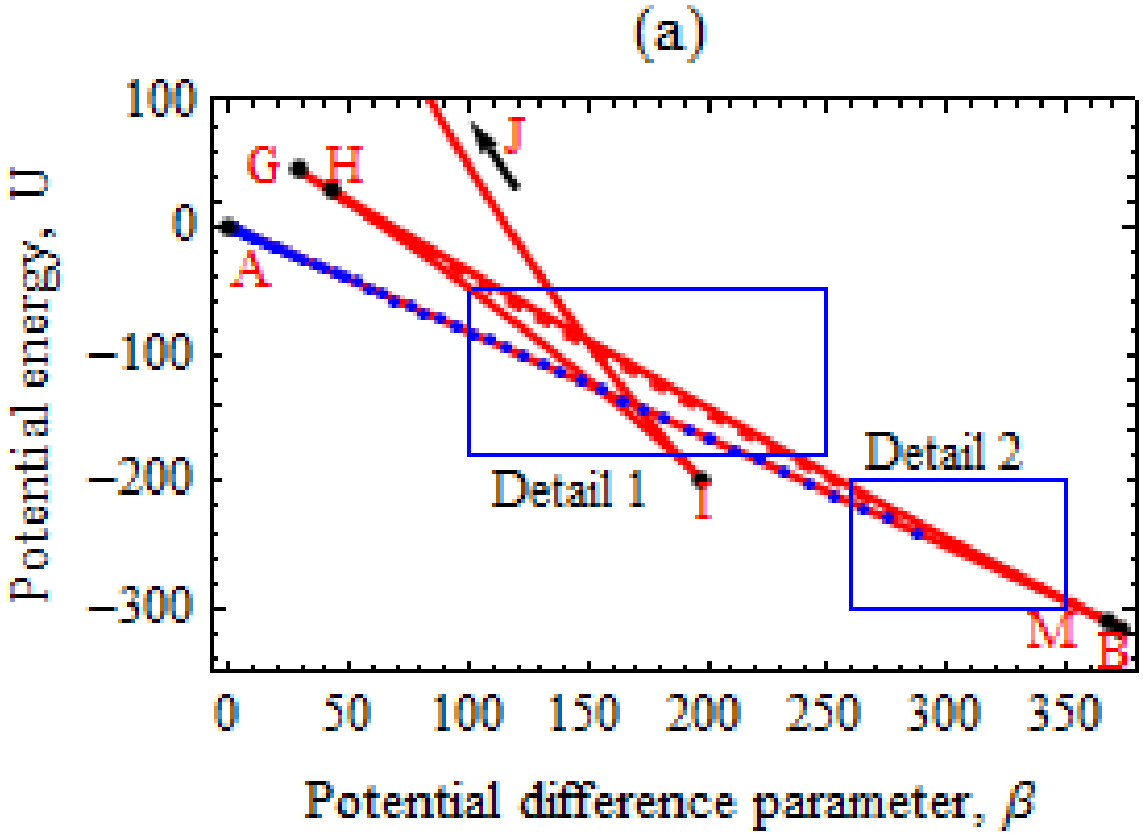

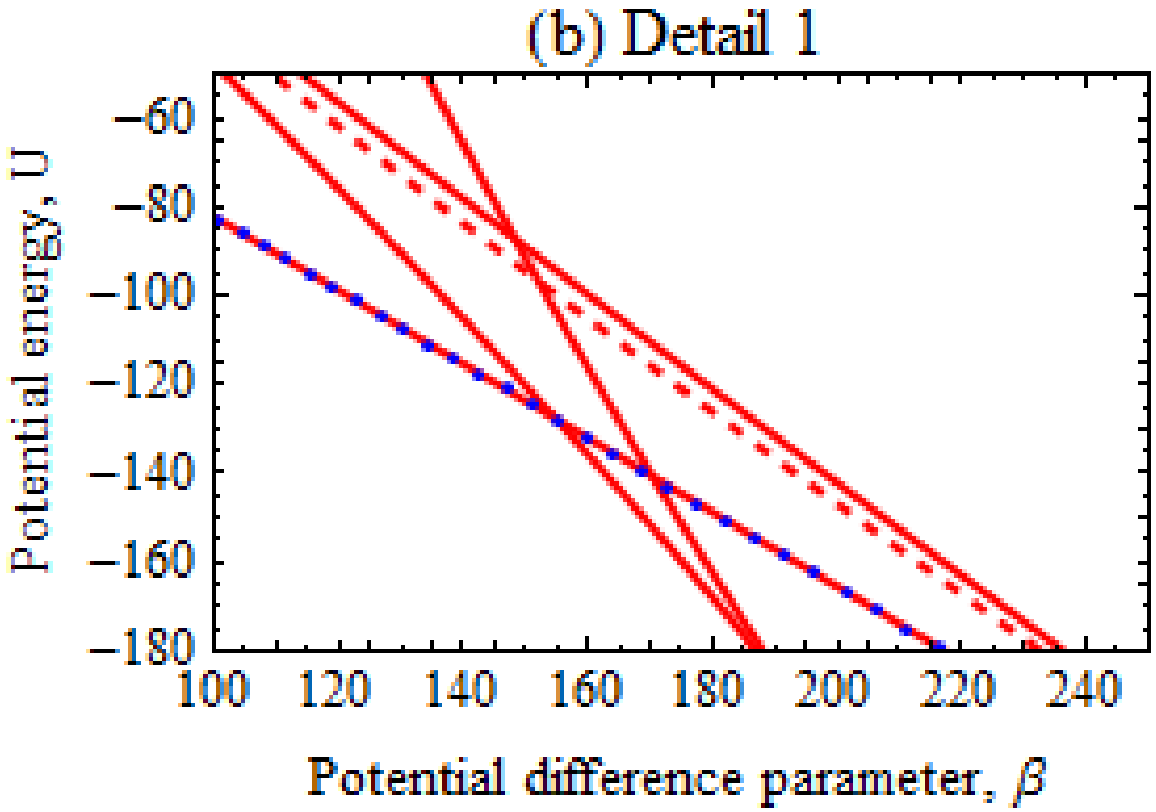
(b) Detail 1
Potential energy, U
−60
−80
−100
−120
−140
−160
−180
100
120
140
160
180
200
220
240
Potential difference parameter, β

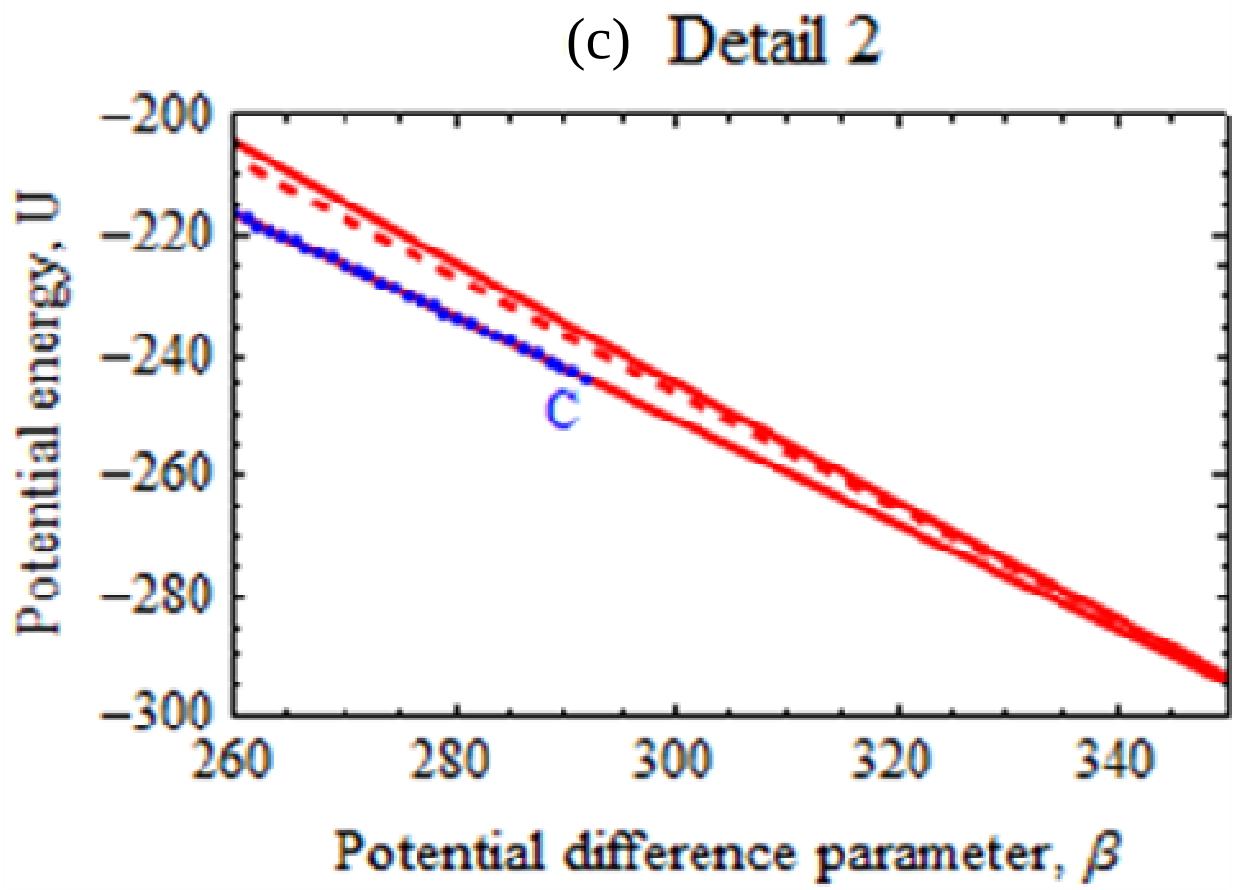

Figure 45. Potential energy *U(β)* versus the potential difference parameter β for $h = 0.5$ for the static problem (red curve), the locus of the minimum potential energy $\underset{0 \le t \le 2}{Min}(U(\beta, t))$ as a function of the step potential difference for the dynamic problem (blue dots).

Figure 45 exhibits the variation of the non-dimensional potential energy U (cf. equation (49)) versus the non-dimensional potential difference parameter β for a static problem with $h = 0.5$ and $\alpha = 110$. In figure 45, we have also plotted for transient problems the locus of the minimum values of U for step voltages β. Points A, B, C, etc. in figure 49 have the same values of β as those in figure 41(a). For a static problem, U decreases from 0 at point A to ~ -300 at point B as β increases from 0 to 370. We note that there is no other solution with lower values of U than that at point B. At point B, the arch experiences the snap-through instability followed immediately by the pull-in instability and no solution exists for a value of β that is higher than the value of β at point B. We also note that for $h = 0.35$ (see figure 37), the value of β at point I

is higher than the value of β at point B, whereas for $h = 0.5$ (see figure 45), the value of β at point I is lower than that at point B. In figure 45(b) the total potential energy for an unstable asymmetric solution corresponding to a point on the dashed curve MH is lower than that for the unstable symmetric solutions represented by the solid curve BH. The locus of the minimum potential energy for the dynamic problem denoted by blue dots in figure 45 follows the curve of U versus β for the static problem from point A to point C. At point C, the snap-through instability and the pull-in instability happen simultaneously for the dynamic problem.

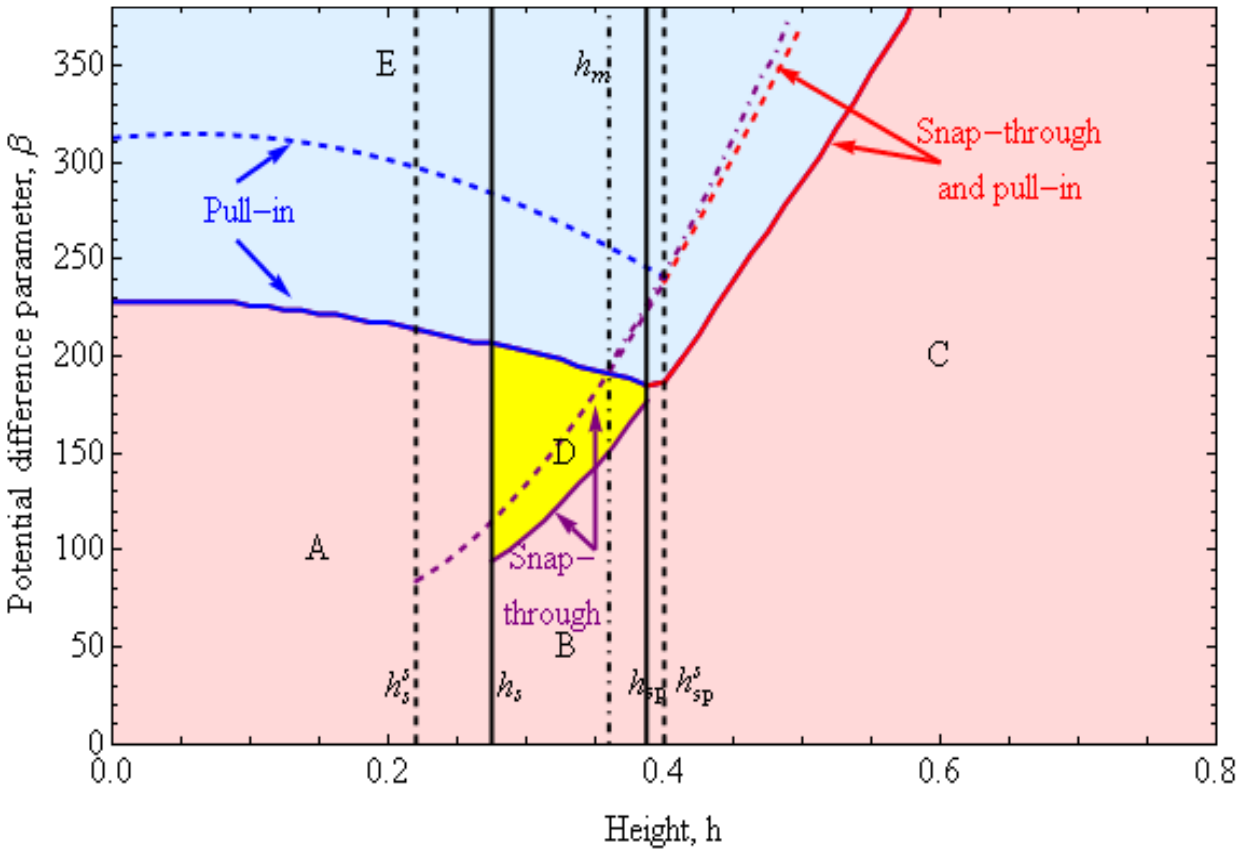

Figure 46. Critical values of β for the snap-through (purple curve) and the pull-in instabilities (blue curve) to occur for an arch with $\alpha = 106.0$. The red curve shows critical values of β for which the snap-through and the pull-in instabilities occur simultaneously. Solid and dashed curves correspond, respectively, to results for the dynamic and the static problems. The dot dashed curve represents results for the dynamic problem with a displacement-independent load.

1.5.4. Comparison of results for dynamic problems with those for static problems

The critical potential difference parameters for the pull-in instability (blue curve), the snap-through instability (purple curve), and the snap-through followed immediately by the pull-in instability (red curve) are plotted as a function of the arch height in figure 46 for α = 106.0. Solid curves correspond to results for dynamic problems due to the application of the step electric potential difference, and the dashed curves to results for static problems. Note that only value of h and β are varied and other parameters for the MEMS are kept unchanged. For h between *0.0* and *0.8* the critical values of β for dynamic problems are 'substatic' in the sense that they are lower than those for the corresponding static problems. The minimum height h_s^s = 0.22 required for the arch to experience the snap-through instability for a static problem is less than the corresponding value of h_s = 0.275 for the dynamic problem. However, the minimum arch heights at which the blue and the purple curves meet each other are almost the same for the static and the dynamic problems (e.g., h^s_{sp} = 0.4, h_{sp} = 0.37). An arch with a height greater than h_{sp} will experience the pull-in instability immediately after the snap-through instability under a step electric potential difference; h^s_{sp} is the corresponding value for the static problem. The dot-dashed purple curve shows critical values of β for the snap-through instability due to a step displacement-independent mechanical load given by equation (48).

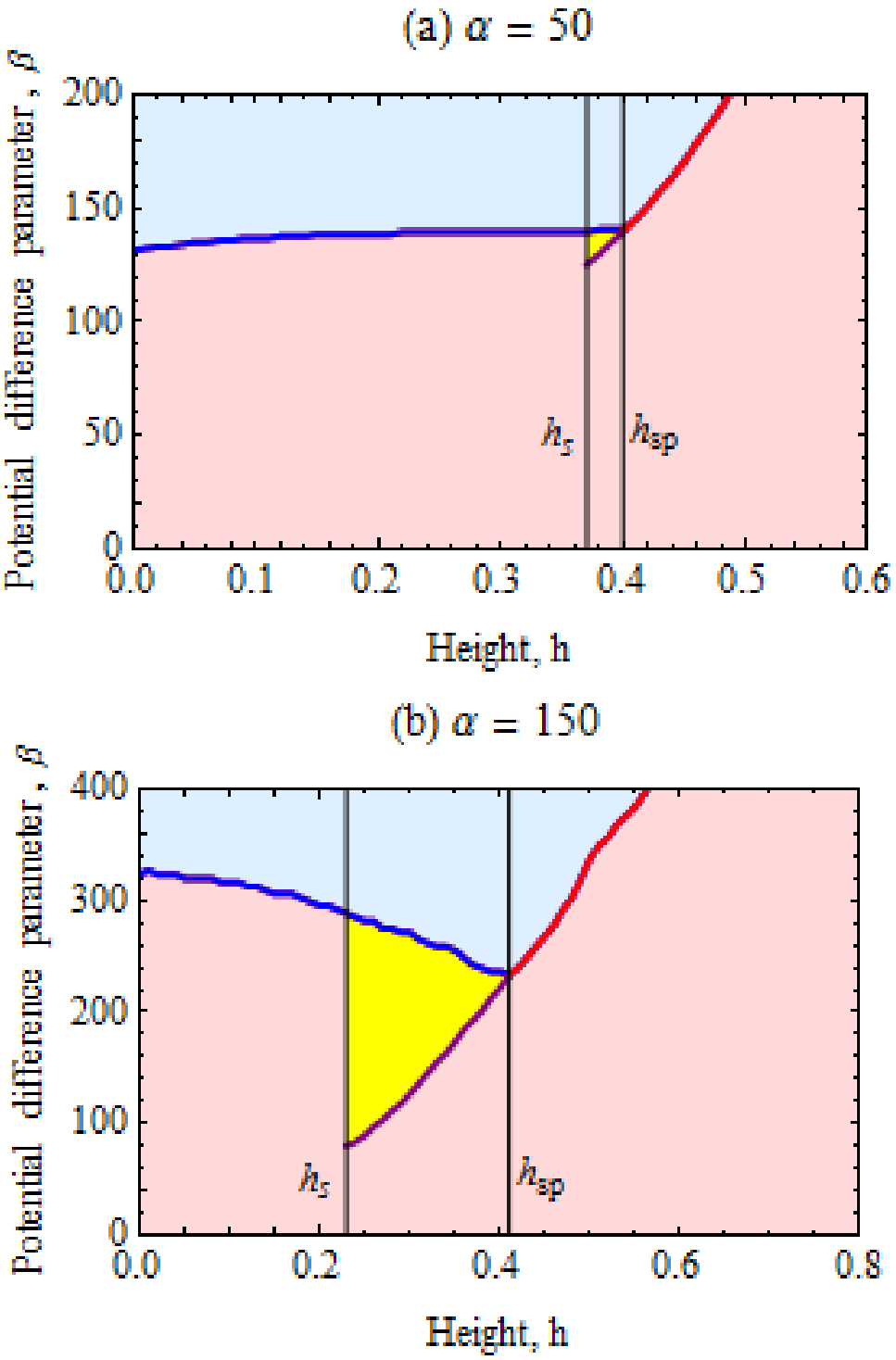

Figure 47. Critical values of β for the snap-through (purple curve) and the pull-in instabilities (blue curve) to occur for an arch with (a) $\alpha = 50.0$ and (b) $\alpha = 150.0$. The red curve shows the critical values of β for which the snap-through and the pull-in instabilities occur simultaneously.

The minimum arch height h_m required for the snap-through instability to occur for this mechanical load is greater than h_s for the displacement-dependent step electric load. Therefore, arches under electric loads are more prone to the snap-through instability, and results from studies of the response of an arch for a displacement-independent load cannot be directly employed to predict the response of the same arch under an electric load.

The curves of critical values of β for step electric loads divide the plot of β vs. h in figure 46 into three regions. An arch of height h under a potential difference β from regions A, B and C (light red) will experience oscillations of relatively small amplitude and time period without experiencing a snap-through instability. On the other hand, an arch of height h under a potential difference β from region D (yellow) will experience oscillations of large amplitude and large time period after undergoing the snap-through. However, an arch under a potential difference β from region E (light blue) will not have any stable motion; it will experience the pull-in instability and will touch the bottom electrode.

Figure 47 exhibits plots of β vs. h for dynamic problems and two values, 50 and 150, of α. Results in figure 47 for the two values of α are quantitatively different but are qualitatively similar to those for α = 106 in figure 46. For different values of α, table 3 lists values of the minimum heights h_s and h_{sp} required for the snap-through and the combined snap-through and pull-in instabilities, respectively. The value of h_s decreases with an increase in the value of α, however, that of h_{sp} remains the same. The size of the yellow region increases with an increase in the value of α. For small values of α, this region will vanish. Figures 46 and 47 provide a qualitative idea of the phase diagram of a micro-arch under a step electric load and give quantitative information for α = 50.0, 110.0 and 150.0. Similarly, one can construct phase diagrams for other values of the stretching parameter α.

Table 3: For different values of α, minimum values of the arch height for the snap-through and the combined snap-through and pull-in instabilities to occur

	α =50	α =110	α =150
h_s	0.37	0.28	0.23
h_{sp}	0.4	0.4	0.4

1.5.6. Effect of viscous damping

For viscous damping coefficient c = 1.0, and different values of the step potential difference β figure 48 evinces time histories of the peak displacement at the mid-span of the arch with h = 0.3 and α = 106. For each value of β, the amplitude of oscillations of the arch decreases with time, and the peak deflection of the arch approaches that of the statically deformed arch. Figure 49 exhibits the static bifurcation curve (black curve) of the arch (h = 0.3, α = 106) and for dynamic problems and different values of c, loci of the maximum displacement (colored curves) under a step electric potential difference. As c increases, the response of the dynamic problem approaches that of the static problem earlier in time. However, the enhanced damping does not suppress the two instabilities, and the peak $w(0.5, t)$ vs. β curves for different values of c are qualitatively similar to each other. Table 4 lists the snap-through and the pull-in parameters for different values of c.

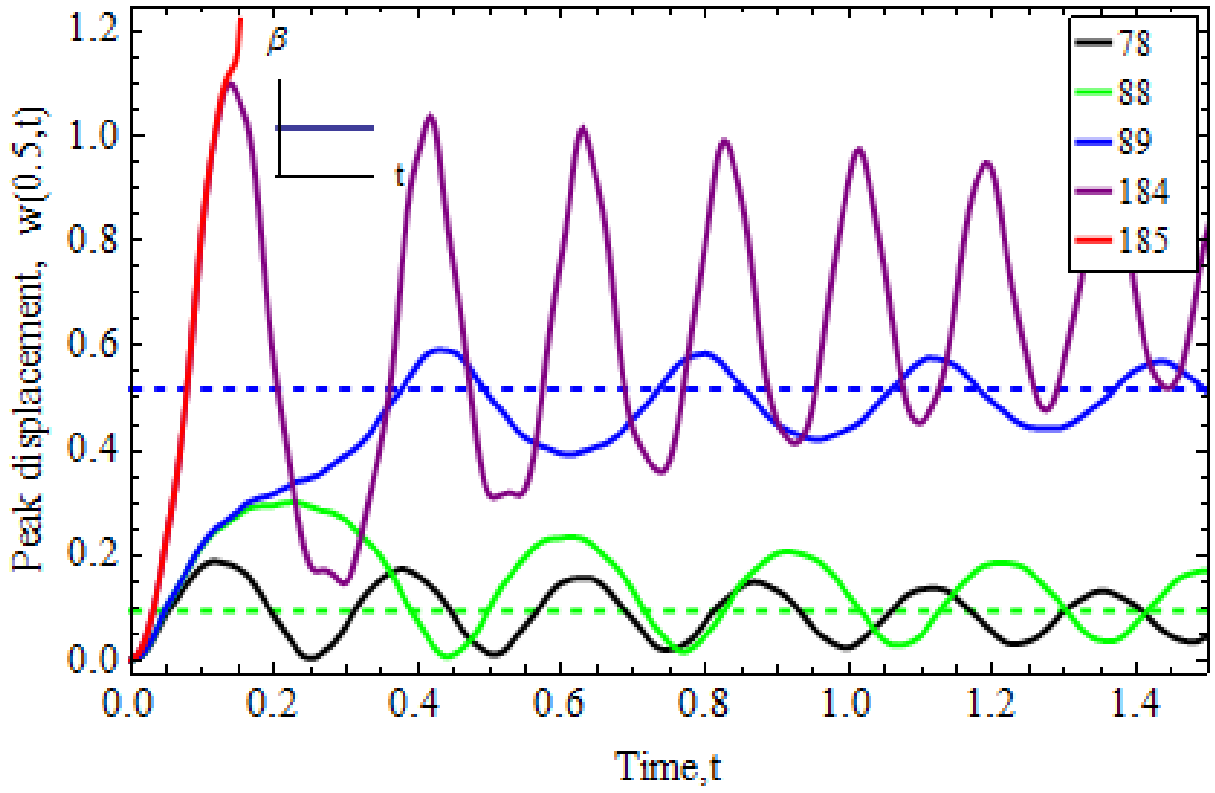

Figure 48. Time histories of the downward displacement of the mid-span of the fixed-fixed bell shaped arch (*h = 0.3, α = 106*) for different applied step voltages. Dashed blue and dashed green curves show the peak deflection for the statically deformed arch after and before the snap-through instability.

Table 4: Critical values of β for different values of the damping coefficient c

Critical values of β	*c = 0*	*c = 1.0*	*c = 5.0*	*c = 10.0*	*Static*
Snap-through	87	88	94	99	106
Pull-in	181	184	194	204	240

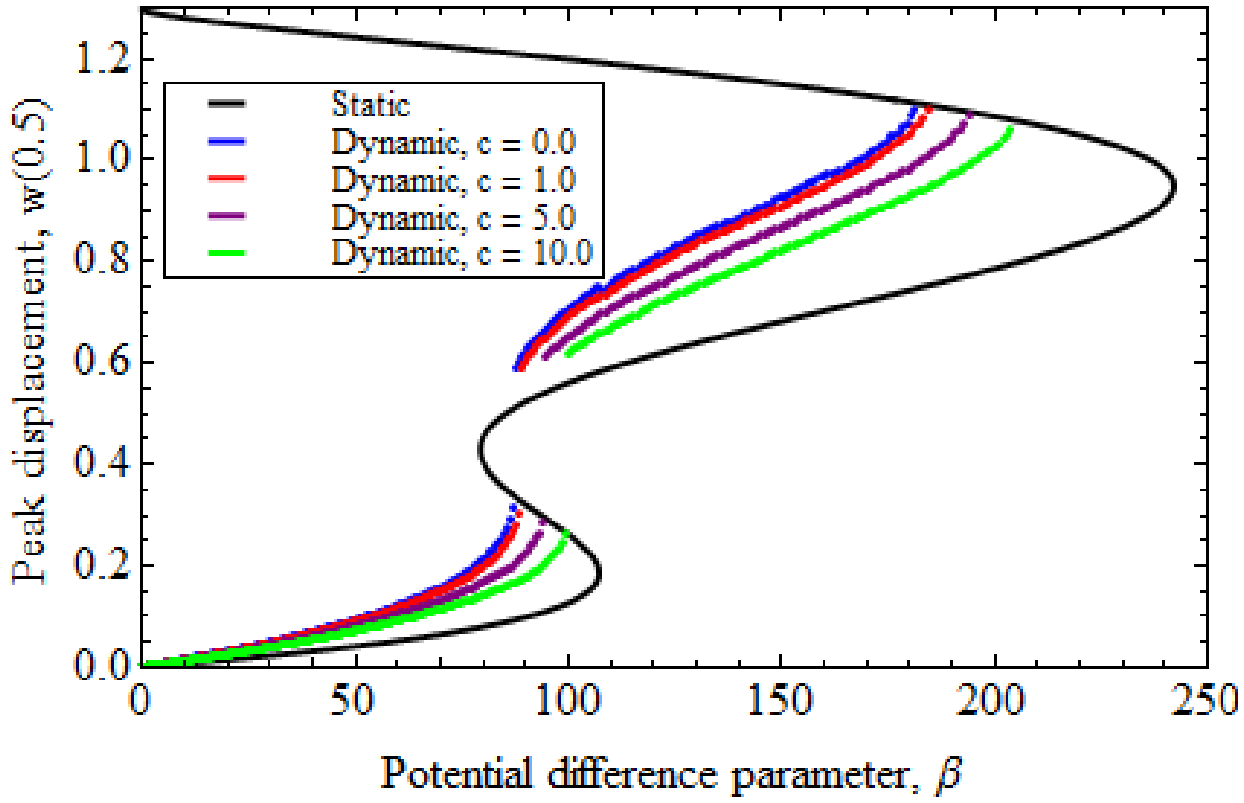

Figure 49. The static bifurcation diagram (*w(0.5)* vs. β, black curve) of the arch ($h = 0.3$, $\alpha = 106$). For different values of the damping coefficient, colored curves are the loci of the maximum displacement $\underset{0\le t\le 2}{Max}(w(0.5,t))$ under a step electric potential difference.

Figure 50(a) exhibits the static bifurcation diagram (black curve) of the arch ($h = 0.7$, $\alpha = 110$). Colored curves are loci of the maximum deflection under a step electric potential difference parameter β for different values of the damping coefficient c. Without damping, the arch experiences the indirect snap-through at point B where the locus of the maximum deflection for the dynamic problem intersects the unstable branch AB of the asymmetric solutions of the static bifurcation curve. However, the introduction of damping suppresses the indirect snap-through and the arch experiences the direct snap-through when the locus of the maximum displacement of the dynamic problem intersects the branch AC of symmetric solutions of the static problem. For $\beta = 597$, which is more than the critical β for snap-through, figure 50(b) exhibits snap-shots of the variation along the span of the deflection of the arch. It is clear from these plots that the arch deforms symmetrically about $x = 0.5$. Therefore, asymmetric deformations and the indirect

snap-through are observed only if the arch height is relatively large ($h \geq \sim 0.5$ for $\alpha = 110$) and there is no damping.

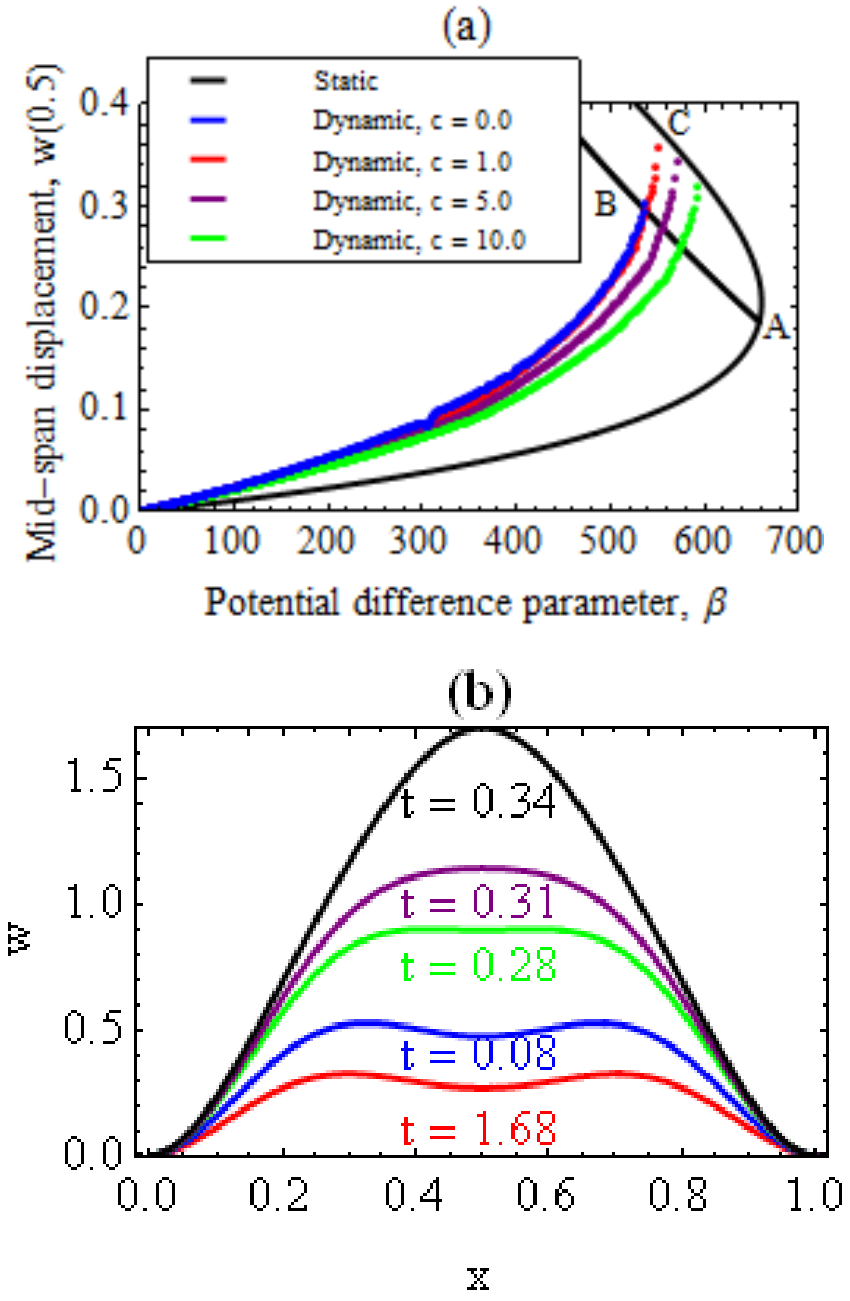

Figure 50. (a) The static bifurcation diagram ($w(0.5)$ vs. β, black curve) of the arch ($h = 0.7$, $\alpha = 110$). Colored curves are the loci of the maximum deflection $\underset{0\leq t\leq 2}{Max}(w(0.5,t))$ under a step potential difference β for different values of the damping coefficient. (b) Snap shots of the arch displacements at different times for $h = 0.7$, $\alpha = 110$, $c = 10$ and $\beta = 597$.

1.5.7. Snap-through and pull-in instabilities under a potential difference linearly varying with time

We study the effect of ramping up the electric potential on the snap-through and the pull-in parameters. First, we study the snap-through under the deflection-independent load given by equation (48). For a bell shaped arch with $\hat{L}$ = 1 mm, width $\hat{b}$ = 30 μm, $\hat{d}$ = 3.0 μm, $\hat{g}_0$ = 12.85 μm, $\hat{h}$ = 4.5 μm, $\hat{E}$ = 169 GPa, $\hat{\rho}$ = 2231 Kg/m^3, the nondimensional parameters are α = 110, h = 0.35 and $t = \hat{t} / \sqrt{(\hat{E}\hat{I})/(\hat{\rho}\hat{b}\hat{d}\hat{L}^4)} = \hat{t} / 7537.45$ where $\hat{t}$ is in second. Figure 51 displays the peak displacement of the mid-span of the arch (h = *0.35* and α = *110*) versus β for different uniform rates of increase of $\hat{V}$. The bifurcation curve ABGB′I for the static problem derived with the PALC algorithm is also exhibited in figure 51. The bifurcation diagram shows only the snap-through instability at point B. For dynamic problems, the first sudden increase in the peak displacement at β = ~ 240 corresponds to the snap-through instability of the arch. For every rate of increase of the applied potential difference the arch vibrates around the snapped through shape after undergoing the snap-through instability.

Figure 52 evinces the peak displacement of the mid-span of the arch (h = *0.35* and α = *110*) versus the potential difference parameter β for different uniform rates of increase of the electric potential. Apart from the snap-through instability at point B, the static bifurcation curve ABGB′IJ obtained from the PALC algorithm shows the pull-in instability at point I and branches BG and IJ corresponding to unstable solutions. For dynamic problems, the first sudden increase in the peak displacement at β = ~ 180 (point B in figure 52) corresponds to the snap-through instability of the arch. For low to medium rates of increase of β (i.e., $\leq$ 25 V/unit non-dimensional time), the arch vibrates around the snapped through shape until the pull-in occurs. For loading rates of 75, 125, and 210 (V/unit non-dimensional time) the snap-through instability is not observed, and only the pull-in instability occurs at β = ~ 241, ~ 270, and ~ 330, respectively. We have summarized in Table 5 the snap-through and the pull-in parameters for different rates of loading. As the rate of increase of the potential difference is decreased, the snap-through voltage gradually decreases to 183 V and the pull-in voltage approaches 215 V. It is evident that the snap-through parameters of the arch approach those of the statically deformed

arch as the rate of loading is decreased. However, the pull-in voltage for the slowest rate of loading considered exceeds by ~ 20% the static pull-in voltage.

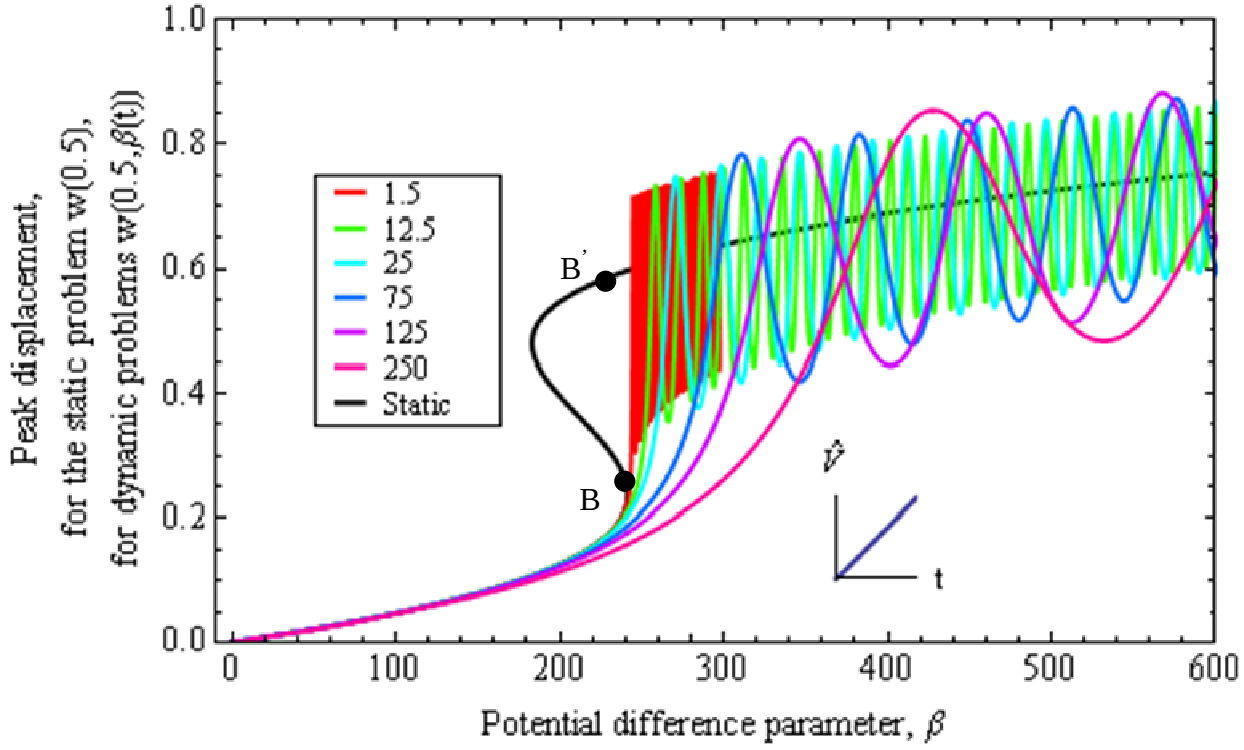

Figure 51. For different rates of increase of the $\hat{V}$ (*unit* $\hat{V}$*/unit non-dimensional time*) the peak displacement of the mid-span of the arch versus β for displacement-independent load.

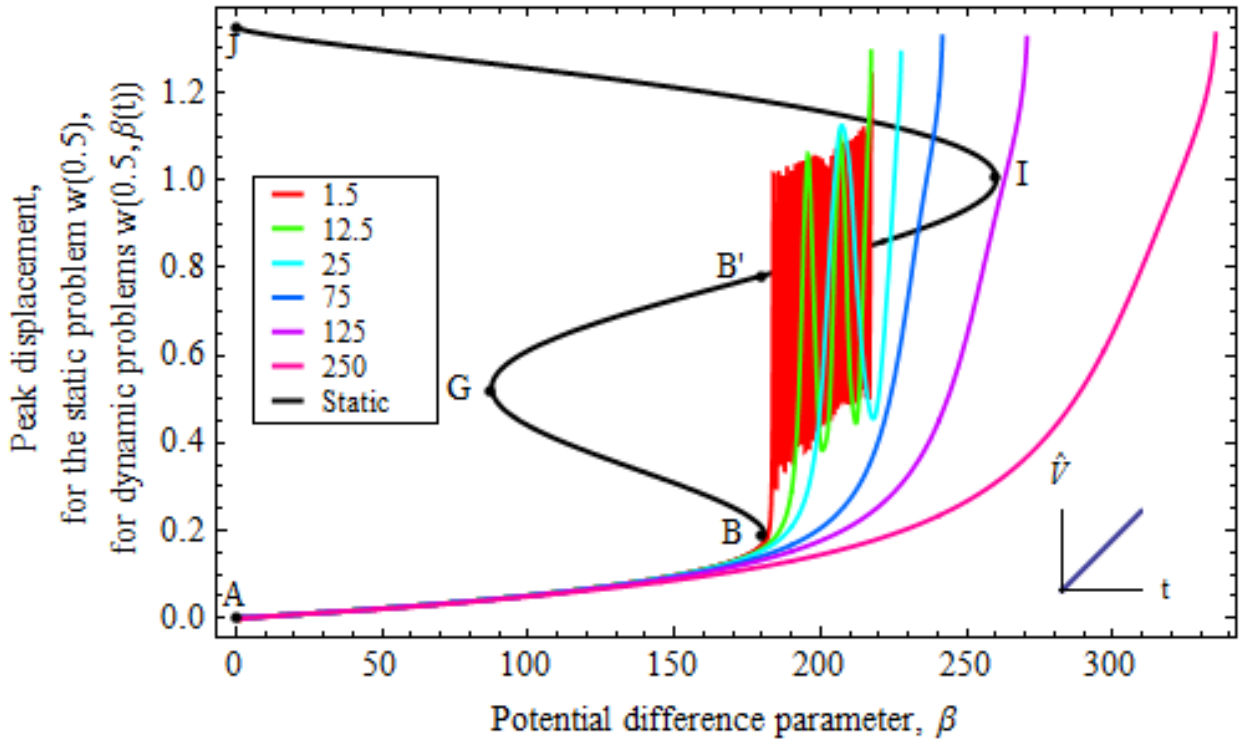

Figure 52. For different rates of increase of the applied potential difference (*V/unit non-dimensional time*) the peak displacement of the mid-span of the arch versus the potential difference parameter, β.

Table 5: The snap-through and the pull-in parameters for the arch for different rates of applied potential difference.

Rate of applied potential difference (V/ unit time)	*β at the snap-through instability*	*β at the pull-in instability*
Static	180	260
1.5	183	215
12.5	191	215
25	197	227
75	-	241
125	-	270
250	-	330
Step	150	200

Figure 53 exhibits the variation of the non-dimensional potential energy U (cf. equation (49)) versus β for the transient problem with displacement-independent load $\hat{V}$ increasing linearly with time. In figure 53, we have also plotted the variation of U for the static problem. The potential energy U for the dynamic problem with linearly varying $\hat{V}$ follows the curve of U versus β for the static problem from point A to point B for every rate of increase of $\hat{V}$. After point B, the snap-through instability occurs at points C_1, C_2 and C_3 for loading rates of 1.5, 12 and 15 (unit $\hat{V}$ /unit non-dimensional time), respectively. With the increase in the rate of loading, the value of β at the snap-through instability increases. For loading rate $\geq$ 75, the snap-through happens but the jump in the deflection at the snap-through instability is not pronounced. After the snap-through, the arch vibrates around the new equilibrium position; the potential energy for the dynamic problem is always more than that for the static problem (curve B′I in figure 53). The minimum values of U for dynamic problems are the same as values of U for the corresponding static problems. Therefore, the stable motion of the arch under a linearly varying $\hat{V}$ is observed before and after the snap-through instability for every rate of increase of $\hat{V}$ and the potential energy for a dynamic problem is $\geq$ the total potential energy of the stable deformations (B′I) for the static problem.

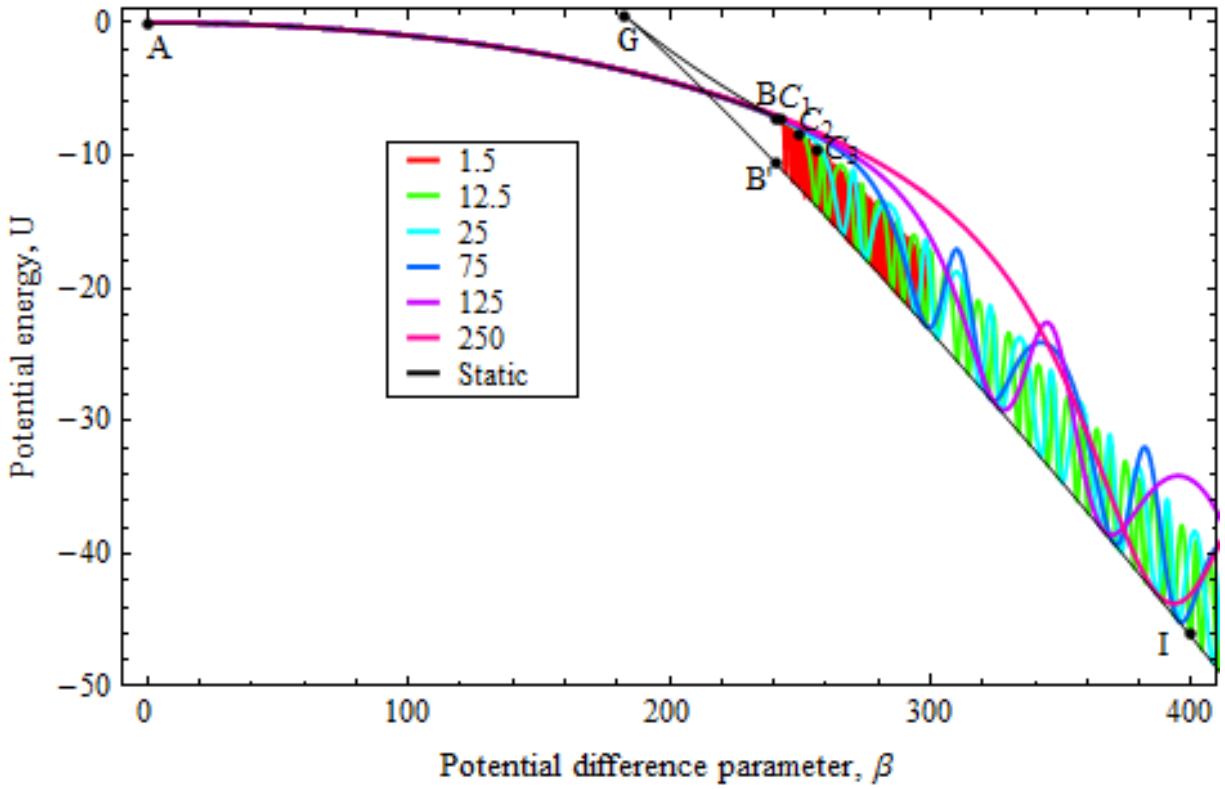

Figure 53. Total potential energy versus β for $h = 0.35$ for the static problem (black curve), the variation of the Total potential energy as a function of β for the dynamic problem when $\hat{V}$ increasing linearly with time (colored curves).

Figure 54 exhibits the variation of the non-dimensional potential energy U (cf. equation (48)) versus the non-dimensional potential difference parameter β for different uniform rates of increase of the electric potential for displacement-dependent electric loads. In figure 54, we have also plotted the variation of U with β for static problems. U for the dynamic problem with linearly varying potential difference follows the curve of U versus β for the static problem from point A to point B for every rate of increase of the applied potential difference. After point B, the snap-through instability occurs at points C_1, C_2 and C_3 for loading rates of 1.5, 12 and 15 (V/unit non-dimensional time), respectively. After the snap-through the arch vibrates around the new equilibrium position and the potential energy for the dynamic problem always remains higher than that for the static problem (curve B'I in figure 54(c)). With the increase in the rate of loading, the value of β at the snap-through instability increases. For loading rates $\geq$ 75 V/unit non-dimensional time, the curve U versus β intersects the curve IJ of U versus β for the static

problem at point P. The curve IJ of the static problem corresponds to unstable deformations of the arch after the pull-in instability. For loading rates ≥ 75 (V/unit non-dimensional time), no snap-through instability is observed. For the loading rate of 75 (V/unit non-dimensional time), the arch experiences the pull-in instability just after its potential energy overshoots the curve IJ. Therefore, the stable motion of the arch under a linearly varying electric potential is observed only when the potential energy is ≥ the potential energy of stable deformations (B′I) for the static problem, and ≤ the potential energy of unstable (IJ) deformations of the static problem.

Table 6: Comparison of present results with those from the continuum mechanics approach

	Pull-in voltage	*Pull-in displacement*	*Snap-through voltage*	*Peak displacement before the snap-through*
Present model	Between 95 V and 96 V	11.2 µm	Between 65 V and 66 V	2.66 µm
Continuum mechanics based analysis [31]	Between 92 V and 93 V	11.0 µm	Between 65 V and 66 V	2.60 µm
Difference	3.2 %	1.8 %	0 %	2.3 %

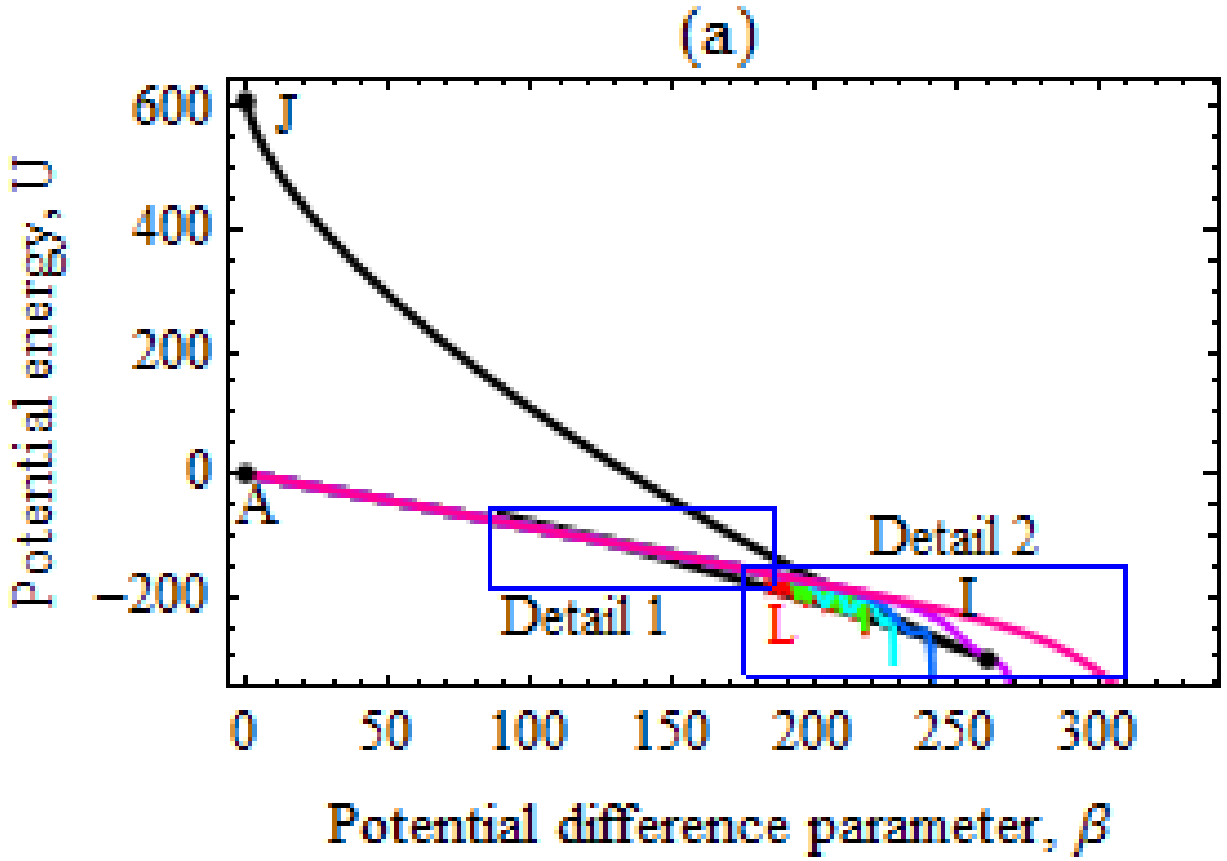
(a)
600
400
200
0
−200
Potential energy, U
J
A
Detail 1
Detail 2
L
I
0
50
100
150
200
250
300
Potential difference parameter, β

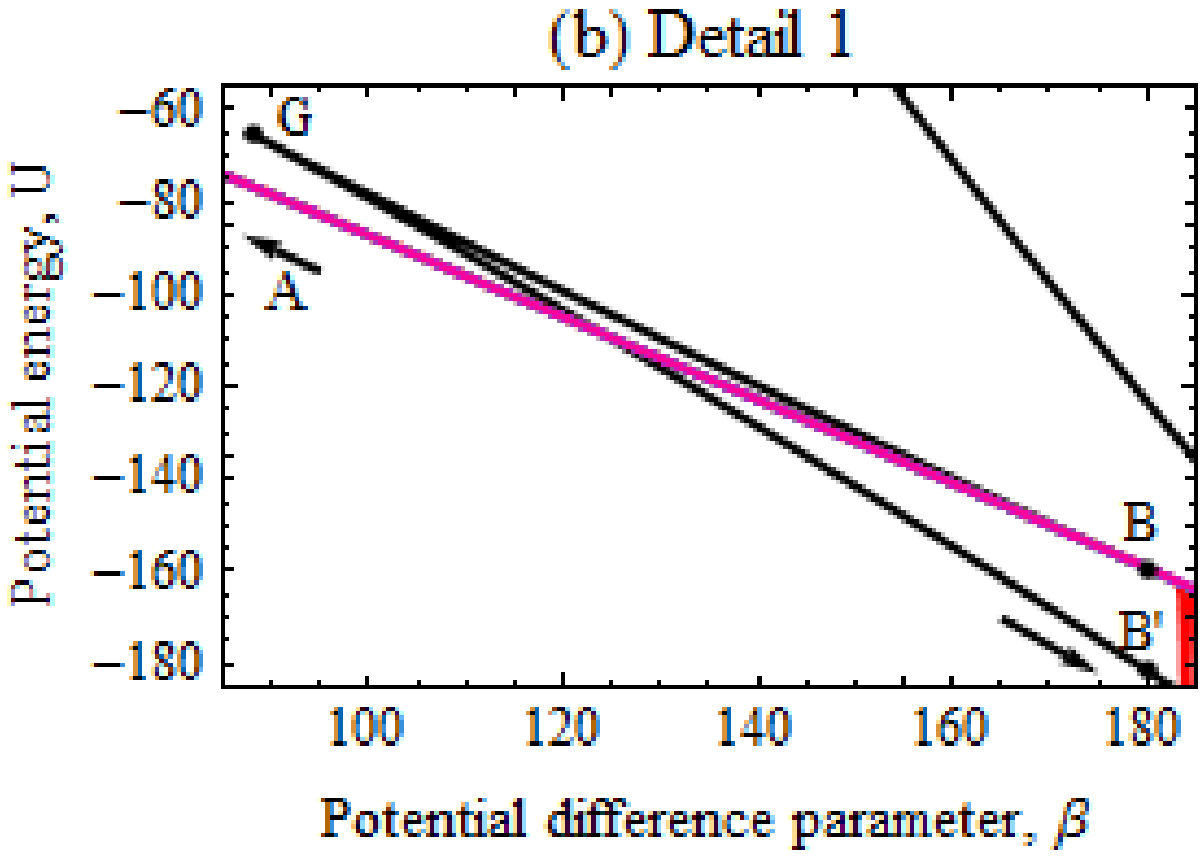
(b) Detail 1
Potential energy, U
−60
−80
−100
−120
−140
−160
−180
G
A
B
B'
100
120
140
160
180
Potential difference parameter, β

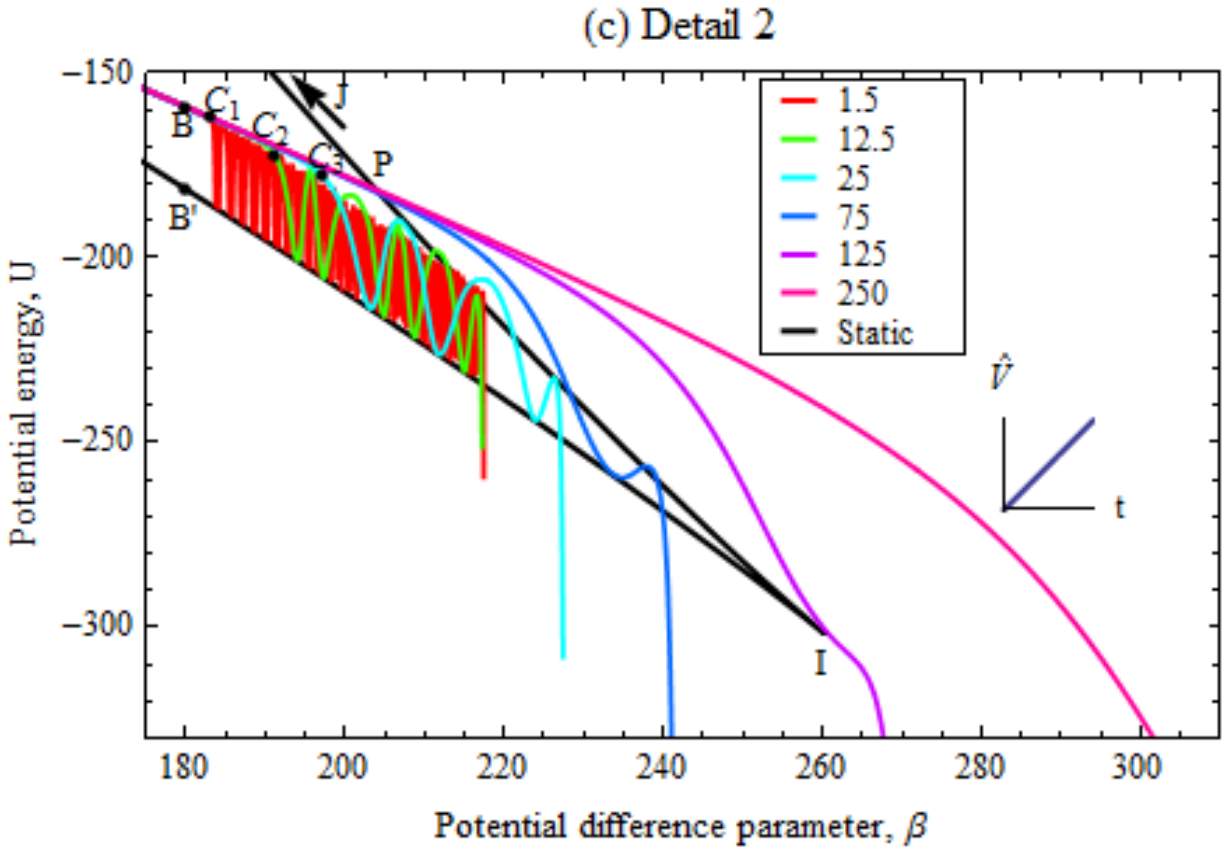

Figure 54. Total potential energy versus the potential difference parameter β for $h = 0.35$ for the static problem (black curve), the variation of the total potential energy as a function of the potential difference parameter for the dynamic problem when the electric potential is increasing linearly with time (colored curves).

1.5.8. Comparison of results from the reduced-order model with those from a continuum mechanics approach

We now compare results from the reduced-order model (ROM) with those from the continuum mechanics approach reported in Section 1.3 where effects of damping were neglected. Table 6 compares results from the ROM with those reported in Section 1.3 for a step potential difference between the two electrodes. It is clear that the ROM with six degrees of freedom gives results very close to those reported in Section 1.3 with hundreds of degrees of freedom (recall that the problem in Section 1.3 was solved numerically with numerous nodes). For a complex shaped MEMS for which mode shapes are not readily available, one needs to either find mode shapes

numerically or use the approach of Section 1.3. The snap-through instability reported in Section 1.3 follows the direct snap-through mechanism.

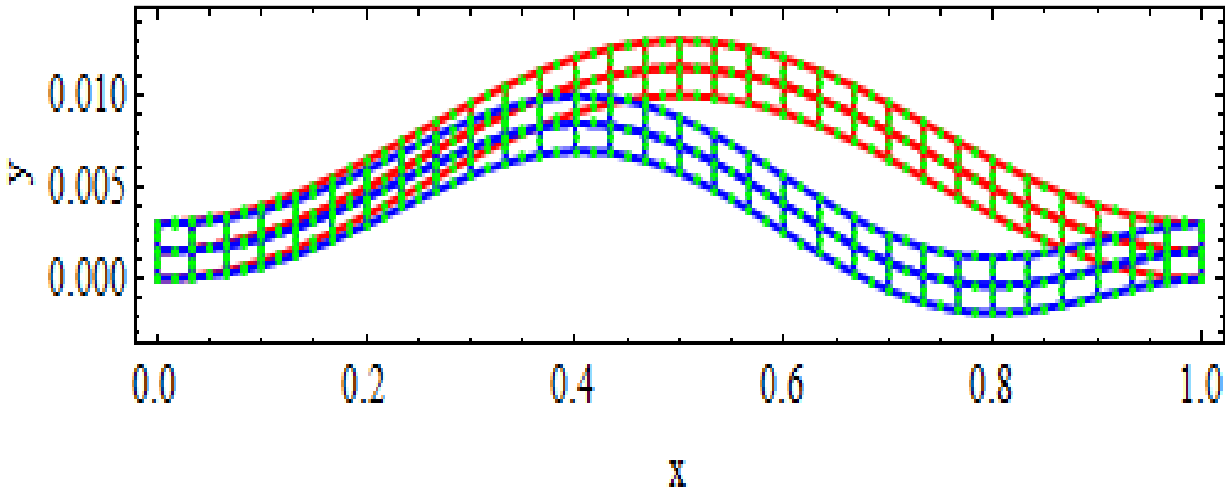

Figure 55. Snap shots of the arch at *t = 0* (red) and *t = 250* s (blue).

In an attempt to compare asymmetric solutions from the two approaches, we study deformations of a bell shaped silicon arch with base length $\hat{L}$= 1 mm, width $\hat{b}$ = 30 μm, thickness $\hat{d}$= 3.0 μm, initial gap $\hat{g}_0$ = 10.0 μm, the arch rise $\hat{h}$= 10.0 μm, and its bottom-surface described by $z_0(\hat{x})$ = $\hat{h}\sin^2\left(\pi\hat{x}/\hat{L}\right)$ using the continuum mechanics approach described in Section 1.3. The arch experiences the indirect snap-through under step electric potential difference. The critical value of the potential difference for the snap-through instability is between 244 V and 246 V from the continuum mechanics analysis and between 258.0 V and 258.2 V from the present model. The difference of 5% between the two values attests to the adequacy of the present reduced order model. Figure 55 exhibits the arch configurations at two different times obtained from the continuum mechanics formulation of the problem. It is clear that the arch deformed asymmetrically subsequent to the snap through. Thus, the continuum mechanics approach also predicts the indirect snap-through with deformations of the arch asymmetric about *x* = 0.5.

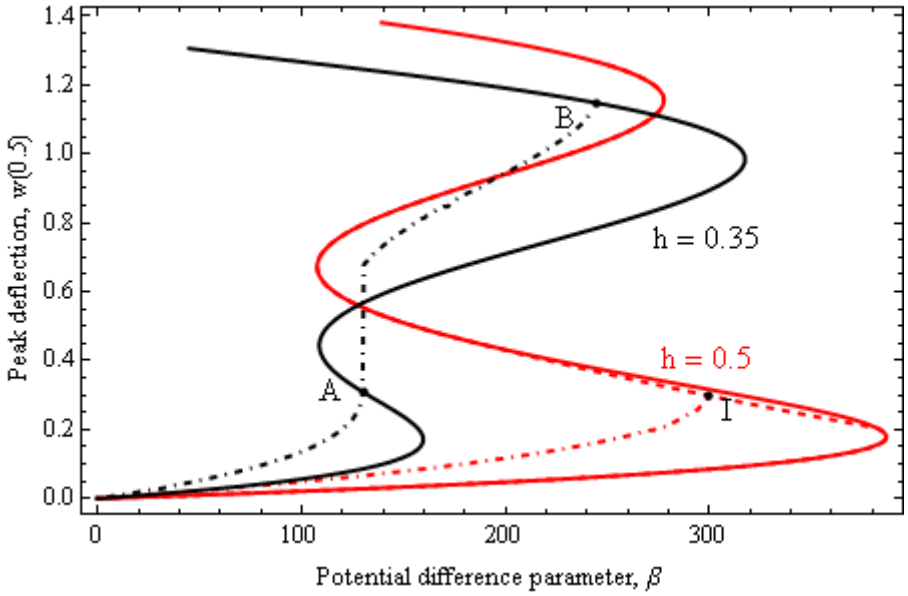

Figure 56. Static bifurcation diagrams (*w(0.5)* vs. β) of the arch for two different values of the arch height *h*. Solid curves are results from the PALC algorithm. Dot-dashed solid curves are the loci of the maximum displacement $\underset{0\le t\le 2}{Max}(w(0.5,t))$ under the step load. The dashed portion of the curve represents arch's deformations asymmetric about *x = 0.5* computed from the PALC algorithm.

1.5.9. Snap-through and pull-in instabilities in a sinusoidal arch

Sinusoidal arches ($z_0(x) = \sin(\pi x)$) studied in this subsection differ from the bell-shaped arches analyzed above primarily in the non-zero slopes of a sinusoidal arch at the two fixed edges and zero slopes for a bell-shaped arch. Figure 56 depicts loci of the maximum deflection (dot-dashed curve) produced by different step potentials and static bifurcation curves (solid curves and a dashed red curve) obtained using the PALC algorithm for two different values of the arch height. The dashed portion of the bifurcation curve for h = 0.5 represents unstable deformations asymmetric about x = 0.5. It is clear that the response of a sinusoidal arch is qualitatively similar to that of a bell-shaped arch (cf. figures 36(a) and 41(a)). For h = 0.35, the direct snap-through due to the step electric potential difference occurs when the locus of the maximum deflection intersects at point A the unstable branch of the bifurcation curve. Similarly, the pull-in instability occurs when the locus of the maximum deflection intersects again at point B the unstable branch

of the bifurcation curve. However, for h = 0.5, the arch experiences the indirect snap-through when the locus of the maximum deflection intersects at point I the unstable branch of the bifurcation curve for asymmetric solutions and the snap-through and the pull-in instabilities ensue simultaneously.

1.5.10. Discussion of results obtained with the ROM

It is mentioned in [84] that methods for estimating critical conditions for elastic structures due to transient loads can be classified in three groups. A method from the first group seeks the response of the structure under the transient load by solving governing equations of the problem [26]. A critical condition is reached if a small change in a load parameter causes a large change in the response of the structure. We have used this criterion when solving numerically governing equation (34) and estimating critical values of β for the snap-through and the pull-in instabilities by monitoring any large change in the peak displacement of the arch for a small change in β.

A method from the second group relates the critical condition of a structure to the total energy-phase plane of the problem [44, 45], and a method from the third group estimates the critical load of a structure by analyzing variation of the potential energy due to a change in a load parameter [83]. The variations of the potential energy of the arch with the electric potential difference parameter for a step and a linearly increasing electric potential difference reported in the previous sections 1.5.2-1.5.9 belong to this third group of methods for analyzing instabilities.

In [84], the snap-through instability of a shallow sinusoidal arch under a transient displacement-independent load is studied using a two-mode approximation (i.e. n = 2 in equation (36)) of the governing equation (34). A sinusoidal variation of the pressure over the span-of the arch is considered. These approximations enable one to express the governing equation in terms of two non-dimensional parameters, the stiffness of the arch, and the load. The lower and the upper bounds of the critical values of the load parameter for the snap-through instability are studied for various loading conditions such as step and impulsive loads. Unlike a ramp load, which varies linearly with time, a step and an impulsive load do not vary with time. The snap-through instability under time varying loads is not studied in [84].

1.6. Conclusions

Nonlinear governing equations (i.e. the continuum balance laws and Maxwell's equations) for an electrically actuated MEMS device have been summarized. These equations have been numerically solved to study finite transient deformations of a perfectly conductive body under the Coulomb pressure by coupling the FEM and the BEM; the former for the structural part of the problem and the latter for the electrical fields. The snap-through and the pull-in instabilities of micro-arches for different potential differences between the two electrodes have been studied. Depending upon how the electrical load is applied a micro-arch may experience either only the pull-in instability or the pull-in and the snap-through instabilities. It has also been found that the pull-in displacement is more for a micro-arch than that for a micro-beam of the same length, width, thickness, and the initial gap as the micro-arch. The pull-in voltage obtained by analyzing the beam problem with the linear strain displacement relation is nearly one-half of that for the same problem studied with the nonlinear strain displacement relation.

As a MEM electrode, micro-arches are advantageous over micro-beams because a micro-arch can have a larger operational range without the pull-in instability than a corresponding micro-beam of same thickness, width and length. Moreover, by changing the rate of application of the potential difference between the two electrodes the snap-through instability may be avoided. This provides another means to control the response of a MEMS device. Also, in a micro-arch under an electric load the softening effect may be dominant before it experiences the snap-through instability but the strain-hardening effect may initially exceed the softening due to electric forces subsequent to the snap-through instability. This can be exploited in designing novel MEMS devices.

In addition to the coupled FE-BE method, the present study investigates the snap-through and the pull-in instabilities in an electrically actuated micro-arch modeled as a damped Euler-Bernoulli beam incorporating the nonlinear mid-plane stretching. The nonlinear time-dependent governing partial differential equation is solved numerically by using the Galerkin method and an adaptive time integration scheme. For the static problem, the displacement control method (DIPIE algorithm) and the pseudo-arc length continuation method (PALC) are used to derive the bifurcation curve of the peak arch deflection versus the non-dimensional step electric potential

difference between the arch and the bottom rigid flat electrode. Two distinct mechanisms, namely the ‘direct’ and the ‘indirect’, snap-through instabilities are found. The relation of the minimum potential energy of the MEMS for a dynamic problem and the total potential energy of the static problem is studied. It is found that the PALC algorithm can compute multiple branches in the bifurcation curve, which correspond to symmetric and asymmetric deformations of the arch. The DIPIE algorithm fails to compute asymmetric solutions.

The phase diagram between the critical load parameter and the arch height showing stable and unstable regions of arch's deformations will help in designing arch-shaped MEMS. It is shown that damping suppresses the indirect mechanism of snap-through and permits only the direct snap-through.

Results, including the indirect snap through and asymmetric deformations subsequent to the snap through instability from the reduced-order model agree well with those from the continuum mechanics based approach.

Other conclusions are summarized below:

1. An undamped arch under a step electric load may experience either a direct or an indirect snap-through instability.
2. For relatively small arch heights (e.g., the non-dimensional $h \leq \sim 0.4$ for $\alpha = 110$), the static problem has solutions with deformations symmetric about the mid-span of the arch and the direct snap-through happens when the locus of the maximum deflection of the dynamic problem intersects the unstable branch of the bifurcation curve for the static problem.
3. For relatively large arch heights (e.g., $h > \sim 0.4$ for $\alpha = 110$), the static problem has solutions with deformations symmetric and asymmetric about the mid-span of the arch. The asymmetric deformed shape has lower potential energy than the corresponding symmetric deformed shape.
4. The indirect snap-through happens when the locus of the maximum deflection of the dynamic problem intersects the unstable branch of the bifurcation curve of the asymmetric deformations for the static problem.

5. For a dynamic problem with the electric potential difference increasing linearly in time, whether or not the arch experiences a snap-through instability depends on the rate of application of the electric potential.
6. For a dynamic problem with the electric potential difference applied either as a step function or as a linear function of time, the arch has a stable motion only when its minimum potential energy is $\geq$ the potential energy of the stable deformed shape of the static problem and $<$ the potential energy of the unstable deformed shape of the static problem.
7. A phase diagram between the arch height and the applied electric potential has been constructed to show regions of different instabilities for static and dynamic problems.
8. Responses of sinusoidal and bell-shaped arches are qualitatively similar to each other.

Chapter 2

Local water slamming impact on sandwich composite hulls

2.1. Introduction:

The local water slamming refers to the impact of a part of a ship hull on water for a short duration during which high peak pressure acting on the hull [35] can cause significant local structural damage. Initial research focused on the problem of a rigid body entering calm water and finding pressures exerted on it by the fluid; i.e., at time $t = 0$, a rigid body touches the free surface of the stationary fluid with a known velocity and for $t > 0$, the velocity of the fluid, the pressure exerted by it on the rigid body, the wetted length, and the position and the velocity of the rigid body are to be determined (figure 57).

An early work on water entry of a rigid v-shaped wedge with small deadrise angle β is due to von Kármán [100]. Wagner [43] also considered a v-shaped wedge of small deadrise angle and generalized von Kármán's solution by including the effect of water splash-up on the body; however, the effect of the jet flow (figure 57) during the impact was not considered. According to Wagner [43], the pressure distribution p_w on the wedge-water interface is given by

$$p_w = \rho V \frac{c_f(t)}{\sqrt{c_f(t)^2 - x_1^2}} \frac{d}{dt}\left(c_f(t)\right) \text{ for } 0 \le x_1 \le c_f(t) \qquad (50)$$

$$= 0 \text{ for } x_1 > c_f(t)$$

where ρ is the mass density of water, V the constant downward velocity of the wedge, x_1 the x_1-coordinate of the solid-fluid interface with respect to the rectangular Cartesian coordinate axes fixed in space with the origin at the vertex of the wedge at time t = 0, and

$$c_f(t) = \frac{\pi V t}{2\tan\beta} \qquad (51)$$

the wetted length.

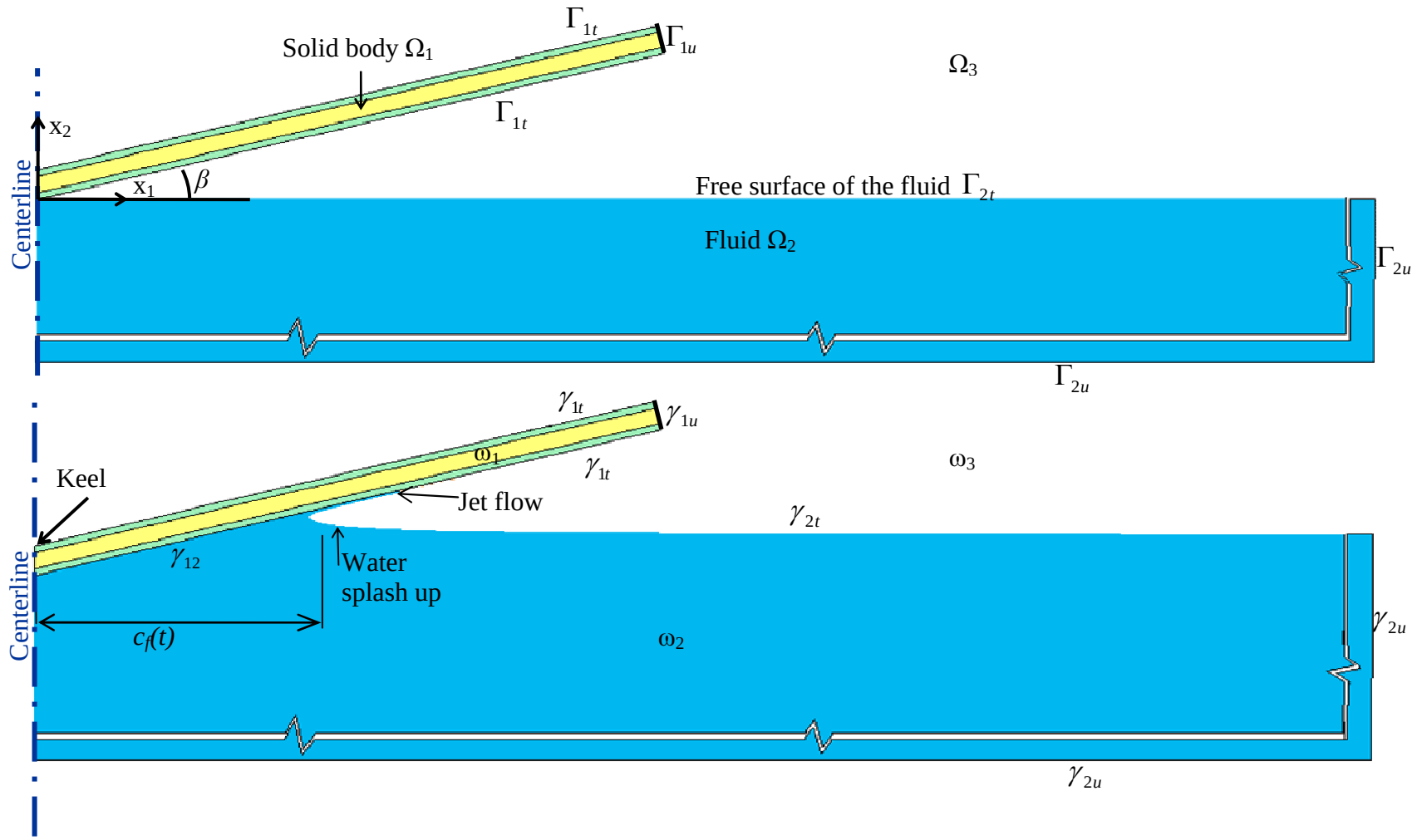

Figure 57. Schematic sketch of the problem studied depicting slamming upon the bottom surface of a hull (Ω_1); top: at $t=0$, position of the hull touching the free surface of the fluid region; and bottom: for $t>0$, the deformed fluid and solid regions. The problem domain is symmetric about the x_2 - axes or the centerline.

Since equation (50) implies that $p_w \to \infty$ as $x_1 \to c_f(t)$, Wagner proposed that the maximum pressure p_m at $x_1 = c_f(t)$ be given by

$$p_m = \frac{1}{2}\rho\left(\frac{d}{dt}c_f(t)\right)^2 . \tag{52}$$

The effect of the jet flow was included in the analysis by Armand and Cointe [9]. Both Wagner as well as Armand and Cointe assumed that a small part of the body enters the water, in other words, the depth of penetration of the rigid body into the fluid region is small. Zhao et al. [106] generalized Wagner's solution to wedges of arbitrary deadrise angles, solved the problem numerically by using a boundary-integral equation method, and ignored effects of the jet flow. The variation of the hydrodynamic pressure on the rigid hull from Zhao et al.'s [106] solution agrees well with that found experimentally suggesting thereby that the jet flow does not significantly affect the pressure variation on a rigid wedge. By neglecting effects of the jet flow, Mei et al. [59] analytically solved the general impact problems of cylinders and wedges of arbitrary deadrise angles, and numerically solved problems by considering effects of the jet flow. In figure 58 we have compared the variation of the non-dimensional pressure $C_p = 2\,p_w/\rho V^2$ on a wedge of deadrise angle 10^0 from Wagner's and Mei et al.'s analyses. It is clear that C_p decreases gradually to zero near $x_2 = c_f(t)\tan\beta$ when the jet flow is considered.

In most slamming impact problems, the solid body is deformable and its deformations affect the motion of the fluid and the pressure on the solid-fluid interface which is usually less than that when the solid body is regarded as rigid [23]. Sun [87] has numerically analyzed, using the boundary element method (BEM), the potential flow problem during slamming impact of a 2-D rigid body of arbitrary geometry. Sun and Faltinsen [89, 91, 88, 90] have considered hydroelastic effects during their studies of deformations of circular shells made of steel and aluminum, by coupling analysis of the fluid deformations by the BEM with that of shells by the modal analysis. Qin and Batra [76] have analyzed the slamming problem by using the {3, 2}-order plate theory for a sandwich wedge and modified Wagner's slamming impact theory to account for wedge's infinitesimal elastic deformations. The plate theory incorporates the transverse shear and the

transverse normal deformations of the core, but such deformations of the face sheets are not considered since they are modeled with the Kirchhoff plate theory.

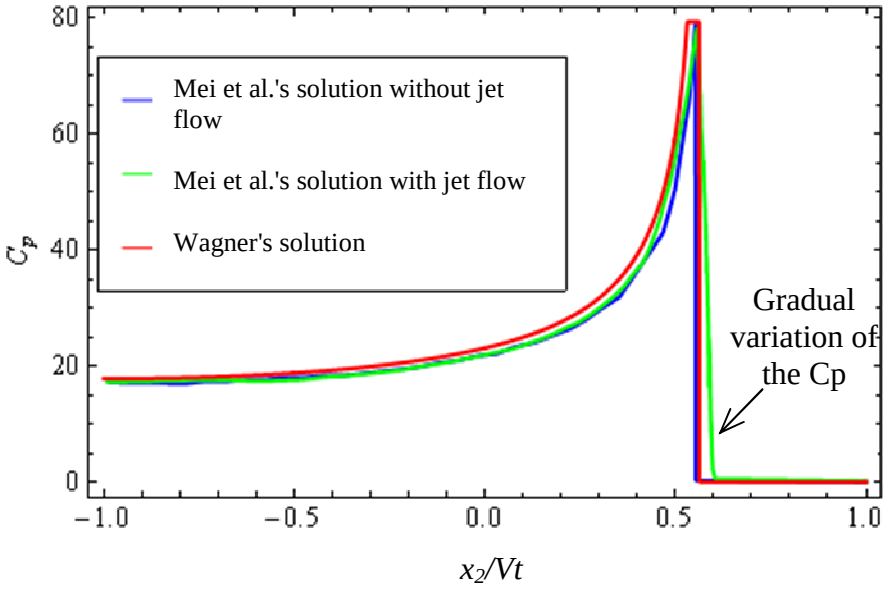

Figure 58. Variation of the pressure coefficient along the water-wedge interface.

In the present study, a commercial finite element (FE) code, LS-DYNA, is used to study finite transient deformations of an elastic fiber-reinforced composite panel due to slamming impact with the water modeled as Navier-Stokes fluid. The damage the in composite panel is delineated by using continuum damage mechanics approach. The rest of the Chapter is organized as follows: Section 2.2 summarizes governing equations and the numerical technique used to solve the initial-boundary-value problem, Section 2.3 has results, and main conclusions of the work are summarized in Section 2.4.

2.2. Mathematical model

2.2.1. Balance laws for deformations of the hull

A schematic sketch of the problem studied is shown in figure 57 that also exhibits the rectangular Cartesian coordinate axes used to describe finite deformations of the solid and the fluid bodies;

the coordinate axes are fixed in space. At time t = 0, let $\Omega_1 \subset \Re^3$ and $\Omega_2 \subset \Re^3$ be regions occupied by the hull and the fluid, respectively; $\Omega_3 \subset \Re^3$ is the region surrounding Ω_1 situated above the fluid body Ω_2, and is modeled as vacuum. Γ_1 (Γ_2) is the boundary of Ω_1 (Ω_2) with disjoint parts Γ_{1u} (Γ_{2u}) and Γ_{1t} (Γ_{2t}). After deformation, bodies occupying regions Ω_i (i = 1, 2 and 3) in the reference configuration occupy regions $\omega_i \subset \Re^3$ in the deformed or present configurations. Γ_{1u} and Γ_{2u} deform to γ_{1u} and γ_{2u}, respectively; Γ_{1t} and Γ_{2t} deform to γ_{1t} and γ_{2t} and γ_{12}, where γ_{12} is the *a priori* unknown interface between ω_1 and ω_2. The free water surface γ_{2t} and the wetted surface γ_{12} vary with time t and are to be determined as a part of the solution of the problem. We note that at t = 0, Γ_{1t} and Γ_{2t} are just about to touch each other, therefore the interface γ_{12} between them is either a point or a line in the reference configuration. We denote coordinates of a point by X_i and x_i (i = *1*, *2*, *3*) in the reference and the current configurations, respectively.

The deformations of a continuous body (the hull and the water in the present problem) are governed by the balance of mass, the balance of linear momentum, and the balance of moment of momentum, given respectively, by equations (53), (54) and (55) written in the referential description of motion:

$$\rho^s J = \rho_0^s \text{ in } \Omega_1 \tag{53}$$

$$\rho_0^s \dot{v}_i = \frac{\partial \hat{T}_{ji}}{\partial X_j} + \rho_0^s f_i \text{ in } \Omega_1 \tag{54}$$

$$\hat{T}_{ik} F_{kj} = \hat{T}_{jk} F_{ki} \text{ in } \Omega_1. \tag{55}$$

Here ρ_0^s and ρ^s are mass densities of the material of the hull in the reference and the current configurations, respectively; J the determinant of the deformation gradient $F_{ij} = \frac{\partial x_i}{\partial X_j}$, v_i the velocity field defined as $v_i = \dot{x}_i$, a superimposed dot denotes the material time derivative, $\hat{T}_{ij}$ the first Piola-Kirchhoff stress tensor, f_i the body force per unit mass and a repeated index implies summation over the range of the index. The first Piola-Kirchhoff stress tensor is related to the Cauchy stress tensor T_{pj} by

$$\hat{T}_{ij} = J \frac{\partial X_i}{\partial x_p} T_{pj} \,. \tag{56}$$

The coupling between deformations of the hull and the fluid is through the hydrodynamic pressure which acts as tractions on γ_{12}, and is in turn affected by deformations of the hull since fluid particles cannot penetrate through the hull. For a viscous fluid, tractions and the velocity must be continuous across the fluid-solid interface, and for an ideal fluid the normal component of velocity and the normal traction (i.e., the pressure) must be continuous across this interface, and the tangential traction vanishes there.

2.2.2. Balance laws for deformations of the fluid

The motion of the fluid occupying the region ω_2 in the present configuration is also governed by the balance of mass, the balance of linear momentum, and the balance of moment of momentum given, respectively, by equations (57), (58) and (59) in the spatial description of motion:

$$\frac{\partial \rho}{\partial t} + \rho \frac{\partial v_i}{\partial x_i} + v_i \frac{\partial \rho}{\partial x_i} = 0 \text{ in } \omega_2 \tag{57}$$

$$\rho \frac{\partial v_i}{\partial t} + \rho v_k \frac{\partial v_i}{\partial x_k} = \frac{\partial T_{ji}}{\partial x_j} + \rho f_i \text{ in } \omega_2 \tag{58}$$

$$T_{ik} = T_{ki} \text{ in } \omega_2. \tag{59}$$

2.2.3. Constitutive relations

We presume that the hull is comprised of an elastic material for which

$$T_{ij} = C_{ijkl} \varepsilon_{kl} \tag{60}$$

where C_{ijkl} are elastic constants for the material, and ε_{ij} the Almansi-Hamel strain tensor defined as

$$\varepsilon_{ij} = \frac{1}{2}\left(\delta_{ij} - \left(F_{jl} F_{il}\right)^{-1}\right). \tag{61}$$

Note that equation (61) considers all geometric nonlinearities, including the von Kármán nonlinearity. With the constitutive assumption (60), the balance of moment of momentum given by equation (55) is identically satisfied. Material damping due to viscous effects can be

incorporated by modifying the constitutive relation (60) but is not considered here. The number of independent elastic constants equals 2, 5 and 9 for isotropic, transversely isotropic and orthotropic materials, respectively. The values of some or all of these elasticities decrease with an increase in the damage induced in the material.

We presume that water can be modeled as a Navier-Stokes fluid for which

$$T_{ij} = -p\delta_{ij} - \frac{2}{3}\mu D_{kk}\delta_{ij} + 2\mu D_{ij} \tag{62}$$

where p is the pressure, μ the shear viscosity, and D_{ij} the strain rate tensor given by

$$D_{ij} = \frac{1}{2}(v_{i,j} + v_{j,i}). \tag{63}$$

In equation (62), Stokes' hypothesis, i.e., λ = - (2/3)μ is used, where λ is the bulk viscosity of water. We also assume that water is compressible, and

$$p = C_1\left(\frac{\rho}{\rho_0} - 1\right) \tag{64}$$

where C_1 is the bulk modulus of water, and ρ_0 its mass density in the reference configuration. For an inviscid fluid, μ = 0, and the state of stress in the fluid is that of hydrostatic pressure.

2.2.4. Initial and boundary conditions

We assume that initially the hull is at rest, and occupies the reference configuration Ω_1. That is

$$u_i(\mathbf{X},0)=0 \tag{65}$$

where u_i is the displacement defined as $u_i = x_i - X_i$ and

$$v_i(\mathbf{X},0)=0. \tag{66}$$

For the boundary conditions, we take

$v_i(\mathbf{x}, t)$ is specified on γ_{1u} for all t and $T_{ji}n^1_j = 0$ on γ_{1t} for all t. (67)

Here n^1_i is an outward unit normal vector on γ_{1t} in the current configuration.

We assume that initially the fluid is at rest, and occupies the reference configuration Ω_2 at time t = 0. Since the fluid problem is formulated in the spatial description of motion, we do not track the motion of each fluid particle. Thus

$$v_i(\mathbf{x},0)=0. \tag{68}$$

Boundary conditions for the fluid are taken to be

$$v_i(x_I, t) = 0 \text{ on } \gamma_{2u} \text{ for all } t \tag{69}$$

and

$$T_{ji} n^2_j = 0 \text{ on } \gamma_{2t} \text{ for all } t. \tag{70}$$

Here n^2_i is an outward unit normal vector on γ_{2t} in the present configuration; γ_{2t} is the free water surface that is not contacting the hull and is to be determined as a part of the solution of the ptoblem. It is tacitly assumed in writing equation (70) that surface tension effects are negligible and air exerts null pressure on the fluid.

For $t > 0$, the solid body ω_1 is in contact with the fluid region ω_2 and the interface γ_{12} between the two varies with time t. We assume that following conditions hold on γ_{12}.

$$\mathbf{v}^s - \mathbf{v}^f = \mathbf{0} \text{ on } \gamma_{12} \tag{71}$$

$$T^s_{ij} n_i = T^f_{ij} n_i \text{ on } \gamma_{12} \tag{72}$$

where superscripts s and f on a quantity denote, respectively, its value for the solid and the fluid particles on the fluid-solid interface γ_{12} and n_i is an outward unit normal vector on γ_{12} in the present configuration.

We note that γ_{2t} varies with time, is *a priori* unknown, is to be determined as a part of the solution of the problem, and γ_{2t} is given by $F(t, x_i) = 0$ such that

$$\frac{DF}{Dt} = v^f_i n^2_i \,. \tag{73}$$

Here DF/Dt denotes the material time derivative of F. For an inviscid fluid, equations (71) and (72) are modified to enforce the continuity of only the normal component of the velocity and the normal component of the traction across γ_{12} (see Appendix A).

2.2.5 Plane strain deformations

We assume that a plane strain state of deformation prevails in the x_1x_2-plane, and accordingly study a 2-dimensional problem.

2.2.6. Numerical solution of the initial-boundary-value problem

The commercial code LS-DYNA is used to find an approximate solution of the nonlinear initial-boundary-value problem defined by equations (53) - (73). We use the FEM incorporated in LSDYNA to solve the initial-boundary-value problem for the hull; the method is described in several references, e.g., see [42, 108]. To solve the initial-boundary-value problem for the fluid, we use the split approach detailed in [8, 7, 22, 21] and implemented in LS-DYNA.

Figure 59(a) shows the rectangular Cartesian coordinate system, and the FE mesh used to analyze the slamming impact of a hull whose undeformed shape is like a V. To analyze deformations in the x_1x_2-plane, we use 8-node brick elements with one point integration rule and with only one element in the x_3-direction to discretize the fluid, the solid and the initially void region, and constrain all nodes from moving in the x_3-direction. The software LS-DYNA rules out spurious modes of deformation by using the hour-glass control algorithm. Figure 59(b) shows the hull whose material is transversely isotropic with the axis of transverse isotropy along the $\bar{x}_1$-direction.

Due to symmetry of the problem geometry and of the initial and the boundary conditions, deformations of bodies occupying regions for which $x_1 \geq 0$ are analyzed (see figure 59 (a)). In figure 59 (a), L_4 and (L_5 - L_3) are the length and the depth of the fluid region, respectively; L_4 and (L_5 -L_3) are at least five times the length of the hull. The depth L_3 of the initially void region above water is such that the void region encloses the hull. The fluid region (L_2 x L_1) near the hull is meshed with smaller elements; L_1 equals at least the length of the hull and L_2 at least five times the anticipated depth of penetration of the hull into the water. The FE mesh for the hull overlaps that for the initially void region. As the hull penetrates into water regions occupied by the hull and the fluid change. On the hull/water interface γ_{12} continuity conditions (71) and (72) are satisfied using the penalty method [8, 7] (see appendix A) by either explicitly stating the value of the penalty stiffness parameter k_d (see equation A.4 in appendix A) or by prescribing the value of k_d as a fraction P_f (see equation A.5 in appendix A) of the bulk modulus of the compressible fluid. In LS-DYNA the penalty method cannot be employed if the fluid is

incompressible. The free water surface is tracked in LS-DYNA using the Simple Linear Interface Calculation (SLIC) technique [101].

Appropriate values of the penalty parameter depend on the speed of impact, elastic moduli of the hull material, hull shape, bulk modulus and viscosity of water, size of FEs, and the deadrise angle. Numerical studies with different parameters show that a low value of the penalty stiffness poorly satisfies equations (71) and (72), thus water penetrates the hull-water interface. The water pressure at the interface becomes oscillatory if a high value of the penalty stiffness parameter is used. Here, most problems are studied with at least three values of the penalty parameter to ascertain its appropriate value for the problem.

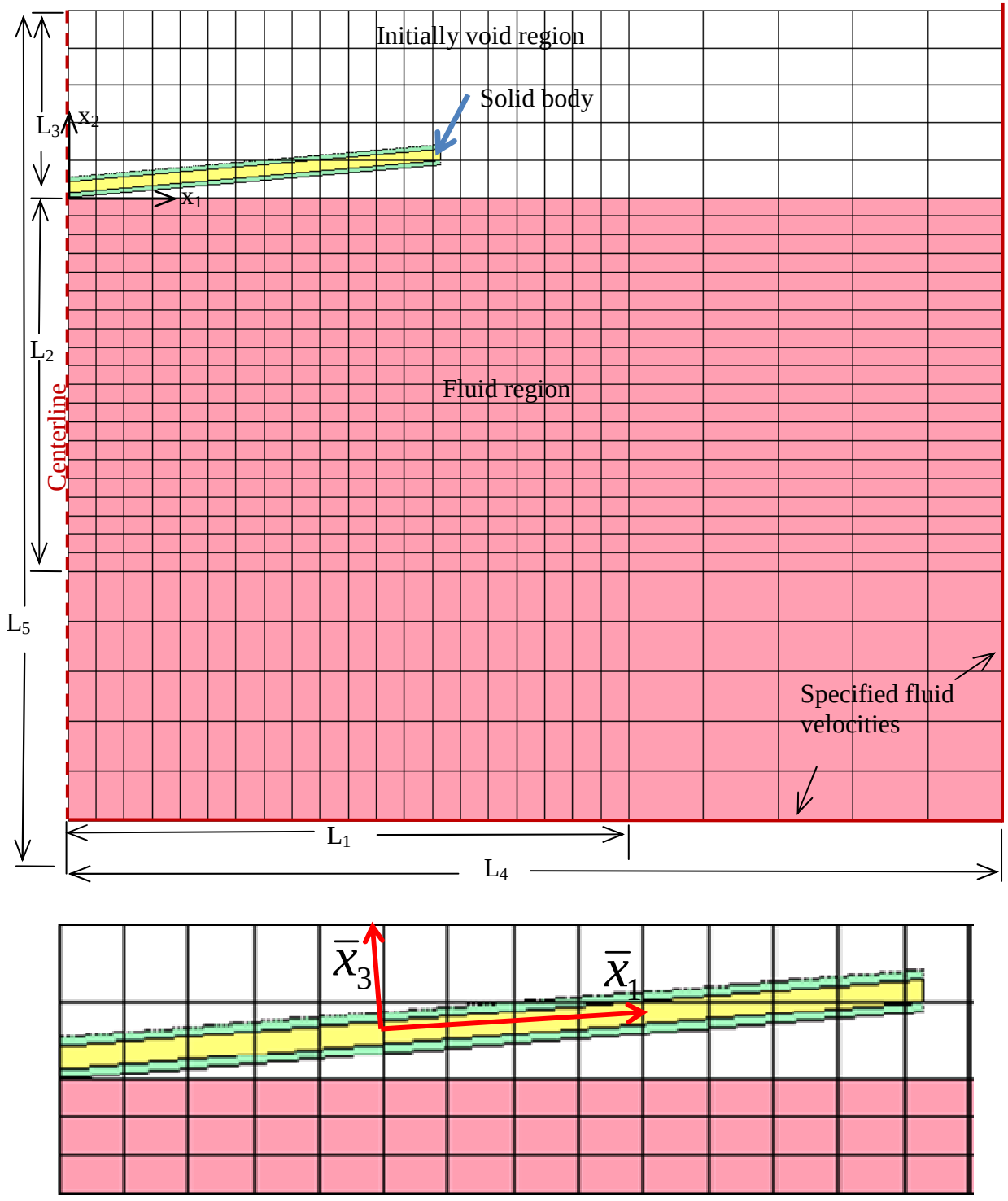

Figure 59. (a) The FE mesh used to study the slamming problem; (b) undeformed shape of the hull made of a transversely isotropic material with the axis of transverse isotropy along the $\bar{x}_1$-axis.

2.2.7. Damage model for fiber reinforced polymer composite

We assume that the hull is made of transversely isotropic fiber reinforced composite laminas with the axis of transverse isotropy along the $\bar{x}_1$-direction; see figure 60. Continuum damage mechanics approach is used to ascertain the progressive damage induced in the laminas, and the resulting degradation of elasticities of the composite. We assume that $T_{33} = 0$, solve this equation for ε_{33}, substitute for ε_{33} in equations for T_{11} and T_{22} and obtain [81, 58]

$$\begin{Bmatrix} T_{11} \\ T_{22} \\ T_{12} \end{Bmatrix} = D \begin{bmatrix} (1-\omega_{11(t,c)})E_{11} & (1-\omega_{11(t,c)})(1-\omega_{22(t,c)})\nu_{21}E_{22} & 0 \\ (1-\omega_{11(t,c)})(1-\omega_{22(t,c)})\nu_{12}E_{11} & (1-\omega_{22(t,c)})E_{22} & 0 \\ 0 & 0 & 2D(1-\omega_{12})G_{12} \end{bmatrix} \begin{Bmatrix} \varepsilon_{11} \\ \varepsilon_{22} \\ \varepsilon_{12} \end{Bmatrix} \quad (74)$$

$$\begin{Bmatrix} T_{13} \\ T_{23} \end{Bmatrix} = \begin{bmatrix} 2G_{13} & 0 \\ 0 & 2G_{13} \end{bmatrix} \begin{Bmatrix} \varepsilon_{13} \\ \varepsilon_{23} \end{Bmatrix} \quad (75)$$

where components are with respect to the material principal axes shown in figure 60. In equations (74) and (75), $D = 1 - (1-\omega_{11(t,c)})(1-\omega_{22(t,c)})\nu_{12}\nu_{21} > 0$, E_{11}, E_{22}, and G_{12} are, respectively, Young's moduli in the longitudinal (the fiber) and the transverse (perpendicular to the fiber) directions, and the shear modulus in the $\bar{x}_1\ \bar{x}_2$-plane; G_{13} is the transverse shear modulus, and ν_{12} and ν_{21} are the major and the minor Poisson ratios, respectively. Furthermore, $\omega_{11(t,c)}$ and $\omega_{22(t,c)}$ are damage variables in the longitudinal and the transverse directions that have different values in tension (ω_{11t}) and in compression (ω_{11c}), and ω_{12} is the damage variable for shear deformations in the $\bar{x}_1\ \bar{x}_2$-plane. Equations (74) and (75) imply that the degradation due to damage of the transverse shear modulus G_{13} is neglected. Most composite laminas fail at strains between 2% and 5%. For such small deformations, the three stress tensors, namely the first Piola–Kirchhoff, the second Piola–Kirchhoff, and the Cauchy, are essentially equal to each other, and so are the Almansi-Hamel and the Green-St. Venant strain tensors.

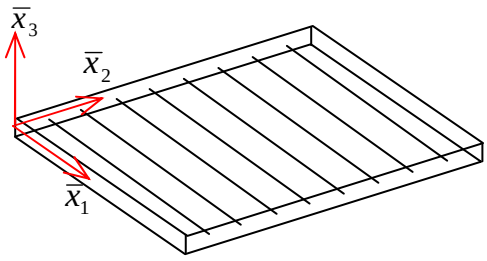

Figure 60. A fiber reinforced composite lamina and the local rectangular Cartesian coordinate axes used to describe deformations of the lamina.

The evolution laws for the damage parameters are taken as follows [81]:

$$\omega_{11(t,c)} = 1 - e^{\frac{\ln \beta_{1(t,c)}}{e}\left(\frac{E_{11}\varepsilon_{11}}{T_{f11(t,c)}}\right)^{\frac{1}{\ln \beta_{1(t,c)}}}} \text{ if } |\varepsilon_{11}| < |\varepsilon_{f11(t,c)}| \text{ or } |T_{11}| > |\alpha_{11(t,c)} T_{f11(t,c)}| \tag{76}$$

$$= 1 - \alpha_{11(t,c)} \frac{T_{f11(t,c)}}{E_{11}\varepsilon_{11}} \text{ if } |\varepsilon_{11}| \geq |\varepsilon_{f11(t,c)}| \text{ and } |T_{11}| \leq |\alpha_{11(t,c)} T_{f11(t,c)}|$$

$$\omega_{22(t,c)} = 1 - e^{\frac{\ln \beta_{2(t,c)}}{e}\left(\frac{E_{22}\varepsilon_{22}}{T_{f22(t,c)}}\right)^{\frac{1}{\ln \beta_{2(t,c)}}}} \text{ if } |\varepsilon_{22}| < |\varepsilon_{f22(t,c)}| \text{ or } |T_{22}| > |\alpha_{22(t,c)} T_{f22(t,c)}| \tag{77}$$

$$= 1 - \alpha_{22(t,c)} \frac{T_{f22(t,c)}}{E_{22}\varepsilon_{22}} \text{ if } |\varepsilon_{22}| \geq |\varepsilon_{f22(t,c)}| \text{ and } |T_{22}| \leq |\alpha_{22(t,c)} T_{f22(t,c)}|$$

$$\omega_{12} = 1 - e^{\frac{\ln \beta_{12}}{e}\left(\frac{2G_{12}\varepsilon_{12}}{T_{f12}}\right)^{\frac{1}{\ln \beta_{12}}}} \text{ if } |\varepsilon_{12}| < |\varepsilon_{f12}| \text{ or } |T_{12}| > |\alpha_{12} T_{f12}| \tag{78}$$

$$= 1 - \alpha_{12} \frac{T_{f12}}{G_{12}\varepsilon_{12}} \text{ if } |\varepsilon_{12}| \geq |\varepsilon_{f12}| \text{ and } |T_{12}| \leq |\alpha_{12} T_{f12}|$$

where $T_{f11(t,c)}, T_{f22(t,c)}$ and T_{f12} are strengths of the lamina in the longitudinal direction, the transverse direction and for shear deformations in the x_1x_2-plane, respectively. Subscripts c and t on T indicate its values for compressive and tensile stresses, respectively; $\varepsilon_{f11(t,c)}, \varepsilon_{f22(t,c)}$ and ε_{f12} are strains at which the material attains strengths $T_{f11(t,c)}, T_{f22(t,c)}$ and T_{f12}, respectively, in uniaxial deformations along the longitudinal and the transverse directions, and in simple shear deformations in the x_1x_2-plane; $0 \leq \alpha_{(11,22)(t,c)}, \alpha_{12} \leq 1$ are scale factors, $\beta_{1(t,c)} = \varepsilon_{f11(t,c)} E_{11} / T_{f11(t,c)}$, $\beta_{2(t,c)} = \varepsilon_{f22(t,c)} E_{22} / T_{f22(t,c)}$, $\beta_{12} = \varepsilon_{f12} G_{12} / T_{f12}$ and $e \approx 2.71828$. As a damage component increases with an increase in the corresponding strain component, the

corresponding elastic modulus decreases, therefore strengths $T_{f11(t,c)}$, $T_{f22(t,c)}$ and T_{f12} are less than $\varepsilon_{f11(t,c)}E_{11}$, $\varepsilon_{f22(t,c)}E_{22}$, and $\varepsilon_{f12}G_{12}$, respectively; in other words $\beta_{1(t,c)}, \beta_{2(t,c)}, \beta_{12} > 1$. The evolution laws (74) - (78) are incorporated in LS-DYNA as material model number 58, namely MAT_LAMINATED_COMPOSITE_FABRIC. We note that ω_{ij} (i, j = 1, 2) depends only on ε_{ij}, and the value of ω_{ij} does not change when the value of ε_{ij} either decreases or remains below its previously reached maximum value. The material model 58 in LS-DYNA can only be used with shell elements because the assumption $T_{33} = 0$ is valid for thin shells.

It is assumed that when a scalar strain measure ε_{scl} given by

$$\varepsilon_{scl} = \frac{2}{\sqrt{3}}\sqrt{\left(3\left(\frac{\varepsilon_{11}+\varepsilon_{22}}{2}\right)^2 + \left(\frac{\varepsilon_{11}-\varepsilon_{22}}{2}\right)^2 + \left(2\varepsilon_{12}\right)^2\right)} \tag{79}$$

exceeds a predetermined failure strain ε_{erod}, the element ceases to bear loads and is deleted from the simulation.

With assumptions $\varepsilon_{13} = \varepsilon_{23} = 0$ and $\varepsilon_{33} = -(\varepsilon_{11} + \varepsilon_{22})$ the effective strain $\sqrt{\frac{2}{3}\left(\varepsilon_{11}^{\ 2} + \varepsilon_{22}^{\ 2} + \varepsilon_{33}^{\ 2} + 2\varepsilon_{12}^{\ 2} + 2\varepsilon_{13}^{\ 2} + 2\varepsilon_{23}^{\ 2}\right)}$ takes the form $\frac{2}{\sqrt{3}}\sqrt{\left(3\left(\frac{\varepsilon_{11}+\varepsilon_{22}}{2}\right)^2 + \left(\frac{\varepsilon_{11}-\varepsilon_{22}}{2}\right)^2 + \left(\varepsilon_{12}\right)^2\right)}$. However, the assumption $\varepsilon_{33} = -(\varepsilon_{11} + \varepsilon_{22})$ is inconsistent with the assumption $\varepsilon_{33} = 0$ made to derive equation (74). The failure criterion (79) implies that the failure of a material point does not depend upon the transverse shear strains there. Also in equation (79), engineering shear strain $2\varepsilon_{12}$ is used instead of ε_{12}. As stated on the website [110] equation (79) is implemented in LS-DYNA. Due to the unavailability of the source code for LS-DYNA we could not modify equation (79).

Figure 61 shows schematically a stress-strain curve for a uniaxial strain test along the longitudinal direction indicating various parameters.

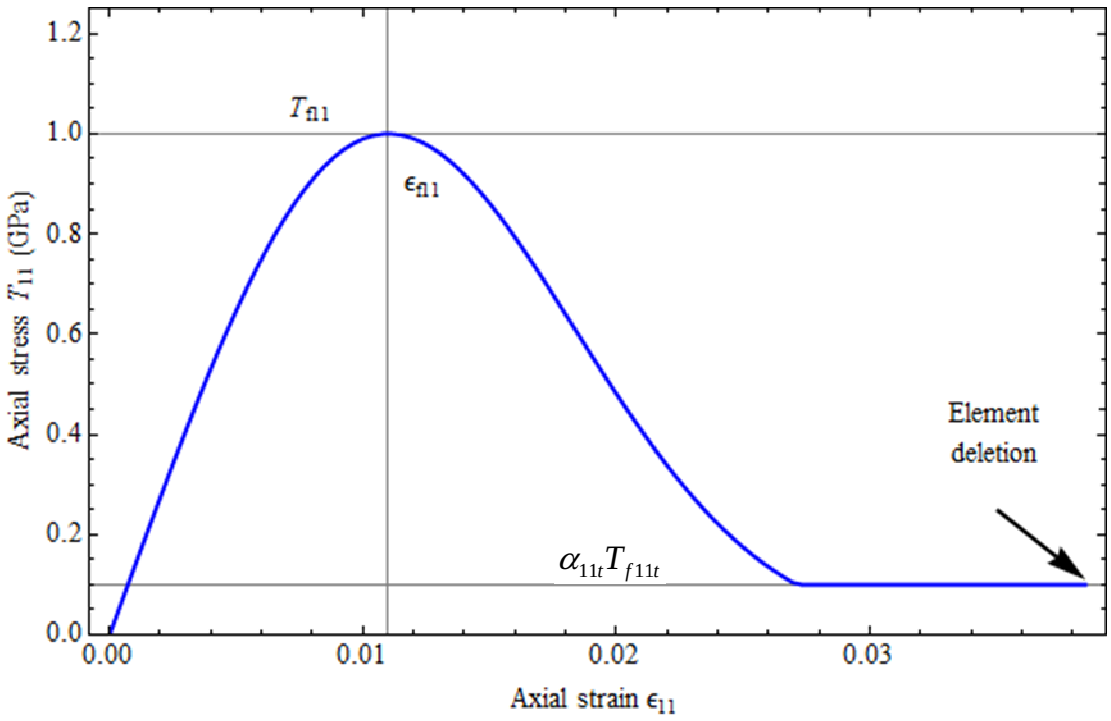

Figure 61. Schematic of a stress-strain curve for a uniaxial strain test along the longitudinal direction indicating various parameters.

2.3. Results and discussion

2.3.1. Tension, compression and shear tests with the damage model

We analyze the damage model described in the previous section by numerically simulating tension, and compression tests using the boxed configuration shown in figure 62(a) so as to prevent the structure from buckling under compressive loads. The boxed shaped structure and the structure for the shear test (see figure 62(b)) are discretized using, respectively, four (one for each lamina) and one fully integrated (four in-plane Gauss points and eight through the thickness Gauss points) [42, 34, 85] shell elements, respectively. Each 1 mm thick lamina is modeled by only one shell element with node numbers shown in Figure 62 and boundary conditions prescribed at nodes listed in table 7. Note that for a transient problem the prescribed boundary conditions need not rule out rigid body motion.

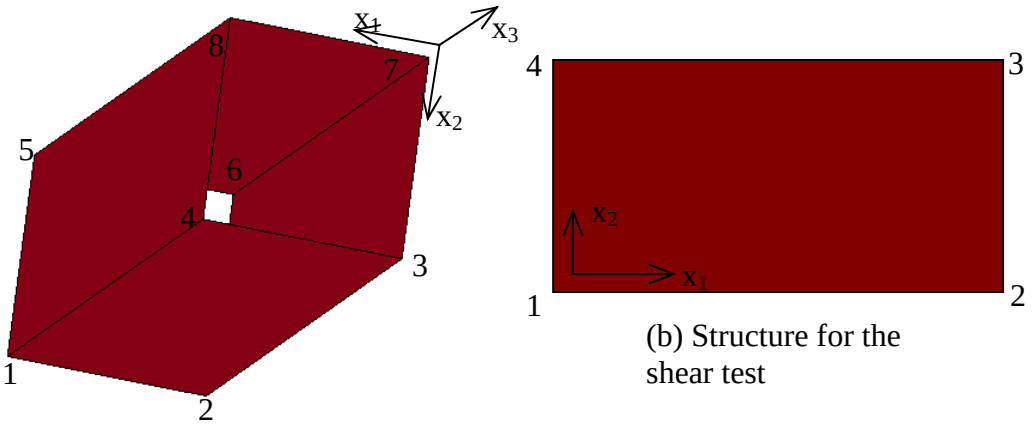

(b) Structure for the shear test

(a) Structure for the tension and the compression test

Figure 62. Structure used in (a) the tension and the compression tests, and (b) the shear test; and the global rectangular Cartesian coordinate systems used to describe deformations of structures.

For the tension and the compression tests in the longitudinal (transverse) direction, the longitudinal direction $\bar{x}_1$ (transverse direction $\bar{x}_2$) of the lamina is aligned along the global x_3-axis. For the shear test, the longitudinal and the transverse directions of the lamina are aligned with the global x_1- and x_2-axes, respectively. Values of material parameters listed in table 8 are for a "*typical*" fiber-reinforced composite, and values assigned (arbitrarily) to $\alpha_{(11,22)(t,c)}$, α_{12}, $T_{f(11,22)(t,c)}$, T_{f12}, $\varepsilon_{f(11,22)(c,t)}$ and ε_{f12} are such that the stress (T_{11}, T_{22} or T_{12}) does not drop suddenly after the strain (ε_{11}, ε_{22} or ε_{12}) reaches $\varepsilon_{f11(c,t)}$, $\varepsilon_{f22(c,t)}$, or ε_{f12}, respectively; a sudden drop in the stress causes numerical instabilities. The LS-DYNA keyword manual suggests the value of 1.0 for α_{11c} and α_{22c} to avoid numerical instabilities; for these values the axial stress remains constant in compression after the material has reached its ultimate strength. A value between 0.05 to 0.1 is suggested for α_{11t}, α_{22t} and α_{12}. We note that a FE is deleted from the simulation when equation (79) is satisfied irrespective of values of stress, strain and damage variables; thus a material point may fail and a FE may be deleted before any one of the damage variable there equals its maximum value 1. The time history of the prescribed velocity v_0 is exhibited in figure 63.

Table 7: Boundary conditions for the tension, the compression, and the shear test

Node number	x_1	x_2	x_3
Tension and compression test			
1	Fixed	Fixed	Fixed
2	Free	Free	Fixed
3	Free	Free	Prescribed velocity v_0
4	Free	Free	Prescribed velocity v_0
5	Free	Free	Fixed
6	Free	Free	Fixed
7	Free	Free	Prescribed velocity v_0
8	Free	Free	Prescribed velocity v_0
Shear test			
1	Fixed	Fixed	Fixed
2	Fixed	Fixed	Fixed
3	Prescribed velocity v_0	Fixed	Fixed
4	Prescribed velocity v_0	Fixed	Fixed

Table 8: Material properties for the lamina; subscripts 11, 22 and 12 refer to material properties along the $\bar{x}_1$-direction, the $\bar{x}_2$-direction and in $\bar{x}_1\ \bar{x}_2$ - plane, respectively; these values have been arbitrarily chosen, and may not correspond to those for a composite material.

ρ	1640 Kg/m^3	T_{f11t}	1.0 GPa
E_{11}	138 GPa	T_{f11c}	1.3085 GPa
E_{22}	8.96 GPa	T_{f22t}	0.09 GPa
ν_{21}	0.019	T_{f22c}	0.1 GPa
G_{12}, G_{13}	7.1 GPa	T_{f12}	0.09 GPa
α_{11t}	0.1	ε_{f11t}	0.011
α_{11c}	1.0	ε_{f11c}	0.011
α_{22t}	0.1	ε_{f22t}	0.0152
α_{22c}	1.0	ε_{f22c}	0.015
α_{12}	0.1	ε_{f12}	0.04
ε_{erod}	0.045		

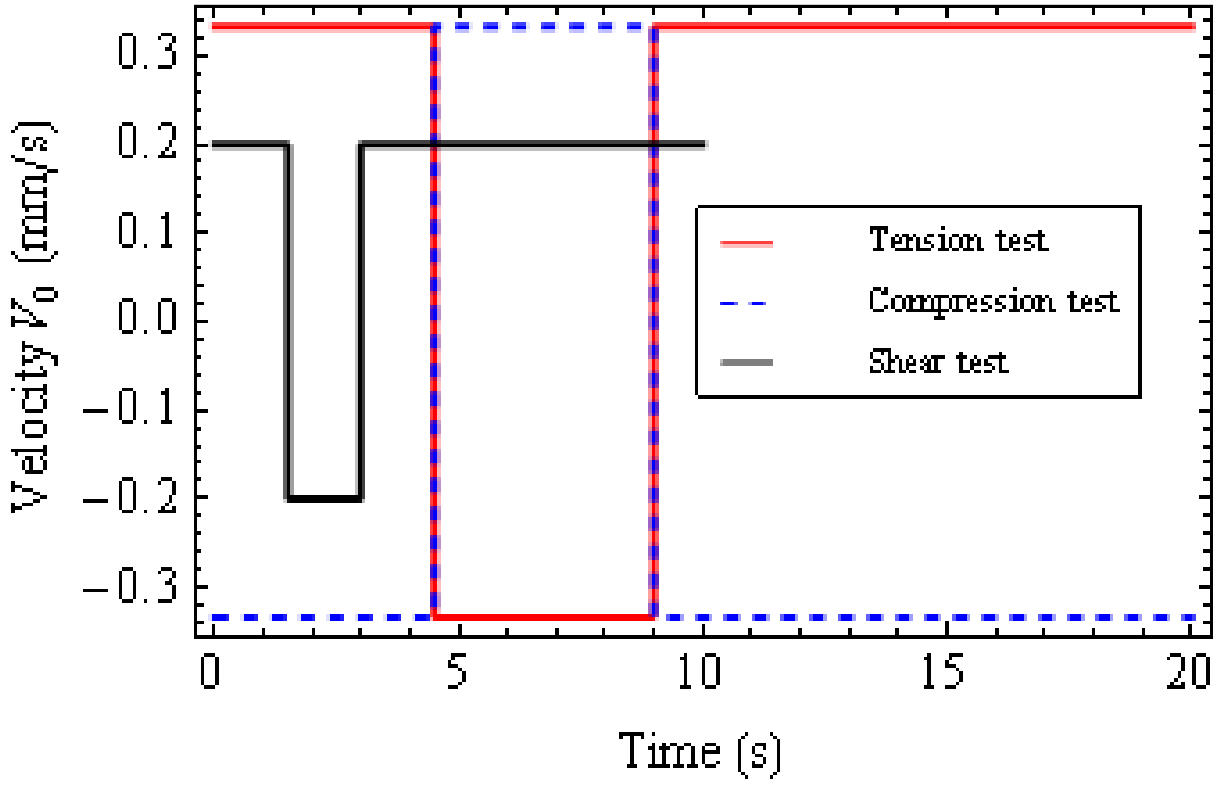

Figure 63. Time history of the specified velocity v_0 .

For the tension and the compression tests in the longitudinal and the transverse directions and for the in-plane shear test, figures 64 through 68 show computed stress-strain curves and variations of damage variables using LS-DYNA. Stress–strain curves during unloading and reloading of the specimen differ from those during initial loading due to the difference in the elastic moduli caused by the damage developed during initial loading. During unloading and reloading, damage variables remain constant, since either the material is unloading or strains induced in the material are below their previously reached maximum values. Thus during repeated loading and unloading under prescribed velocity of constant amplitude that does not cause failure of the material during the first cycle, there will be no additional damage developed, and according to the present damage model the lamina has a rather unrealistic infinite life. This does not affect results presented below since for the short time durations considered material points of a hull do not undergo many cycles of loading and unloading.

The material model with parameters reported in table 8 predicts a gradual decrease in the stress with an increase in the corresponding strain after the material reaches the ultimate strength in tension and shear. In addition, it predicts that the axial stress remains constant in compression after the material reaches its ultimate strength. In results presented in figures 64(b), 65(b), 66(b), 67(b) and 68(b) damage parameters do not reach a value of one because equation (79) is satisfied before damage variables equal 1, and the FE is deleted. Ideally, at least one of the damage variables should equal 1 when the material fails.

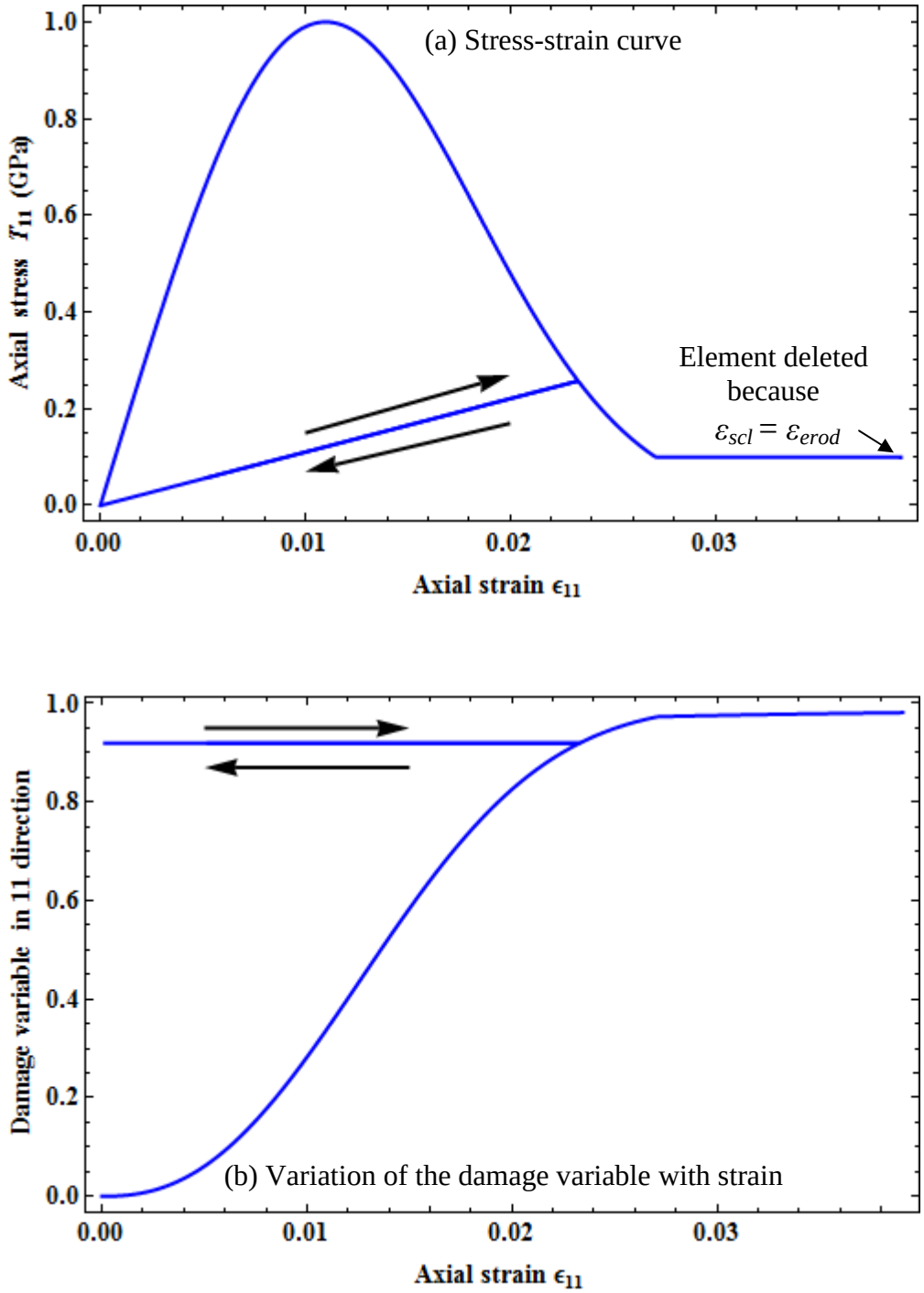

Figure 64. The stress-strain curve (a) and the variation of the damage variable (b) in tension test in the longitudinal direction.

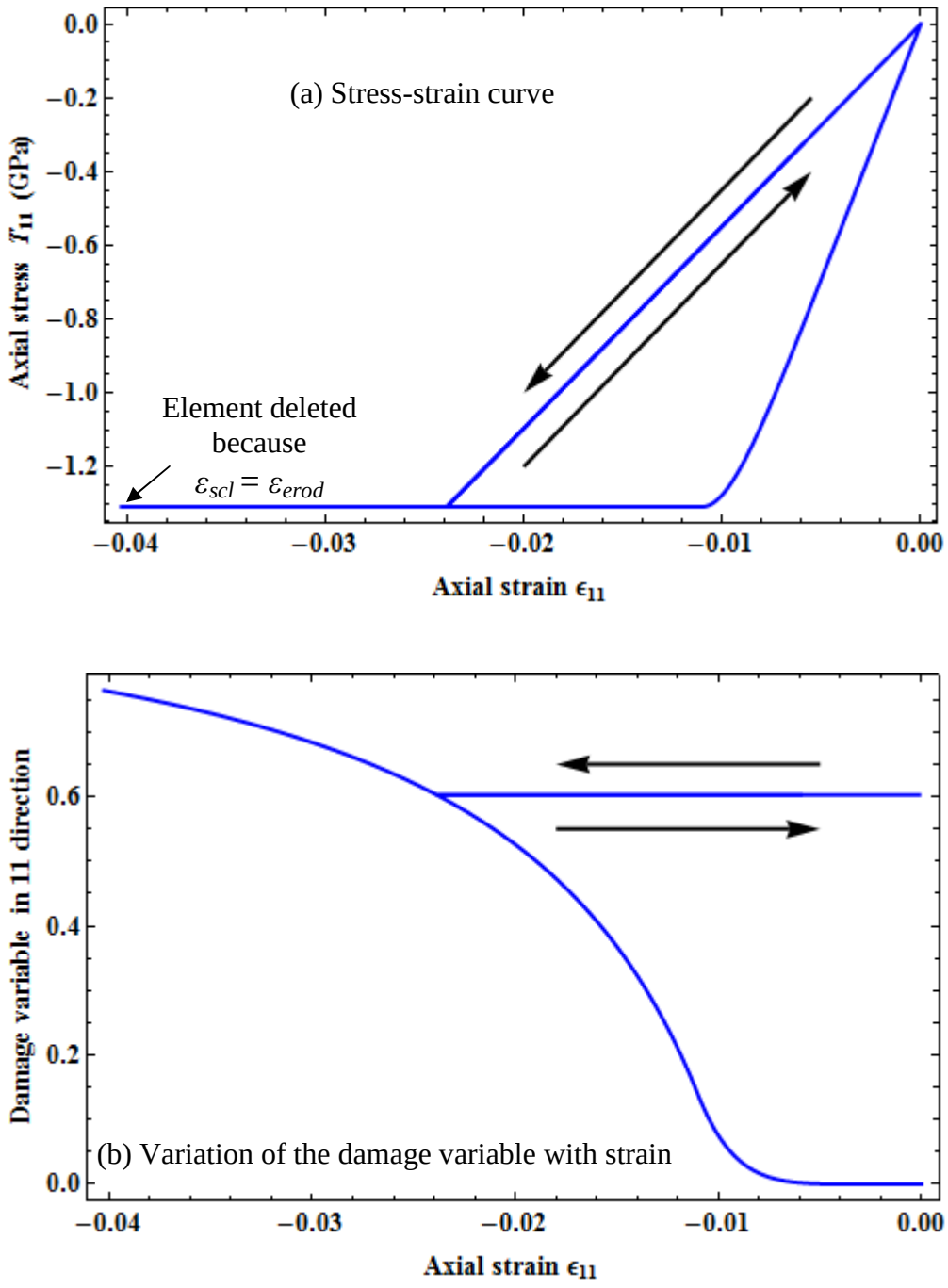

Figure 65. The stress-strain curve (a) and the variation of the damage variable (b) in compression test in the longitudinal direction.

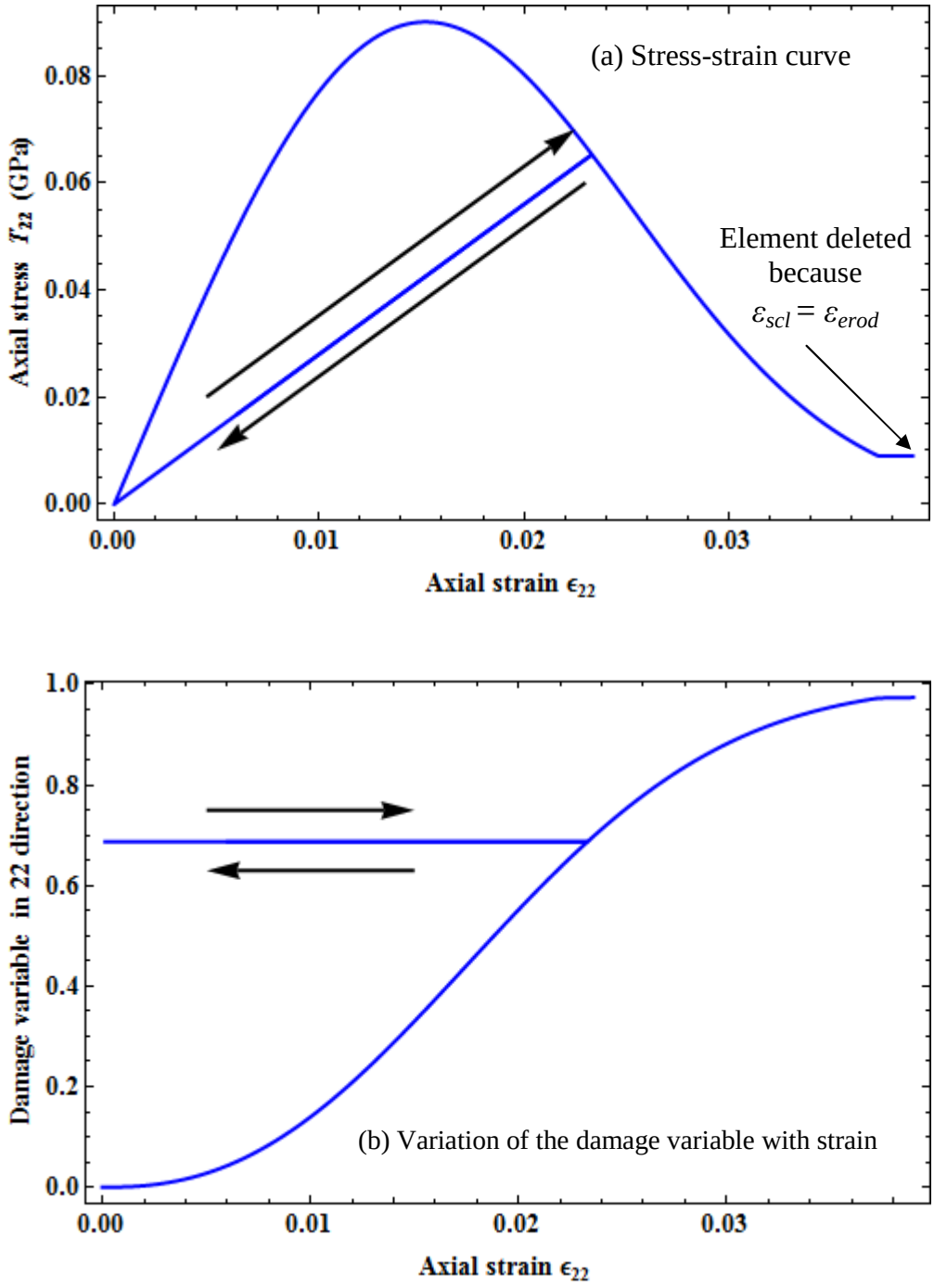

Figure 66. The stress-strain curve (a) and the variation of the damage variable (b) in tension test in the transverse direction.

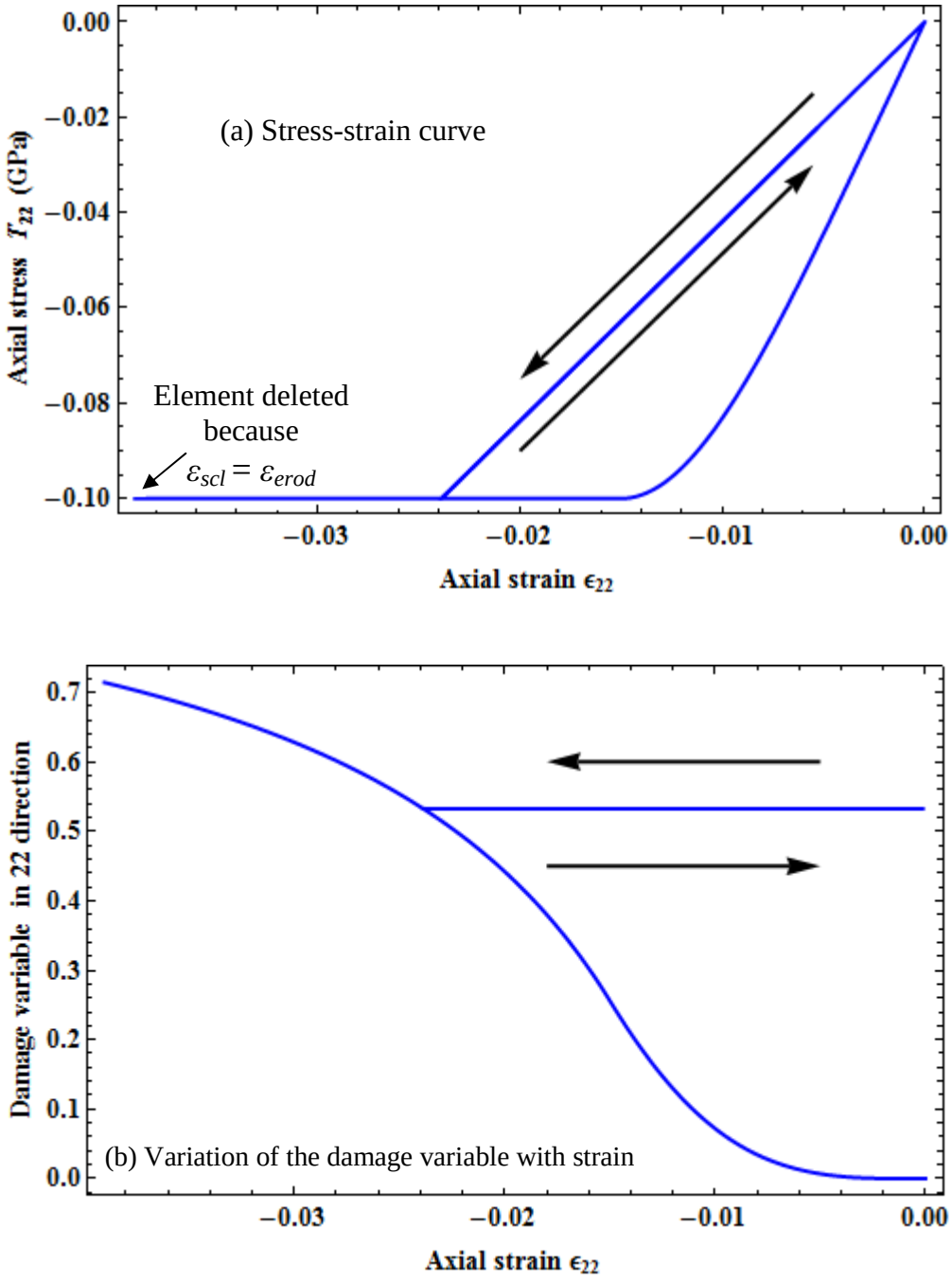

Figure 67. The stress-strain curve (a) and the variation of the damage variable (b) in compression test in the transverse direction.

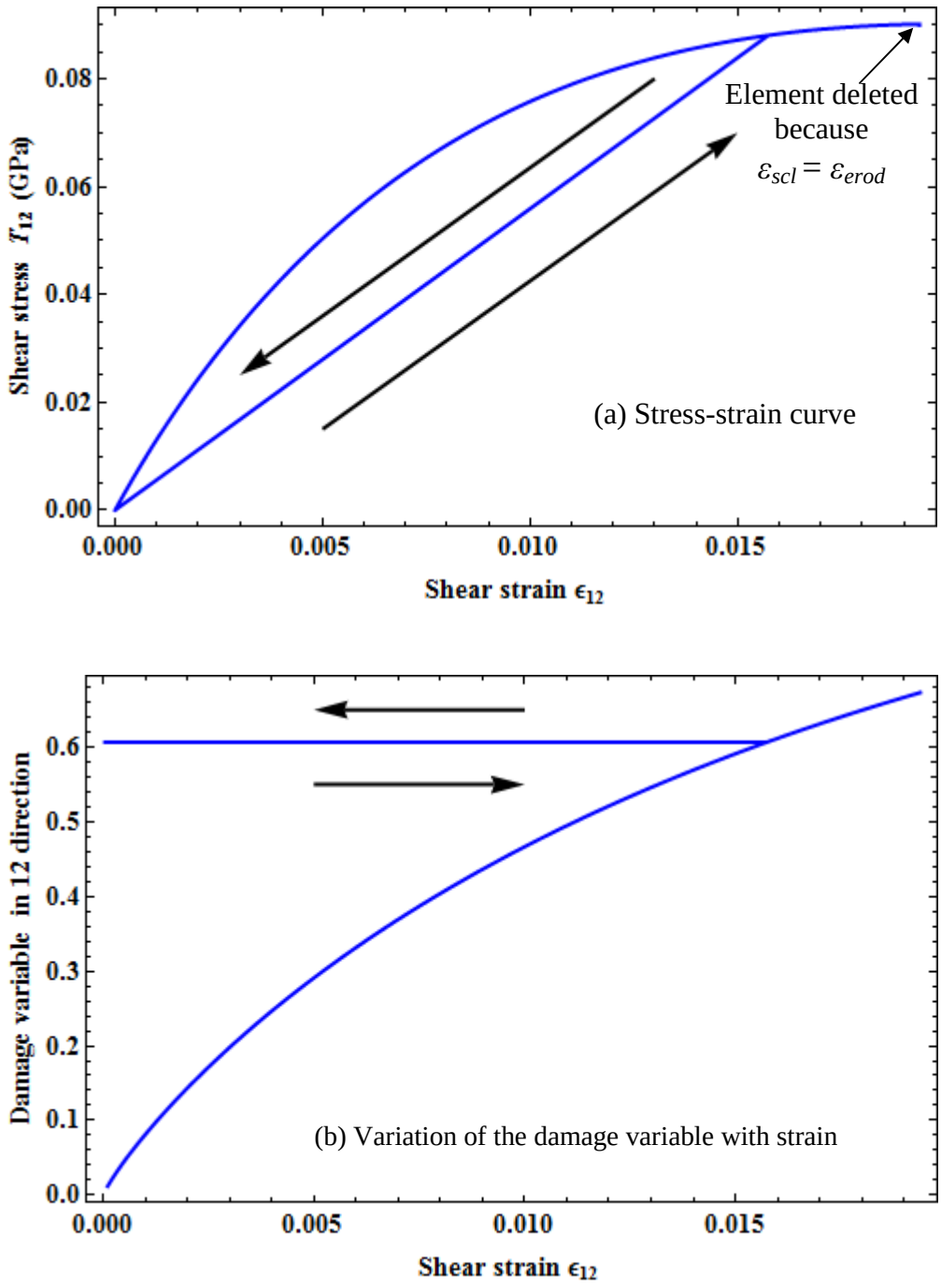

Figure 68. The stress-strain curve (a) and the variation of the damage variable (b) in shear test in x_1x_2-plane.

2.3.2. Water slamming on rigid wedges moving with constant downward velocity

The problem studied is a rigid V-shaped wedge entering calm water with a constant downward velocity of 10 m/s, each arm of V 1 m long and having deadrise angles of 10^0, 30^0, 45^0 and 81^0. Because of symmetry, deformations of materials in the region $x_1 \geq 0$ are studied with the computer code LS-DYNA. The fluid domain (L_1 x L_2) with L_1 = 2 m, L_2 = 2 m, L_3 = 1 m, L_4 = 5 m, L_5 = 6 m and width in the x_3-direction = 0.25 m (figure 59 (a)) near the rigid hull is discretized by 100 x 100 x 1 8-node brick elements. The mesh covering the entire domain (initially void and fluid domains, L_4 x L_5) has 150 x 150 x 1 8-node brick elements, and the wedge is discretized into 100 x 1 4-node shell elements along the length and the width (along x_3-direction) directions. All nodes of the fluid, the void and the solid structure are restrained from motion in the x_3-direction. The water is modeled as an inviscid fluid with bulk modulus of 2.9 GPa and ρ_0 = 1000 kg/m^3; thus the speed of volumetric equal ~ 1700 m/s. Thus the wave reaches the right boundary at ~ 3 ms and the bottom surface at ~ 2.4 ms. The effect of waves reflected from these boundaries will be felt by the wedge at ~ 5 ms implying that pressures computed at the wedge surface approximate those acting on the wedge striking an infinite body of water only for times less than ~ 5 ms.

(a) Deadrise angle = 10^0, t = 20 ms

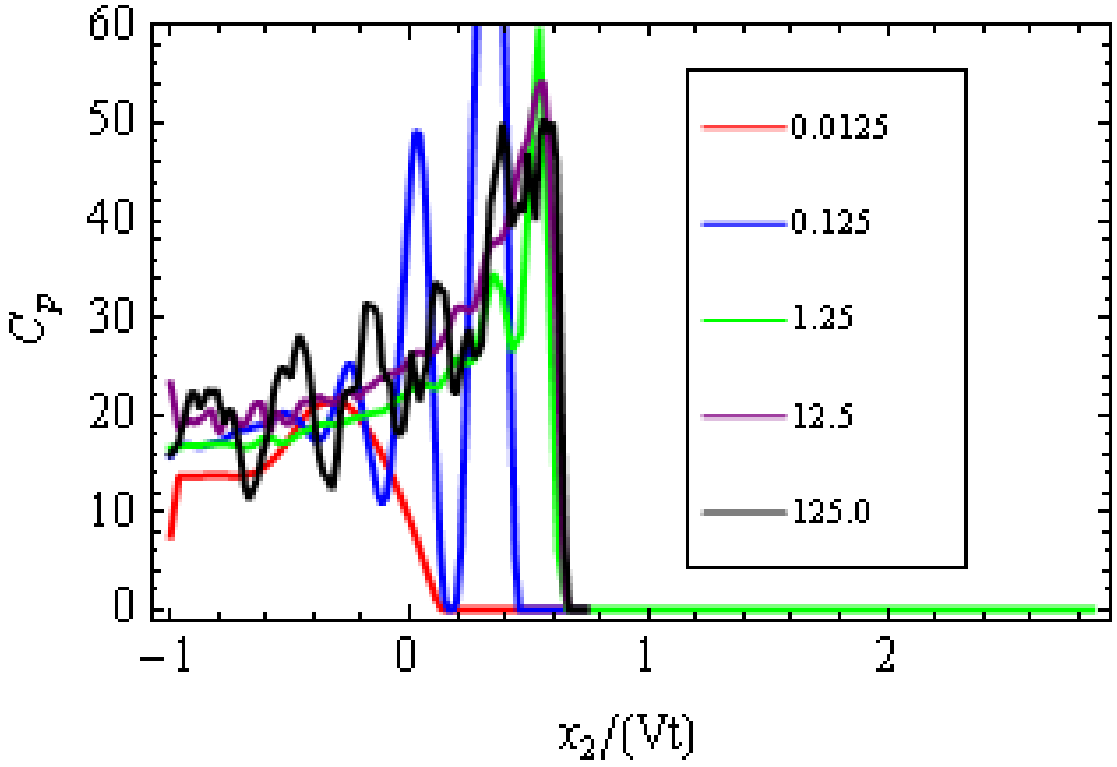

(b) Deadrise angle = 30^0, t = 40 ms

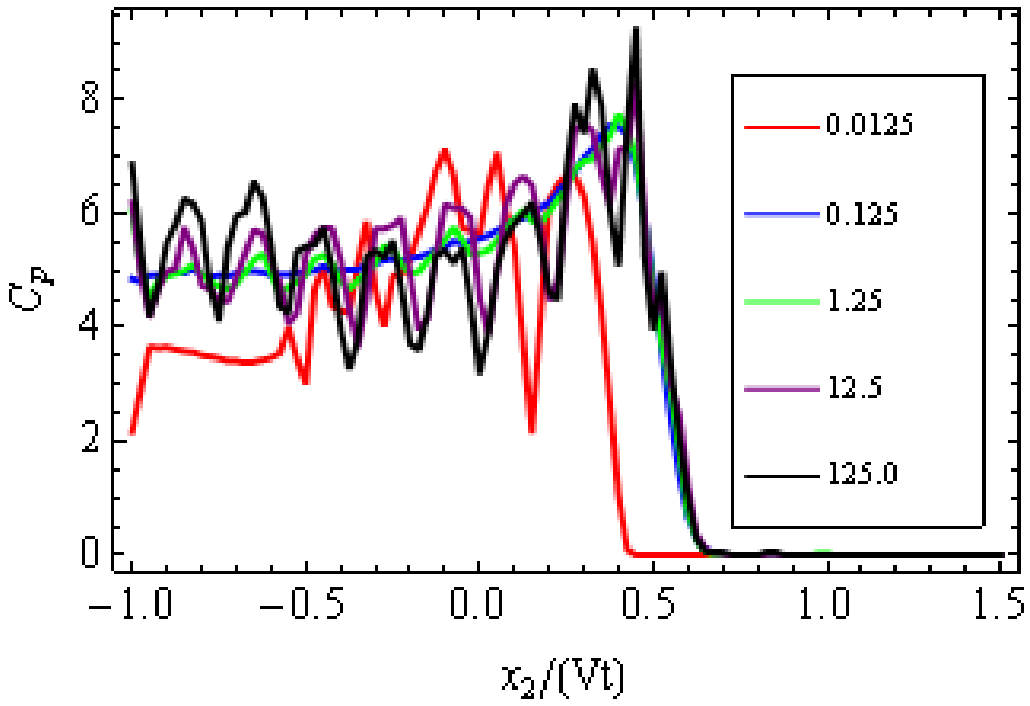

(c) Deadrise angle = 45^0, t = 65 ms

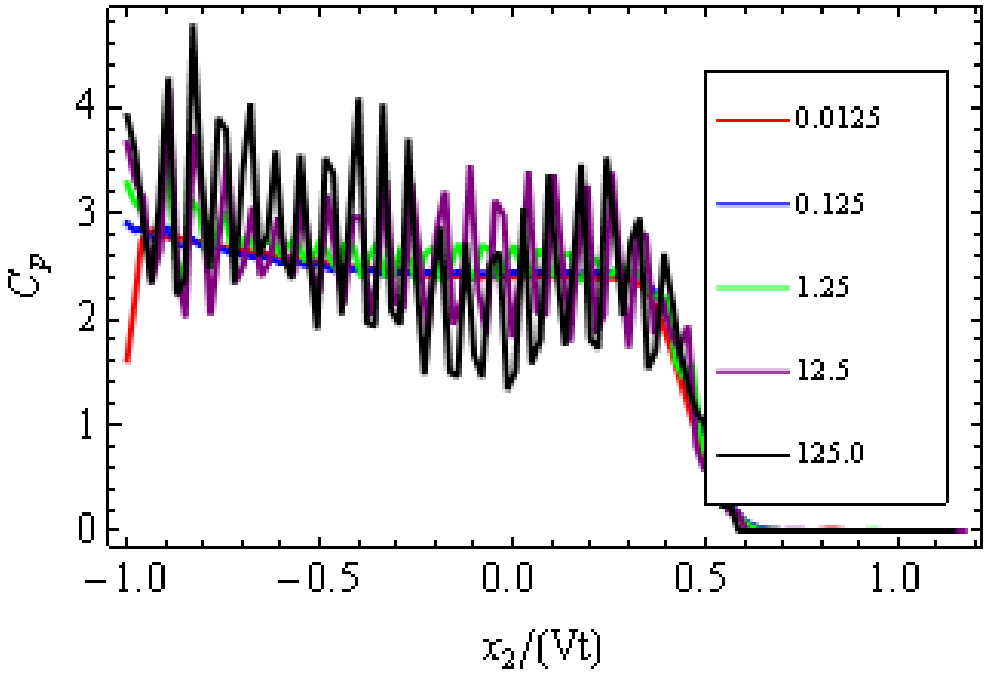

(d) Deadrise angle = 81^0, t = 66 ms

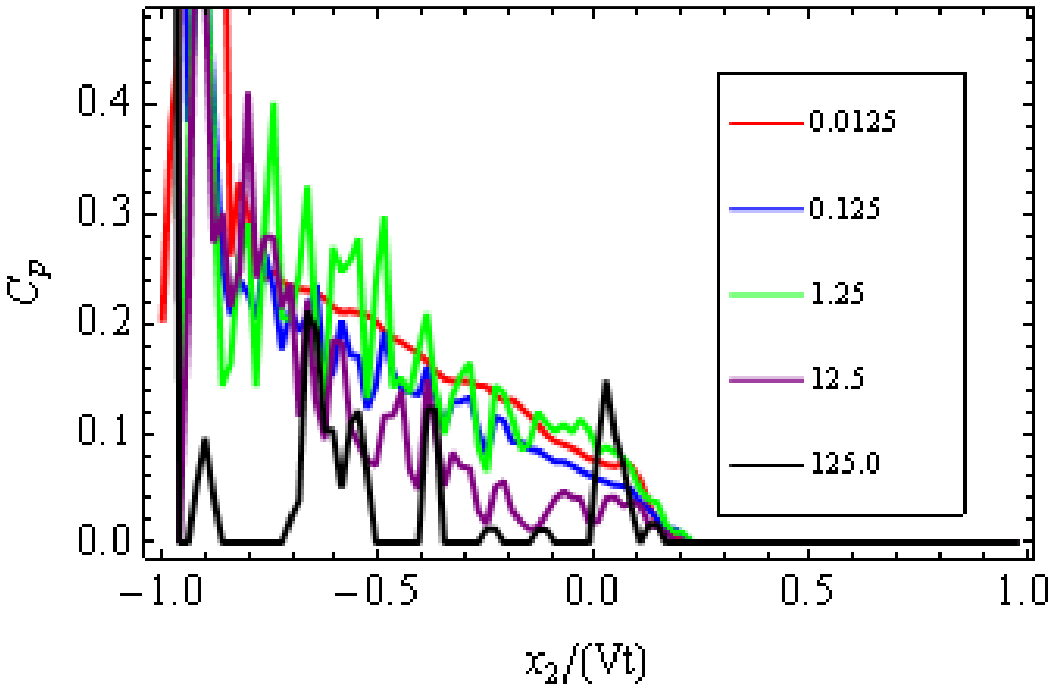

Figure 69. Variations of the pressure coefficient along the span of the hull for different values of the contact stiffness k_d (GPa).

In order to find an appropriate value of k_d we have plotted in figure 69 variations of the pressure coefficient C_p along the length of the water-wedge interface for various explicitly specified values of k_d with the damping coefficient c = 0. The times when results are plotted in the figure are different because the variations of C_p along the span are shown when the water level reached $x_1 = 2\cos\beta$ m, which is the edge of the wedge. After having found the optimum value of k_d, present results are compared with those reported by Mei et al. [59]. It is evident from results plotted in figure 69 (a) for the wedge of deadrise angle 10^0 penetrating water at 10 m/s that for k_d = 0.125, 1.25, 12.5 and 125 GPa/m the maximum amplitudes of oscillation of C_p are 60, 10, 5 and 20, respectively. For very low values of k_d (e.g., k_d = 0.0125 GPa/m), a noticeable amount of water penetration through the fluid-structure interface occurs because continuity conditions at the interface are not well satisfied, and for k_d = 1.25 and 125.0 GPa/m the maximum amplitude of oscillations in values of C_p divided by its mean value is large. Only for k_d = 12.5 the variation of C_p is relatively smooth along the span. Similarly, from results plotted in figures 69(b), (c) and (d), it is found that the variation of C_p is relatively smooth for k_d = 0.125 GPa/m, 0.125 GPa/m, and 0.0125 GPa/m for deadrise angles of 30^0, 45^0, and 81^0, respectively. Results exhibited in figure 70 suggest that with an increase in the value of the contact stiffness k_d, the amount of water penetration through the wedge-water interface decreases. The water level reaches the mid-span of the wedge at 10 ms, 23 ms, 34 ms and 78 ms for $\beta = 10^0$, 30^0, 45^0 and 81^0, respectively. It is clear from the plots of figure 70(a) that for the deadrise angle of 10^0, the water penetration through the interface at t = 10 ms equals ~ 6 kg and 3 kg for k_d = 0.0125 GPa/m and 0.125 GPa/m, respectively; further increase in the value of k_d does not decrease the amount of water penetration which saturates at ~ 1.7 kg. In comparison, the mass of the water displaced by the wedge of deadrise angle 10^0 in 10 ms equals 12 kg. The length of each arm of the V-shaped hull is 1 m and the width is 0.25 m; therefore, 2 kg water penetration means the average penetration distance of water through the fluid-structure interface is 8 mm for 100 mm penetration of the wedge. For each one of the four values of the deadrise angle, table 9 lists values of k_d for which the pressure profile is "smoother" than that for other values of k_d. Note that some of the oscillations in the pressure on the interface may be caused by waves reflected from the boundaries. One can eliminate reflected waves by either using non-reflecting boundaries or infinite elements at the bounding surfaces.

Table 9: Optimum values of k_d

Deadrise angle	10^0	30^0	45^0	81^0
Optimum value of k_d (GPa/m)	12.5	0.125	0.125	0.0125

Table 10: Optimum values of P_f

Deadrise angle	10^0	30^0	45^0	81^0
Optimum value of P_f	0.1	0.05	0.05	0.01

(a) Deadrise angle = 10^0

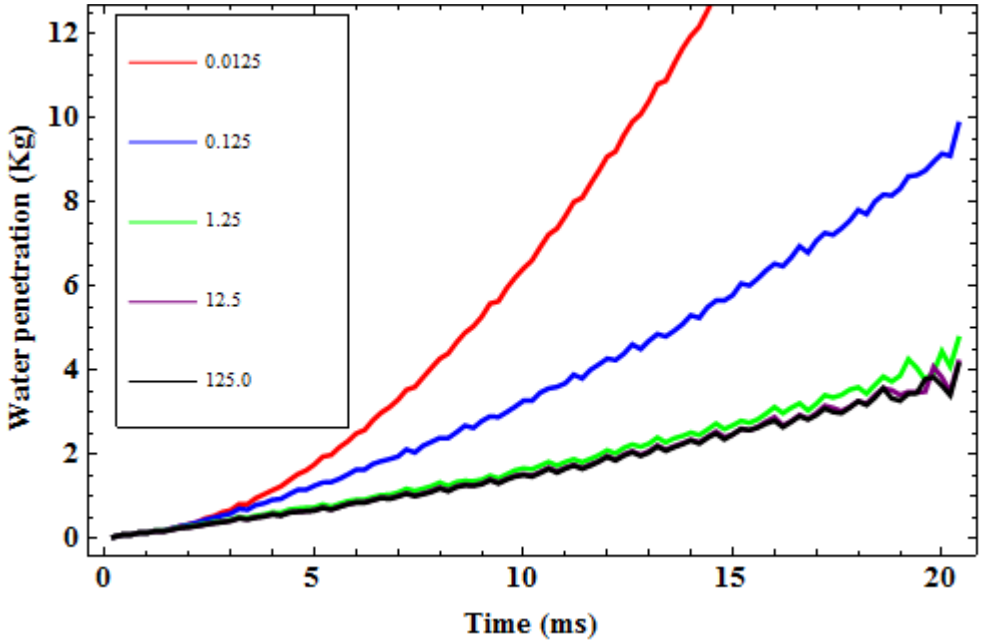

(b) Deadrise angle = 30^0

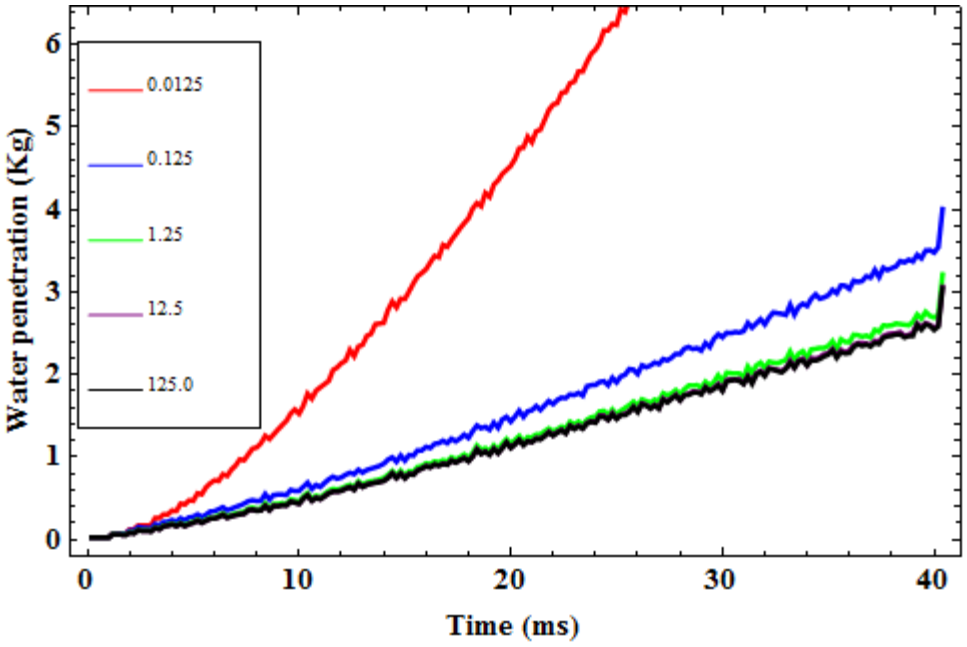

(c) Deadrise angle = 45^0

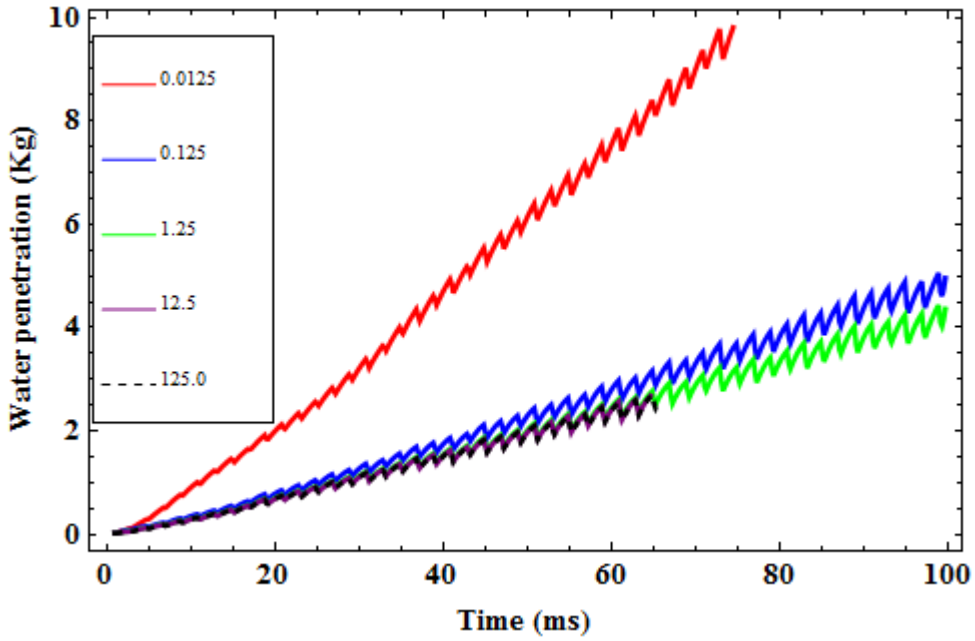

(d) Deadrise angle = 81^0

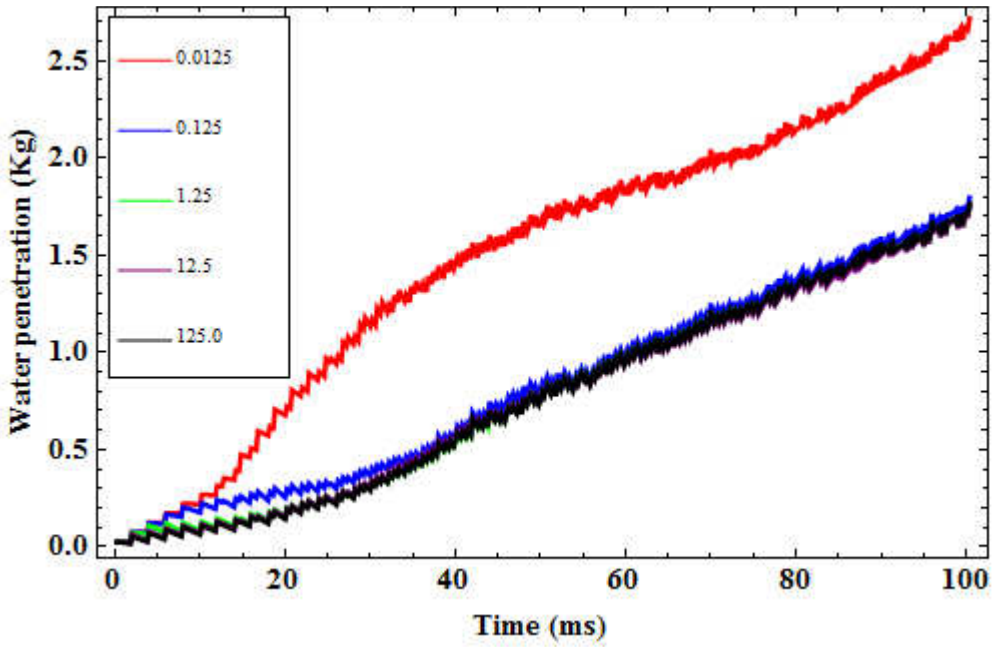

Figure 70. For different values of the contact stiffness k_d (GPa), time histories of the mass of water penetration through the water-wedge interface.

(a) Deadrise angle = 10^0, k_d = 12.5 GPa/m

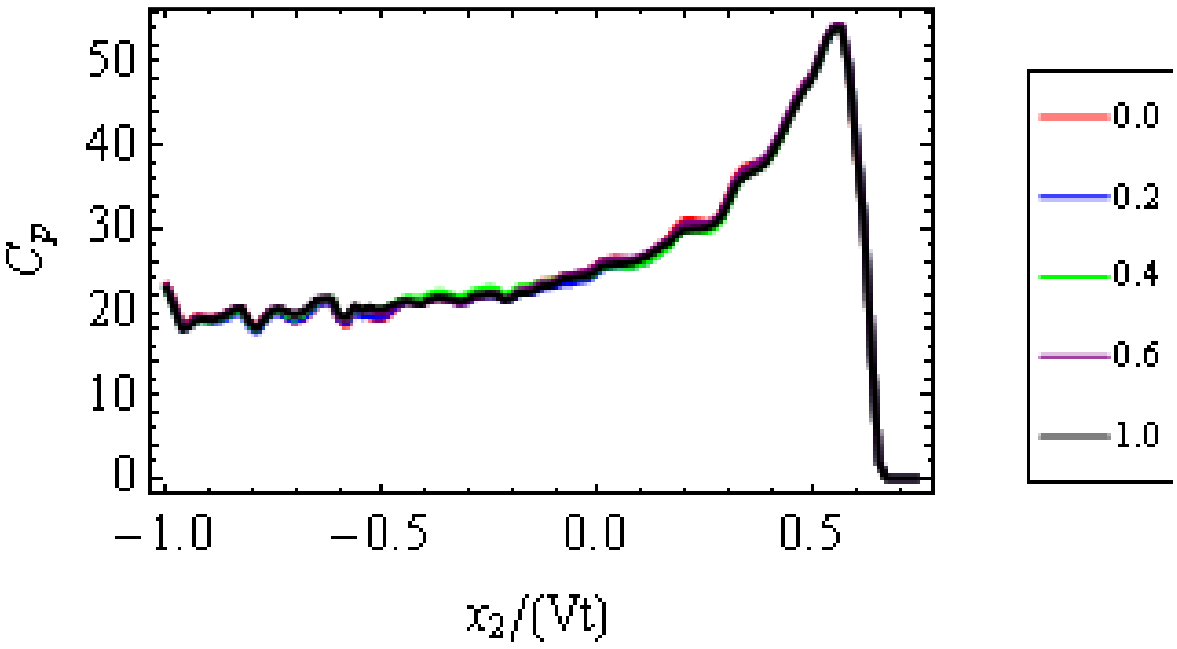

(b) Deadrise angle = 30^0, k_d = 0.125 GPa/m

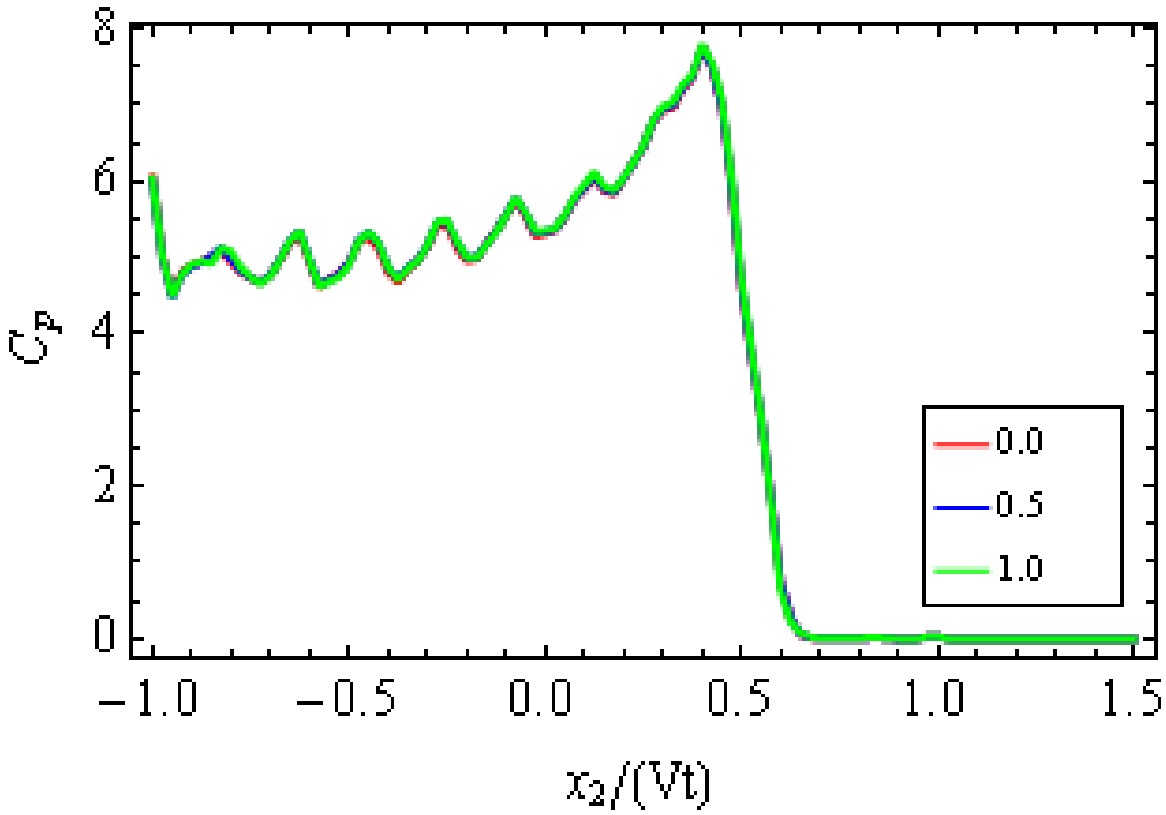

(c) Deadrise angle = 45^0, k_d = 0.125 GPa/m

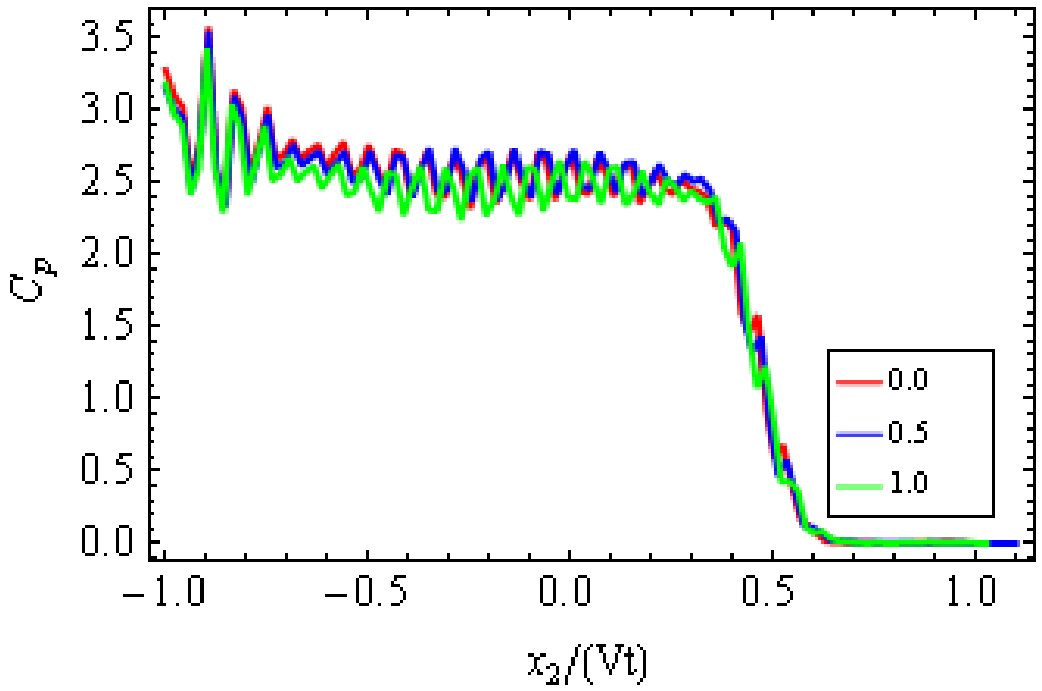

(d) Deadrise angle = 81^0, k_d = 0.0125 GPa/m

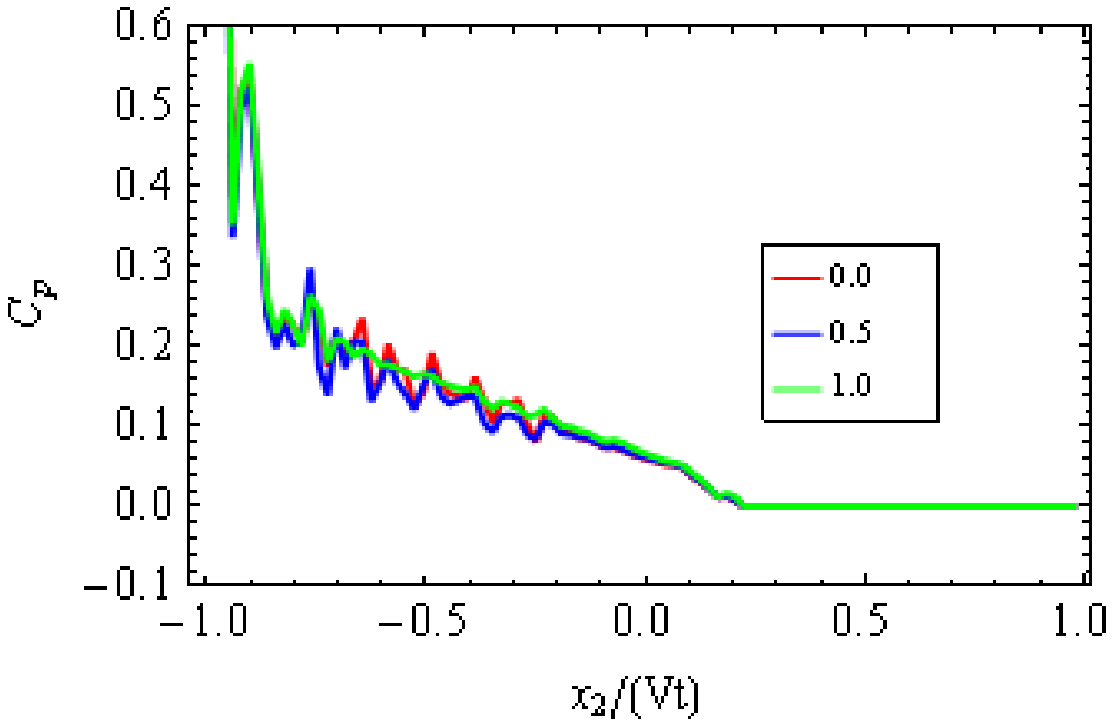

Figure 71. Variations of the pressure coefficient along the span of the hull for different values of the contact damping factor *c*.

For the four values of deadrise angles considered above and the corresponding optimal values of k_d listed in table 9, we have plotted in figure 71 variations of the pressure coefficient C_p along the span of the wedge for three values of the contact damping factor c. It is evident that the value assigned to the contact damping does not appreciably affect the value of C_p.

The effect of the mesh size on values of the pressure coefficient C_p is illustrated in figure 72 where results for two FE meshes are plotted; the FE mesh 2 is obtained from the FE mesh 1 by subdividing each brick (shell) element in mesh 1 into 4 equal brick (2 equal shell) elements. In addition to FE meshes 1 and 2, the wedge with deadrise angle of 10^0 is simulated with FE mesh 3 which has the same number of elements as mesh 2 but is only 0.01 m long in the x_3-direction. For the four deadrise angles considered above and the corresponding optimal values of k_d listed in table 9, results reported in figure 72 evince that the variations of C_p along the wedge-water interface for the deadrise angles of 30^0 and 45^0 are essentially independent of the mesh used. However, for deadrise angles of 10^0 and 81^0, the peak value of C_p computed using mesh 2 is ~20 % higher than that obtained with mesh 1. For deadrise angle of 81^0, mesh 2 produces smoother variation of C_p than that given by mesh 1. Results computed from FE meshes 2 and 3 for the wedge of 10^0 deadrise angle are virtually the same indicating that the length of the domain in the x_3-direction does not affect results as all nodes are constrained in the x_3-direction (see figure 72(a)). From results exhibited in figure 73 we conclude that for each deadrise angle, the amount of water penetration through the wedge-water interface is less for mesh 2 than that that for mesh 1.

(a) Deadrise angle = 10^0, k_d = 12.5 GPa/m

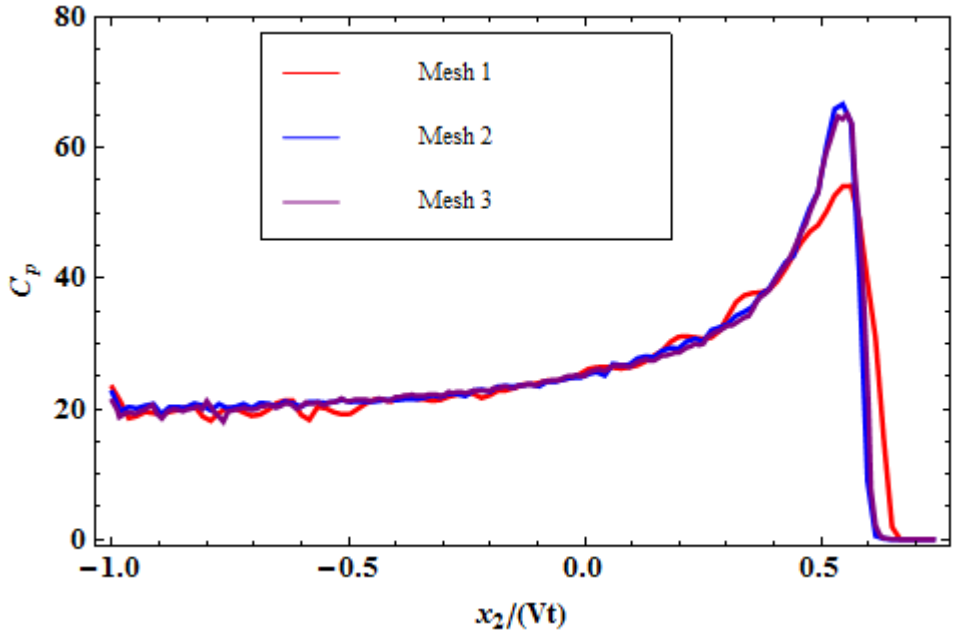

(b) Deadrise angle = 30^0, k_d = 0.125 GPa/m

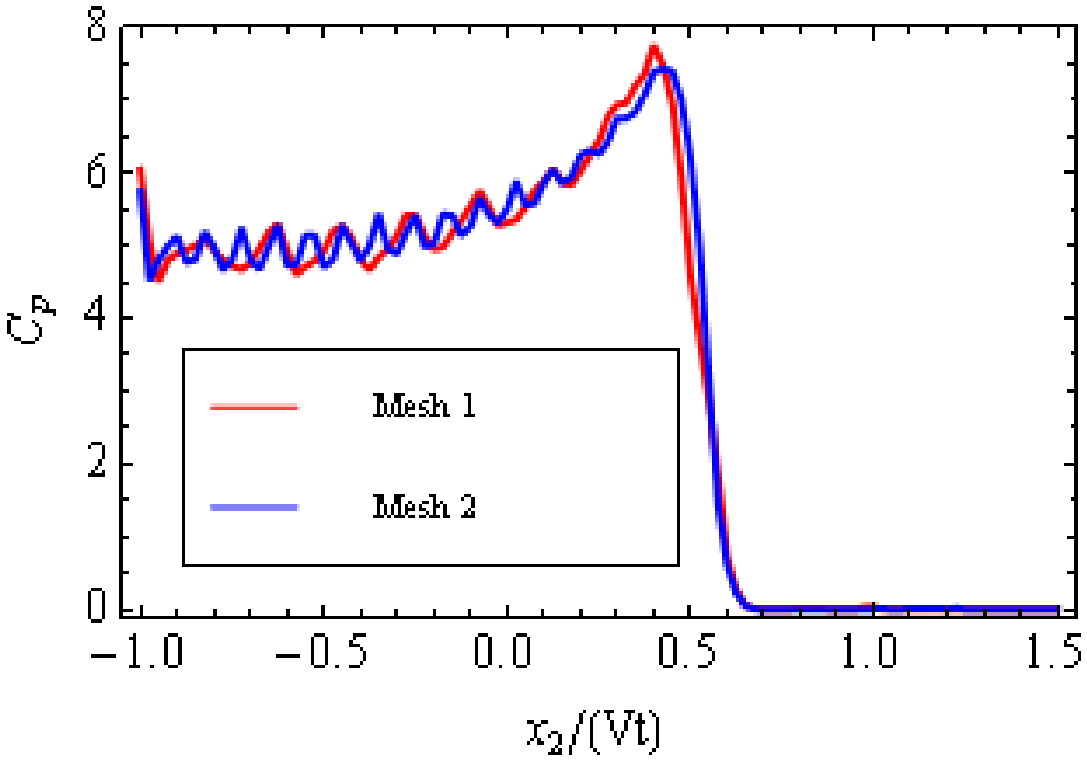

(c) Deadrise angle = 45^0, k_d = 0.125 GPa/m

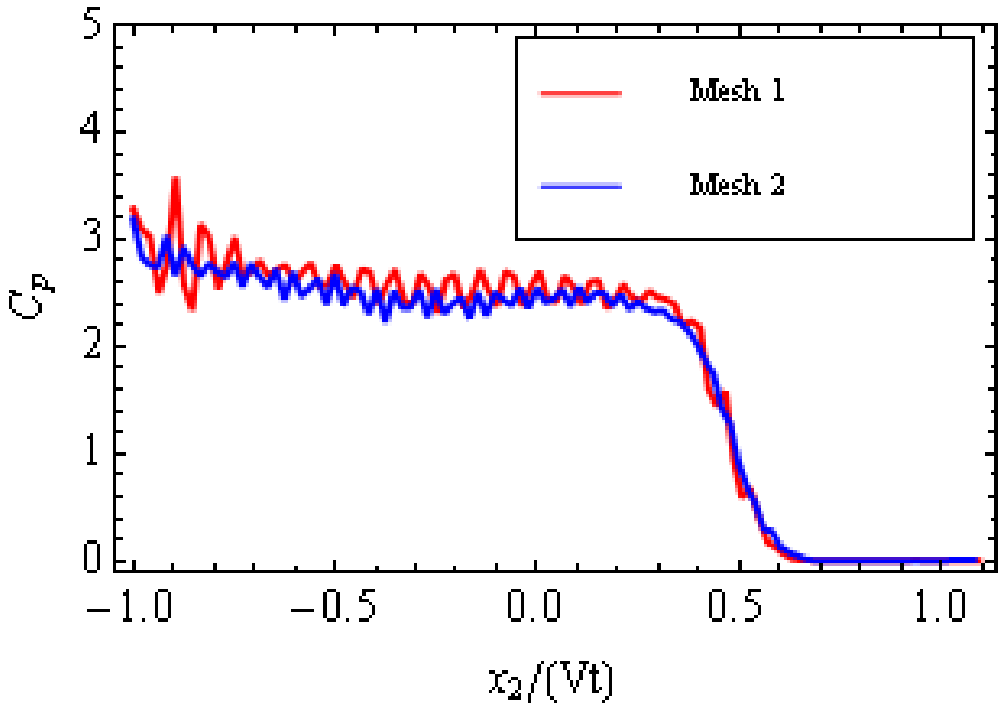

(d) Deadrise angle = 81^0, k_d = 0.0125 GPa/m

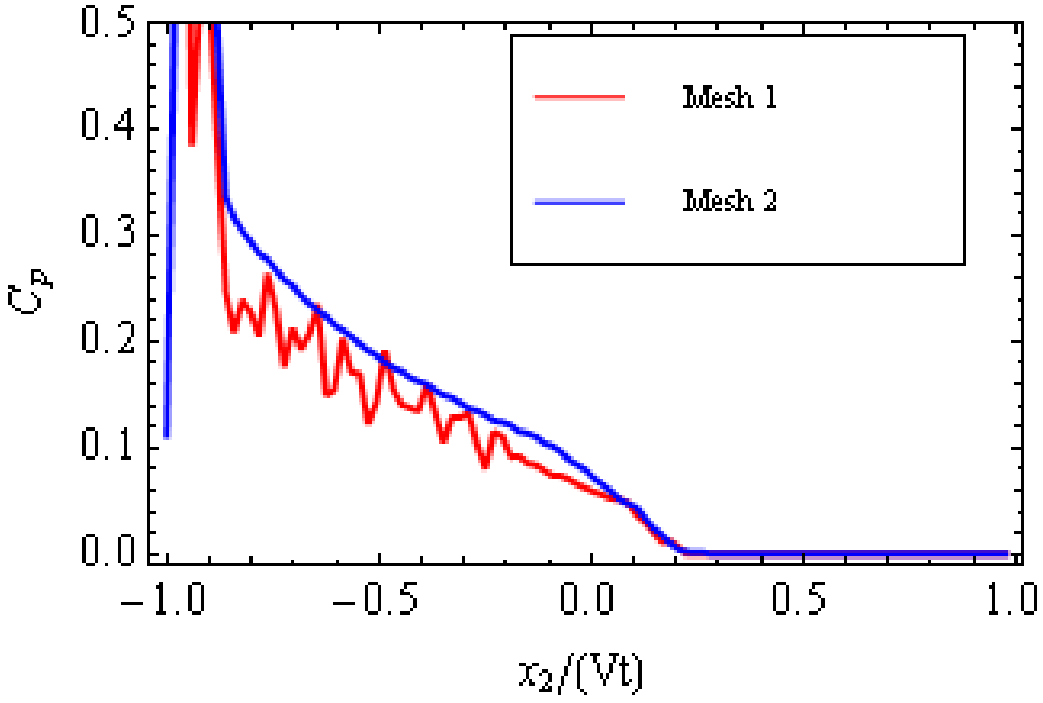

Figure 72. Variation of the pressure coefficient along the span of the hull for two FE meshes.

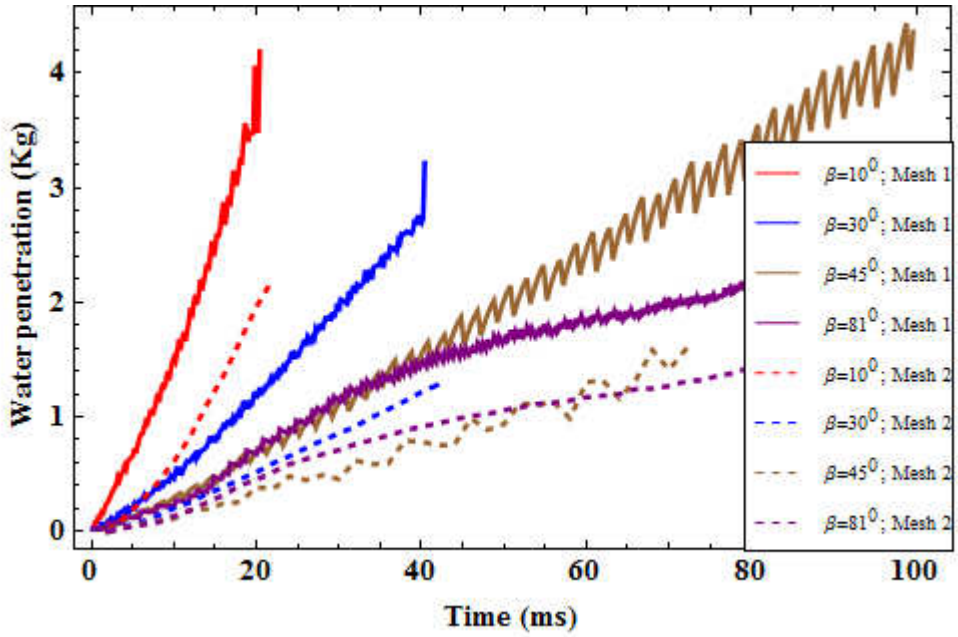

Figure 73. Time histories of the amount of water penetration through the hull-water interface for different deadrise angles and the two FE meshes.

Figures 74 and 75 delineate the dependence of C_p and the water penetration through the hull-water interface for three values of P_f (cf. equation (A.5)); figure 74 also exhibits the variation of C_p computed using the optimal values of k_d given in table 9. It is clear from these results that the amount of water penetration does not change significantly with an increase in the value of P_f, and the maximum amplitude of the oscillation in C_p is about 1, 0.5 and 0.35 for P_f = 0.1, 0.05 and 0.005, respectively. Thus the amplitude of oscillation in C_p decreases as P_f decreases. For each one of the four deadrise angles, the optimum value of P_f for which the variation of C_p is smoother than that for other values of P_f is listed in table 10.

(a) Deadrise angle = 10^0

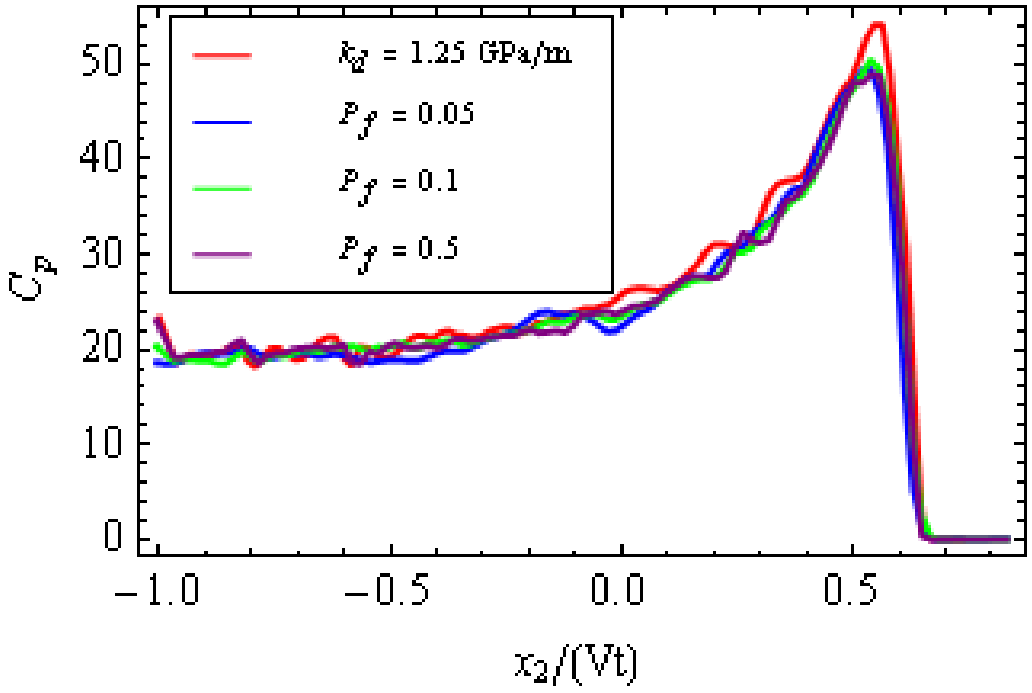

(b) Deadrise angle = 30^0

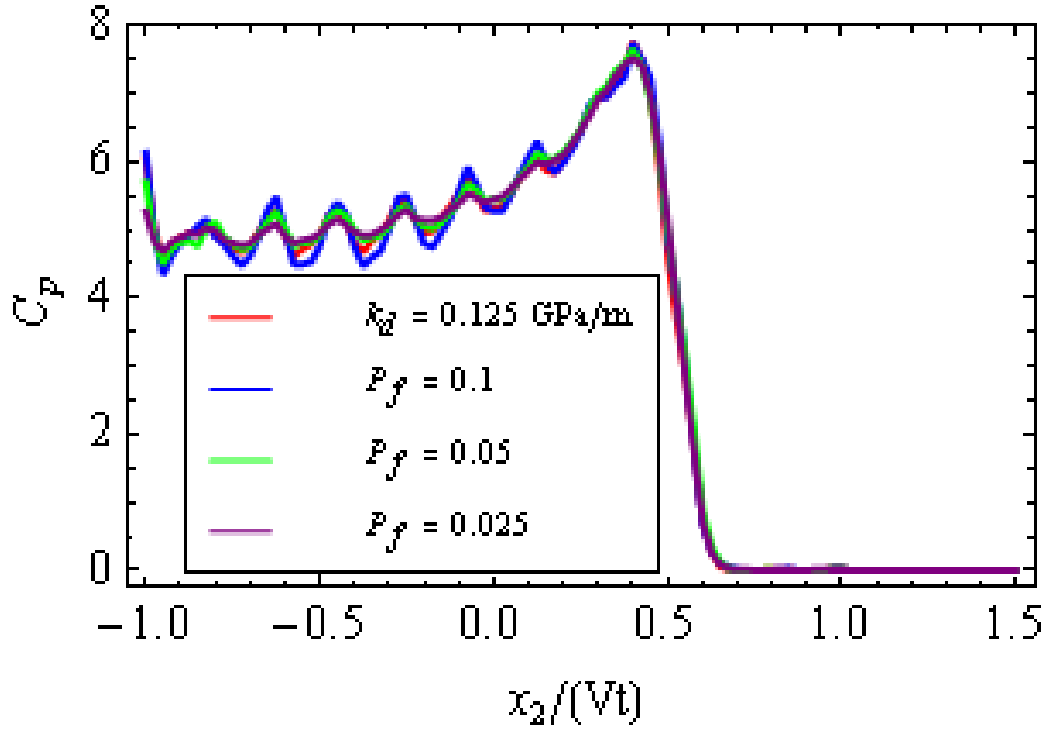

(c) Deadrise angle = 45^0

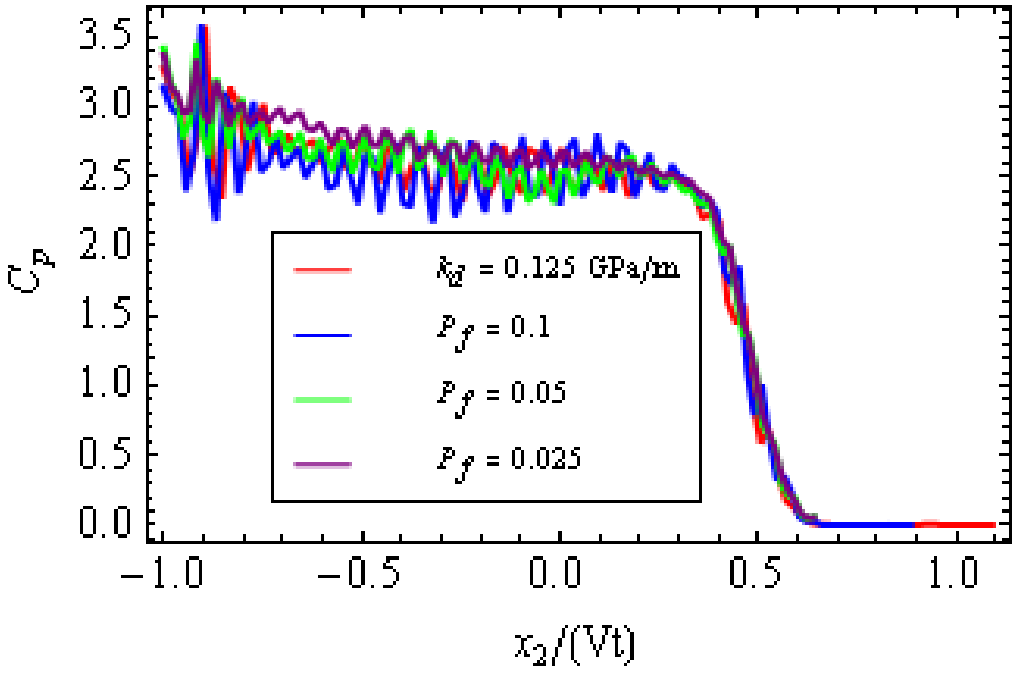

(d) Deadrise angle = 81^0

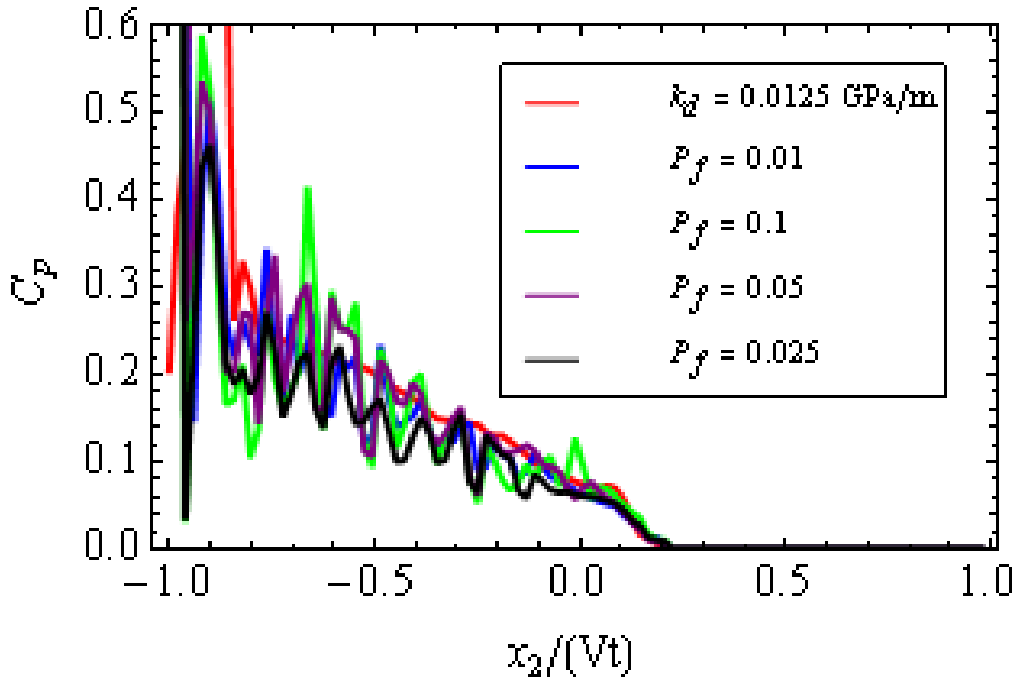

Figure 74. Variation of the pressure coefficient along the span of the wedge for different values of the variable P_f.

(a) Deadrise angle = 10^0

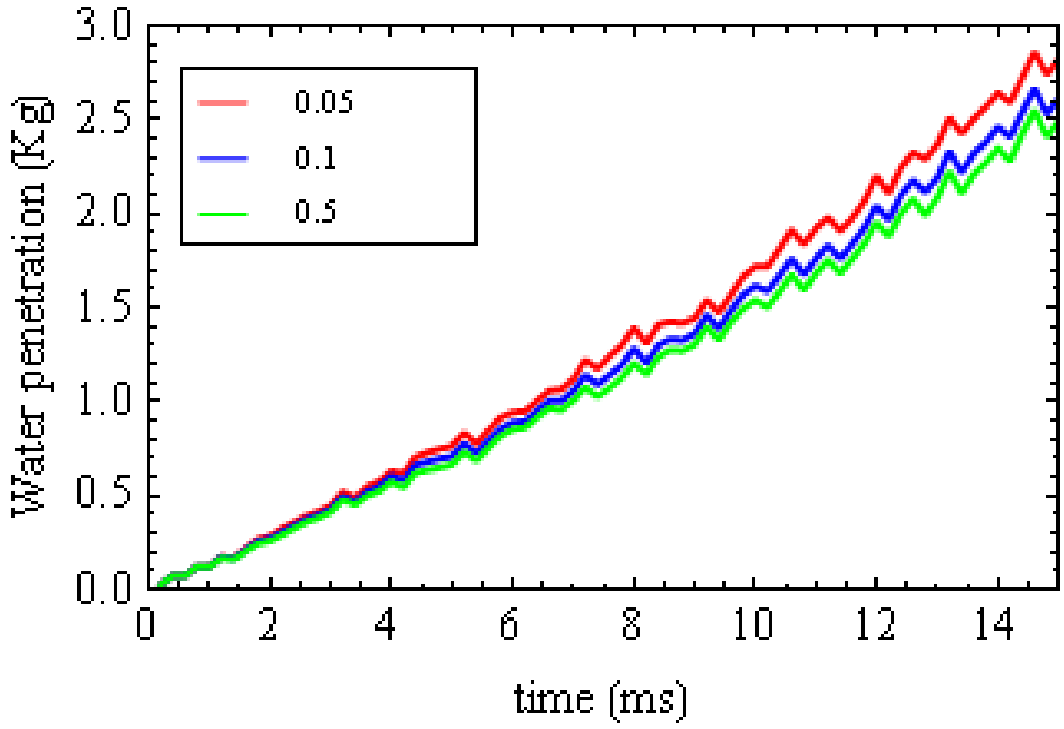

(b) Deadrise angle = 30^0

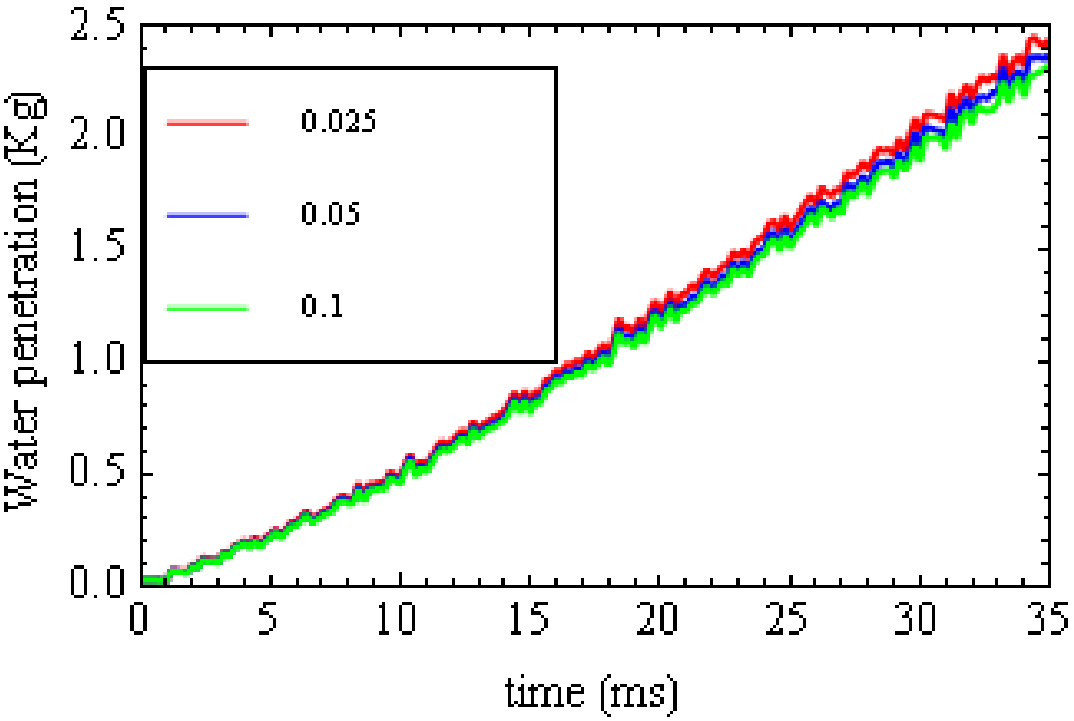

(c) Deadrise angle = 45^0

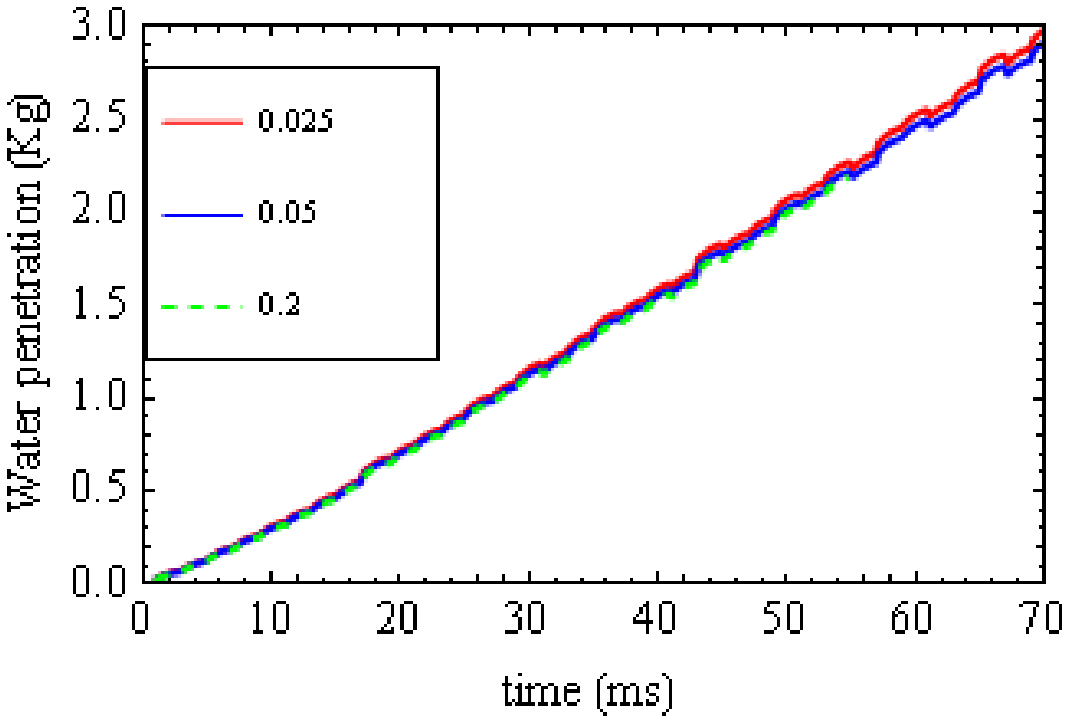

(d) Deadrise angle = 81^0

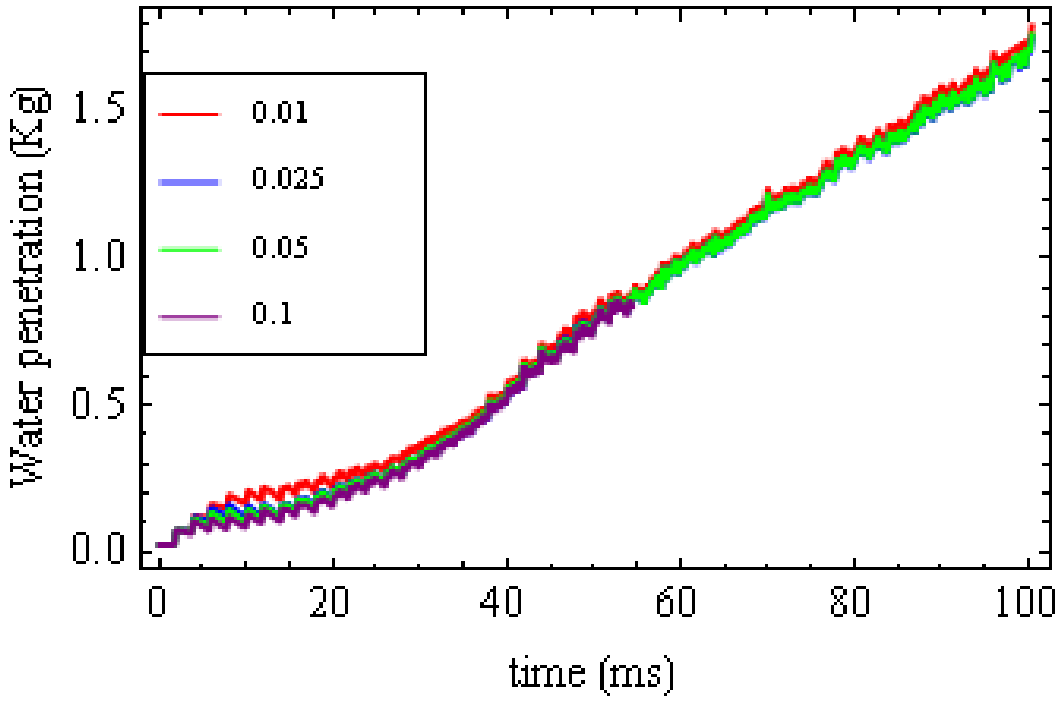

Figure 75. Time history of the amount of water penetration through the water-rigid wedge interface for different values of the variable P_f.

Using the optimal values of k_d and P_f, we compare in figure 76 presently computed values of the pressure coefficient with those reported by Mei et al. [59]. We note that the solution obtained using LS-DYNA incorporates effects of the jet-flow. The maximum percentage difference between the pressure coefficient computed with LS-DYNA and that reported by Mei et al. [59] with consideration of the jet flow is listed in table 11. For the deadrise angle of 81^0 the pressure coefficient near the keel computed with LS-DYNA does not compare well with that reported by Mei et al. [59] with the consideration of jet flow. For 81^0 deadrise angle, the apex of the wedge penetrating water is very sharp, a finer mesh is needed to accurately compute the variation of the pressure coefficient near the keel, which is the apex of the wedge. Due to limited computational resources, computations with a finer mesh were not performed. We note that in practice, hulls have relatively small deadrise angles. In figure 77 we have compared shapes of the deformed water regions computed using LS-DYNA with those from Mei et al. [59] without the consideration of the jet flow since they did not report water levels computed with the consideration of the jet flow. For deadrise angles of 30^0 and 45^0, a significant jet flow is found in our numerical simulations. Except for the jet flow region, the water splash-up in the present numerical solution compares well with that reported by Mei et al. [59]. Our assumption that cavitation occurs when the tensile pressure at a fluid particle exceeds 10 GPa [2] results in the formation of water bubbles at the tip of the jet flow depicted in figure 77. The formation of water bubbles is affected by the limiting value of the tensile pressure; however, we did not compute results with other values of the limiting tensile pressure. Except for the bubbles formed, the consideration of the jet flow does not affect much the shape of the free surface of the deformed water region.

(a) Deadrise angle = 10^0

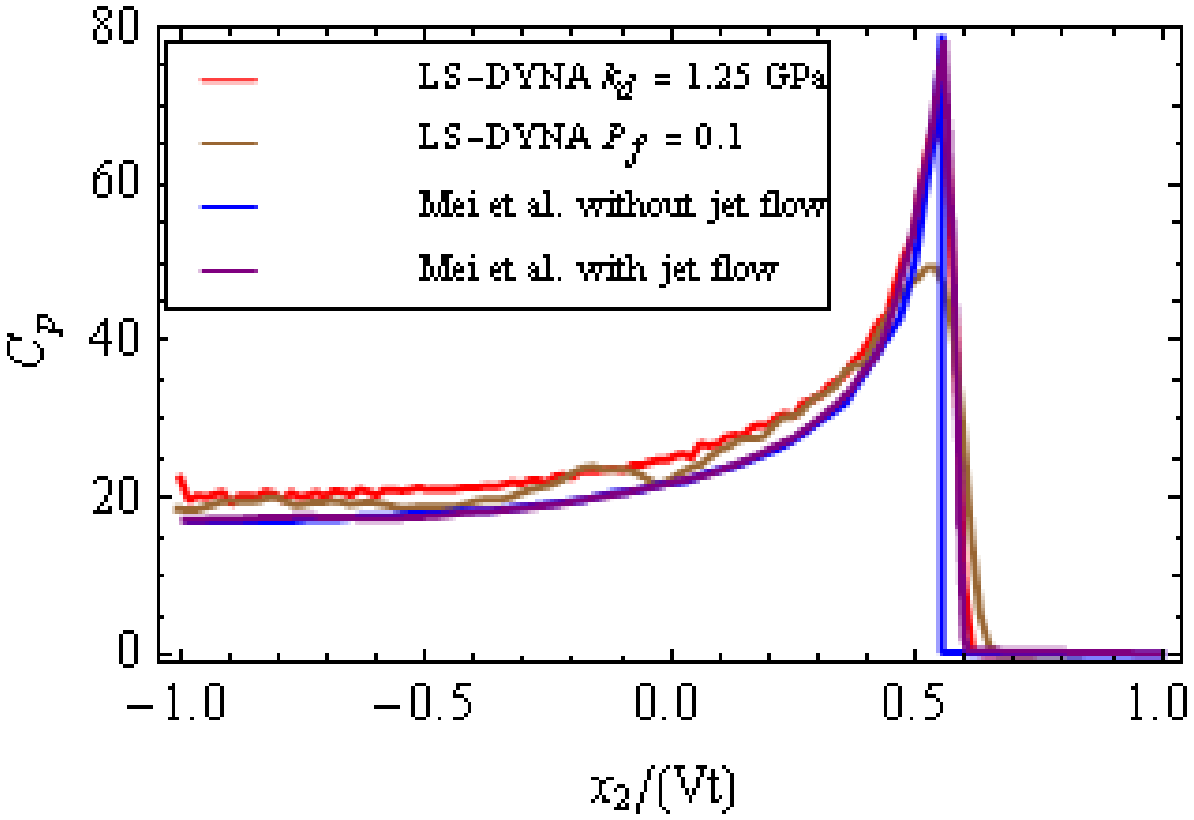

(b) Deadrise angle = 30^0

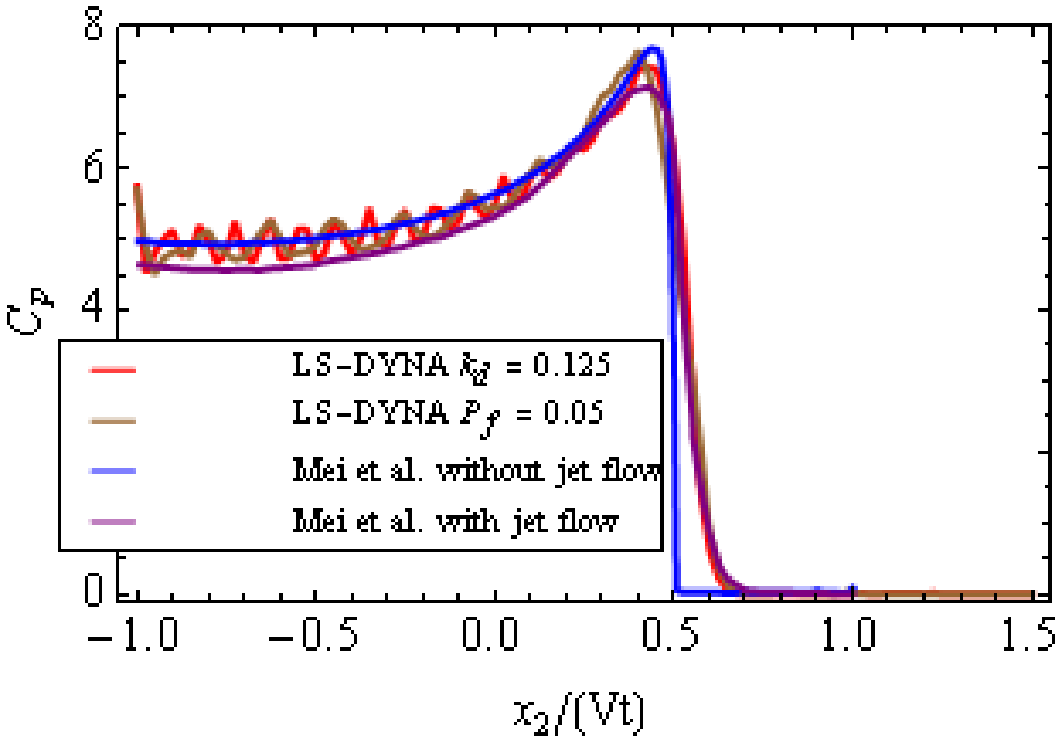

(c) Deadrise angle = 45^0

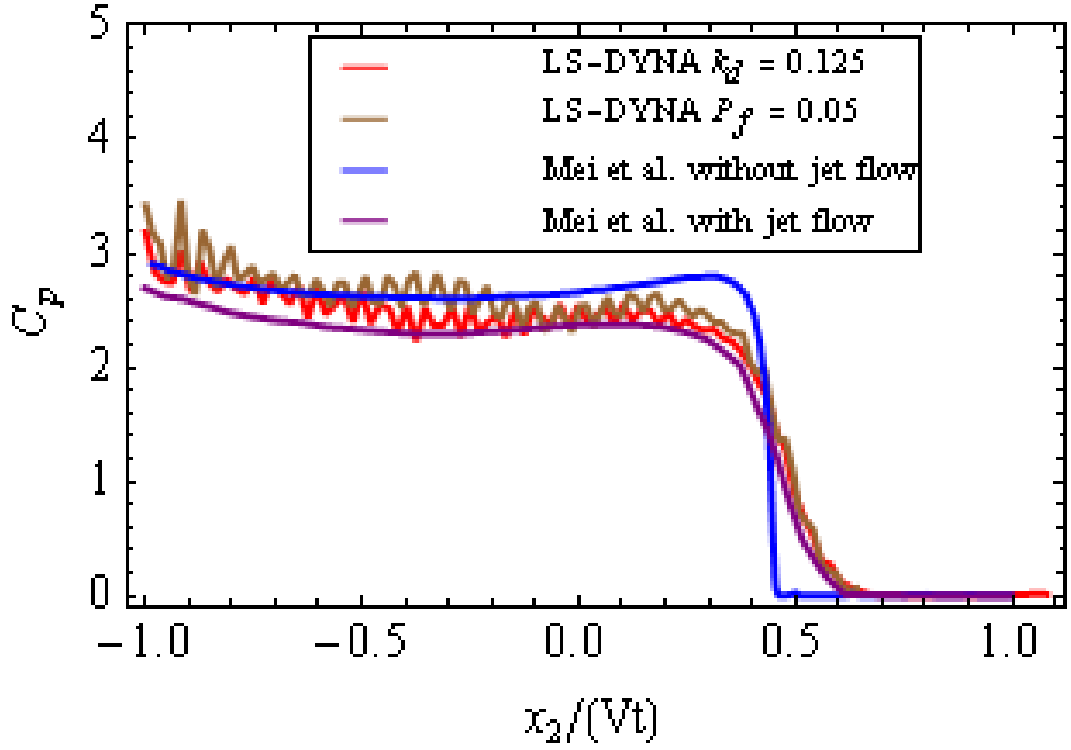

(d) Deadrise angle = 81^0

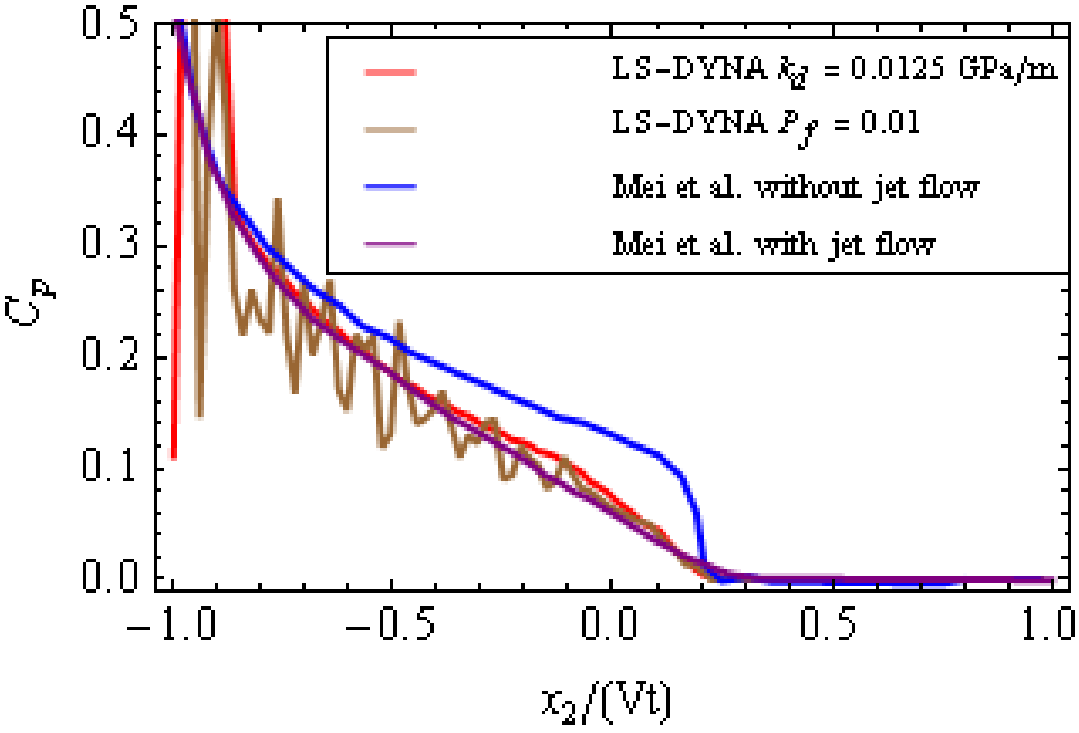

Figure 76. Variation of the pressure coefficient along the span of the wedge.

Table 11: Maximum difference in values of the pressure coefficient obtained from the present solution and that reported by Mei et al. [59] with the consideration of the jet flow.

	$\beta = 10^0$	$\beta = 30^0$	$\beta = 45^0$	$\beta = 81^0$
Specified k_d	20%	9%	9%	~30% (for $x_2/Vt > 0.2$)
Specified P_f	15% (for $0<x_2/Vt<0.4$) 45% (for $x_2/Vt>0.4$)	15%	16%	~10% (for $x_2/Vt > 0.2$)

In results presented and discussed above, the interface pressure or the slamming pressure on the hull was calculated from forces in contact springs (see Appendix A) on the fluid-structure interface used to enforce the continuity of the normal component of velocity. Alternatively, we can find this from values of the pressure at centroids of elements in the fluid region. Figure 78 (a) shows the position of the hull and the deformed water region at t = 10.0 ms, and in figure 78 (b) we compare the pressure coefficient computed from the two approaches. Pressures at centroids of FEs marked with dark green color in figure 78(a) are plotted in figure 78(b) which also shows the interface pressures computed from forces in springs used in the contact algorithm. These two sets of results agree well with each other except at points near the extremities of the wetted region. Near the boundary of the wetted region, the pressure found from forces in springs used in the contact algorithm is close (at least qualitatively) to that reported by Mei et al. However, the pressure on the interface determined from pressures at centroids of fluid elements is noticeably less than that from forces in the springs. A better estimate of the shape of the jet flow region and hence of the pressure distribution there requires using a very fine FE mesh in that region which has not been done here. For subsequent analyses, the interface pressure is computed from forces in springs used in the contact algorithm since they are readily available.

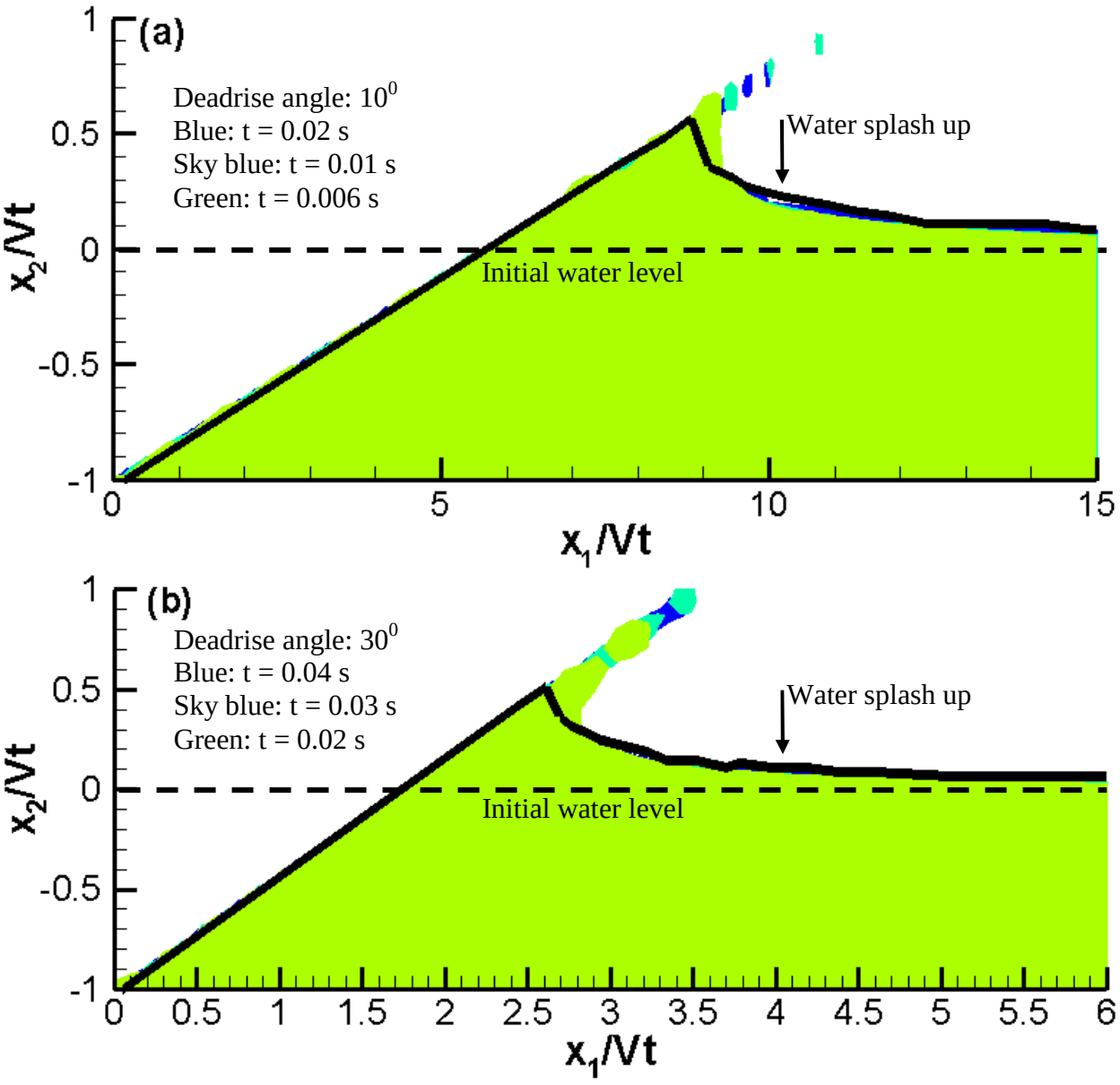
(a)
Deadrise angle: 10^0
Blue: t = 0.02 s
Sky blue: t = 0.01 s
Green: t = 0.006 s
Water splash up
Initial water level
x2/Vt
x1/Vt
1
0.5
0
-0.5
-1
0
5
10
15
(b)
Deadrise angle: 30^0
Blue: t = 0.04 s
Sky blue: t = 0.03 s
Green: t = 0.02 s
Water splash up
Initial water level
x2/Vt
x1/Vt
1
0.5
0
-0.5
-1
0
0.5
1
1.5
2
2.5
3
3.5
4
4.5
5
5.5
6

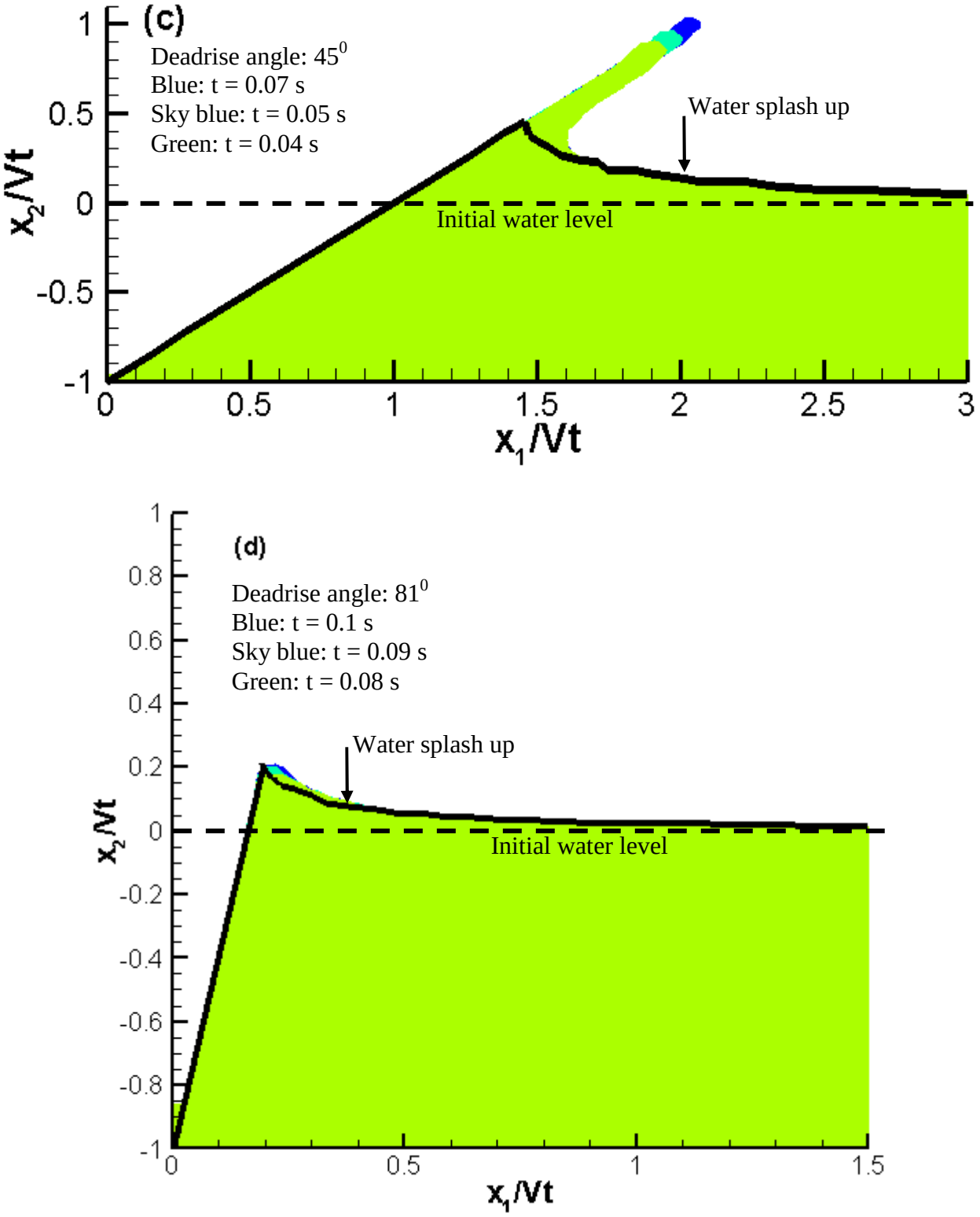

Figure 77. Deformed shapes of the water region during the water entry of rigid wedges; black lines are water surfaces from Mei et al.'s solution without considering the jet flow [59].

(a) Position of the rigid wedge (β = 10^0, downward velocity = 10 m/s) and of the deformed water body at t = 10 ms. The entire length of the hull is not shown.

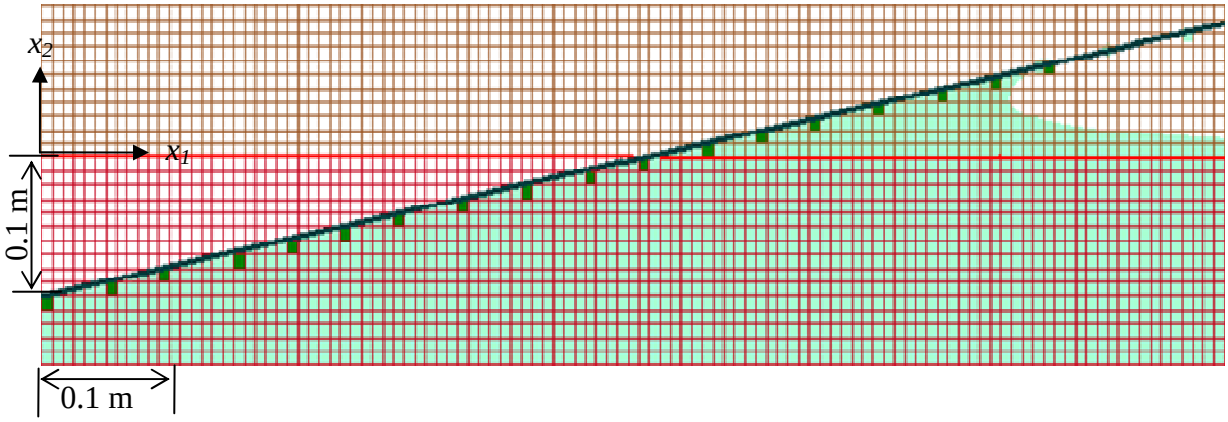

(b) Comparison of the slamming pressure coefficient computed from forces in springs used in the contact algorithm and that at centroids of fluid elements adjoining the hull-water interface.

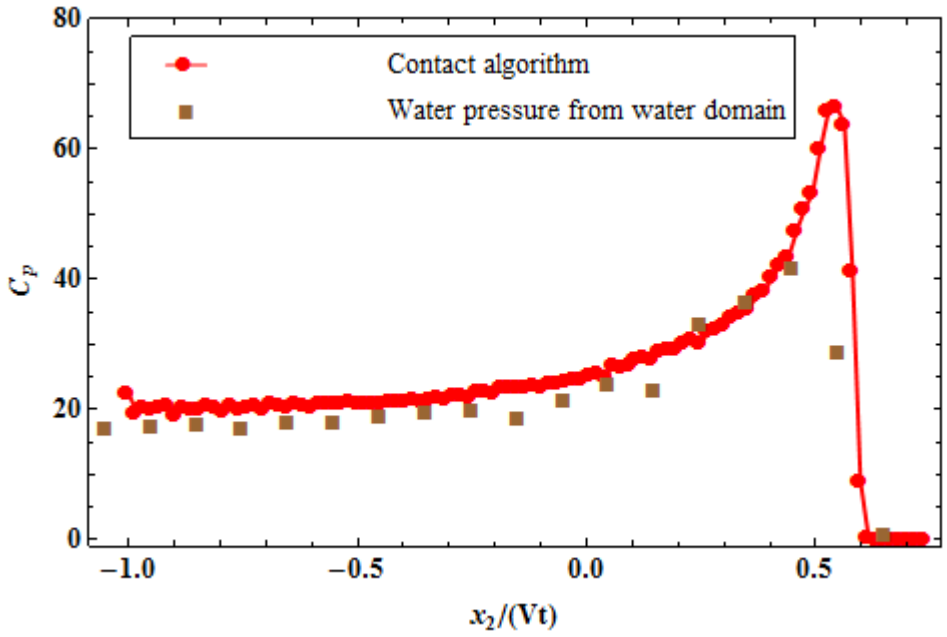

Figure 78. (a) Position of the hull and the water, (b) Comparison of the pressure coefficients computed using two different techniques.

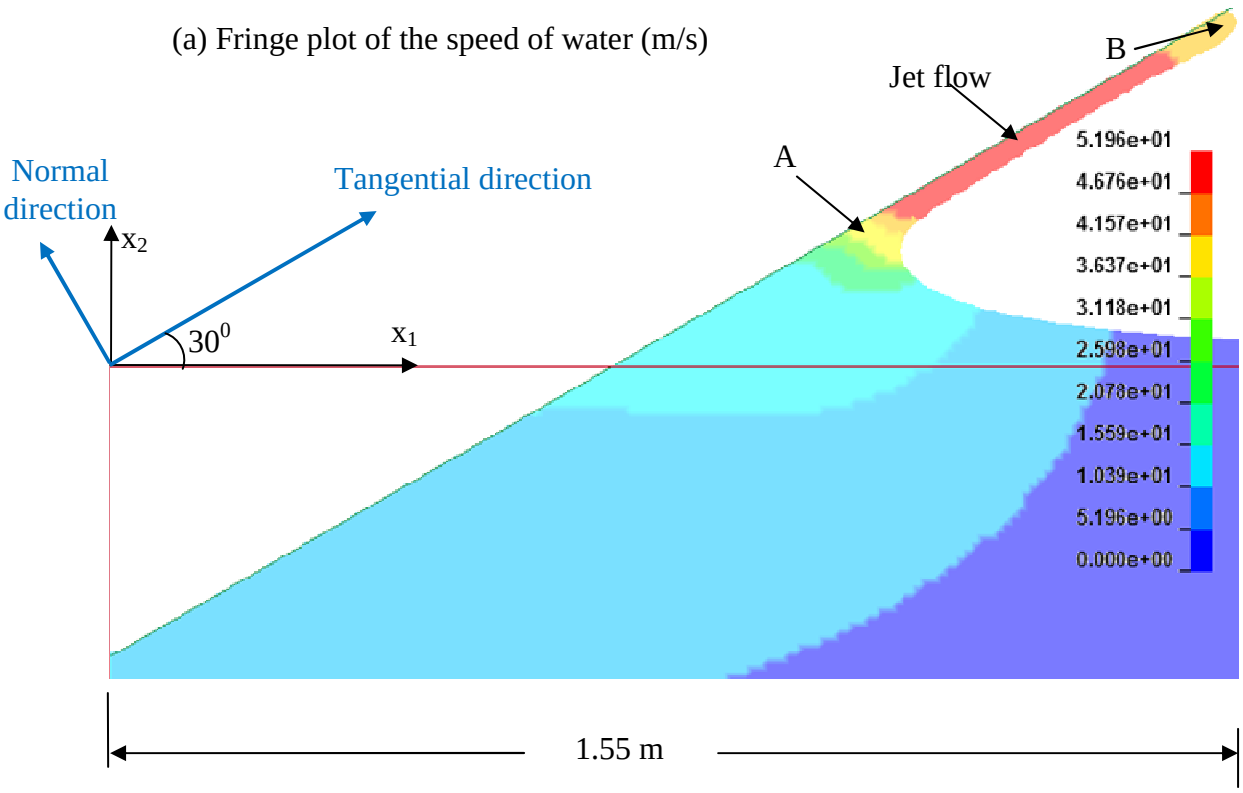
(a) Fringe plot of the speed of water (m/s)
B
Jet flow
A
Normal direction
Tangential direction
x_2
30^0
x_1
5.196e+01
4.676e+01
4.157e+01
3.637e+01
3.118e+01
2.598e+01
2.078e+01
1.559e+01
1.039e+01
5.196e+00
0.000e+00
1.55 m

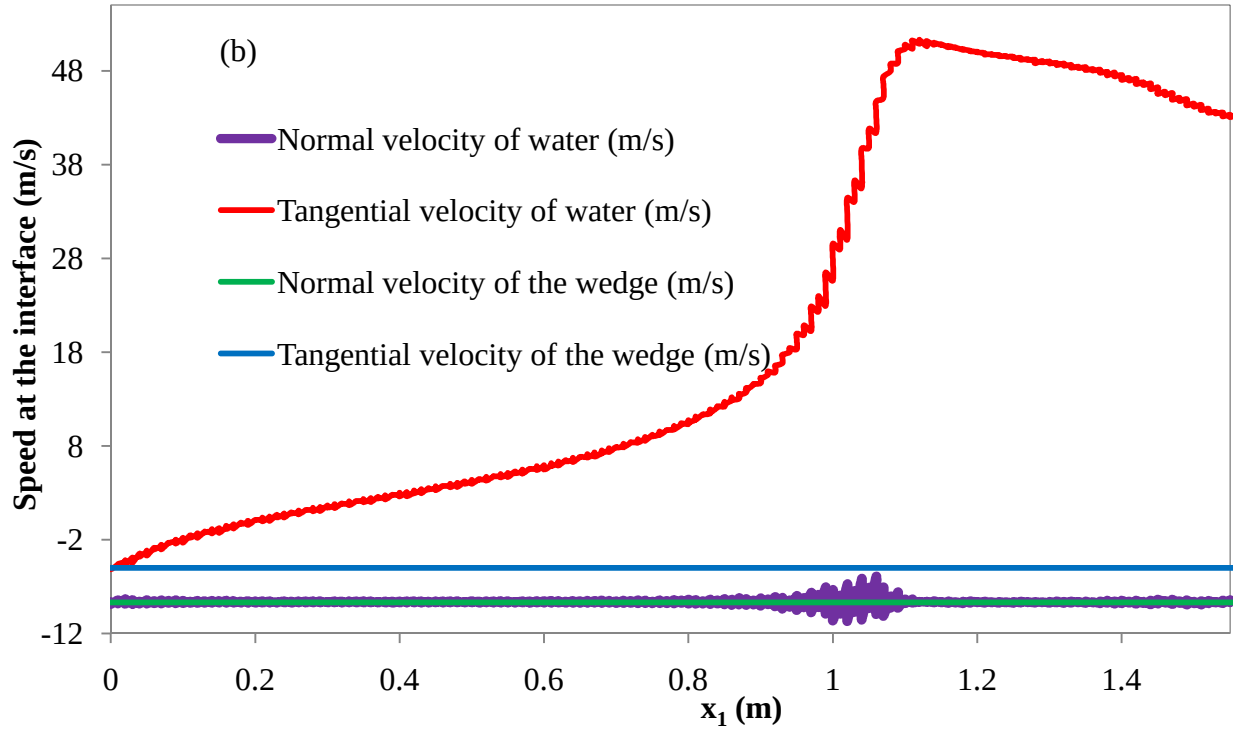
(b)
Normal velocity of water (m/s)
Tangential velocity of water (m/s)
Normal velocity of the wedge (m/s)
Tangential velocity of the wedge (m/s)
Speed at the interface (m/s)
48
38
28
18
8
-2
-12
0
0.2
0.4
0.6
0.8
1
1.2
1.4
x_1 (m)

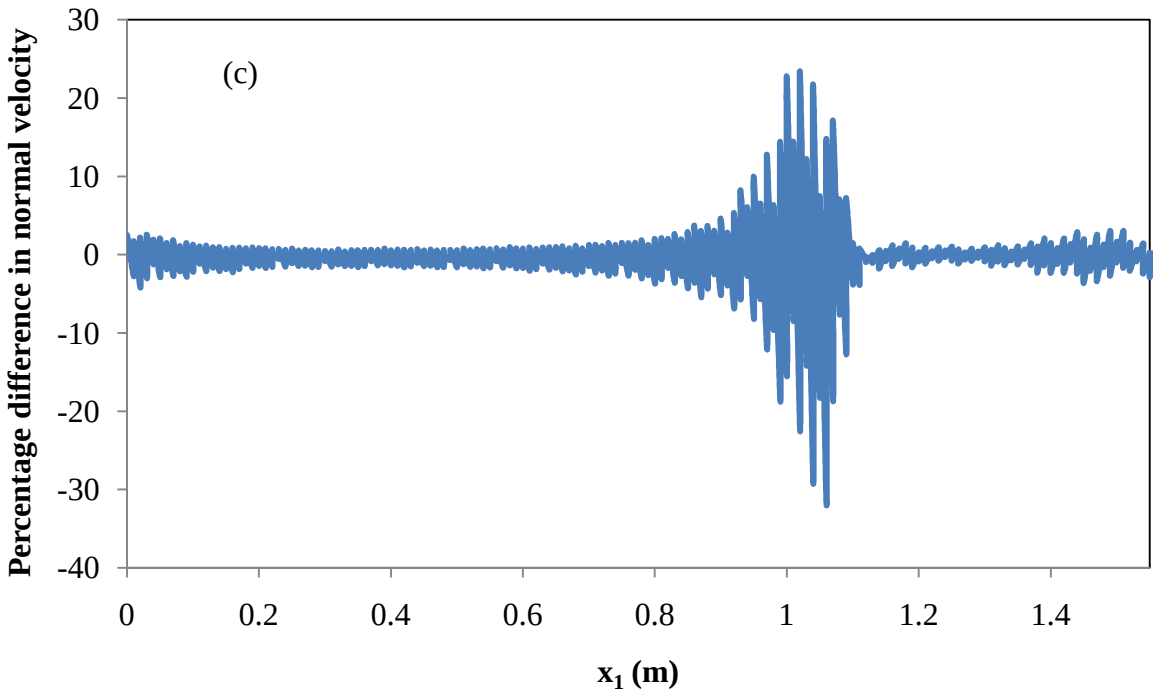

Figure 79. At t = 4 ms, (a) rigid wedge and deformed water region, (b) variation of the velocity of the wedge and the water particle at the wedge-water interface versus the x_1-coordinate of the water particle, (c) percentage difference in the normal velocities of the wedge and the water particle at the wedge-water interface versus the x_1-coordinate of the water particle.

Figure 79(a) shows at 4 ms the position of the rigid wedge of deadrise angle 30^0 moving vertically downwards at a velocity of 10 m/s, the deformed water region, and fringe plots of the speed of water particles. The normal and the tangential velocities of a point on the wedge are -10 $\cos(30^0)$ = -8.66 m/s and -10 $\sin(30^0)$ = -5.0 m/s, respectively. Figure 79(b) exhibits variations of the normal and the tangential velocities of water particles at the wedge-water interface, and also of a point on the wedge. Water is assumed inviscid, therefore only the normal component of velocity should be continuous at the wedge-water interface which is confirmed by results plotted in figure 79(b) and (c) except at points in the region A of the jet flow. Figure 79(c) shows that the percentage difference between the normal velocities of the wedge point and the corresponding water particle touching it is about 3% except in region A of the jet flow. The tangential velocity of water particles on the wedge-water interface is considerably higher than that of the corresponding wedge particles indicating slipping there. Also, there are noticeable oscillations in the normal velocity of fluid particles in region A of the jet flow. The tangential velocity of the water at the interface increases from zero at the keel to about 8 m/s in the region A of the jet flow. Within a small portion of the span of the wedge (~ 0.2 m) in region A of the jet flow, the tangential velocity of the water increases from 8 m/s to 50 m/s before decreasing to ~ 42 m/s in region B of the jet flow.

2.3.3. Water slamming of rigid wedges freely falling in water due to gravity

We study the local slamming of a rigid wedge impacting at normal incidence the initially calm water and consider effects of gravitational forces acting on the hull and the water; thus the downward velocity of the wedge need not stay constant in time. This problem has been studied both analytically and experimentally in [103] using two different wedges each 1.2 m long and 1.2 m wide. Here we assume that deformations of the fluid and the wedge are plane strain in the x_1x_2-plane. Referring to figure 59, we set L_1= 2 m, L_2=1 m, L_3=1 m, L_4= 5 m and L_5=2 m; these dimensions are the same as those in the experimental set up of [103]. We analyze the problem using two FE meshes; for the first mesh, regions L_1 x L_2 and L_4 x L_5 are discretized, respectively, with 100 x 50 x 1 and 110 x 100 x 1 8-node brick elements (see figure 59), and the rigid wedge, modeled as a shell, by 60 x 1 elements. The second FE mesh is constructed by dividing each brick (shell) element of the first mesh into four (two) equal elements and the two meshes have only one element along the x_3-direction. Two different values of the contact parameters are used

to ascertain their influence on the solution of the problem. It has been found that results computed using FE meshes 1 and 2 with either P_f = 0.025 or k_d = 0.01 GPa/m are virtually the same. The FE mesh 2 with P_f = 0.025 and c = 1 is used to compute results reported in figures 80, 81 and 82, and results shown in figures 83 and 84 are computed using the FE mesh 2 with k_d = 0.01 GPa/m and c = 1. At t = 0 the downward velocity of the wedge equals 5.05 m/s and the apex of the wedge just touches the calm water surface.

For the wedge of mass 94 Kg and deadrise angle 25^0, we have plotted in figure 80 the computed time histories of the downward velocity v_2 of the wedge and that found experimentally in [103]. It is clear that the velocity computed with LS-DYNA matches well with the experimental one. Results plotted in figure 81 show that the percentage difference, $100(v^{sim}_2 - v^{exp}_2) / v^{exp}_2$, between the velocity v^{sim}_2 from the simulation and that from the experiment v^{exp}_2 is less than 4%. Figure 82 shows the time history of the total upward force exerted by the water on the rigid wedge which is not reported by [103].

In order to demonstrate that results reported in figures 81 and 82 are also valid for other wedges, we analyzed the problem for another rigid wedge that was also studied analytically in [103]. Figure 83 shows the time history of the total upward force F_{up} exerted by the water on a rigid wedge of mass 153 Kg and deadrise angle 30^0 obtained analytically in [103] and that computed with LS-DYNA. From results plotted in figure 84 we conclude that the maximum percentage difference $100\ (F^{sim}_{up} - F^{ana}_{up}) / F^{ana}_{up}$ in the force from the numerical simulations and the analytical solution [103] is ~ 17%. We note that results plotted in figures 81 and 83 are for different wedges, and the computed velocities are compared with the experimental values and the computed force with that derived from the analytical solution; this was necessitated by results given in [103].

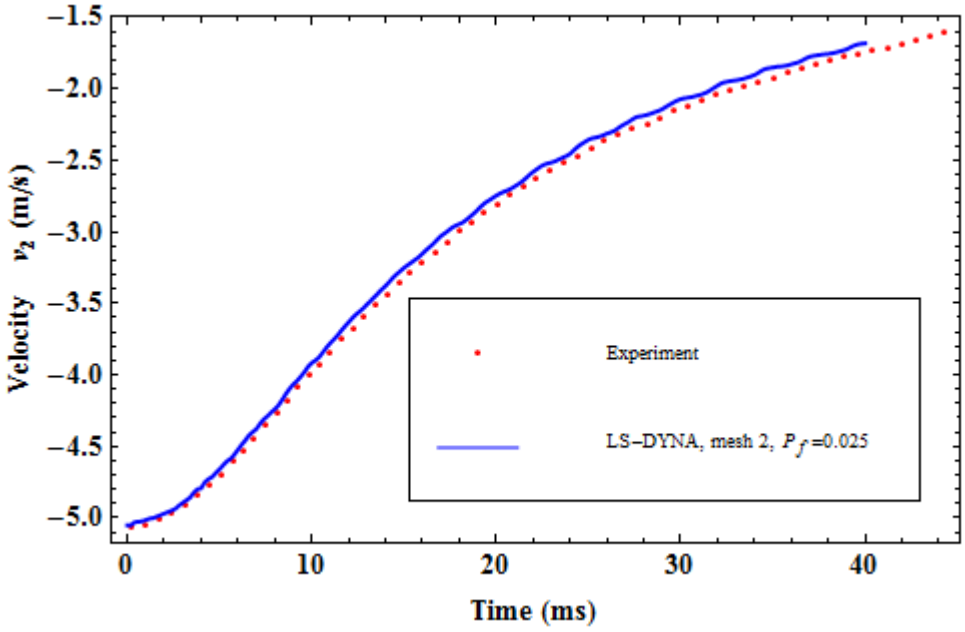

Figure 80. Time history of the downward velocity of the rigid wedge.

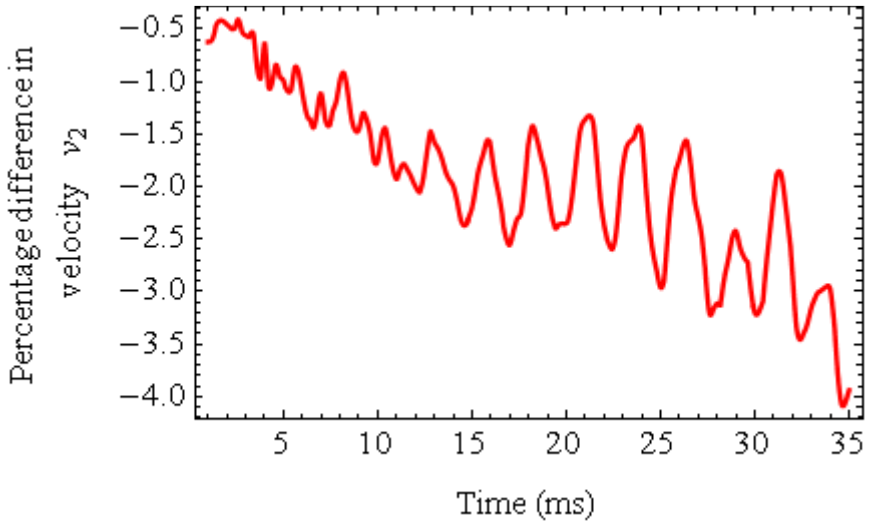

Figure 81. Time history of the percentage difference in the computed and the experimental values of the downward velocity of the rigid wedge.

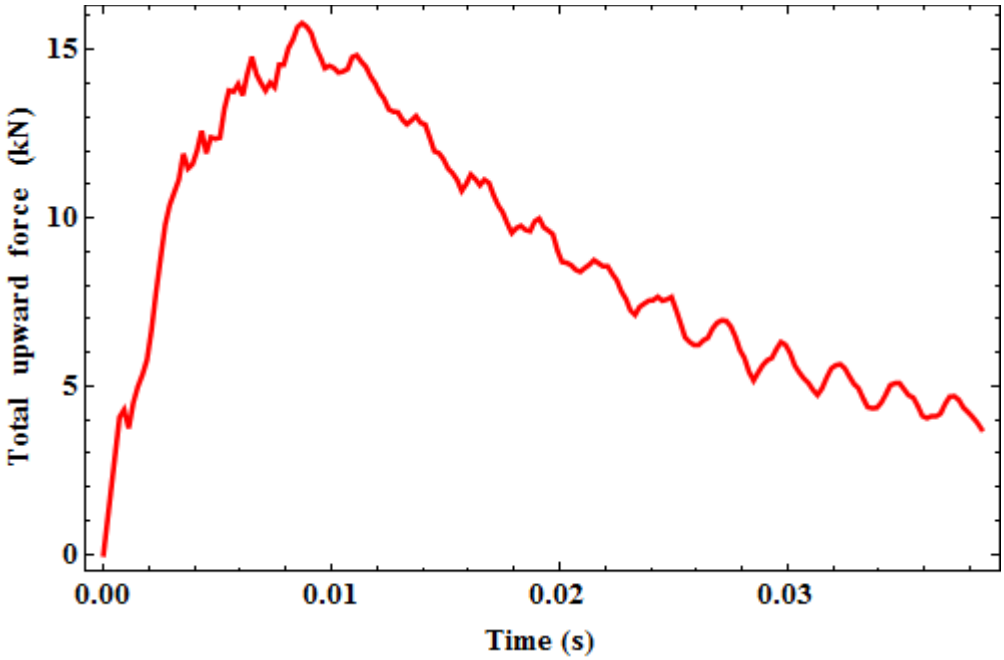

Figure 82. The time history of the total upward force on the rigid wedge.

The results reported in [103] are reproduced here from figures provided in [103]. Explicit expressions for the velocity of the wedge and the pressure on the wedge exerted by water are not provided in [103]; whereas it is possible to reproduce results given in [103] by solving the initial-boundary-value problem following the procedure explained in [103] but it has not been done here.

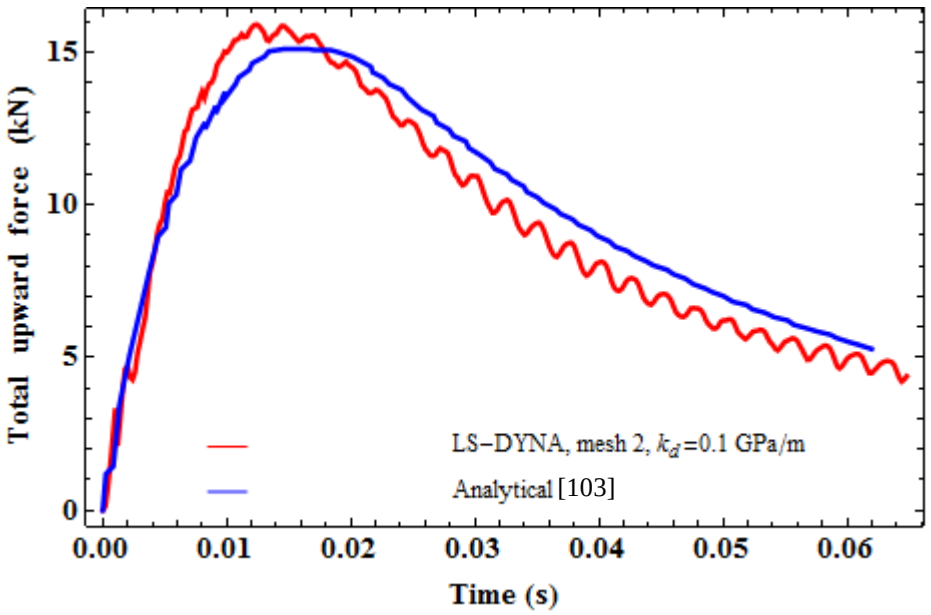

Figure 83. The time history of the total upward force on the rigid wedge.

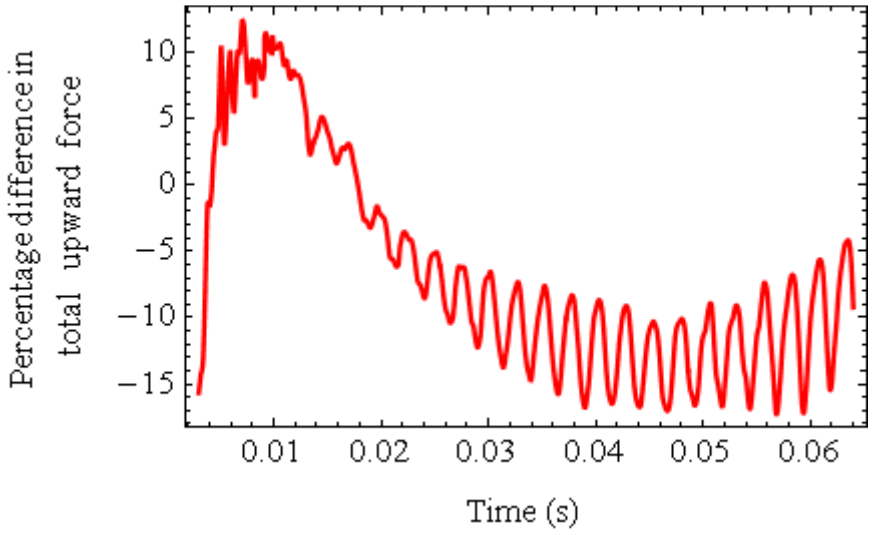

Figure 84. The time history of the percentage difference in the total upward force on the rigid wedge.

Figure 85 shows variations of the analytically [103], experimentally [103], and computationally obtained pressures along the span of the hull at four different times for a wedge of mass 153 Kg and deadrise angle of 30^0 computed using the FE mesh 2, k_d = 0.1 GPa/m and c = 1; values for the analytical solution are taken from results plotted in [103] and not from the analytical solution of the problem provided by the authors. Although the analytical and the presently computed values of the total force reported in figure 83 compared well with each other, the pressure variations are not close to each other. If we find areas under curves shown in figure 85 and multiply them with the width 1.2 m of the hull and $cos(30^0)$ we should get the total force reported in figure 83. The total force at 14.7 ms, 23.7 ms, 35.5 ms, and 48.5 ms computed by integrating numerical results of figure 85 (solid red, blue, green and purple curves) differ by 1.8%, 2.7%, 3.2% and 3.4% , respectively, from the values reported in figure 83. However, the total forces computed by integrating results represented by dotted red, blue, green and purple curves in figure 85 differ from the analytical total force reported in figure 83 (purple curve) by 25.5%, 33.1%, 43.1% and 53.3% , respectively, for 14.7 ms, 23.7 ms, 35.5 ms, and 48.5 ms. Thus the total upward force reported in [103] differs significantly from that obtained by integrating over the wedge span the pressure profile reported in [103]. The presently computed pressures differ from the experimental ones indicated in figure 85 by solid circles.

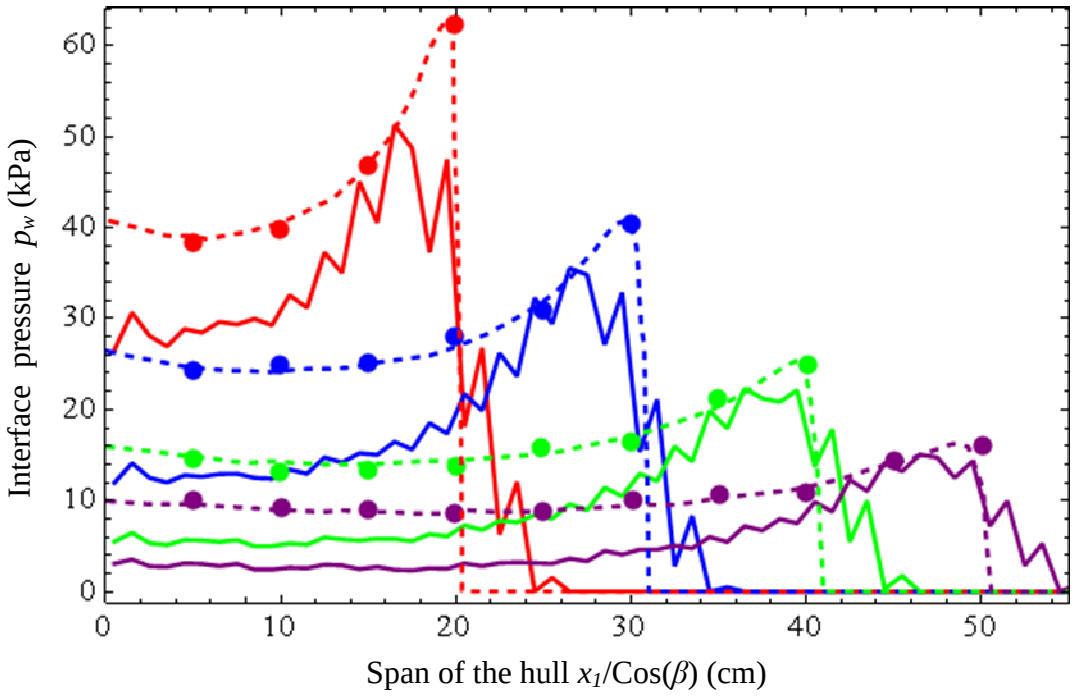

Figure 85. Variations of the pressure along the span of the hull at four different times. Values of time for different curves are: red, 14.7 ms; blue, 23.7 ms; green, 35.5 ms; and purple, 48.5 ms. Solid lines are from LS-DYNA simulations; dashed lines are taken from plots of the analytical results reported in [103]; solid circles are experimental results from [103].

2.3.4. Water slamming of deformable hulls

We now study plane strain deformations in the x_1x_2-plane of 1 m long, 30 mm thick core sandwich composite plate with 12 mm thick face sheets and clamped at both ends. The dimensions of the fluid and the vacuum domains are L_1 = 1.5 m, L_2 = 1 m, L_3 = 0.5 m, L_4 = 2.5 m, and L_5 = 2m. The material of the face sheets is transversely isotropic with the axis of transverse isotropy along the length ($\overline{x_1}$ – axis, cf. figure 59(b)) of the hull, Young's modulus along the length E_1 = 138 GPa, Young's modulus along the thickness E_2 = 8.66 GPa, Poisson's ratio v_{12} = 0.3, and the shear modulus G_{12} = 7.1 GPa. The core material is isotropic with Young's modulus E = 2.8 GPa and Poisson's ratio υ = 0.3. For results reported in this subsection, unless stated otherwise, the deadrise angle and the downward velocity of the plate equal 5^0 and 10 m/s, respectively. Mass densities of the core and the face sheets are 150 kg/m^3 and 31400 kg/m^3,

respectively; the mass density of the face sheets includes the non-structural dead weight. The problem studied is the same as that analyzed by Qin and Batra [76] and presently computed results are compared with those reported in [76] using the {3,2}-order plate and the modified Wagner theories for finding the hydrodynamic pressure acting on the hull.

To analyze the structural response of the hull using LS-DYNA, we first study free and forced vibrations of the plate, and compare frequencies and mode shapes with those reported by Qin and Batra [76]. The core is modeled with 8-node brick elements, and the face sheets with 4-node Belytschko-Tsay [2] shell elements. The fixed-fixed sandwich hull is deformed by suddenly applying a uniform pressure on its top surface, and a fast Fourier transform is carried out of the time history of the downward displacement of the hull centroid. Natural frequencies so found and those reported [76] are summarized in table 12; the corresponding mode shapes are depicted in figure 86. Presently computed frequencies of the first three modes differ from those reported by Qin and Batra [76] by using the {3,2}-order plate theory by13%, 11 % and 19 % , and by 11%, 8%, and 7% from those obtained using the commercial FE code ABAQUS. The effect of the FE mesh on the natural frequencies is also listed in table 12. For analyses reported in this subsection either FE mesh 2 or FE mesh 3 or a finer mesh is used to discretize the hull.

(a) 1st mode shape

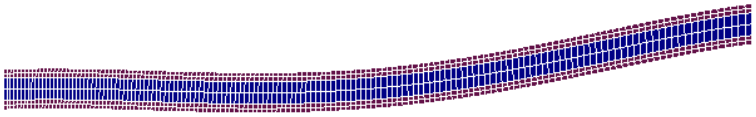

(b) 2nd mode shape

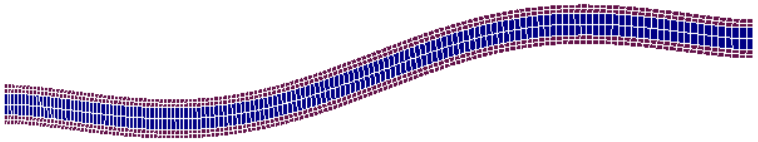

(c) 3rd mode shape

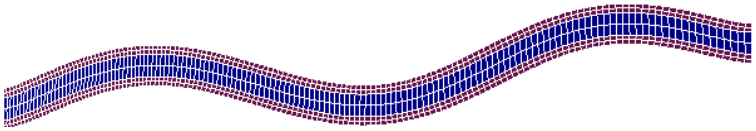

Figure 86. Mode shapes from free vibration analysis using mesh 2.

Table 12: Summary of results of vibration analysis of the sandwich composite hull

	Description of the mesh	1st natural frequency from forced vibration analysis (Hz)	Natural frequencies from free vibration analysis (Hz)		
			1st	2nd	3rd
Mesh 1: Solid elements	30 uniform elements along the length, 6 along the thickness (2 in each face sheet and 2 in the core), 1 element along the x_3-direction	107.5	109.1	238.71	390.36
Mesh 2: Solid elements	100 uniform elements along the length, 6 along the thickness (2 in each face sheet and 2 in the core), 1 element along the x_3-direction	LS-DYNA 94.5	99.57	223.79	370.48
		ANSYS $\beta=0^0$	109.73	240.62	394.74
		ANSYS $\beta=5^0$	109.55	240.39	394.45
		ANSYS $\beta=10^0$	109.02	239.68	393.57
		ANSYS $\beta=14^0$	108.33	238.75	392.41
Mesh 3: Shell elements	30 uniform elements along the length, 1 element along the x_3-direction. 8 through the thickness uniformly spaced Gauss points (2 in each face sheet, 4 in the core). *	107.7			
Mesh 4: Shell elements	100 uniform elements along the length, 5 elements along the x_3-direction. 16 through the thickness uniformly spaced Gauss points (4 in each face sheet, 8 in the core). *	107.8			
Qin and Batra [76]	$\beta=0^0$		114.4	252.8	417.9
ABAQUS	(reported by Qin and Batra)		112	244	400

* The parameter LAMSHT is set equal to 1 in the LS-DYNA keyword input card CONTROL_SHELL. LAMSHT = 1, and no shear corrections are required when elastic moduli of different layers of a shell are noticeably different from one another [2].

Figure 87 exhibits time histories of the slamming pressure at three different locations on the hull for various values of k_d with c = 0, 100 uniform elements along the length of the hull, 6 along the thickness (2 in each face sheet and 2 in the core), and regions L_1 x L_2 (see figure 59), L_1 x L_3, and L_4 x L_5 of the water, air and water domains, respectively, having 150 x 150, 150 x 65, and 165 x 230 elements, respectively. Henceforth we designate this FE mesh as the coarse mesh. For k_d = 2.5 GPa/m, the maximum amplitude of oscillation in the pressure at x_1 = 0.24 m exceeds 6 MPa, and a significant amount of water penetration through the hull-water interface is found (not shown here). For k_d = 1.25, 62.5 and 312.5 GPa/m, the maximum amplitudes of oscillation during 2 ms < t < 8 ms are, respectively, ~1 MPa, ~2 MPa and ~2.5 MPa. Therefore, for k_d = 1.25 GPa/m, the time histories of the slamming pressure are relatively smoother than those for k_d = 62.5 and 312.5 GPa/m; similar observations can also be made from results reported in figures 87(b) and (c).

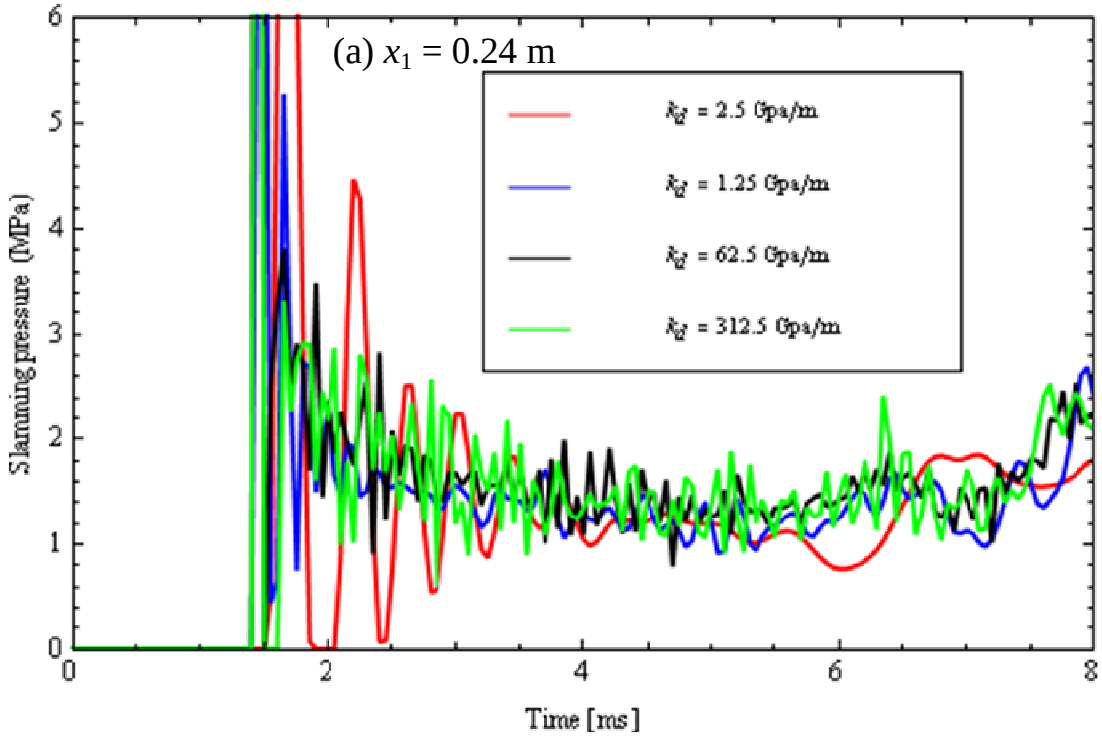
(a) x_1 = 0.24 m
k_d = 2.5 Gpa/m
k_d = 1.25 Gpa/m
k_d = 62.5 Gpa/m
k_d = 312.5 Gpa/m
Slamming pressure (MPa)
Time [ms]
0
1
2
3
4
5
6
0
2
4
6
8

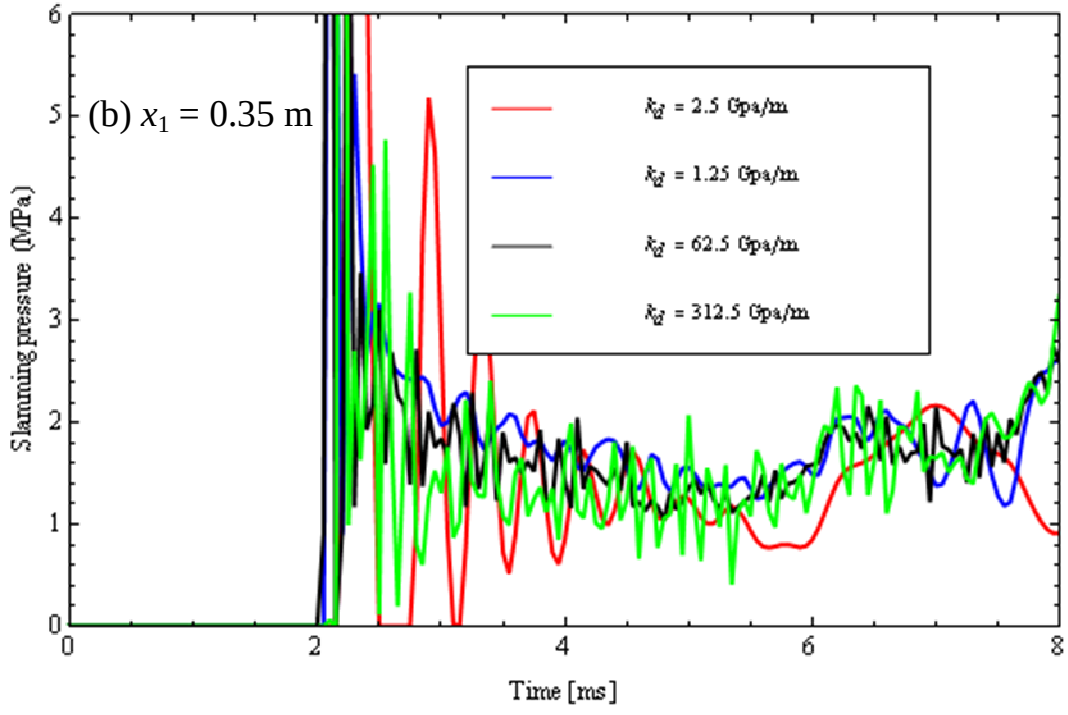
(b) x_1 = 0.35 m
k_d = 2.5 Gpa/m
k_d = 1.25 Gpa/m
k_d = 62.5 Gpa/m
k_d = 312.5 Gpa/m
Slamming pressure (MPa)
Time [ms]
0
1
2
3
4
5
6
0
2
4
6
8

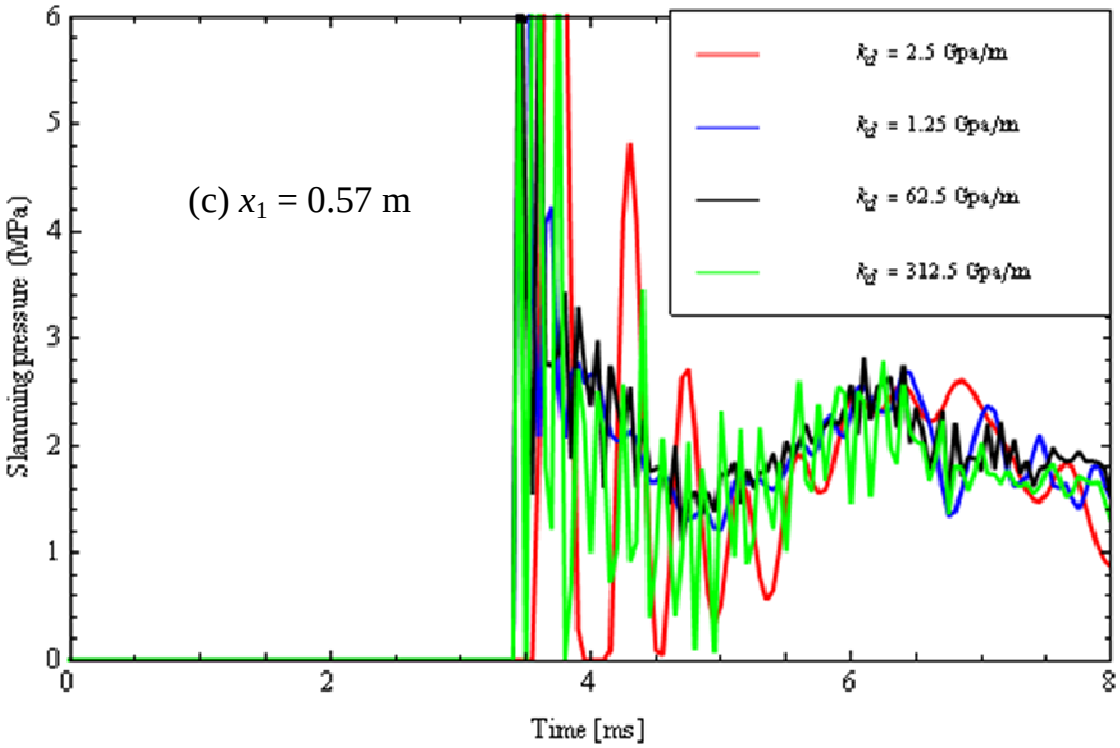

Figure 87. Time histories of the pressure at three locations on the hull-water interface for different values of the contact stiffness k_d.

Figure 88 exhibits deflection of the centroid of the hull for three different deadrise angles computed using LS-DYNA and those reported in [76]. Values assigned to penalty parameters are k_d = 1.25 GPa/m, c = 1, and two different FE meshes, namely the fine mesh and the coarse mesh, are used with the fine mesh constructed by subdividing each brick element of the coarse mesh, which is used to generate results shown in figure 87, into four uniform brick elements, and that of the shell into two equal elements but keeping only one element along the x_3-direction. For deadrise angles of 5^0 and 10^0, deflections computed using LS-DYNA with both FE meshes and those reported by Qin and Batra [76] are close to each other; however, for the deadrise angle of 14^0, the maximum deviation of the deflection found using LS-DYNA and the fine FE mesh from that given in [76] is 50%. Qin and Batra's analysis [76] of the slamming pressure on the hull by using Wagner's theory modified to consider hull's infinitesimal elastic deformations is valid for small deadrise angles. Using the fine FE mesh, and for the hull deadrise angle of 5^0, we have compared in figure 89(a) variation along the span of the hull of the presently computed deflection, $w_0^{LS\text{-}DYNA}(x_1)$, of the centerline of the hull with that, $w_0^{Qin}(x_1)$, found by Qin and Batra [76]. The relative L_2 norm $\left(\int_0^{1m}(w_0^{LS-DYNA}(x_1)-w_0^{Qin}(x_1))^2\right)^{0.5}\Big/\left(\int_0^{1m}(w_0^{Qin}(x_1))^2\right)^{0.5}$ of the difference between these two sets of results equals 0.26, 0.19, 0.17, 0.15, and 0.11 for t = 2.735, 3.247, 4.026, 5.471, and 6.018 ms, respectively. We note that the L_2 norm does not compare local deflections which may differ noticeably over a small length even though the value of the L_2 norm is small. The local deadrise angle of the hull at different times depicted in figure 89(b) varies between 2.6^0 and 6.8^0; it is computed by numerically differentiating the deflected shape of the hull shown in figure 89(a) and adding to the local slope the initial deadrise angle of 5^0.

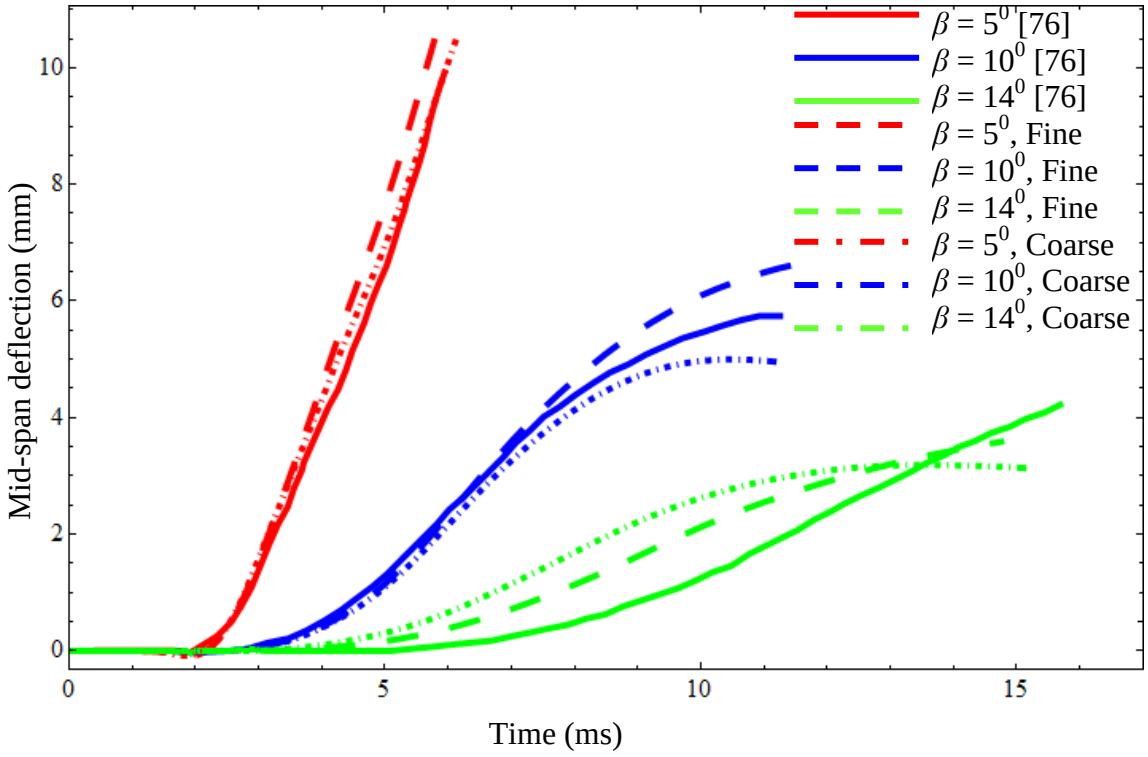

Figure 88. Time histories of the downward deflection of the centroid of the hull for three different deadrise angles; fine and coarse in the inset correspond to results computed from the fine and the coarse FE meshes.

(a) Deflection of the centerline of the hull

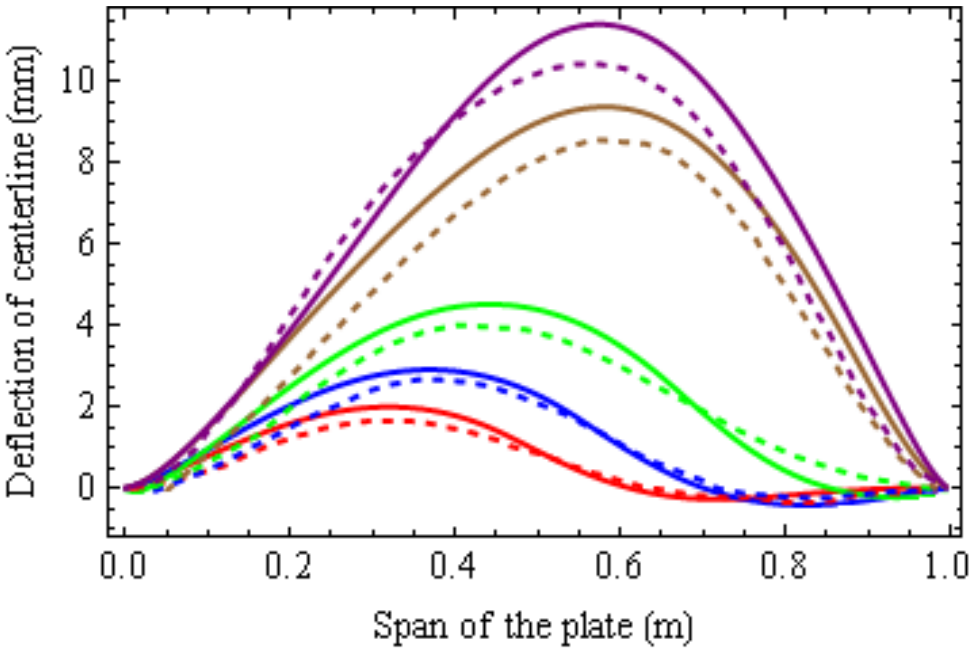

(b) Local deadrise angle along the centerline

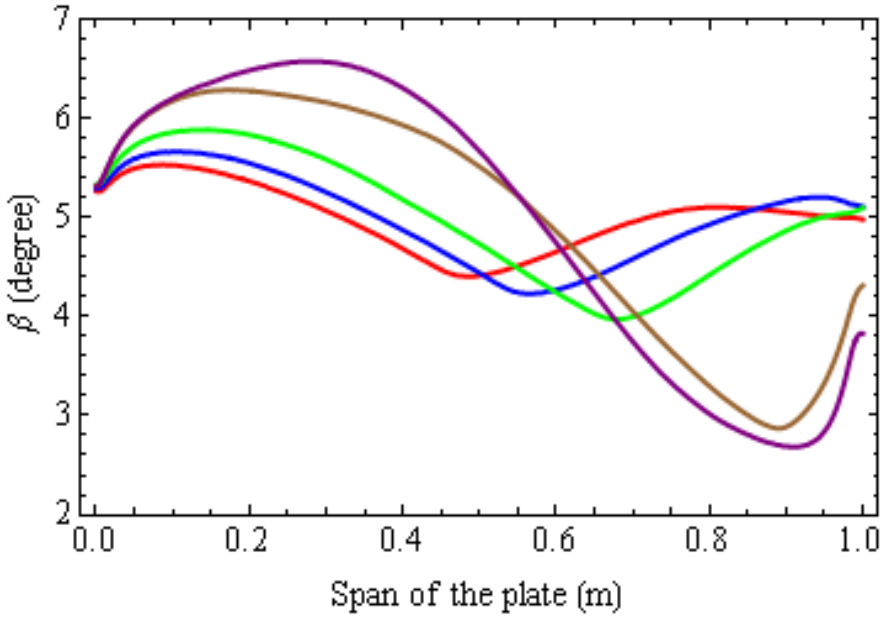

Figure 89. (a) Deflections of the centerline of the hull; red: t = 2.735 ms, blue: t = 3.247 ms, green: t = 4.026 ms, brown: t = 5.471 ms, purple: t = 6.018 ms; dashed line: results from Qin and Batra [76], solid line: present solution using LS-DYNA. (b) Local slopes (deadrise angle) of the centerline of the hull for an initial deadrise angle of 5^0.

In figures 90 and 91 we have compared the presently computed time histories of the slamming pressure at three different locations on the span of the sandwich hull by taking k_d = 1.25 GPa/m and either c = 0 (figure 90) or c = 1 (figure 91) with those reported in [76]. As expected, the non-zero value of c suppresses oscillations in the time history of the slamming pressure; however, it also reduces the peak pressure at a point from ~ 10 MPa to ~ 6 MPa which is undesirable. Whereas the present solution gives finite values of the hydrodynamic pressure, Qin and Batra's solution, because of the singularity in the expression for the pressure, provides an unrealistically high value of the pressure when water just reaches the point under consideration. Except for these large initial differences, the two sets of pressures are close to each other.

Results reported in figures 92 to 97 are computed using k_d = 1.25 GPa/m and c = 1. The water level reaches locations x_1 = 0.24, 0.35 and 0.57 m, respectively, at 1.4, 2 and 3.2 ms; the decay with time of the slamming pressures at x_1 = 0.24, 0.35 and 0.57 m compare well with those reported by Qin and Batra [76]. At different times, the distributions of the pressure on the hull wetted surface from the two approaches plotted in figure 92 reveal that the two sets of results agree only till t = 3.2 ms; at subsequent times the two approaches give significantly different pressure distributions on the wetted surface. These differences could partly be due to the waves reflected from the boundaries in the present analysis but not in Qin and Batra's approach. Recall that the two approaches give reasonably close deformed shapes of the hull centerline.

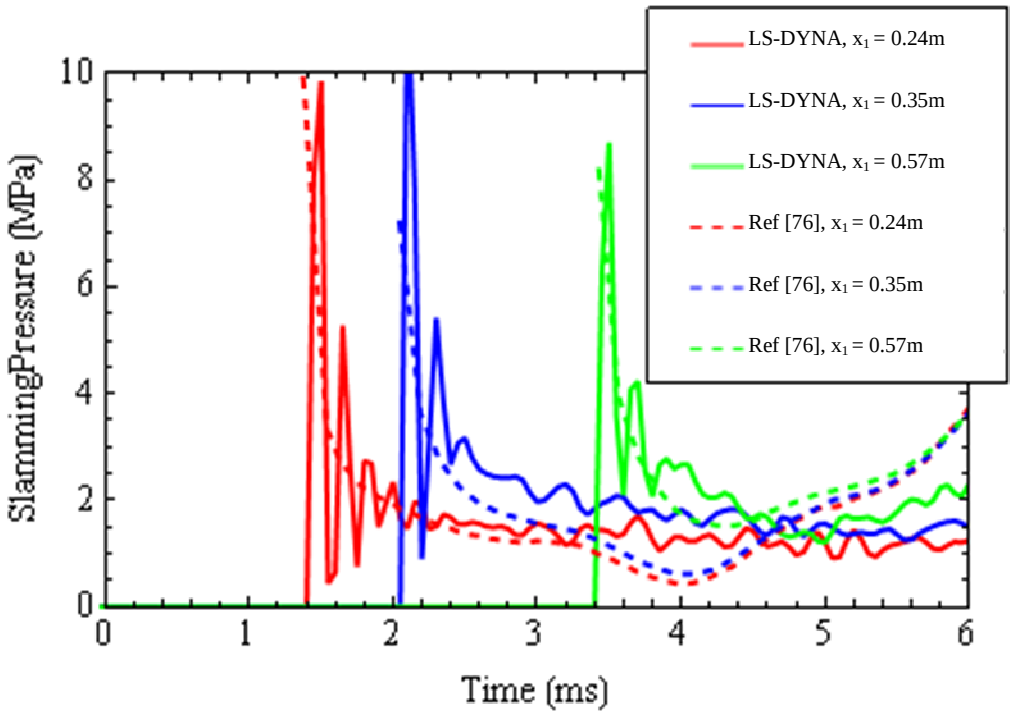

Figure 90. Time histories of the interface pressure at three locations on the hull-water interface for k_d = 1.25 GPa/m and c = 0.

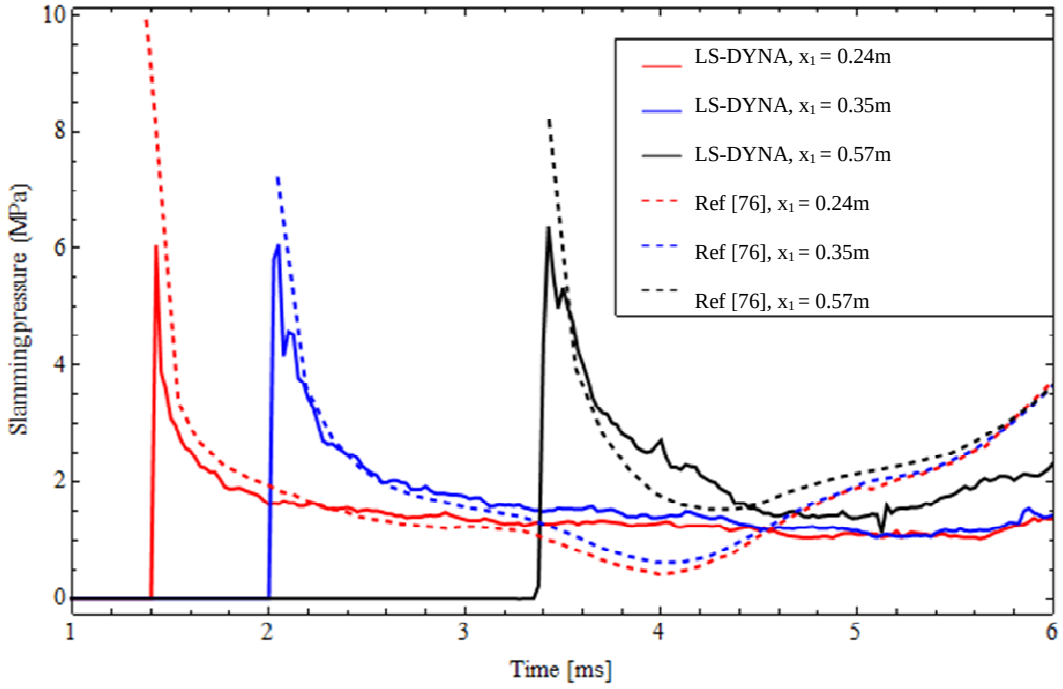

Figure 91. Time histories of the interface pressure at three locations on the hull-water interface for k_d = 1.25 GPa/m and c = 1.

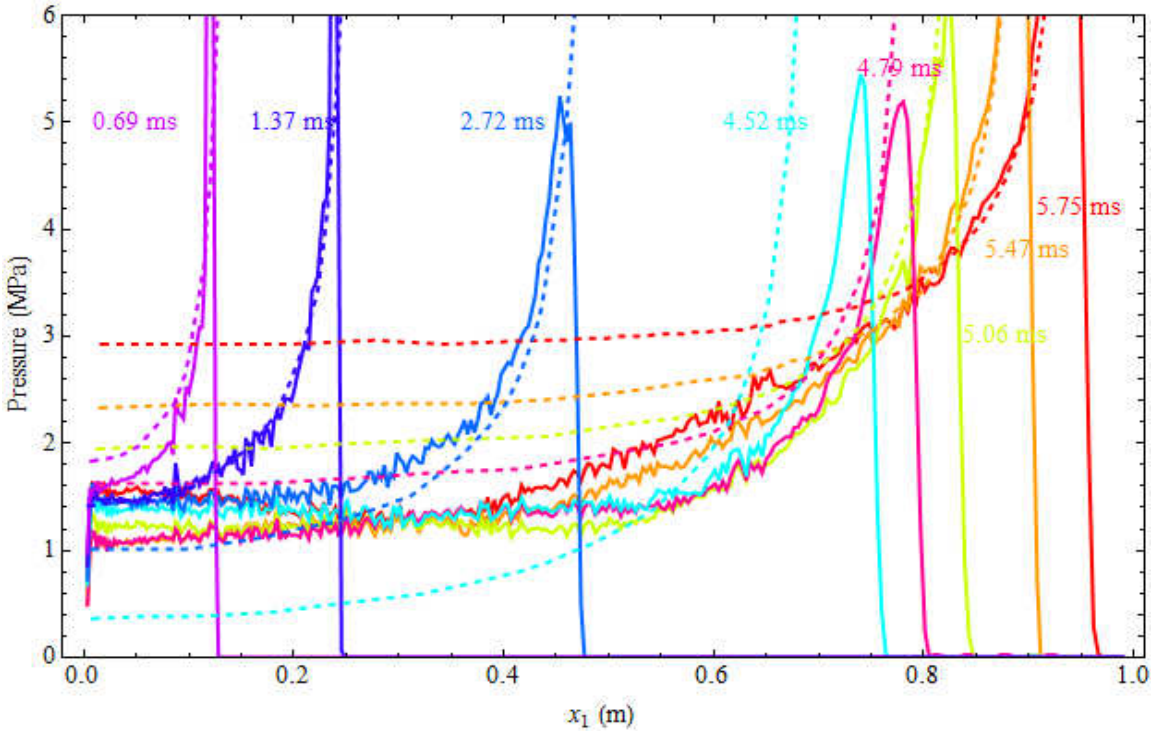

Figure 92. Distribution of the slamming pressure along the hull; solid curves: solution using LS-DYNA, dashed curves: results from [76].

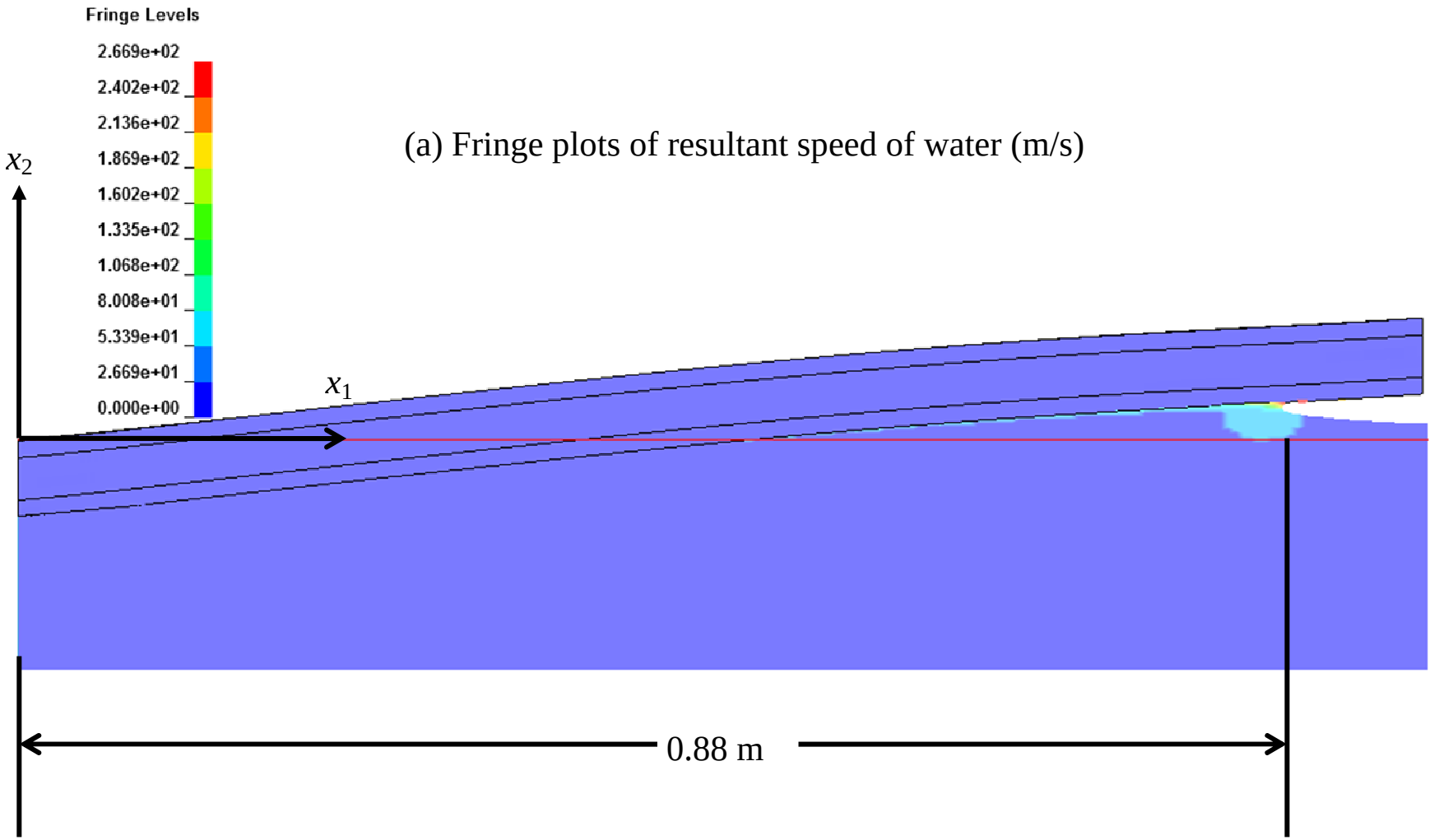

(a) Fringe plots of resultant speed of water (m/s)

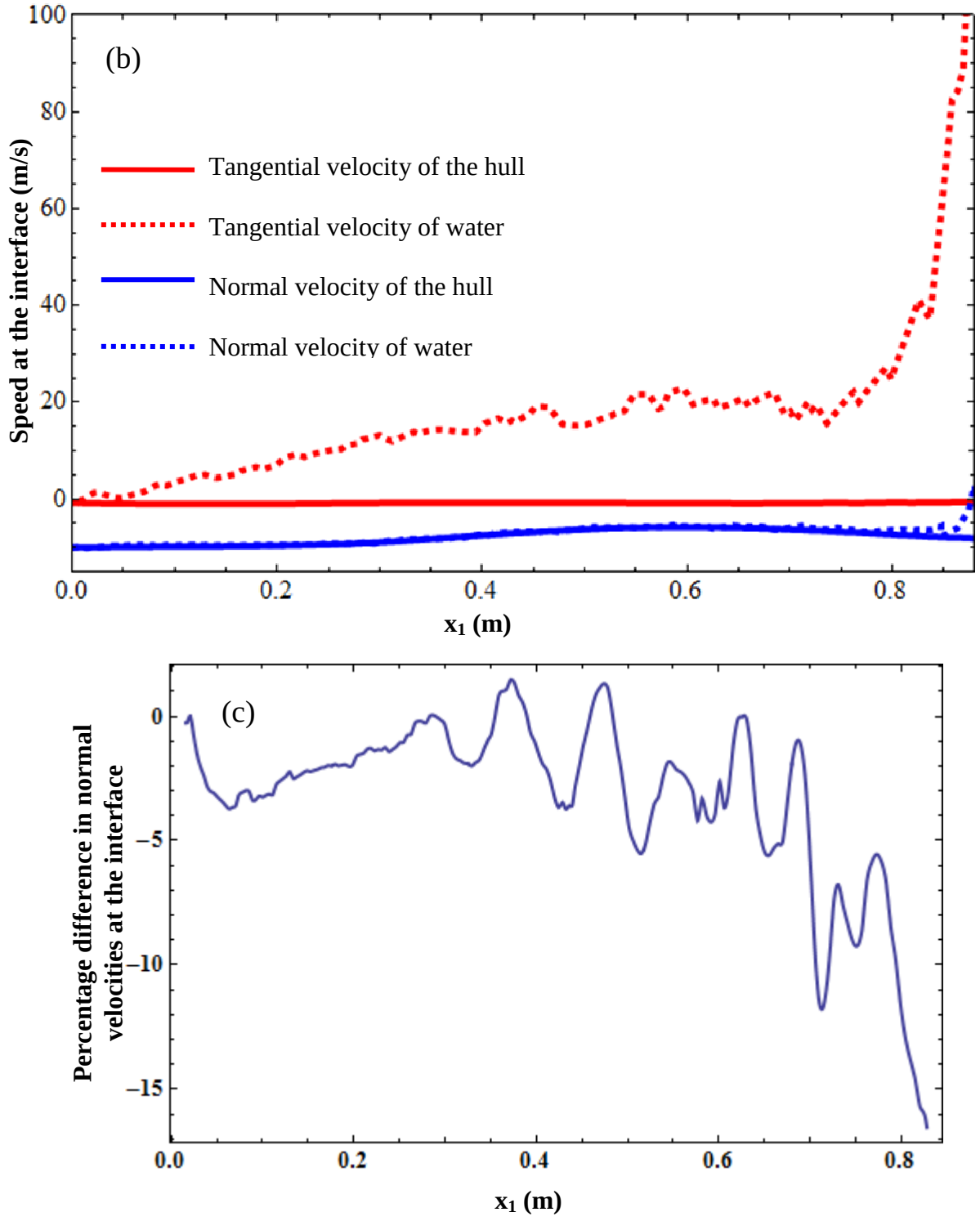

Figure 93. At t = 5.471 ms, (a) deformable hull and water region, (b) variations of the velocity components of the hull and the adjoining water particle, (c) percentage difference between normal velocities of the water particle and the hull at the hull-water interface versus the x_1-coordinate of a point.

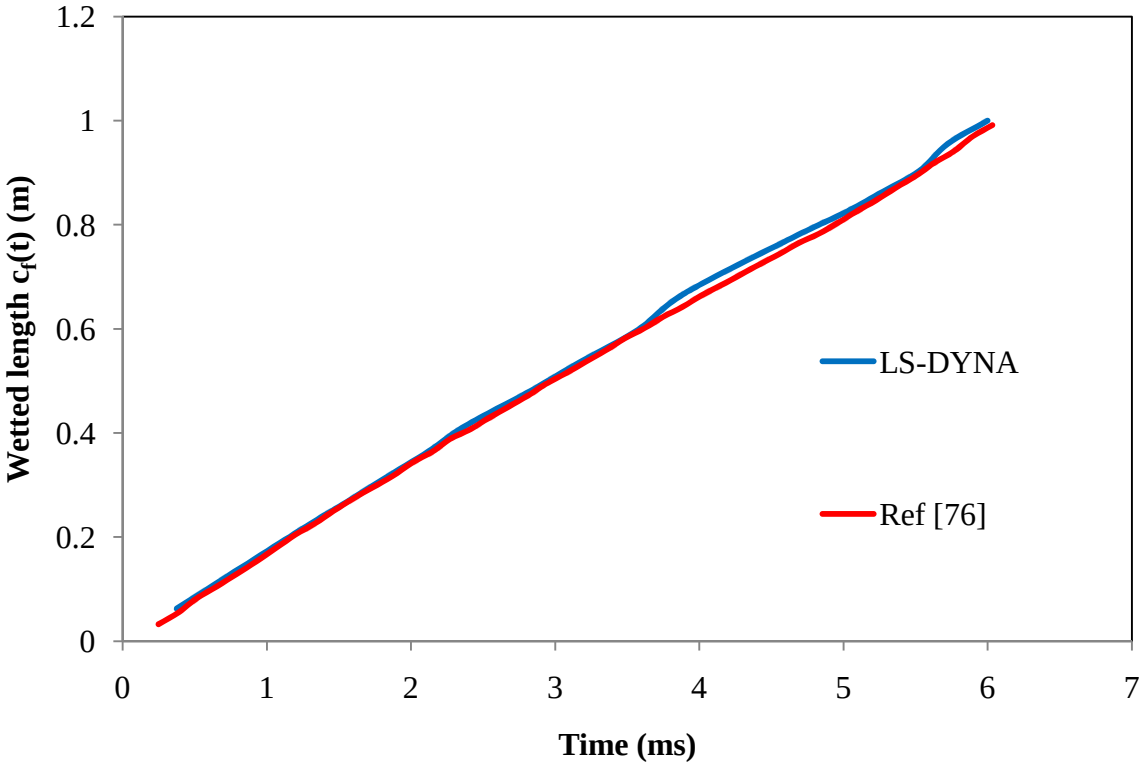

Figure 94. Time history of the length $c_f(t)$ of the wetted surface.

For t = 5.741 ms, we have plotted in figures 93(a) and 93(b) deformed position of the hull, the water, fringe plots of the speed, and variations of the normal and the tangential velocities of water and hull particles on the interface versus their x_1-coordinates. Since water has been assumed to be inviscid, therefore, only the normal component of velocity should be continuous at the hull-water interface which is verified by results shown in figure 93(c), which exhibits the percentage difference in normal velocities of the hull and water particles on the hull-water interface. Except in the jet flow, the percentage difference is less than 10. Oscillations in the normal component of the water velocity at the jet flow are possibly due to errors in estimating the local slope of the hull-water interface. The tangential velocity of the water at the interface increases from zero at the keel to ~ 30 m/s at a point near the jet flow; in the jet flow the tangential velocity of water rapidly increases to ~ 100 m/s. We note that the maximum tangential velocity of water in the jet flow of a rigid wedge of deadrise angle 30^0 impacting water at 10 m/s was about 50 m/s (cf. Section 2.3.2). The presently computed time history of the wetted length agrees well with that reported in [76]; cf. figure 94. For this problem, the wetted length increases at the rate of 170 m/s.

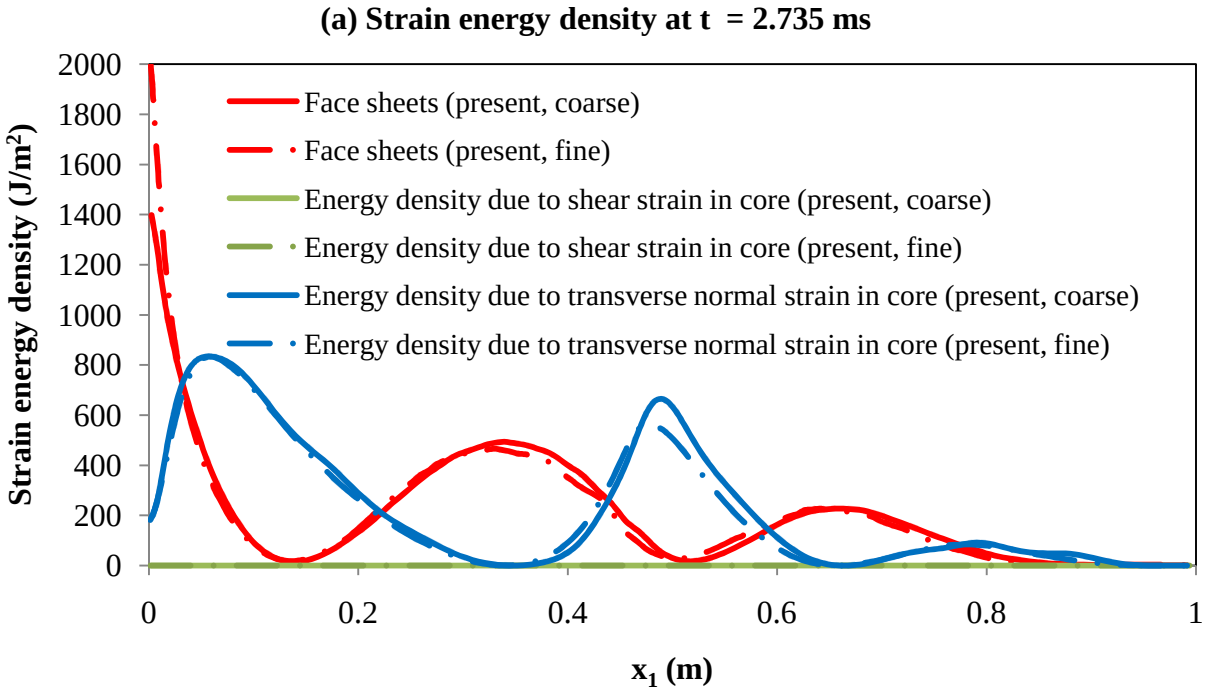
(a) Strain energy density at t = 2.735 ms
Strain energy density (J/m²)
2000
1800
1600
1400
1200
1000
800
600
400
200
0
0
0.2
0.4
0.6
0.8
1
x1 (m)
Face sheets (present, coarse)
Face sheets (present, fine)
Energy density due to shear strain in core (present, coarse)
Energy density due to shear strain in core (present, fine)
Energy density due to transverse normal strain in core (present, coarse)
Energy density due to transverse normal strain in core (present, fine)

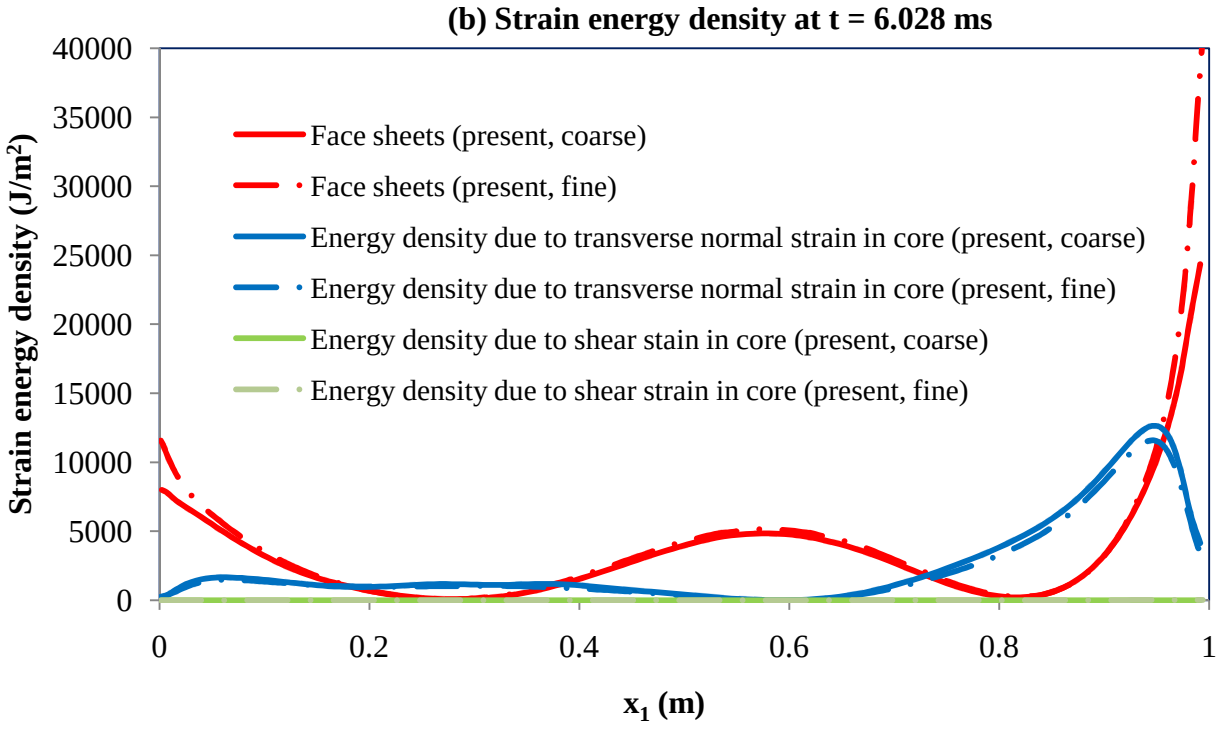
(b) Strain energy density at t = 6.028 ms
Strain energy density (J/m²)
40000
35000
30000
25000
20000
15000
10000
5000
0
0
0.2
0.4
0.6
0.8
1
x1 (m)
Face sheets (present, coarse)
Face sheets (present, fine)
Energy density due to transverse normal strain in core (present, coarse)
Energy density due to transverse normal strain in core (present, fine)
Energy density due to shear stain in core (present, coarse)
Energy density due to shear strain in core (present, fine)

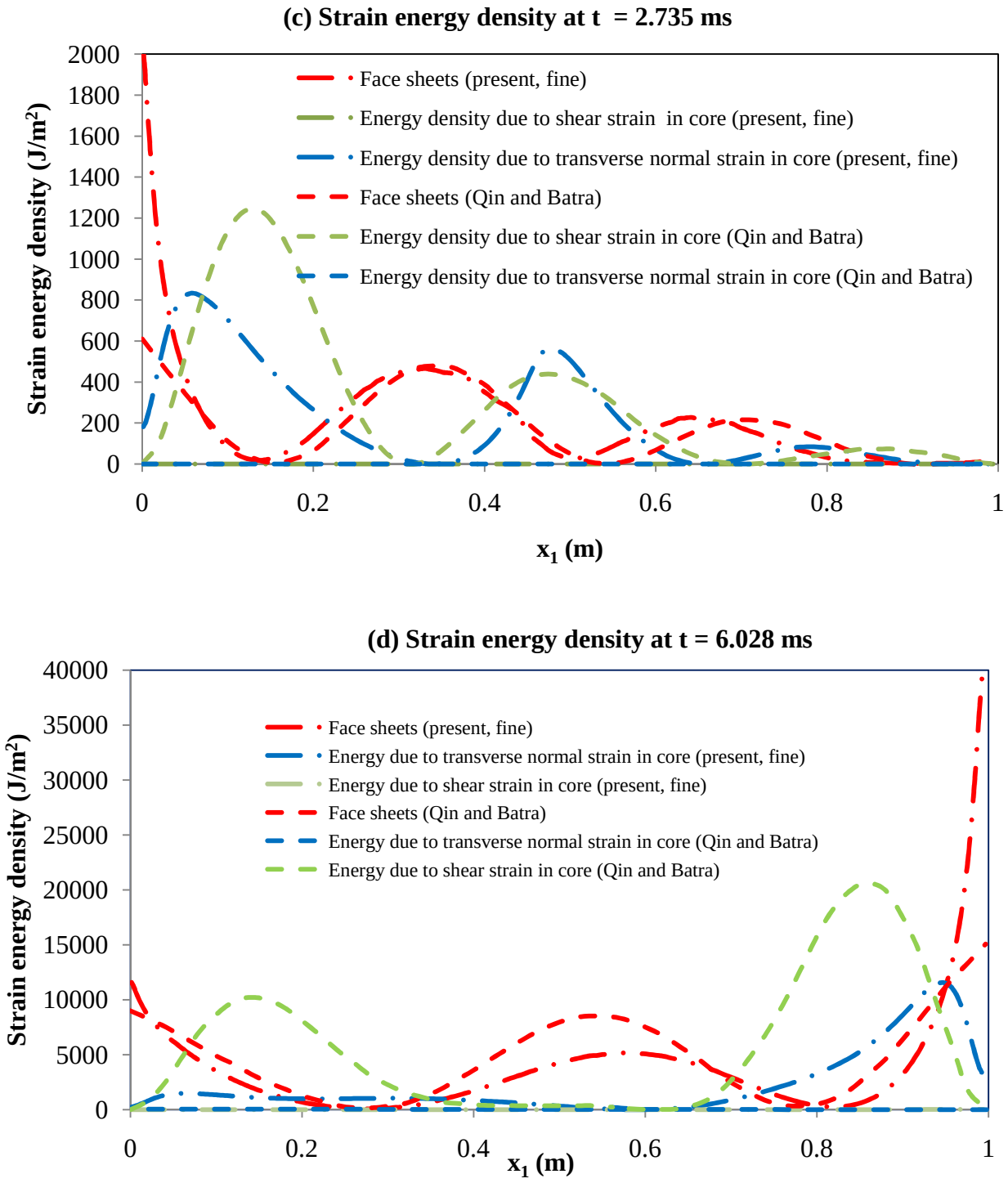

Figure 95. Strain energy density in the core and face sheets at (a, c) an early stage of slamming when t = 2.735 ms; (b, d) an ending stage at t = 6.018 ms. Results computed from LS-DYNA are compared with those reported by Qin and Batra [76].

Figures 95(a) and 95(b) exhibit distributions of the strain energy density stored in the two face sheets and the core at an early and at a terminal stage of the slamming impact event computed using two different FE meshes. We compute the strain energy density of the face sheets using the expression $U_{total} = 0.5\ \varepsilon_{ij} T_{ij,}$ here U_{total} is the strain energy density and a repeated index implies summation over the range 1, 2 of the index. The strain energy densities due to the transverse shear and the transverse normal strains in the core are given, respectively, by $U_{shear} = \varepsilon_{12} T_{12}$ and $U_{normal} = 0.5\ \varepsilon_{22} T_{22}$. The strain ε_{ij} is obtained at the centroid (Gauss point) of each FE, T_{ij} is computed using the constitutive relation (60) from $\varepsilon_{ij,}$ and U_{total}, U_{shear}, and U_{normal} are integrated through the thickness of either the face sheets or the core using the trapezoidal rule to obtain the strain energy densities, which are exhibited in figure 95. Note that the damage in the sandwich composite panel is not considered. Results from the solution of the problem with the fine mesh differ from those from the solution of the problem with the coarse mesh only at points near the fixed supports. In figures 95 (c) and (d) we have compared strain energy densities reported by Qin and Batra [76] with those presently computed using the fine FE mesh. Whereas the variation of the strain energy stored in the face sheets at 2.735 ms computed from the present solution agrees well with that found by Qin and Batra [76], values from the two approaches differ noticeably at 6.028 ms. Whereas Qin and Batra found that strain energy in the core is mainly due to transverse shear deformations, present results suggest that it is primarily due to the transverse normal strains. This difference could be due to the {3, 2}-order plate theory employed by Qin and Batra whereas we have modeled face sheets as thin shells and the core as a homogeneous isotropic linear elastic material, and the significant differences in the slamming pressure distributions reported in figure 92. With either approach, deformations of the core account for a significant portion of the work done by the slamming pressure.

Figures 96 and 97 exhibit fringe plots of ε_{12} and ε_{22} in the hull at t = 2.735 and 6.028 ms, respectively. At t = 2.735 (6.028) ms, the magnitude of ε_{22} in the core varies between 4.52×10^{-3} and -3.66×10^{-2} (6.80×10^{-3} and -1.90×10^{-2}), whereas the magnitude of ε_{12} varies between 1.14×10^{-3} and -8.97×10^{-6} (6.34×10^{-4} and -1.47×10^{-3}). This corroborates results exhibited in figure 95, i.e., the strain energy in the core is mainly due to the transverse normal strains. Note that fringe plots display a range of values of the strain rather than its exact value.

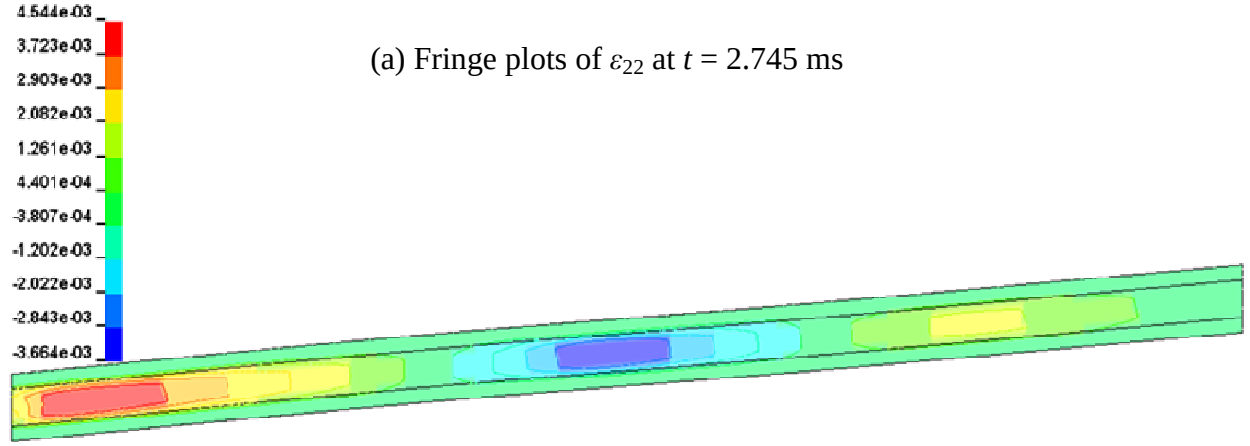

(a) Fringe plots of ε_{22} at t = 2.745 ms

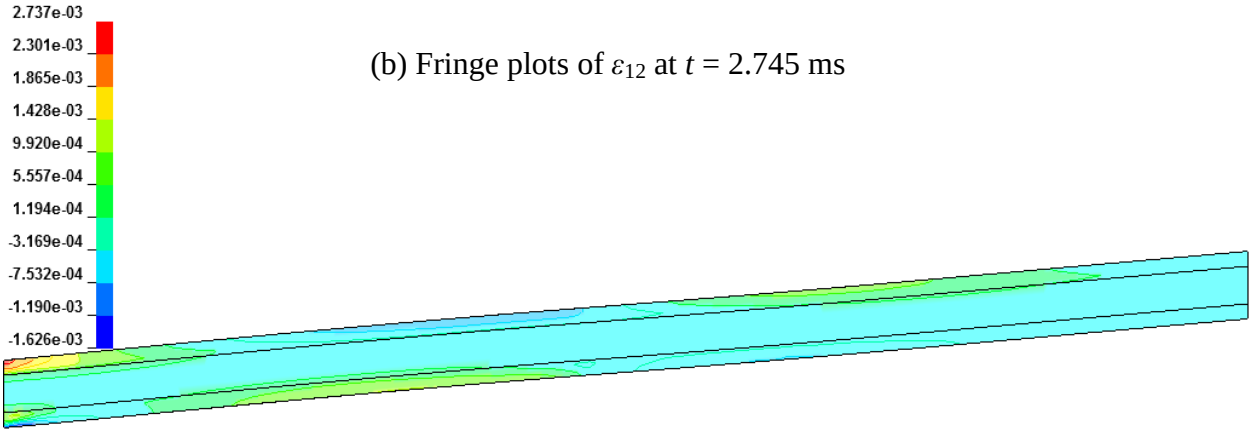

(b) Fringe plots of ε_{12} at t = 2.745 ms

Figure 96. Fringe plots of (a) ε_{22} and (b) ε_{12} at t = 2.745 ms.

(a) Fringe plots of ε_{22} at t = 6.018 ms

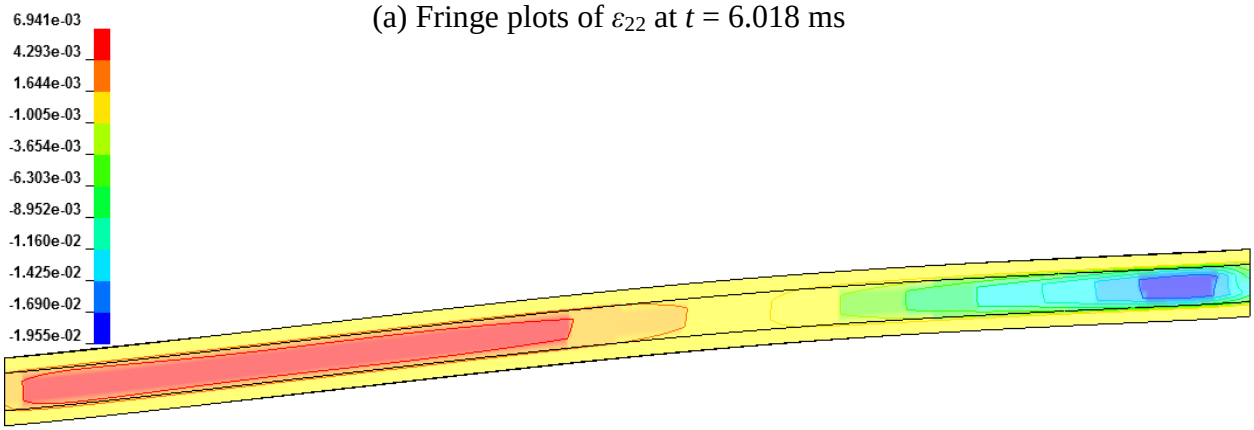

(b) Fringe plots of ε_{12} at t = 6.018 ms

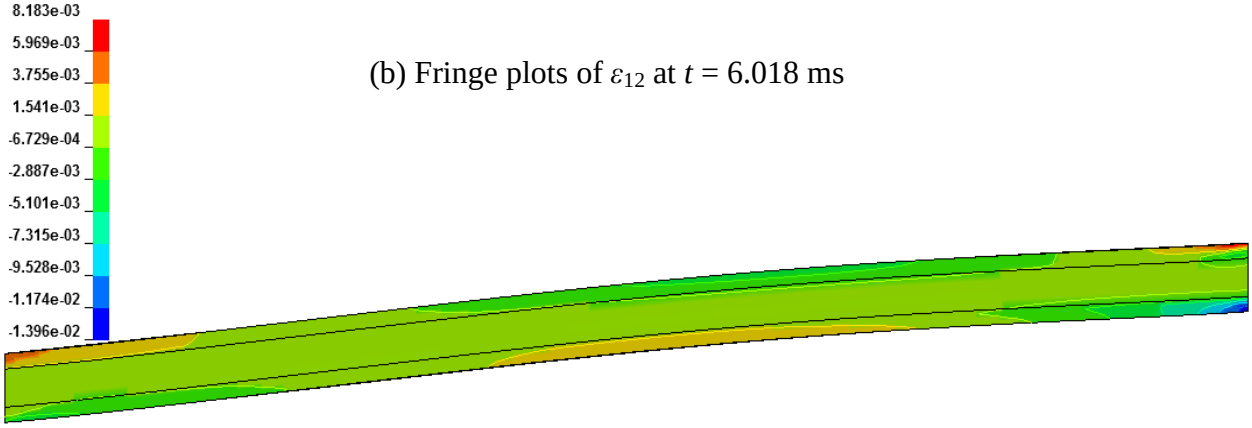

Figure 97. Fringe plots of (a) ε_{22} and (b) ε_{12} at t = 6.018 ms.

2.3.5. Damage in fiber reinforced composite due to the local slamming

We assume that the hull is made of a transversely isotropic 8 mm thick and 1 m long composite plate with the axis of transverse isotropy along the length of the plate (figure 59(b)), set L_1 = 2 m, L_2 = 2 m, L_3 = 1 m, L_4 = 5 m, L_5 = 6 m, width in the x_3 - direction = 0.25 m (figure 59(a)), and use two different FE meshes to study plane strain deformations of the hull and the fluid. In the first FE mesh, the fluid domain (L_1 x L_2) near the hull is discretized by 100 x 100 x 1 8-node brick elements, the FE mesh covering the entire domain (initially void and fluid domains, L_4 x L_5) has 150 x 150 x 1 elements, and the hull is discretized by 50 x 1 4-node shell elements along the length and the width (the x_3-direction). Each element of the fluid (shell) domain of the first FE mesh is divided into four (two) equal elements to get the second FE mesh, thus the FE mesh covering the entire domain (initially void and fluid domains, L_4 x L_5) has 300 x 300 x 1 elements. The water is modeled as inviscid with bulk modulus = 2.9 GPa and ρ_0 = 1000 kg/m^3 and the hull material as elastic using constitutive equations (74)-(78) when considering damage, and with constitutive equation (60) when the degradation of material properties due to progressive damage is ignored. Values of material parameters are listed in table 8, the left (x_1 = 0) and the right ($x_1 = cos\beta$) (deadrise angle = 5^0) edges of the hull are restrained from motion in the x_1-direction, from all rotations, and the hull has a constant velocity of -20 m/s in the x_2-direction. Impact speeds of 10 and 15 m/s were also studied, however, no significant damage in the panel at those impact speeds occurred and results are not reported here.

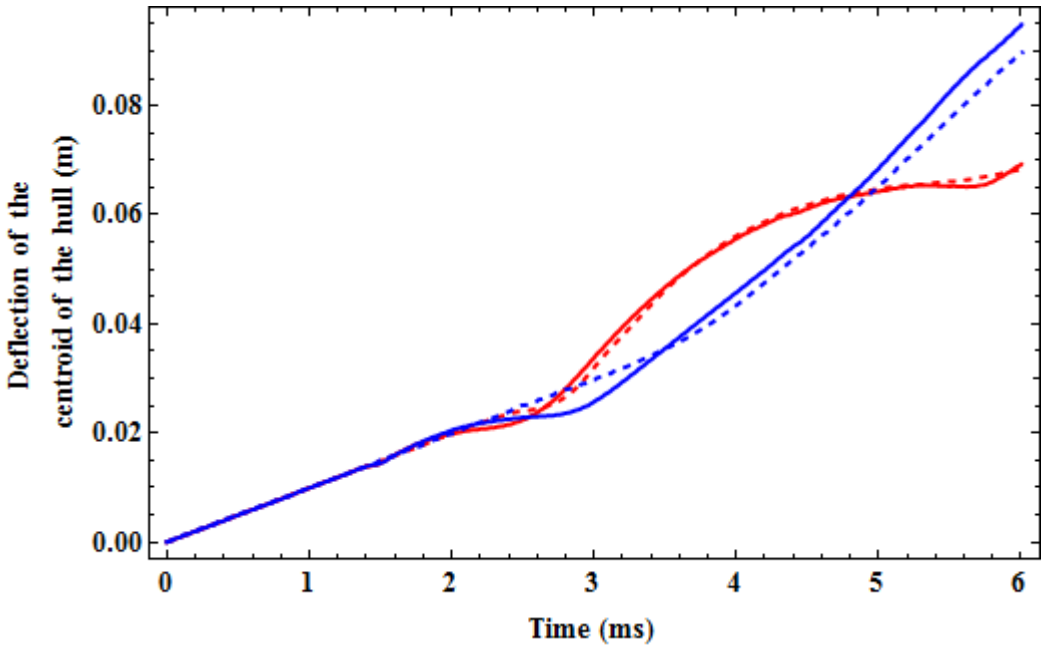

Figure 98. Time histories of the deflection of the centroid of the hull; red curve: without the consideration of damage; blue curve: with the consideration of damage; solid: mesh 2; dashed: mesh 1.

For the two FE meshes used, we have plotted in figure 98 time histories of the deflection of the hull centroid for the two material models. It is evident that the two FE meshes give nearly the same value of the deflection, and the consideration of damage has virtually no effect on the deflection till t = 2 ms. The left end of the hull fails at about 1.57 ms when damage induced in the hull material is considered. Subsequent to the failure of the hull at the left edge, the deflection of the hull centroid is less than that of the centroid of the undamaged hull. After the separation of the hull from the left support, water can flow from the region below the hull to that above it and the pressure distribution on the hull changes. The hull deforms as a cantilever "beam" rather than as a fixed-fixed "beam". Results presented in the rest of this subsection are with the FE mesh 2.

Figure 99(a) exhibits the deflected shape of the centroidal axis of the hull at t = 1.57, 2.9 and 4 ms. After failure of the hull at the left support, hull particles near this support undergo large deflections; the % difference (figure 99(b)) between centroidal deflections of hull points near the left and the right supports computed with and without the consideration of degradation of

material properties due to damage are magnified because of their very small values. Near the midspan and the three-quarter span, the two sets of deflections differ by 20 and 80% respectively.

Figure 99(c) shows the local x_2-velocity of particles on the centerline of the hull. For the undamaged case, both the left and the right supports have downward velocities of 20 m/s, whereas in the damaged case, at 2.9 and 4 ms, the downward velocity of the left end of the panel decreases to 16 m/s. Variations of the two sets of downward velocities along the hull span are significantly different.

The pressure distributions on the hull wetted surface at different times are exhibited in figure 100. The pressure profiles computed with and without the consideration of the damage are quite close to each other for t = 0.74 ms. Just before (t = 1.5 ms) and after (t = 2 ms) the failure of the panel at the left support, peak pressures are slightly reduced by the consideration of the damage. However, the three pressure profiles at t = 2.9, 3.5 and 4.1 ms are quite different. For a fixed value of time (e.g., for 3.5 and 4.1 ms), the peak pressure for the damaged panel is less than that for the undamaged panel possibly because the flow of water through the opening created at the left support relieves the pressure exerted on the hull. At t = 2.9 ms, the peak pressure at x_1 = 0.45 m for the damaged panel is higher than that for the undamaged panel possibly because the local (at x_1 = 0.45 m) x_2-velocity of 8 m/s at t = 2.9 ms without the consideration of damage is upward (e.g., see the purple curve in figure 99(c)) as opposed to equaling 2.5 m/s downward (see dashed purple curve in figure 99(c)) when the damage is considered.

When the damage is not considered, the peak pressure at t = 2.9 ms is lower than that at other times. It could be due to the local velocity of the panel at x_1 = 0.45 m, where the pressure peak occurs at 2.9 ms, is upwards and equals 8 m/s (e.g., see the purple curve in figure 99(c)), whereas at t = 1.57 ms and 4.1 ms the local velocities are downward and equal 1 m/s and 7.75 m/s (e.g., see the red and the blue curves in figure 99(c)), respectively, at x_1= 0.25 m and 0.8 m where the peak pressures occur. Table 13 lists local velocities of the panel and the peak pressures; however, there is no quantitative correlation between local impact velocities and the peak pressures. Thus factors other than the local impact velocity affect the peak pressure.

In this problem, the thickness of the panel is smaller and the impact velocity is higher than those studied in the other sections. The panel studied in this section undergoes large oscillations which are not observed for the other problems. Pressure profiles computed for the thin panel may be affected by these large oscillations, and thus may differ from those for the other panels.

Table 13: Local velocity of the panel and the peak pressure on the panel with and without the consideration of damage.

Time (ms)	With damage			Without damage		
	x_1-coordinate of the location of the peak pressure (m)	Local velocity (m/s)	Peak pressure (MPa)	x_1-coordinate of the location of the peak pressure (m)	Local velocity (m/s)	Peak pressure (MPa)
0.74	0.1	-10.0	5.05	0.1	-11.0	5.1
1.57	0.25	-0.8	3.2	0.25	-1.0	4.0
2.00	0.325	3.3	3.3	0.325	1.0	4.75
2.90	0.45	-2.5	5.0	0.45	8.0	2.5
3.50	0.5	0.8	1.2	0.55	-4.0	9.0
4.10	0.55	-3.25	1.3	0.8	-7.75	35.0

The time histories of the slamming pressure at three different locations of the hull with the consideration of damage are exhibited in figure 101. These suggest that a material point undergoes cyclic loading with diminishing amplitude of the load and the pressure usually staying non-negative. The oscillations in the time histories of pressure are possibly due the presence of the contact springs (see Appendix A) and due to this oscillation negative pressure is observed at some places along the span (not shown in figures 100 and 101), however, no water separation from the panel at those places is allowed.

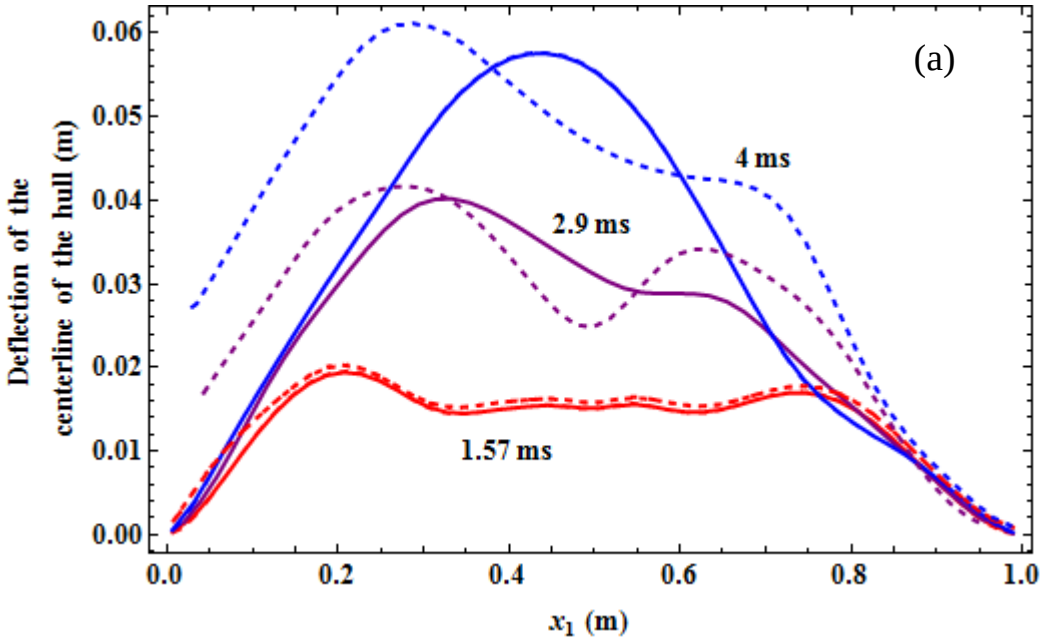
(a)
Deflection of the centerline of the hull (m)
0.06
0.05
0.04
0.03
0.02
0.01
0.00
0.0
0.2
0.4
0.6
0.8
1.0
x_1 (m)
4 ms
2.9 ms
1.57 ms

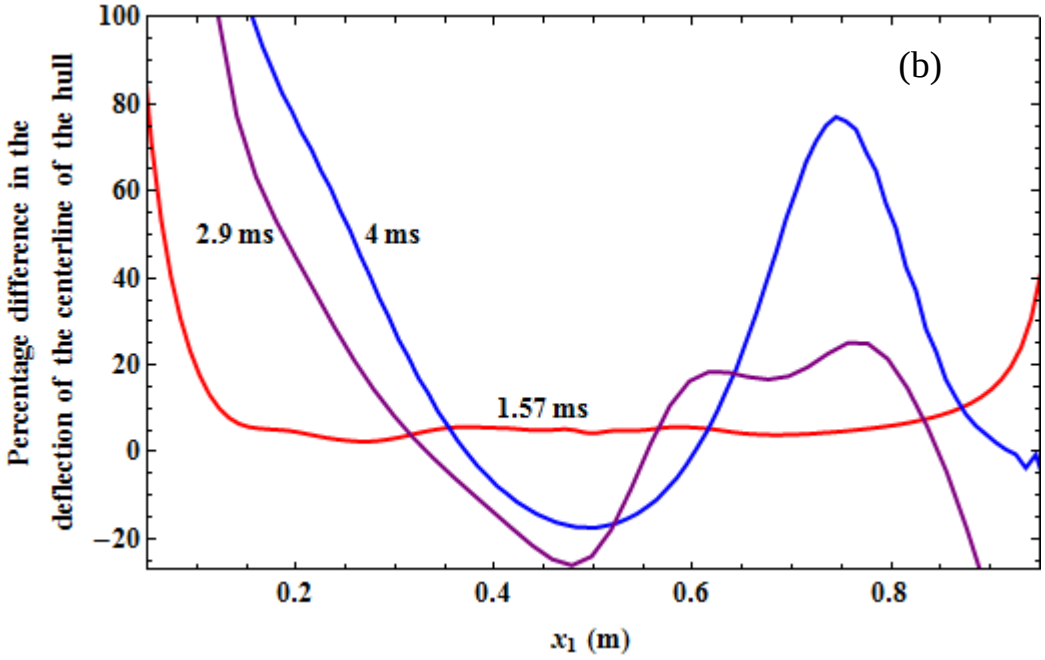
(b)
Percentage difference in the deflection of the centerline of the hull
100
80
60
40
20
0
−20
0.2
0.4
0.6
0.8
x_1 (m)
2.9 ms
4 ms
1.57 ms

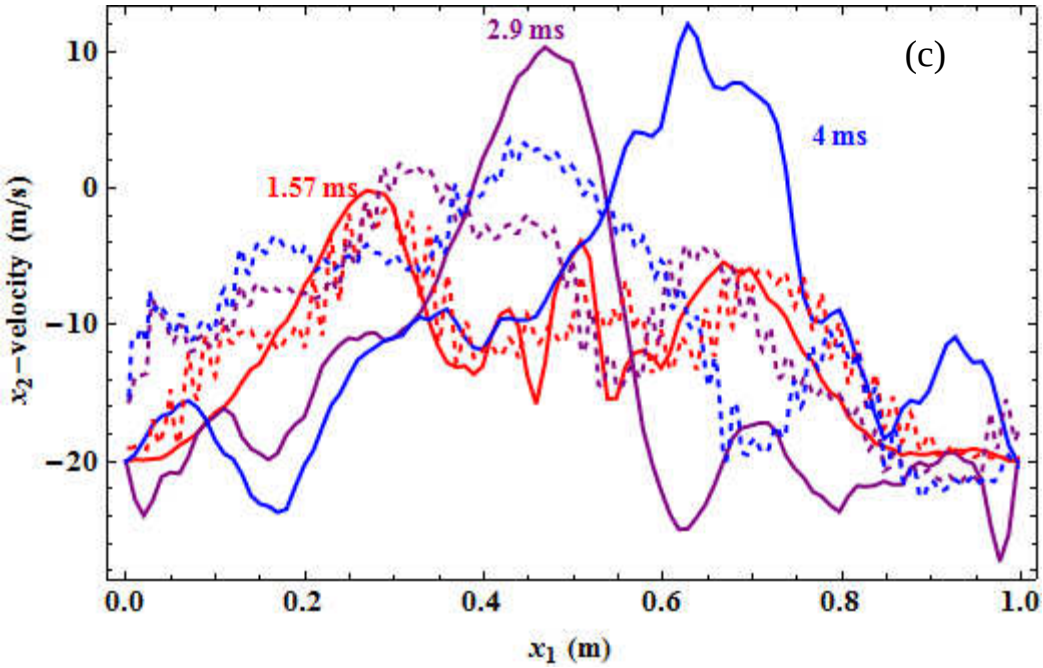

Figure 99. (a) Deflection of the centroidal axis of the hull at three different times. Solid line: without damage; dashed line: with damage; (b) difference in deflections computed with and without damage, (c) x_2-velocity of particles on the centroidal axis of the hull at three different times. Solid line: without damage; dashed line: with damage.

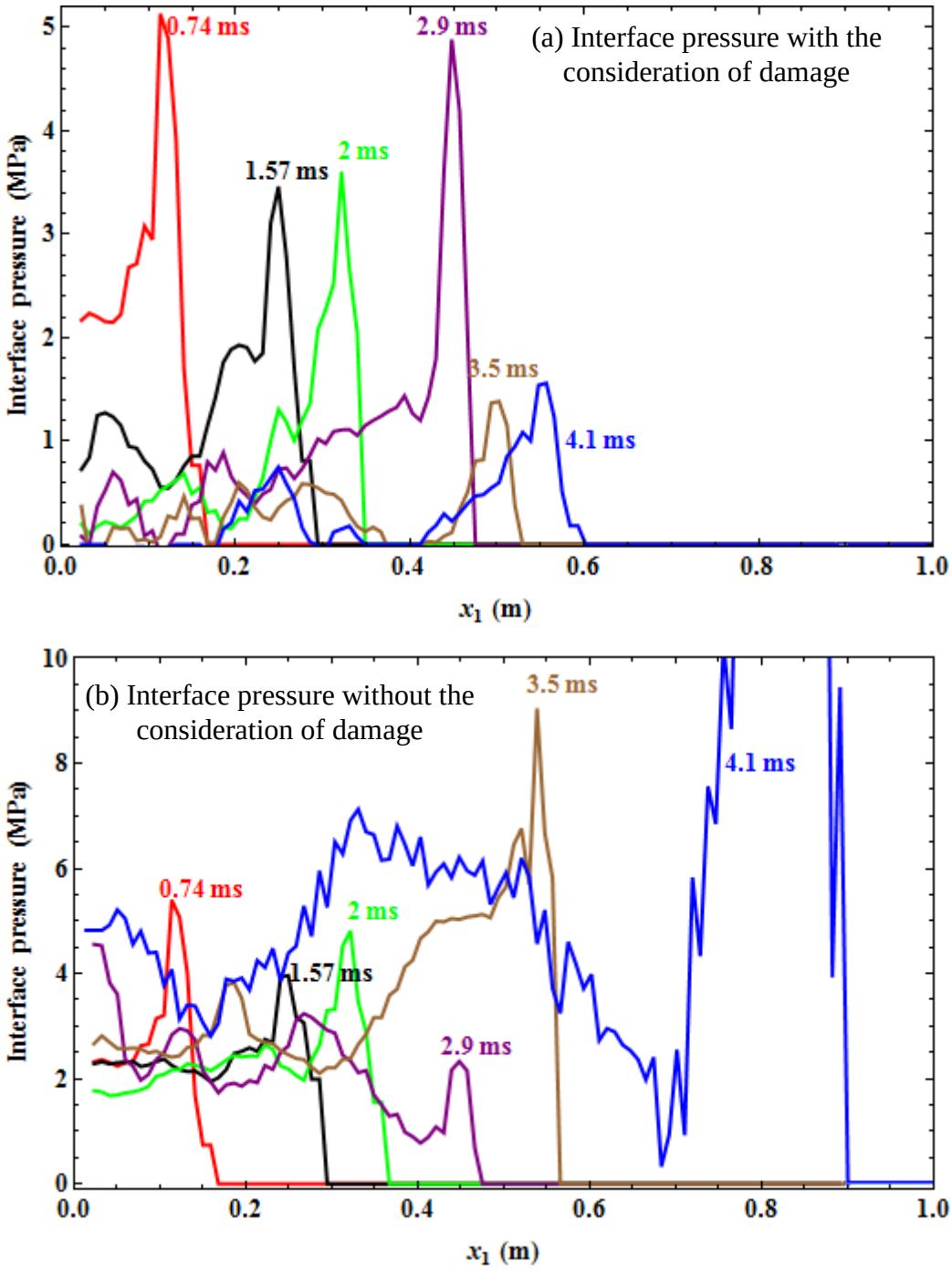

Figure 100. Interface pressure variation over the span of the hull at different times.

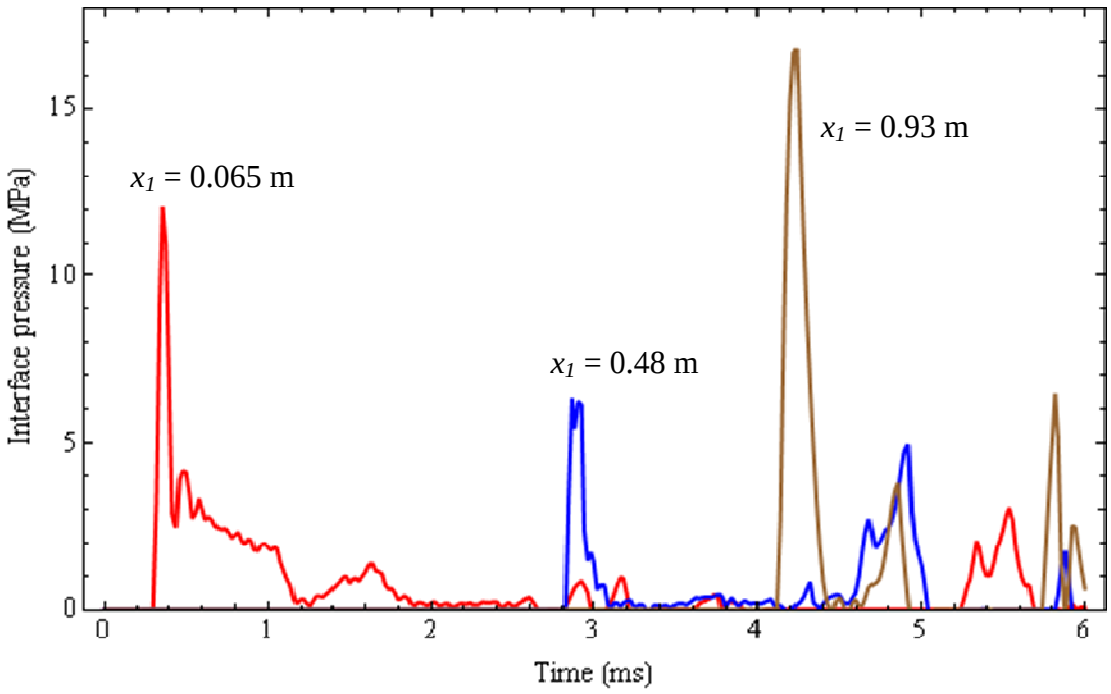

Figure 101. Time histories of the pressure at three points on the hull.

Figure 102 exhibits variations of ε_{11} across the thickness at the mid span of the damaged panel. We note that at t = 0.52 and 1.02 ms, the strain ε_{11} across the thickness is nearly uniform implying that deformations of the hull are due to in-plane stretching. However, at t = 1.52, 2.02, and 2.52 ms the axial strain ε_{11} varies almost linearly across the thickness with equal and opposite values at the top and the bottom surfaces implying that deformations are due to bending. Thus the deformation mode changes as the pressure distribution on the hull span varies with time.

In figures 103 (a) and (b) we have plotted time histories of ε_{11} and ω_{11} at x_1 = 0.5 m on the bottom and the top surfaces of the hull, respectively. At the point on the bottom surface, ω_{11} remains insignificant until 1.5 ms when it increases to ~ 0.20 as ε_{11} increases to ~ 0.70 %. From 1.5 ms to 2.8 ms, ε_{11} decreases and increases again, however ω_{11} remains constant since the absolute value of ε_{11} either decreases or is not large enough to cause additional damage. At ~ 3 ms, ε_{11} and ω_{11} increase to 1.25 % and 0.4, respectively. On the top surface, ω_{11} remains insignificant until 1.15 ms. At 1.15 ms and 1.7 ms, ω_{11} increases slightly in discrete jumps to ~ 0.03 and 0.05 as ε_{11} increases to ~ 0.37 % at 1.7 ms. From 1.7 ms to 2.95 ms, ε_{11} decreases and

increases again, however ω_{11} remains constant since the absolute value of ε_{11} either decreases or is not large enough to cause additional damage. At about 2.95 ms, ε_{11} decreases to -1 % and ω_{11} increases to 0.1. At any time, values of the damage variable are different at points on the top and the bottom surfaces when (see figure 103) magnitudes of the axial strain are the same because the damage variable not only depends on the current value of the strain but also on the previously reached maximum value. If either the material is unloading or strains induced in the material are below their previously reached maximum values, the corresponding damage variables remain constant.

Figures 104 (a) and (b) show, respectively, time histories of ε_{11} and ω_{11} on the bottom and the top surfaces of the section at x_1 = 0.01 m that is near the left support. On the bottom surface, ω_{11} and ε_{11} gradually increase to about 1 and 0.4% in 1.0 ms. Once the value of ω_{11} becomes 1 at a Gauss point, the elastic modulus E_{11} becomes zero and for all practical purposes the material at that Gauss point ceases to bear any load. However, a FE is not deleted until equation (79) is satisfied at least at one of the Gauss points in the FE. On the top surface, ω_{11} increases to 0.2 and ε_{11} decreases to -0.17 % at 1 ms. From 1 ms to 1.5 ms, ε_{11} increases, however ω_{11} remains constant since the absolute value of ε_{11} either decreases or is not large enough to cause additional damage. At 1.5 ms, ω_{11} and ε_{11} increase to 1 and 0.35%, respectively. At 1.57 ms, the material near the left support fails and elements adjacent to the left support are deleted.

Figure 105 shows fringe plots of ω_{11} on the top surface of the plate at four different times. Initially damage initiates at points about 0.1 m away from the supports. The damage increases to 1 at 1.5 ms and the failure criterion (cf. equation 79) is met at the left support at 1.57 ms. After failure, the damage increases at x_1= 0.7 m. However, at a cross-section, neither ω_{11} reaches 1 nor failure criterion given by equation (79) is met for $0 < t \leq 4$. Figure 106 shows fringe plots of ω_{11} on the bottom surface of the plate at four different times. Unlike on the top surface, damage initiates at the supports. At the left support, damage increases to 1 and the failure criteria is met at 1.5 ms. After failure, the damage increases at points near the mid-span and at points adjacent to the right support of the plate.

Figure 107 shows fringe plots of ε_{11} on the top surface of the plate at four different times. Initially peak values of ε_{11} are observed at points about 0.1 m away from the supports. However, at 1.5 ms, ε_{11} attains the peak value of 0.35% at the left support before elements adjacent to the left support fail. After failure, the peak value of ε_{11} is observed near x_1 = 0.75. A correlation between the peak values of ε_{11} in figure 107 and peak values of ω_{11} in figure 105 is apparent; i.e., ω_{11} is high at points where ε_{11} also has relatively large values. Figure 108 shows fringe plots of ε_{11} on the bottom surface of the plate at four different times. Unlike on the top surface, initially high values of ε_{11} can be seen at points near the left support. At the left support, ε_{11} increases to 1.4% before failure. After failure, ε_{11} increases on near the right support of the plate. A correlation between the peak values of ε_{11} in figure 108 and peak values of ω_{11} in figure 106 is apparent.

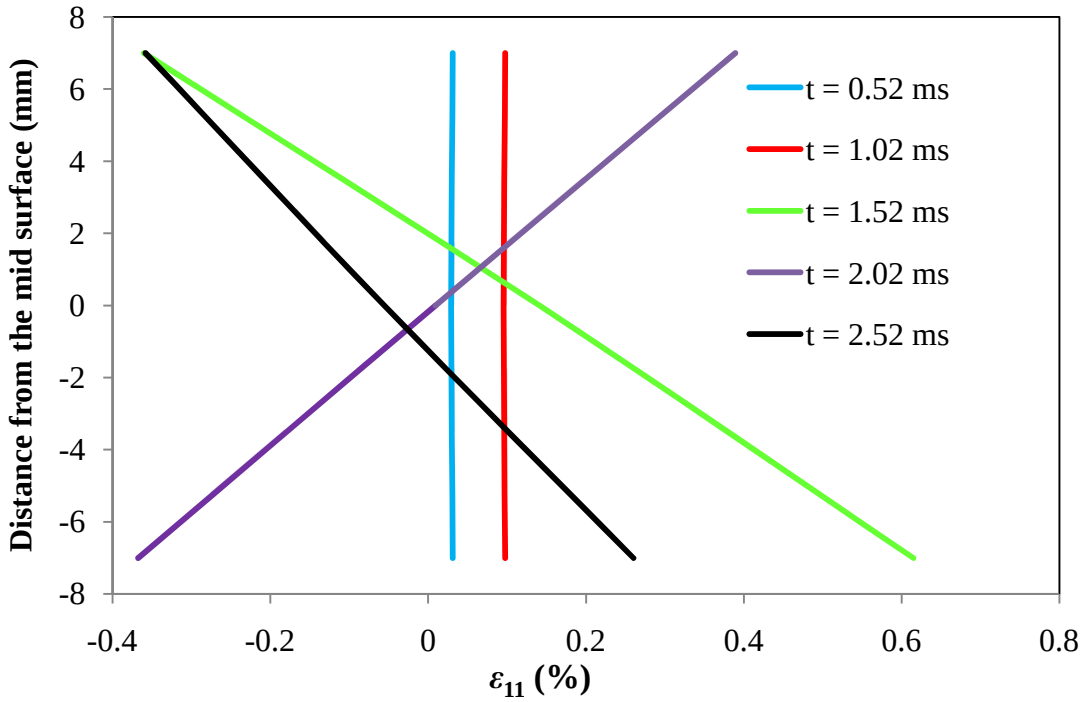

Figure 102. Variations of ε_{11} through of thickness of the panel at different times at x_1 = 0.5 m.

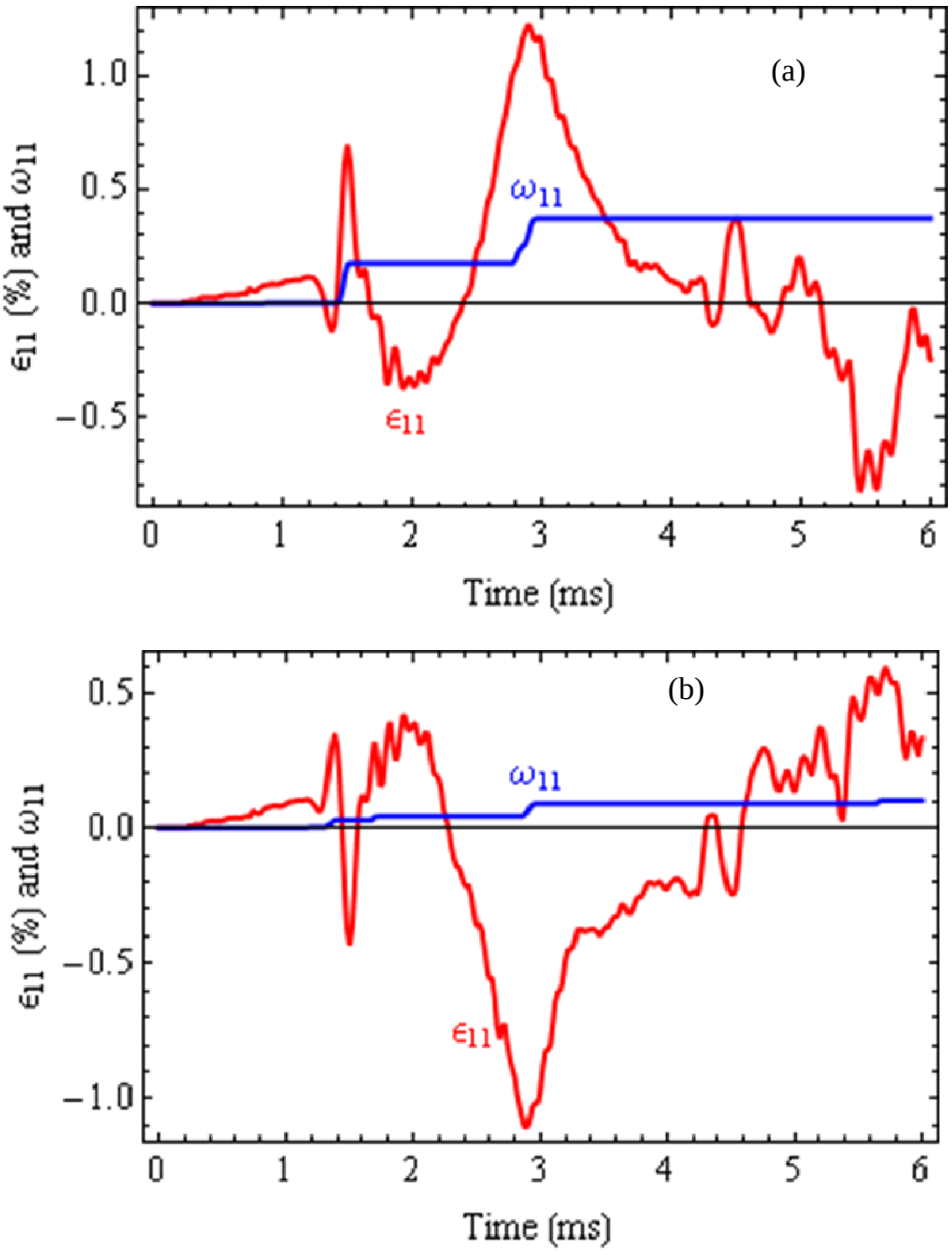

Figure 103. Time histories of ε_{11} and ω_{11} at $x_1 = 0.5$ m on (a) the bottom and (b) the top surface of the plate.

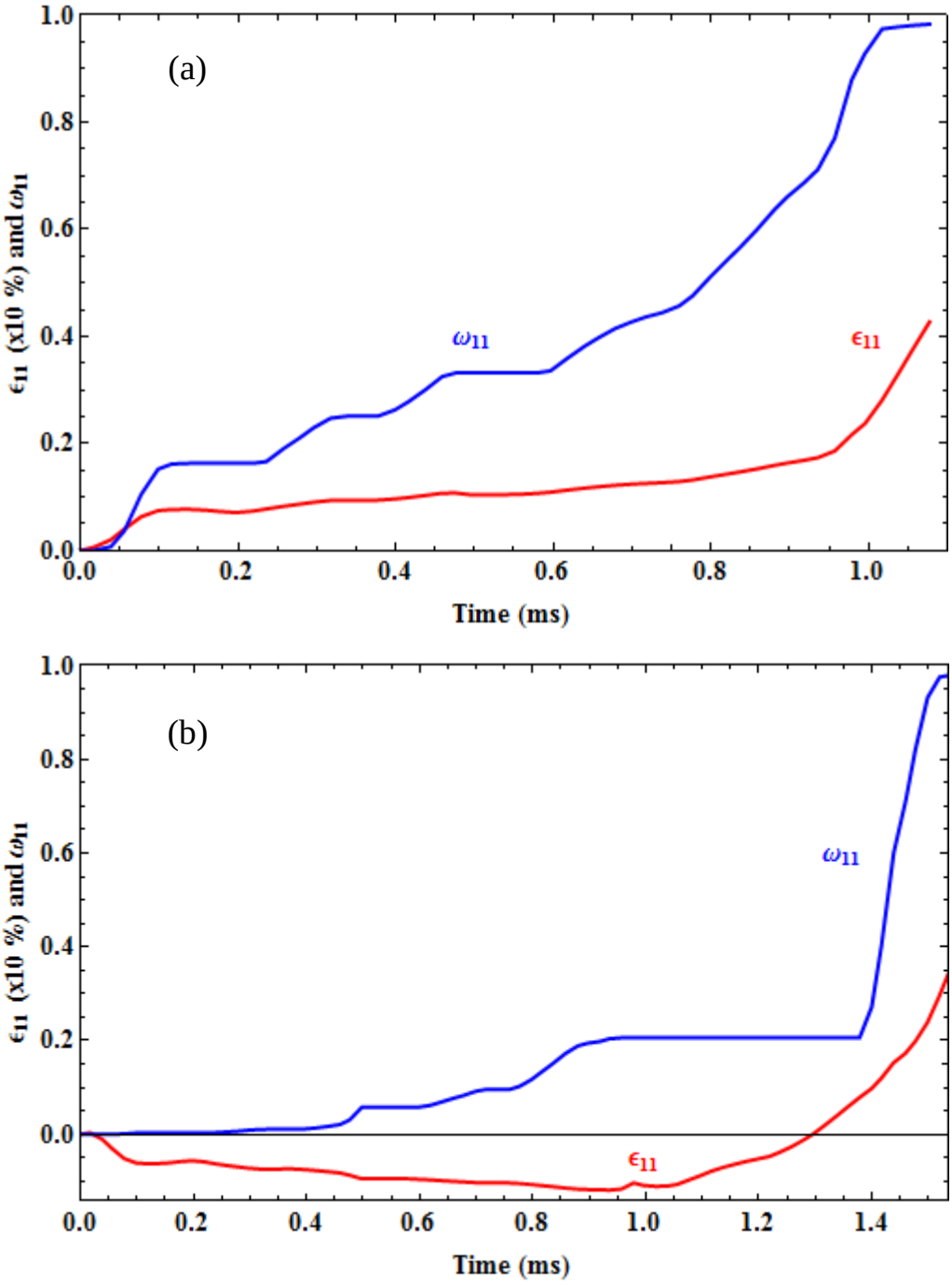

Figure 104. Time histories of ε_{11} and ω_{11} at x_1 = 0.01 m on (a) the bottom and (b) the top surface of the hull at the cross-section near the left support.

(a) t = 0.7 ms

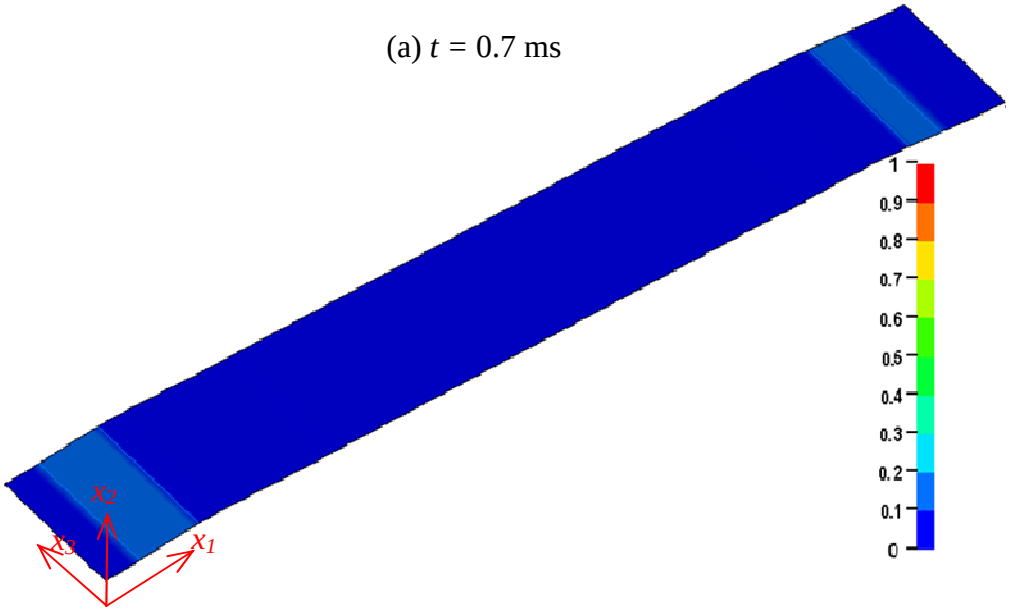

(b) t = 1.5 ms

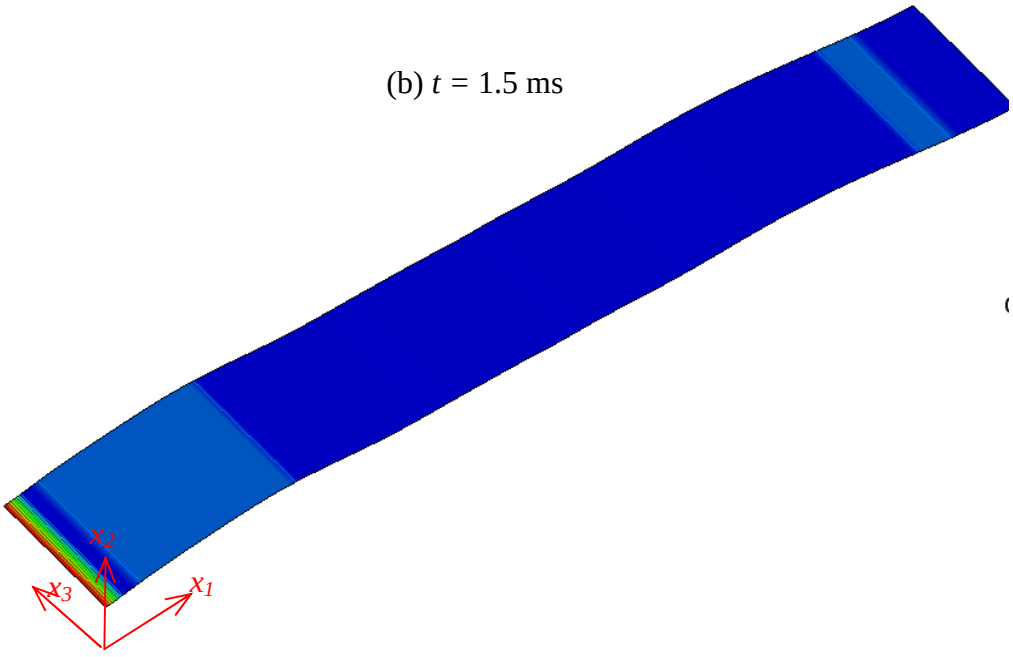

(c) t = 3.5 ms

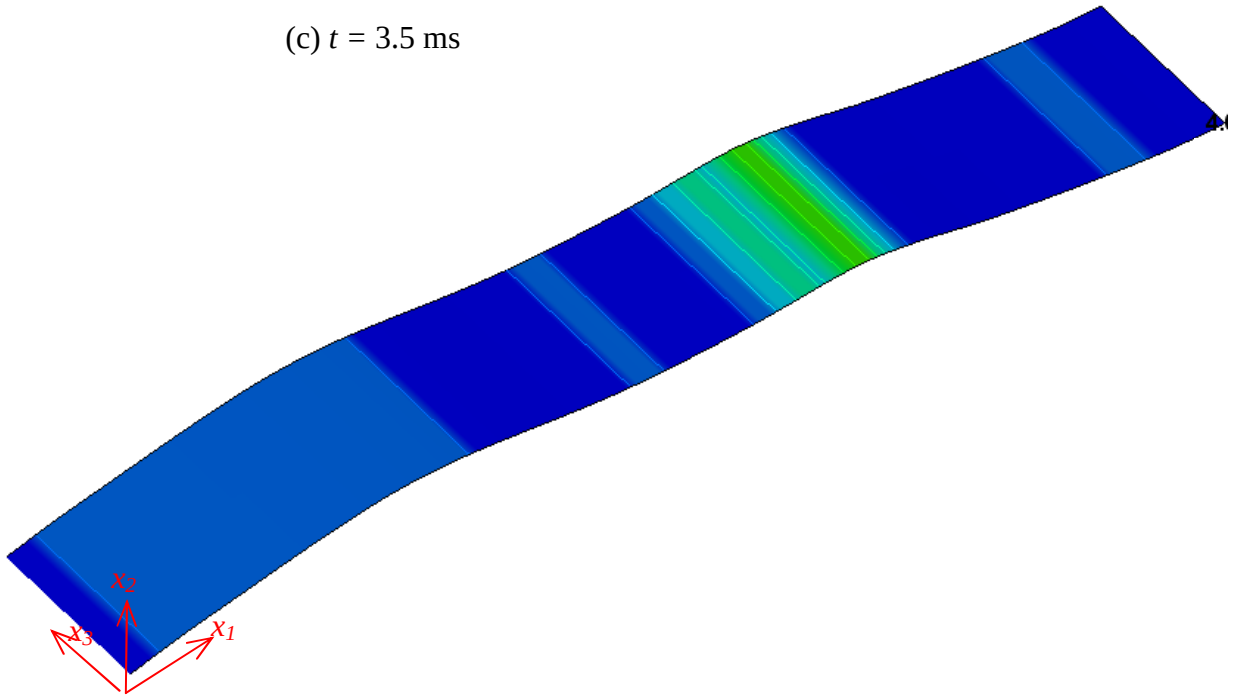

(d) t = 4.0 ms

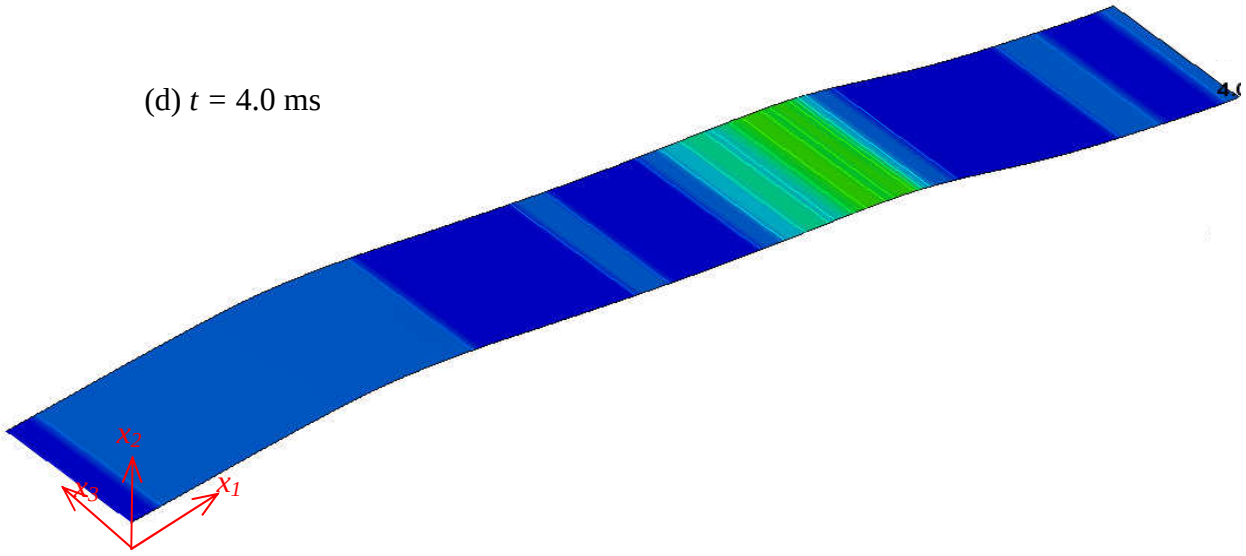

Figure 105. Fringe plots of the damage variable ω_{11} on the top surface of the plate.

(a) t = 0.7 ms

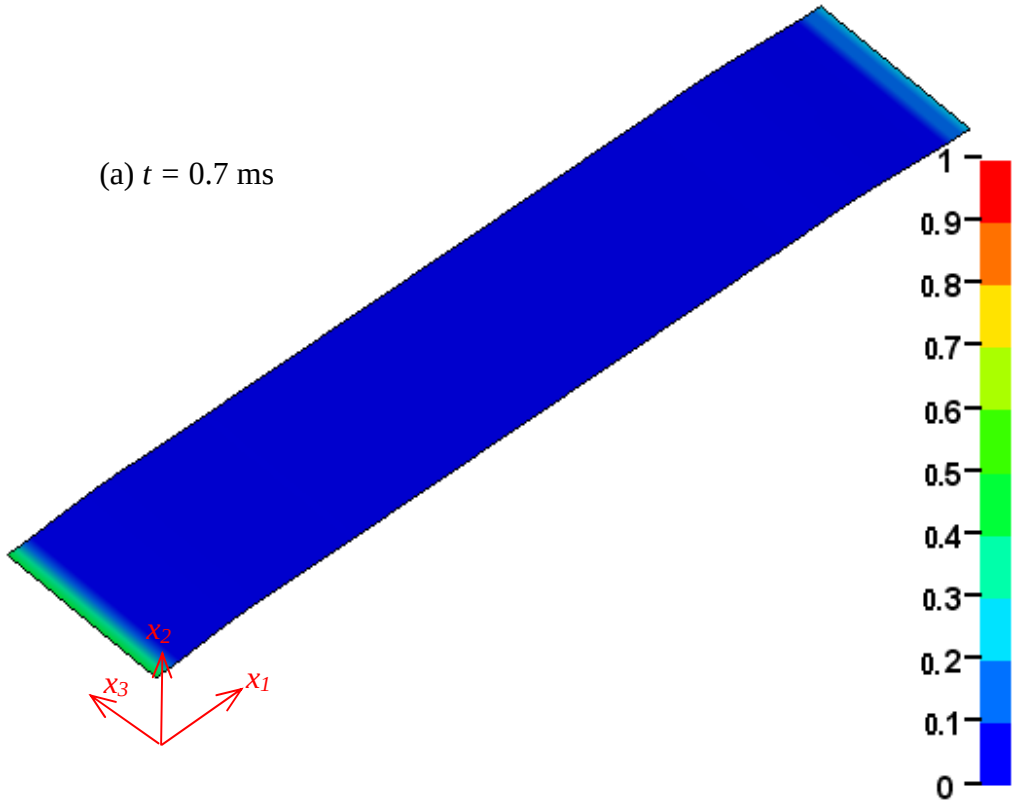

(b) t = 1.5 ms

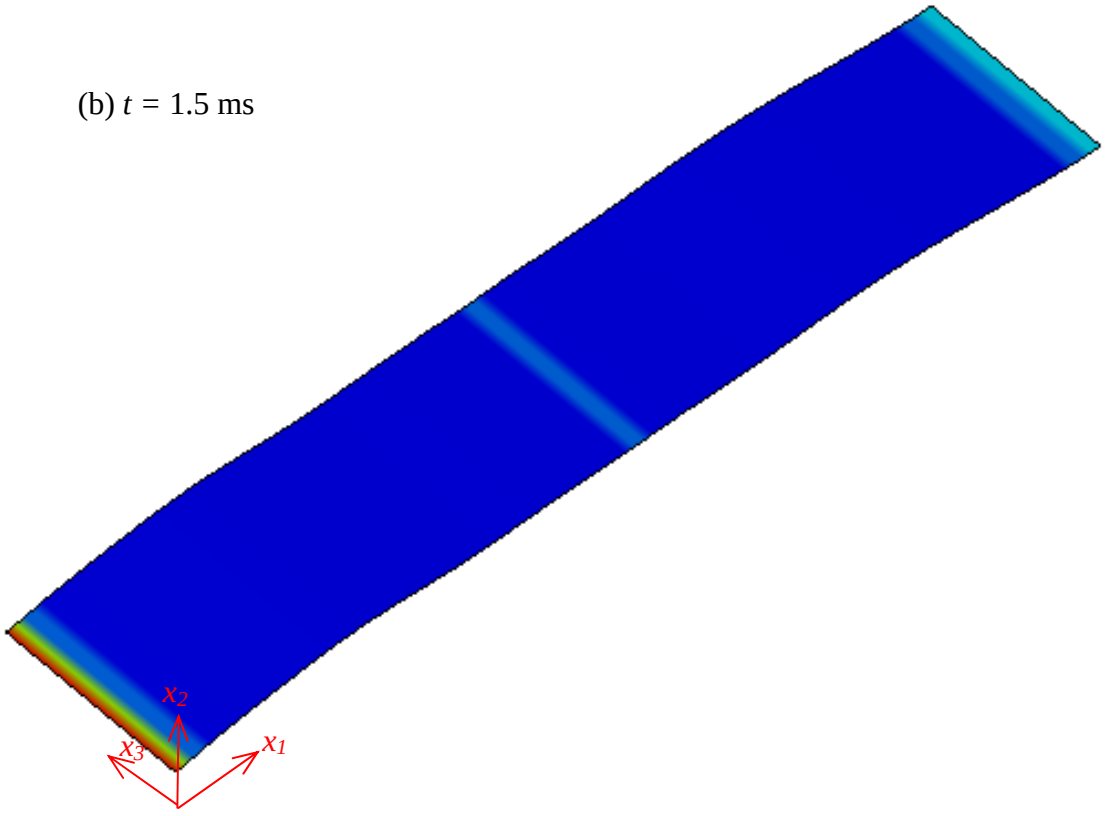

(c) t = 3.5 ms

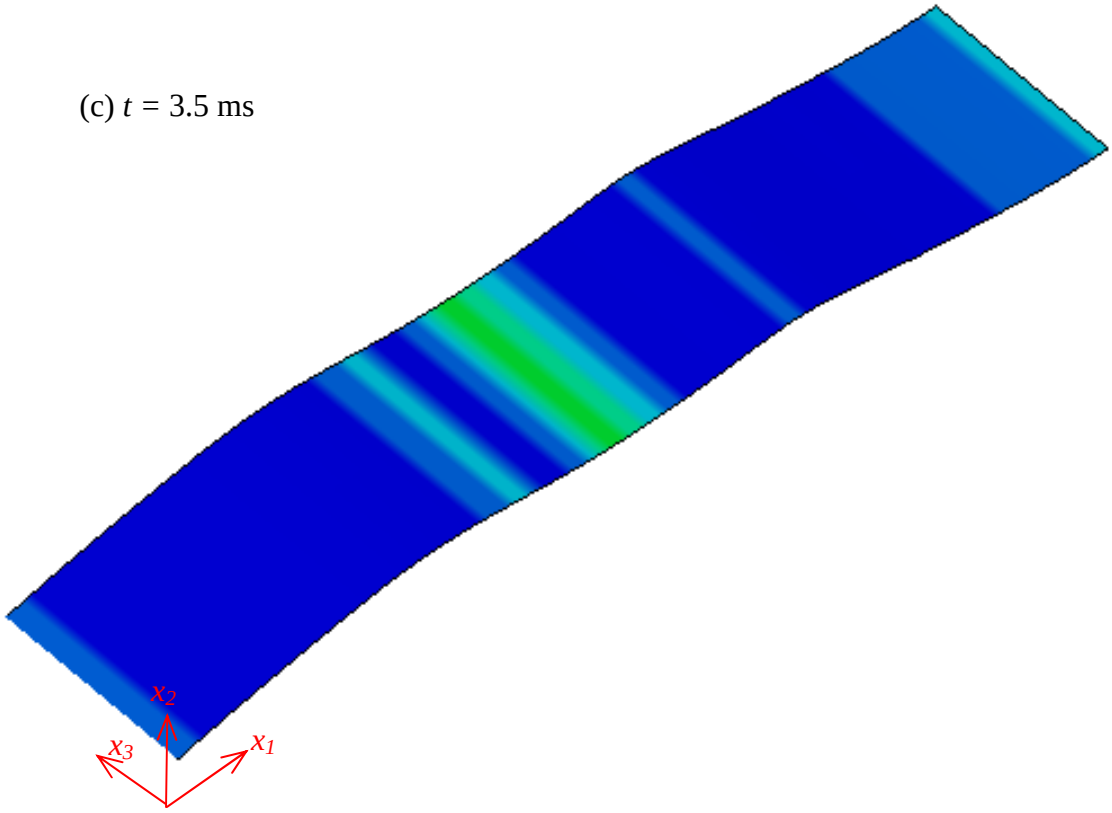

(d) t = 4.0 ms

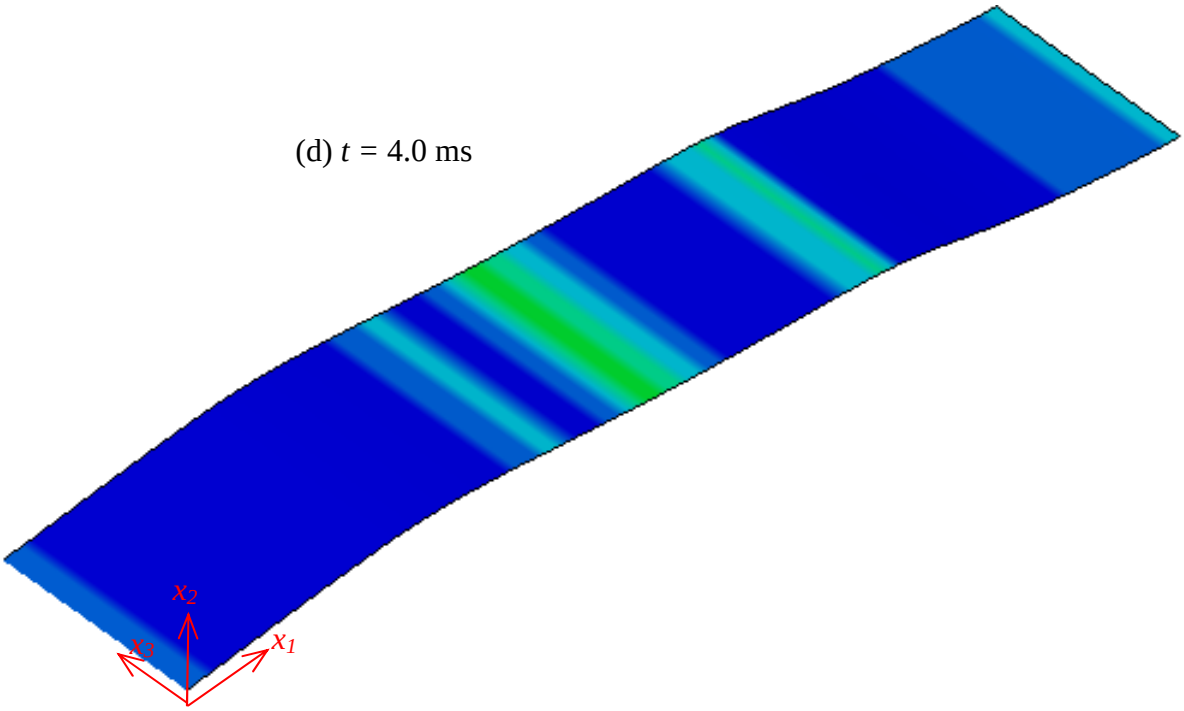

Figure 106. Fringe plots of the damage variable ω_{11} on the bottom surface of the plate.

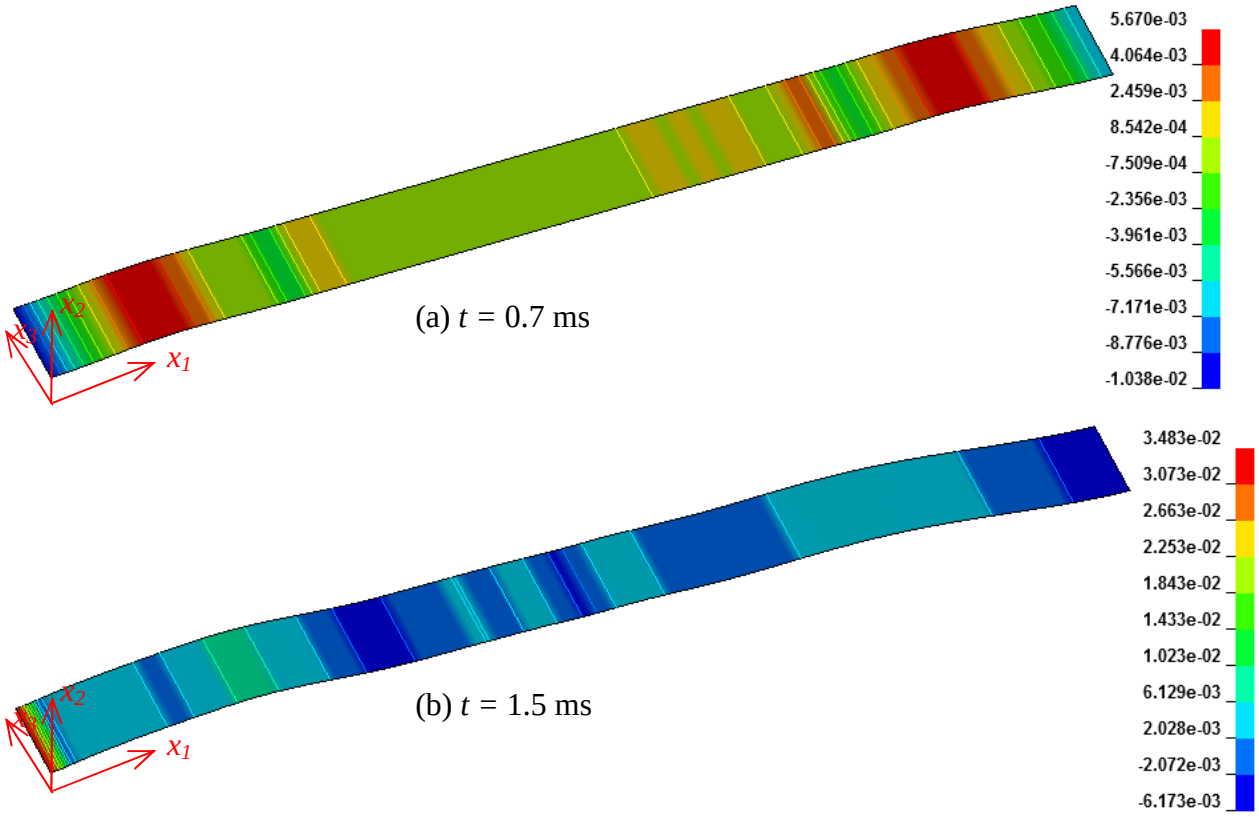

(a) t = 0.7 ms

(b) t = 1.5 ms

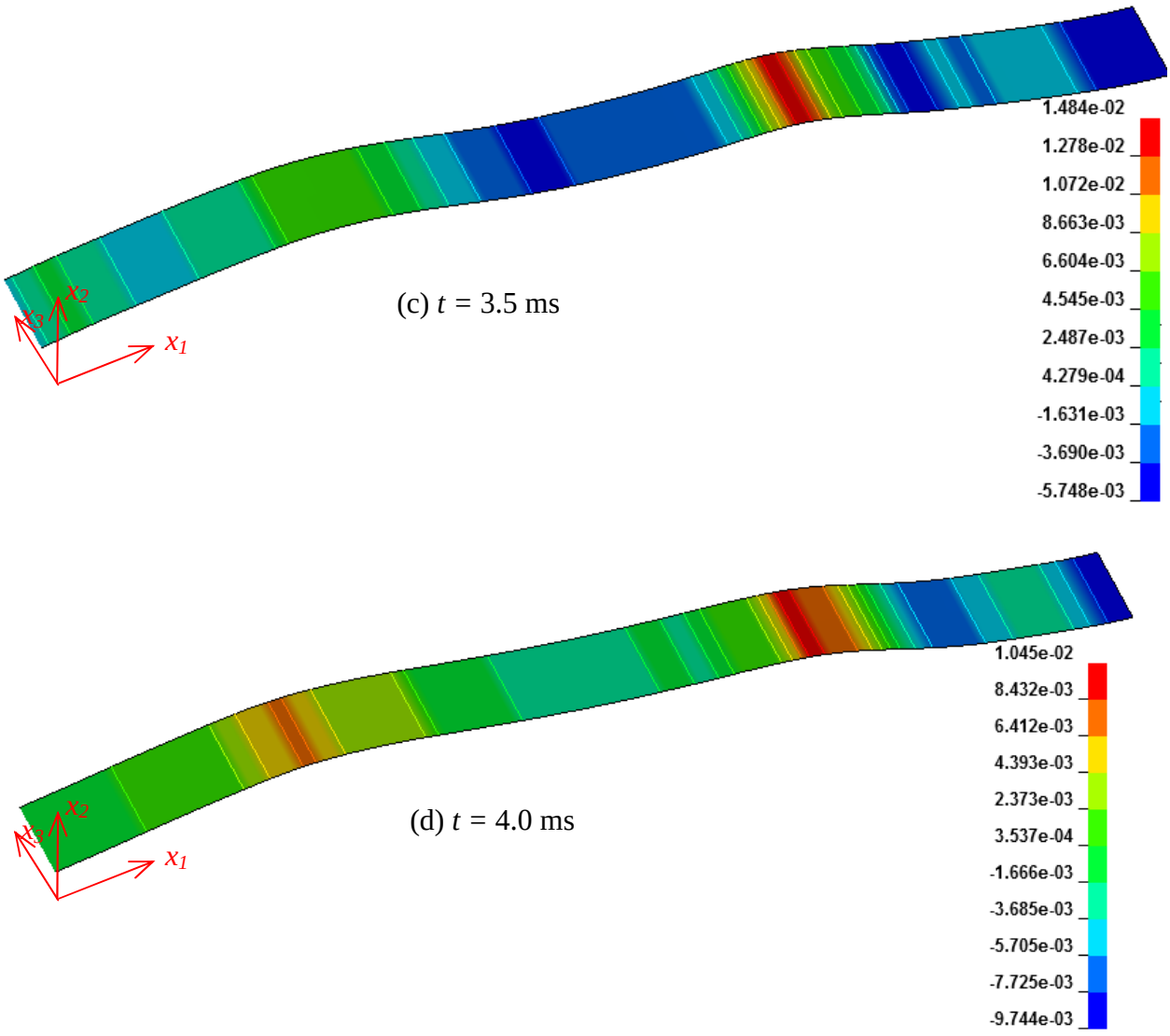

Figure 107. Fringe plots of the strain ε_{11} on the top surface of the plate.

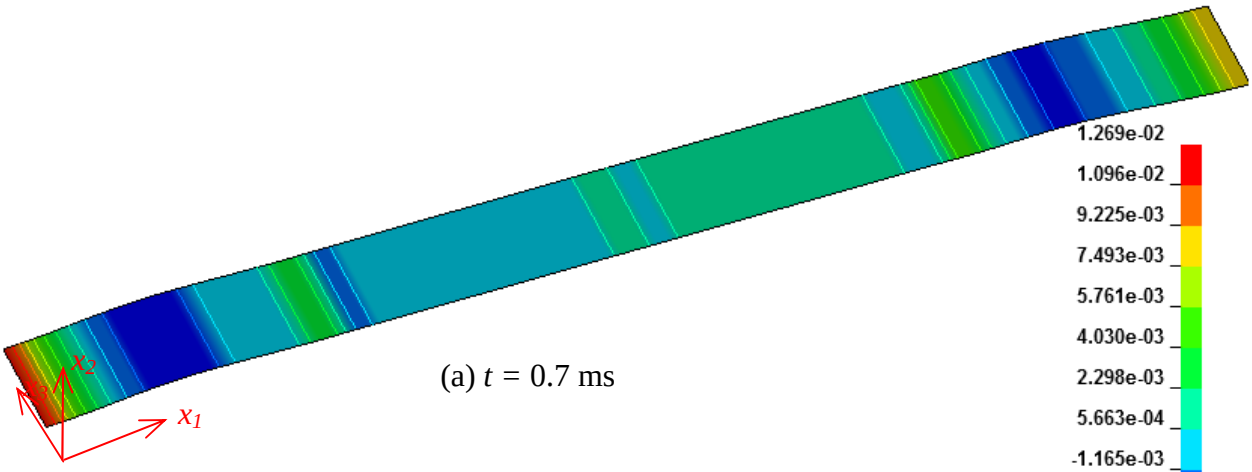

(a) t = 0.7 ms

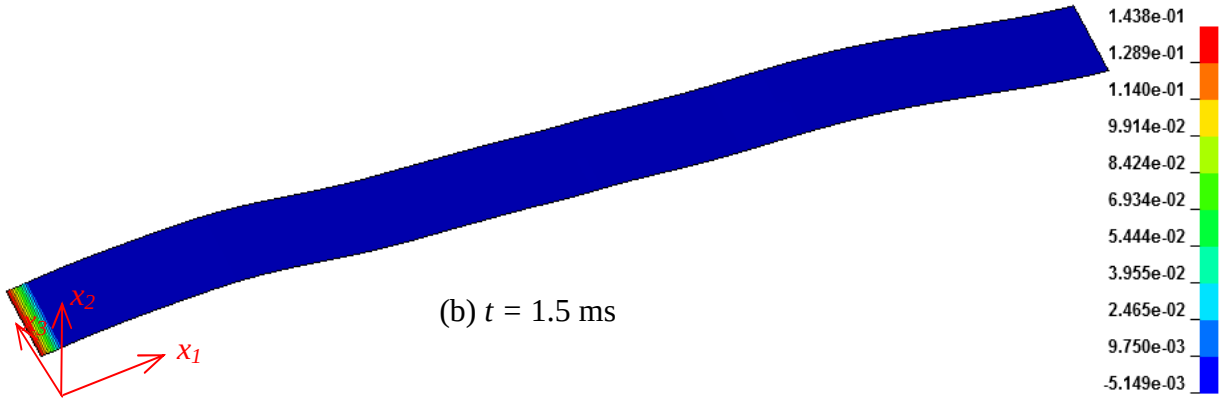

(b) t = 1.5 ms

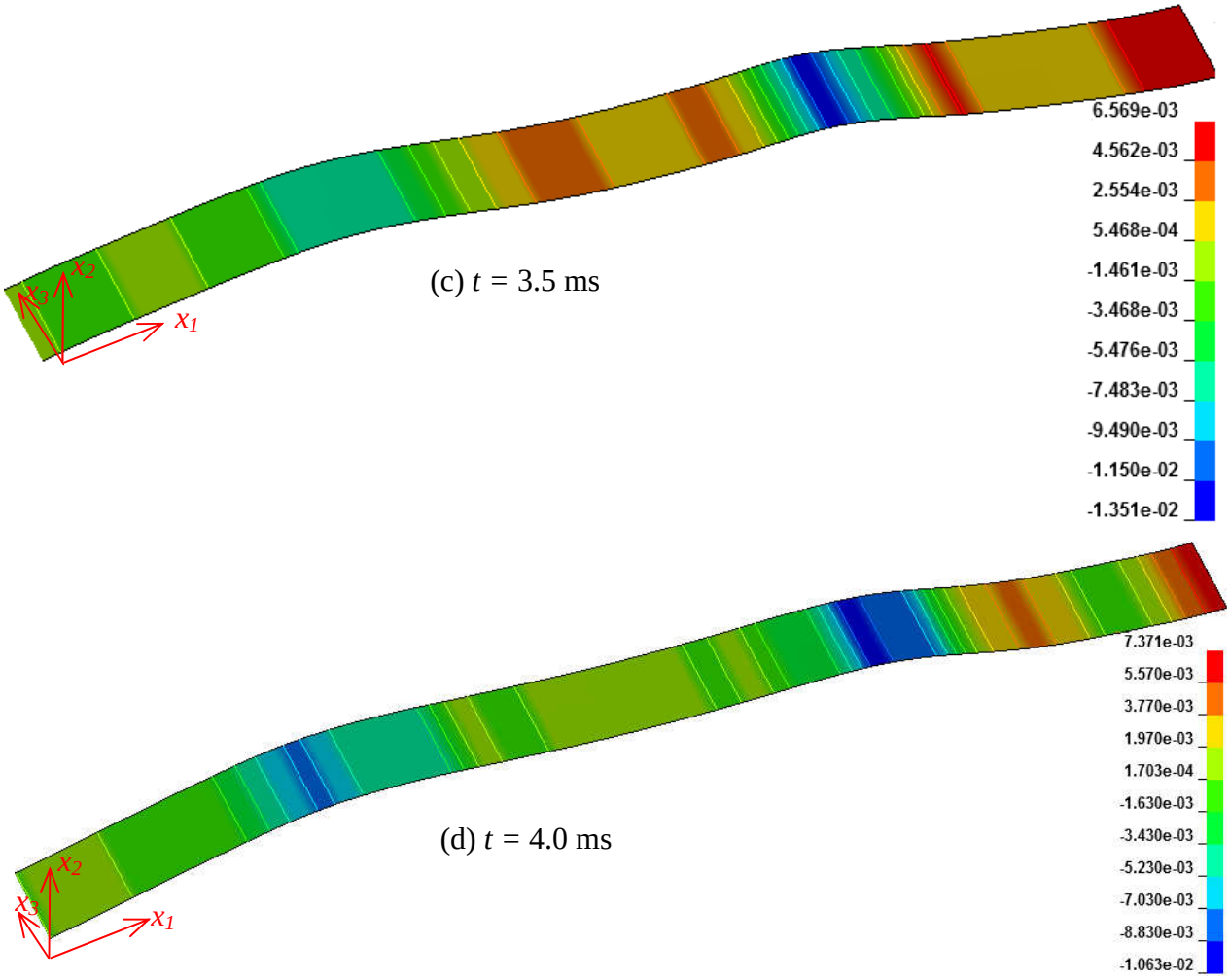

Figure 108. Fringe plots of the strain ε_{11} on the bottom surface of the plate.

Figure 109 (a) exhibits the deformed shape of the hull and the water and figure 109 (b) shows variations of the normal and the tangential velocities of the water at the interface of the deformable panel and water along the x_1-direction at 1.57 ms; similar results at 3 ms are shown in figures 110 (a) and (b). The normal and the tangential velocities of the panel at the interface are also shown. Just after 1.57 ms, the hull fails near the keel. Water is assumed inviscid, therefore only the normal component of the velocity should be continuous at the panel-water interface. Figures 109 (c) and 110 (c) show that the percentage difference in the normal component of the velocity of the panel and the water at the interface is less than 10% everywhere along the span of the panel except at the jet flow. The tangential component of the velocity of the water and the panel are not same along the span of the panel indicating slipping of water over the panel-water interface. We observe oscillations in the normal component of the water velocity, which could be due to the approximate evaluation of the local slope of the hull/water interface. The jet length is considerably smaller than that found for simulations reported in the previous sections. A very fine mesh is needed to resolve the normal and the tangential component of velocities inside the jet flow, and the sudden jump of the normal component of the water velocity at the jet flow (at x_1 = 0.25 m and 0.45 m for 1.5 ms and 3 ms, respectively) is probably due to errors in the numerical solution. The tangential velocity of the water at the interface increases from zero near the keel to about 60 m/s and 50 m/s in the jet flow at 1.57 ms and 3.0 ms, respectively.

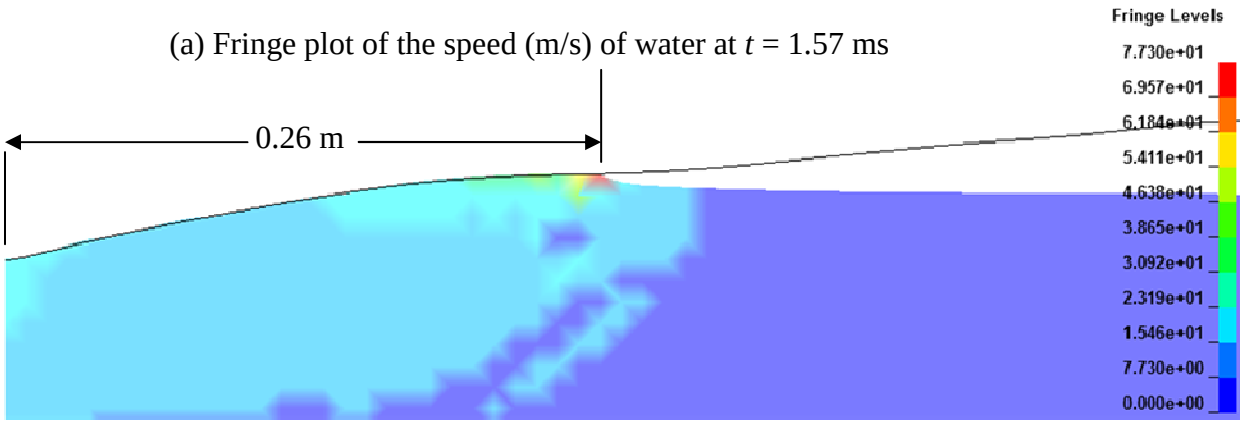
(a) Fringe plot of the speed (m/s) of water at t = 1.57 ms
0.26 m
Fringe Levels
7.730e+01
6.957e+01
6.184e+01
5.411e+01
4.638e+01
3.865e+01
3.092e+01
2.319e+01
1.546e+01
7.730e+00
0.000e+00

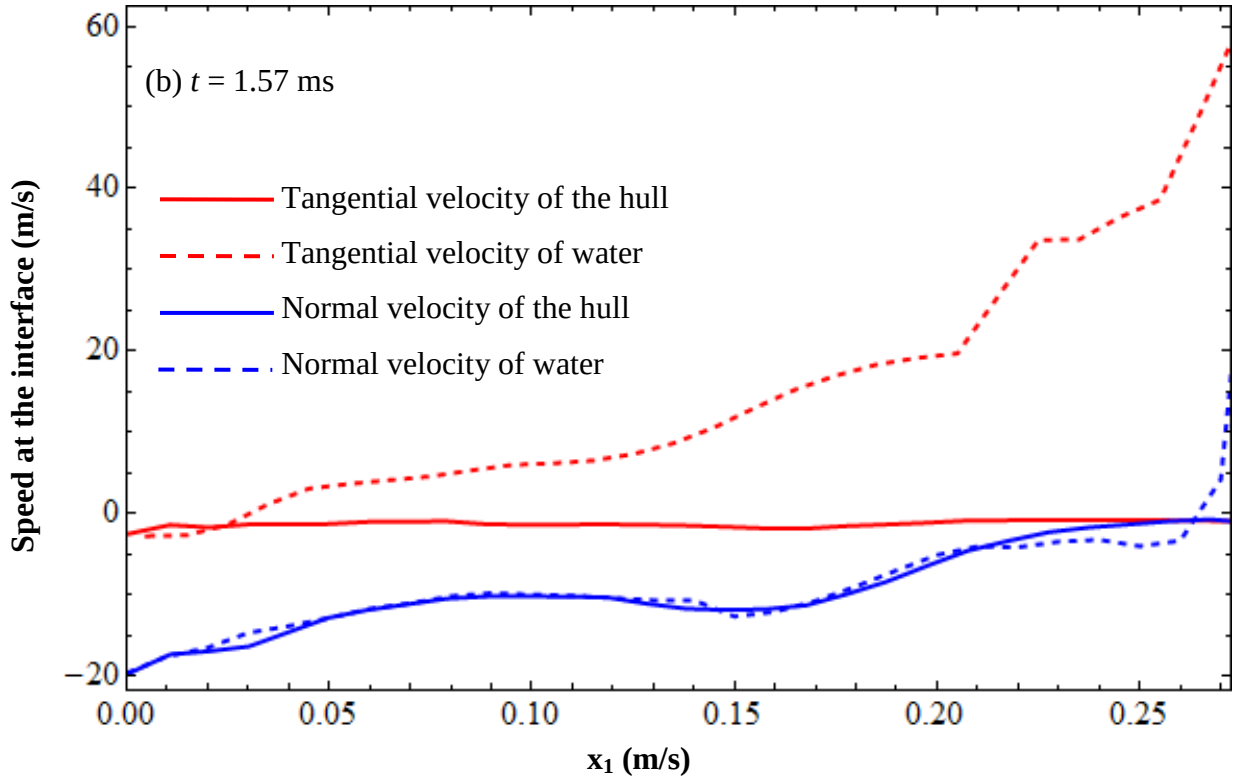
(b) t = 1.57 ms
Tangential velocity of the hull
Tangential velocity of water
Normal velocity of the hull
Normal velocity of water
Speed at the interface (m/s)
60
40
20
0
−20
0.00
0.05
0.10
0.15
0.20
0.25
x1 (m/s)

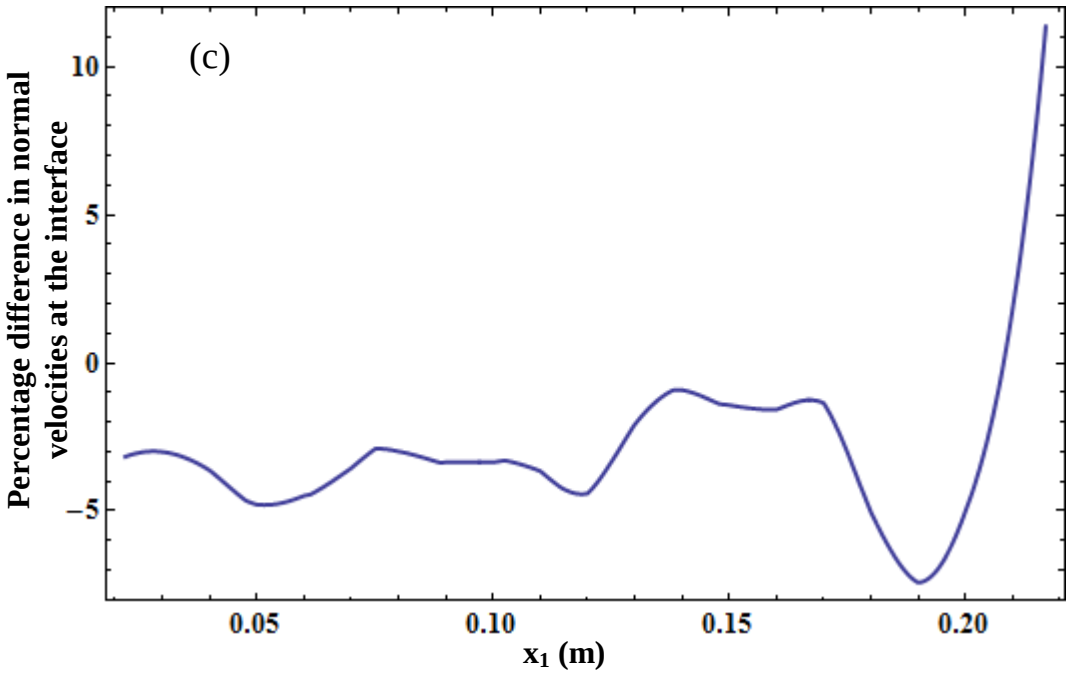

Figure 109. At t = 1.57 ms, (a) deformable panel and deformed water region, (b) variation of the velocity of the panel and the water particle at the panel-water interface, (c) percentage difference in the normal velocities of the panel and the water particle at the panel-water interface versus the x_1-coordinate of the water particle.

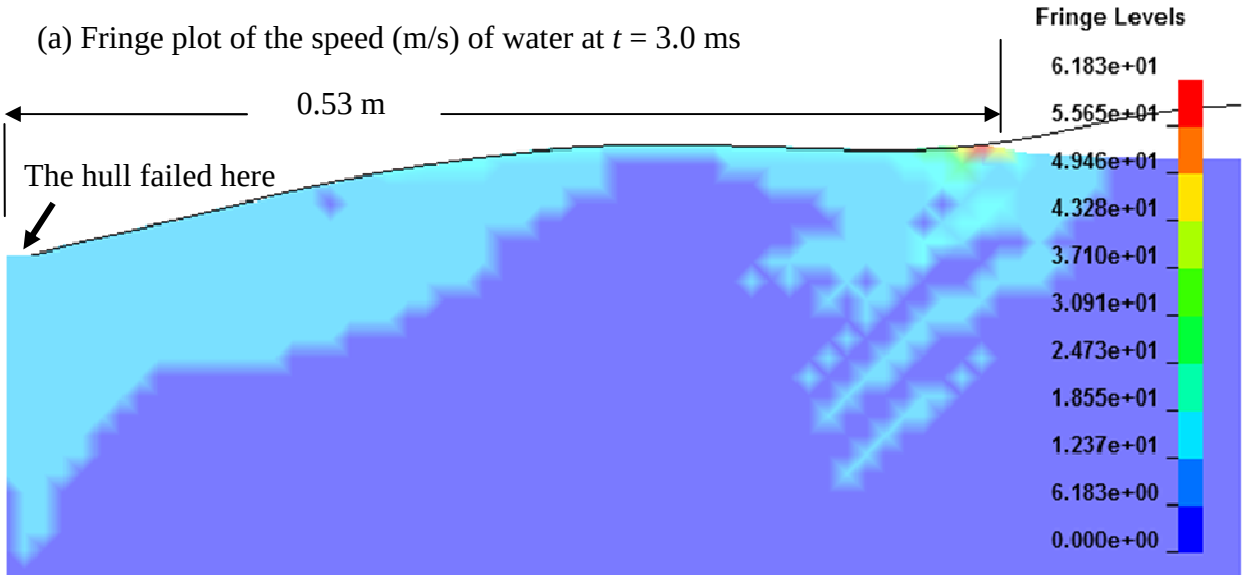
(a) Fringe plot of the speed (m/s) of water at t = 3.0 ms
0.53 m
The hull failed here
Fringe Levels
6.183e+01
5.565e+01
4.946e+01
4.328e+01
3.710e+01
3.091e+01
2.473e+01
1.855e+01
1.237e+01
6.183e+00
0.000e+00

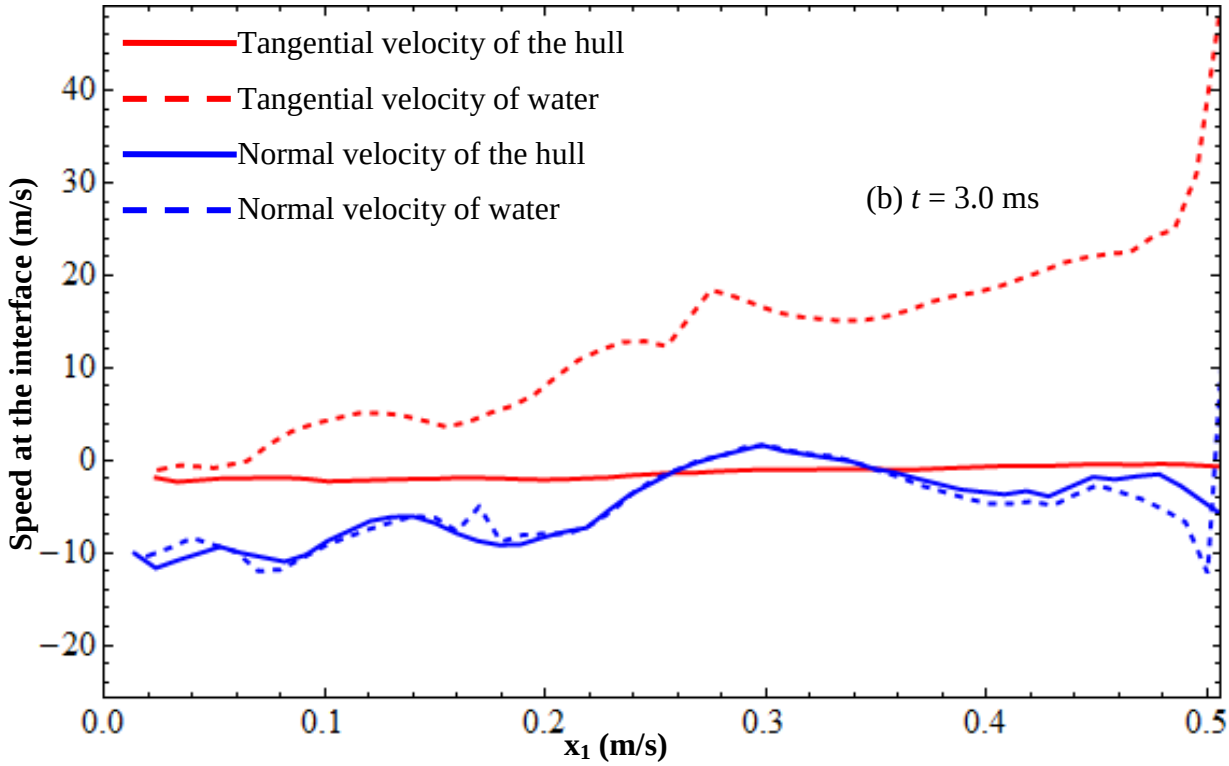
Tangential velocity of the hull
Tangential velocity of water
Normal velocity of the hull
Normal velocity of water
(b) t = 3.0 ms
Speed at the interface (m/s)
40
30
20
10
0
−10
−20
0.0
0.1
0.2
0.3
0.4
0.5
x_1 (m/s)

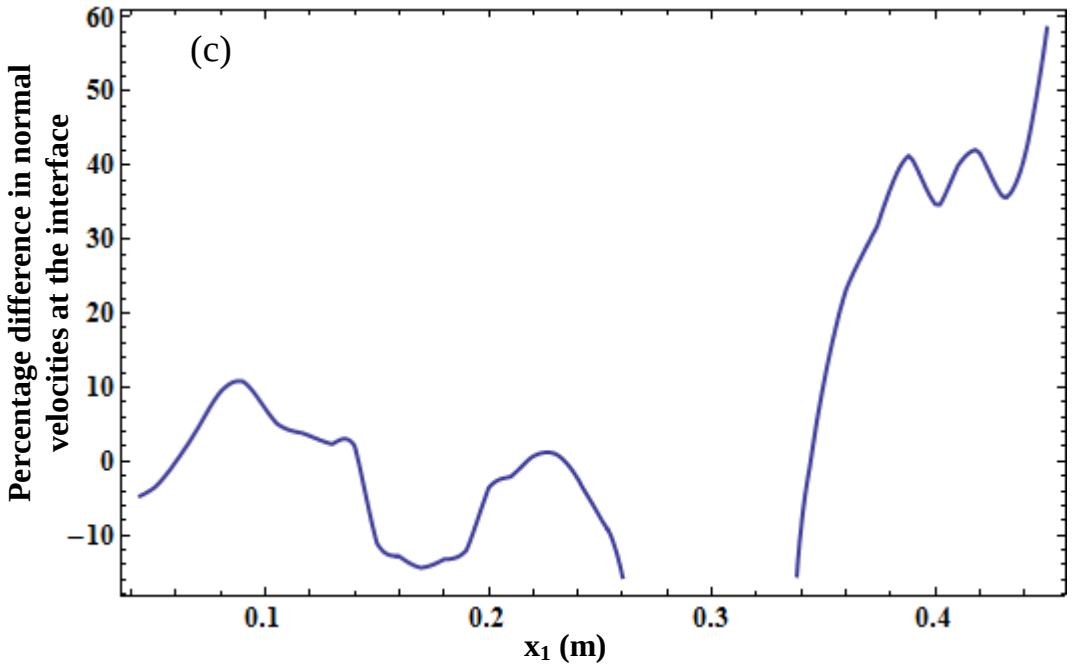

Figure 110. At t = 3 ms, (a) deformable panel and deformed water region, (b) variation of the velocity of the panel and the water particle at the panel-water interface, (c) percentage difference in the normal velocities of the panel and the water particle at the panel-water interface versus the x_1-coordinate of the water particle.

2.3.6. Slamming of a rigid wedge and a sandwich composite panel of deadrise angle 10^0

During the slamming of either a rigid panel or a composite sandwich panel of deadrise angle 10^0 deformations of water will be non-symmetric with respect to the x_2-axis (see figure 111); we assume that a plane strain state of deformation prevails. Thus the focus here is to understand how this asymmetry in deformations of water affects the pressure distribution on the hull. We assume that the 0.5 m long hull simply supported at both ends enters calm water with a downward velocity of 3 m/s, and for a sandwich panel, the 15 mm thick core is made of an isotropic foam with ρ^s = 130 Kg/m^3, E = 110 MPa, v = 0.170 and $G = E/(2(1+ v))$ = 47 MPa. The two face sheets, each 2.5 mm thick, are made of an isotropic material with ρ^s = 1800 Kg/m^3, E = 17.8 GPa, v = 0.156 and $G = E/(2(1+ v))$ = 7.7 GPa. Computed results are compared with test findings of Allen and Battley [109] who designed their experiments such that deformations could be considered symmetric about the left edge of the hull. We note that the mass density of face sheets does not account for the mass of the rig. The fixed end of the panel has constant downward velocity of 3 m/s.

The water domain simulated is 3.5 m long and 1.4 m high, and the height of the initially void domain above the water is 0.135 m. When studying the problem for a rigid hull, the FE mesh for water (the void) region has 700 and 480 (700 and 30) uniform elements along the x_1- and the x_2-directions, respectively; the FE mesh for the hull has 100 shell elements along its span. For analyzing deformations of a sandwich panel, the water (void) domain has 960 (500) and 500 (50) elements along the x_1- and the x_2- directions; the core and each face sheet are divided into 4 and 2 uniform elements in the thickness direction and they have 170 uniform elements along the span. We simulated this problem using three combinations of interface parameters to ascertain their optimum values; however, results computed using k_d = 2.4 GPa/m and c = 1 are reported here.

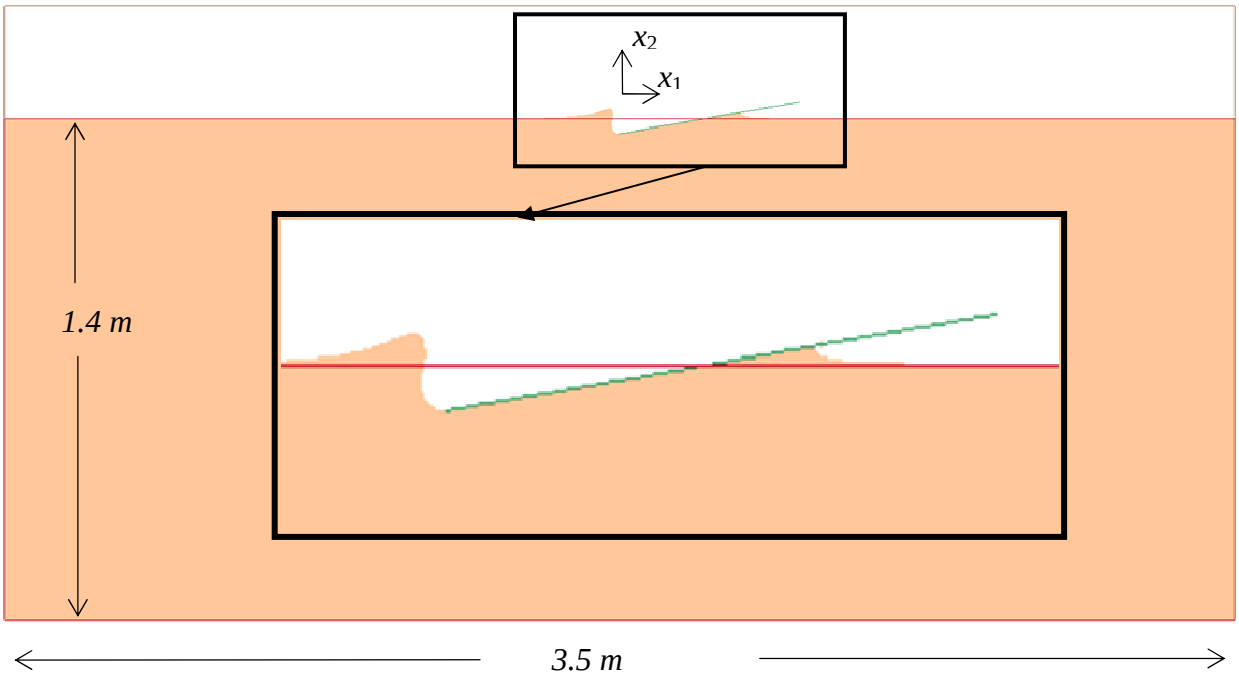

Figure 111. The deformed water and the rigid hull at t = 14 ms.

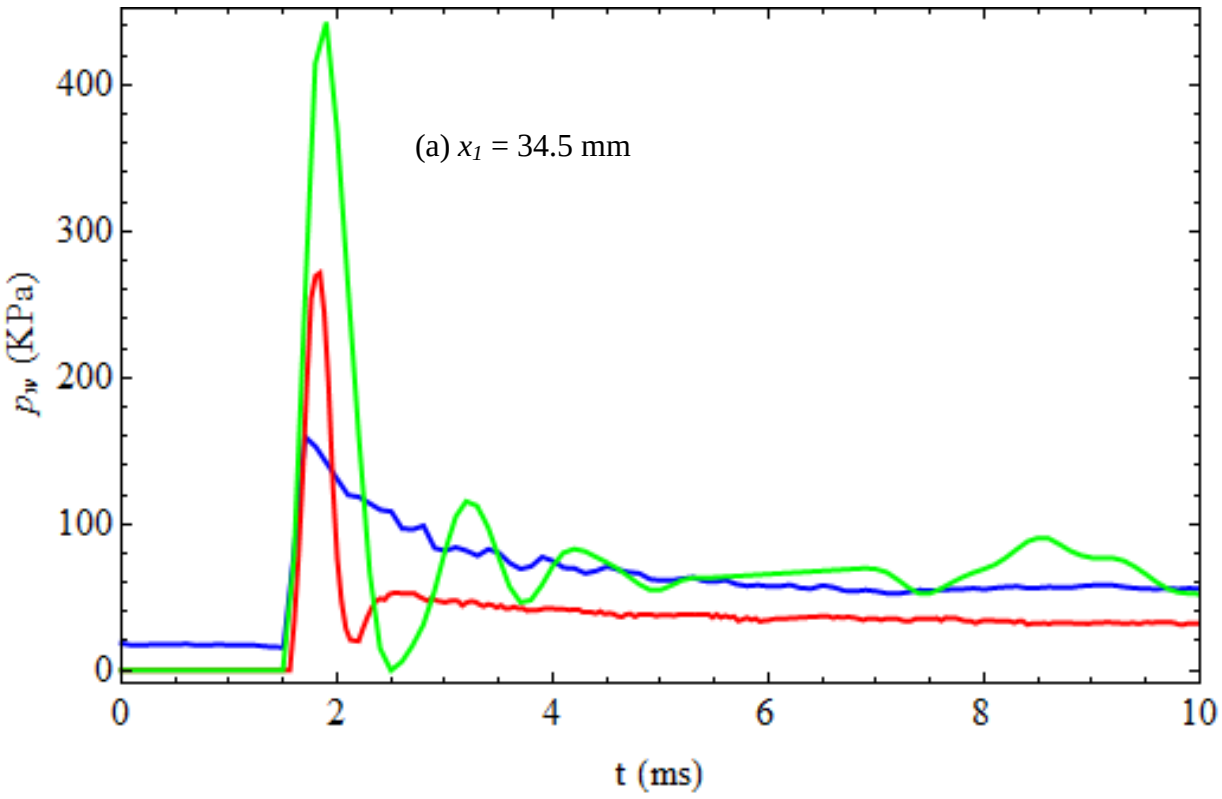

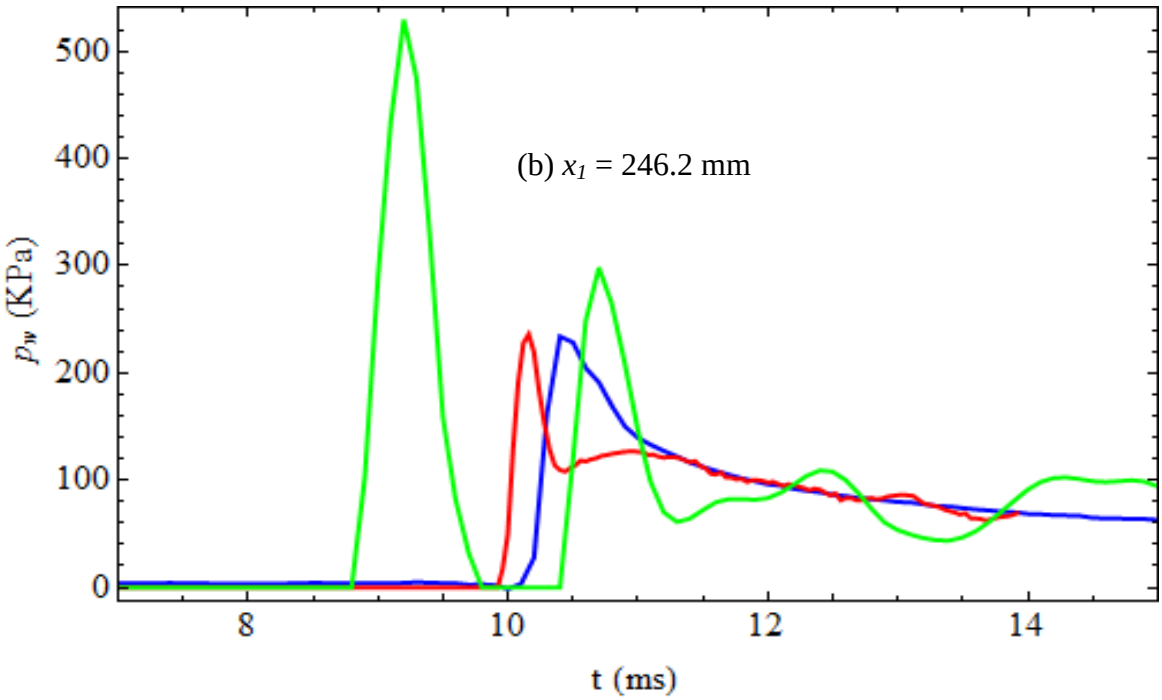

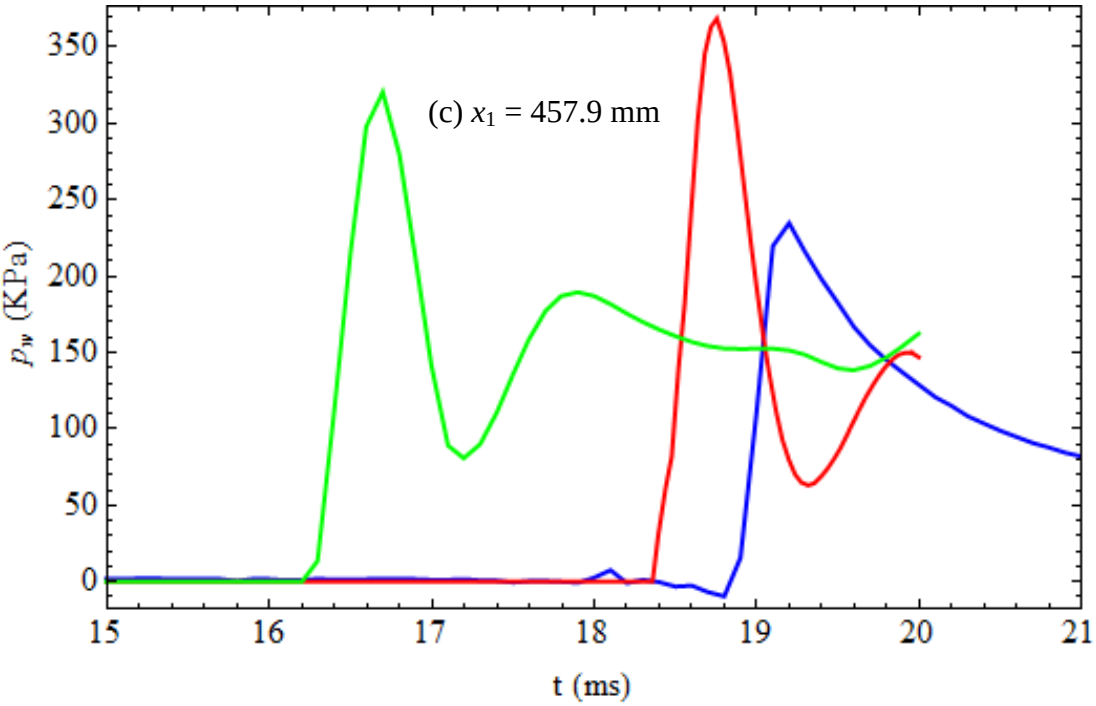

Figure 112. Time histories of the interface pressure at three locations on the rigid hull-water interface for k_d = *2.4* GPa/m and c = 1; red curves: present non-symmetric deformations; green curves: present symmetric deformations; blue curves: experiment results [109].

Figure 111 shows the deformed water region and the rigid hull at 14 ms; time histories of the pressure at three locations on the rigid hull based on symmetric and asymmetric deformations about the left edge are compared with the test results in figure 112. Only the time history of the pressure at x_1=246.2 mm computed with the assumption of asymmetric deformations about the left edge agrees well with the test results; the computed pressure at the other two locations noticeably differs from that found experimentally. It is clear that boundary conditions imposed at the left edge significantly influence the pressure at the three locations on the hull. It is not clear whether differences between the computed and the test results are due to the assumption of the hull being rigid since no real body is rigid. The computed time histories of the pressure at three locations on the sandwich hull are compared with the corresponding experimental ones in figure 113, and computed times for three wetted lengths (approximated as x_1-coordinate of the edge of the wetted surface) of the rigid and the sandwich wedges are compared in tables 14 and 15 with the experimental ones. These comparisons also reveal that the assumption of asymmetric deformations gives results that are closer to test findings than those based on the assumption of symmetric deformations.

Figure 114 shows the deformed water body and the deformed panel at 22 ms after impact. The jet shape near the right edge of the sandwich panel is quite different from those for a rigid wedge and for a deformable wedge composed of a fiber-reinforced composite.

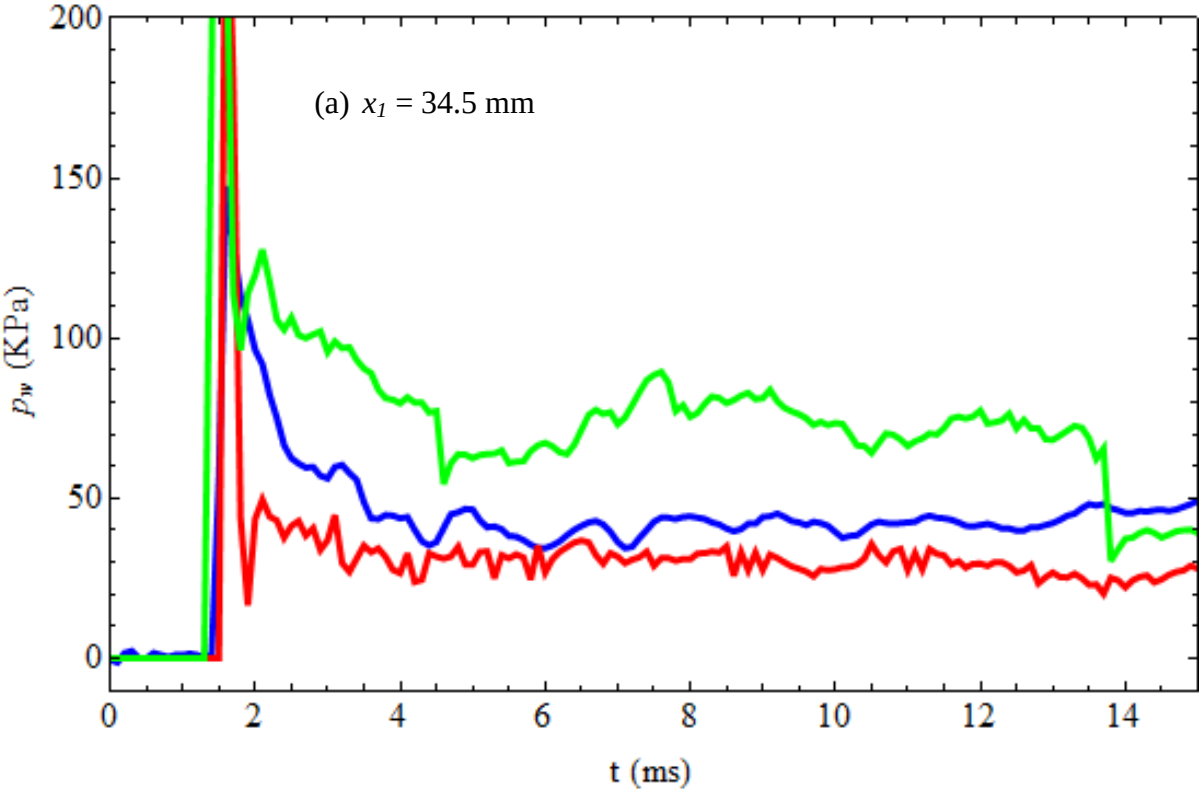
(a) x_1 = 34.5 mm
p_w (KPa)
t (ms)
0
50
100
150
200
0
2
4
6
8
10
12
14

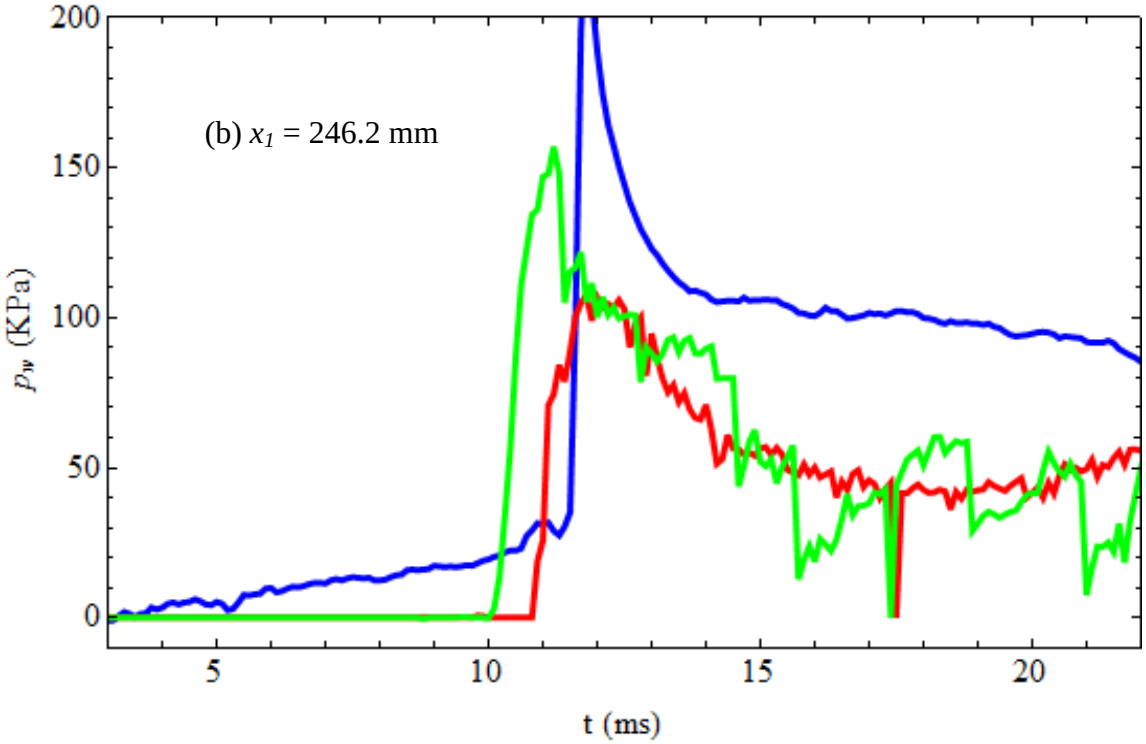
(b) x_1 = 246.2 mm
p_w (KPa)
t (ms)
0
50
100
150
200
5
10
15
20

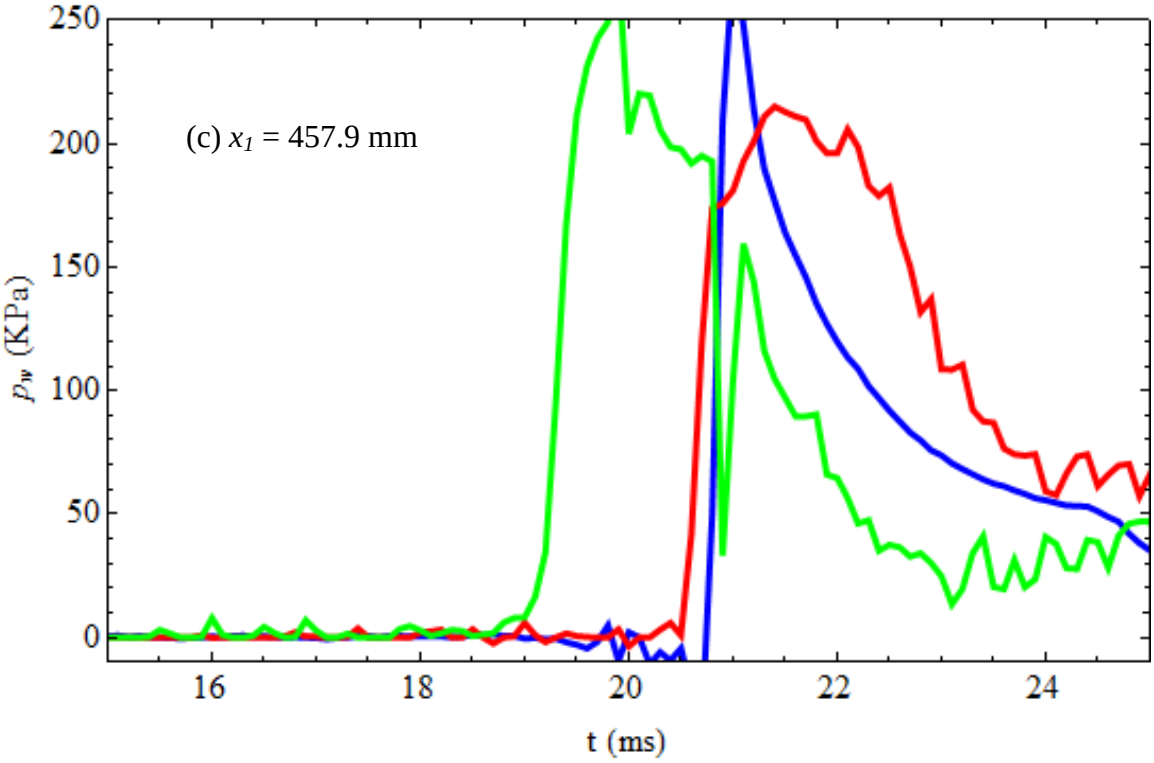

Figure 113. Time histories of the pressure at three locations on the hull-water interface for k_d = 2.5 GPa/m and c = 1. Red curves: present non-symmetric deformations; green curves: present symmetric deformations; blue curves: experiment results [109].

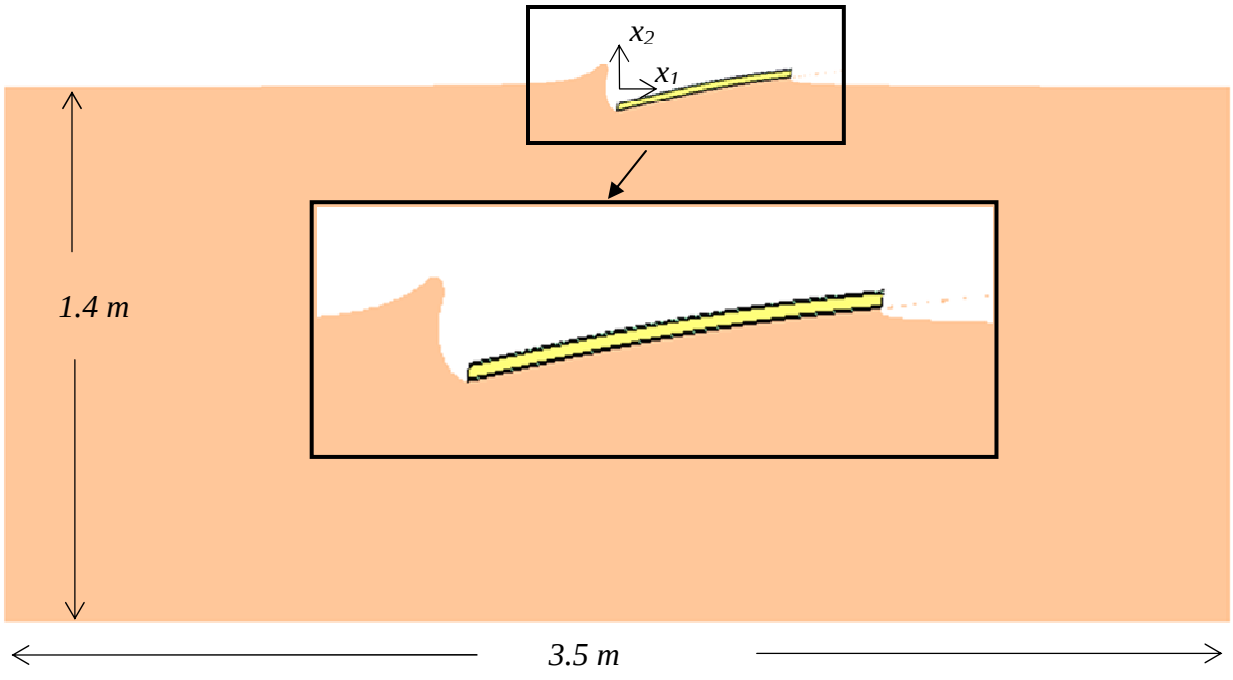

Figure 114. The deformed water region and the deformed sandwich panel at t = 22 ms.

Table 14: Time for wetted length of the rigid wedge

Wetted length (mm)	Time (ms)		
	Symmetric deformations	Asymmetric deformations	Experiment
34.5	1.5	1.5	1.5
246.2	8.7	9.8	10.0
457.9	16.2	18.4	18.8

Table 15: Time for wetted length of the sandwich wedge

Wetted length (mm)	Time (ms)		
	Symmetric deformations	Asymmetric deformations	Experiment
34.5	1.5	1.5	1.5
246.2	10.0	10.9	11.6
457.9	19.0	20.5	20.7

2.3.7. Delamination of the foam core from face sheets in a sandwich composite plate

For the sandwich hull studied in Section 2.3.4, we examine if delamination occurs at the core/face sheet interface. The FE mesh used in the simulation is similar to the fine mesh described in subsection 2.3.4 except that at the interface between the core and the face sheets the FE mesh for the core and the face sheets have separate nodes which are tied using the contact algorithm CONTACT_TIED_SURFACE_TO_SURFACE_FAILURE in LS-DYNA, and the tie is released when the following condition is satisfied at a node.

$$\left(\frac{Max(0.0, T_{nomal})}{F_{normal}}\right)^2 + \left(\frac{T_{shear}}{F_{shear}}\right)^2 - 1 > 0 \tag{80}$$

Here T_{normal} and T_{shear} are the normal and the tangential tractions at a point on the interface between the core and the face sheet, F_{normal} and F_{shear} are corresponding strengths of the interface, and we have set F_{normal} = 1.0 MPa and F_{shear} = 1.0 MPa. After the tie is released between two overlapping nodes, the core and the face sheet nodes can slide over each other as if

the two contacting surfaces were smooth but not interpenetrating; the contact algorithm CONTACT_AUTOMATIC_SURFACE_TO_SURFACE in LS-DYNA is used to accomplish this.

The contact algorithm is checked by studying forced vibrations of the hull as described in subsection 2.3.4. For a very high value assigned to F_{normal} and F_{shear} to prevent delamination, the lowest natural frequency of the plate is found to be 107 Hz, which is the same as that computed in subsection 2.3.4 without using the tie and the contact algorithms. With F_{normal} = 1.0 MPa and F_{shear} = 1.0 MPa, delamination occurred all along the interface during the forced vibration analysis, and the lowest natural frequency of the delaminated plate decreased to 30 Hz.

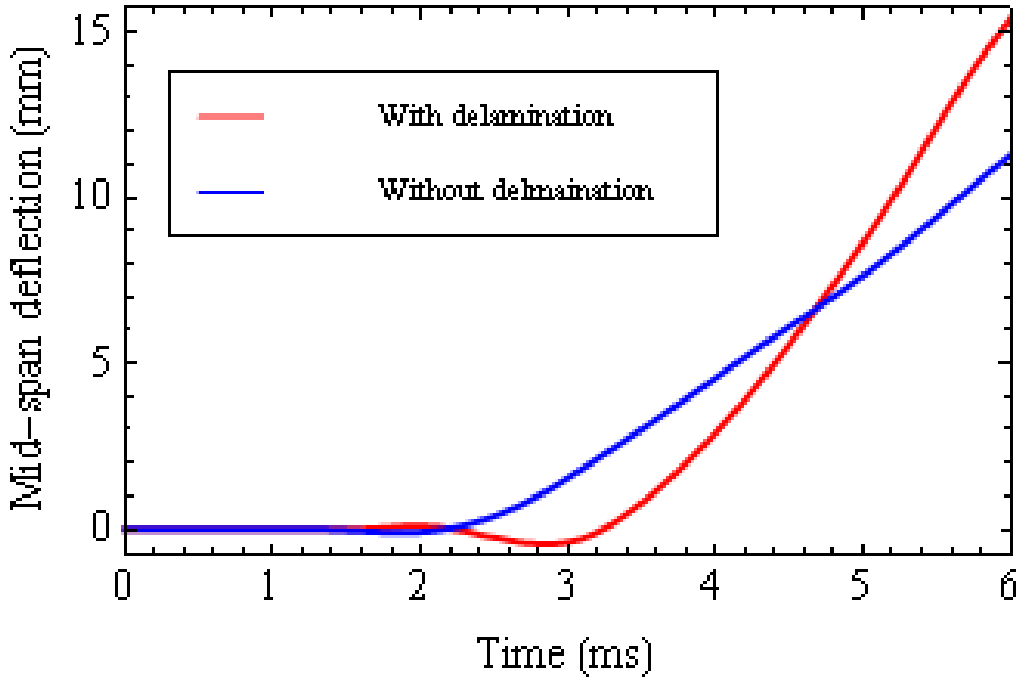

Figure 115. Time histories of the deflection of the hull centroid with and without the consideration of delamination.

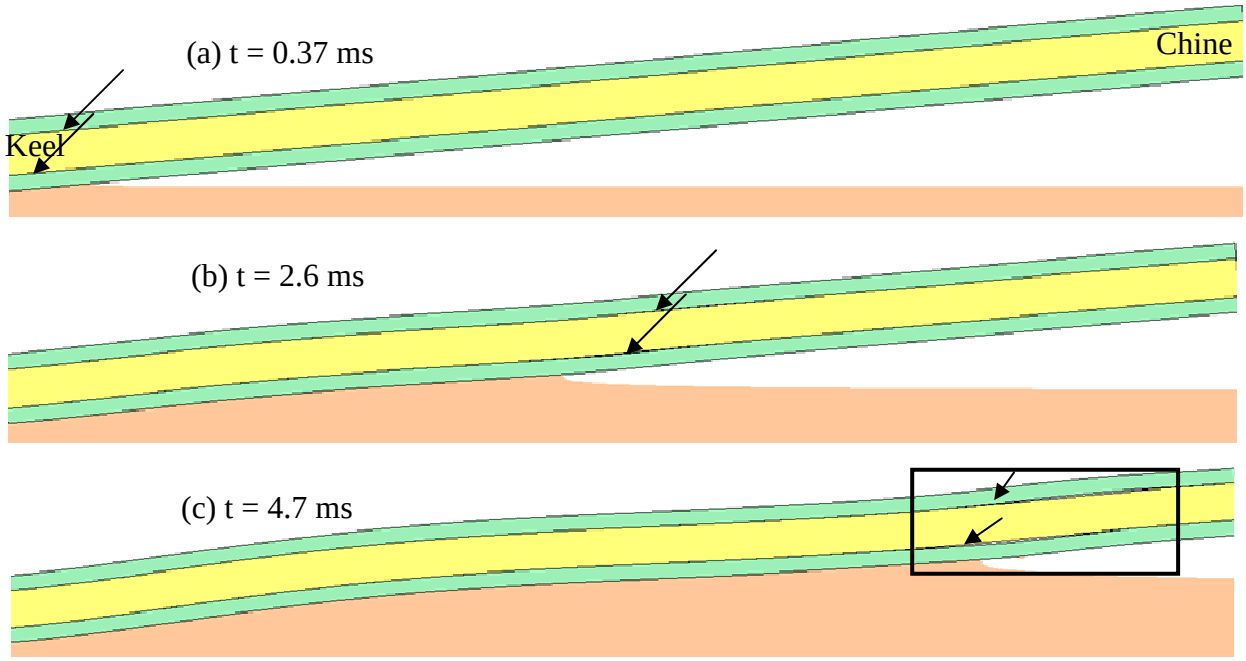

Figure 116. Deformed shapes of the hull and the water at three different times showing the delamination (indicated by arrows). The boxed area in figure 116(c) is zoomed in figure 117.

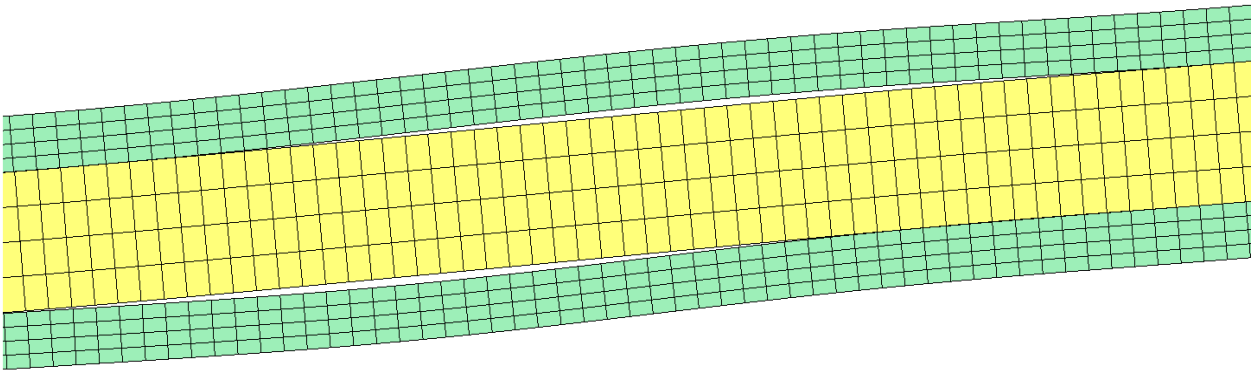

Figure 117. Deformed shapes of a part of the hull near the chine (see the boxed area in figure 116(c)) showing the separation of the core from face sheets due to the delamination at t = 4.7 ms.

Results exhibited in figure 115 illustrate that time histories of the deflection of the centroid of the hull with and without the consideration of delamination between the core and the face sheets are quite different. At 6 ms, when the water level reaches the chine, the difference in the two sets of results is about 40%. Figure 116 shows the deformed hull at three times, and arrows point to the delaminated regions. A portion of the hull with delaminated face sheets at t = 4.7 ms is exhibited in figure 117.

Figure 118(a) shows local slopes ζ and η of the top face sheet and the core at points (x_1, x_2) and (y_1, y_2). Two points (x_1, x_2) and (y_1, y_2) on the top face sheet and the core, respectively, are initially coincident (X_1=Y_1 and X_2=Y_2) and are at the mid span of the panel, therefore, $X_1 = Y_1 =$ 0.5 m. At 1.5 ms the delamination occurs and two points separate from each other. Until about 1.5 ms the two slopes are the same and equal the initial slope (deadrise angle) of 5 degree. After 1.5 ms, the local slopes of the face sheet and the core deviate from each other until about 3 ms, at which time, the two slopes again become equal. At 5 ms, the slopes again deviate from each other. Figure 118(b) shows the components of relative displacement u_n and u_t, which are, respectively, normal and tangential to the top surface of the core at (y_1, y_2) and are given by

$$u_n = (x_2\text{-}y_2)\cos\eta - (x_1\text{-}y_1)\sin\eta \tag{81}$$

and

$$u_t = (x_2\text{-}y_2)\sin\eta + (x_1\text{-}y_1)\cos\eta. \tag{82}$$

Displacements u_n and u_t remain zero till 1.5 ms indicating no delamination. From 1.5 ms till about 3 ms, u_n and u_t increase and then decrease to zero. This implies that the gap between the two points increases initially from 1.5 ms to 2.5 ms before closing at about 3 ms. From 3 ms to 5.5 ms u_n remains almost zero while the absolute value of u_t increases indicating sliding between the core and the face sheet at the interface after the closure of the gap between them.

Figure 118(c) exhibits tangential (normal) velocities v_t^1 (v_n^1) and v_t^2 (v_n^2) of points (x_1, x_2) and (y_1, y_2), respectively. These velocities are given by

$$v_t^1 = v^1{}_1\cos\zeta + v^1{}_2\sin\zeta \tag{83}$$

$$v_n^1 = -\,v^1{}_1\sin\zeta + v^1{}_2\cos\zeta \tag{84}$$

$$v_t^2 = v^2{}_1\cos\eta + v^2{}_2\sin\eta \tag{85}$$

$$v_n^2 = -\,v^2{}_1\sin\eta + v^2{}_2\cos\eta. \tag{86}$$

Here, $v^1{}_1$ ($v^1{}_2$) and $v^2{}_1$ ($v^2{}_2$) are the x_1- (x_2-) velocities of points (x_1, x_2) and (y_1, y_2), respectively. After delamination at 1.5 ms tangential velocities of the two points deviate from each other. Normal velocities of the two points deviate from each other between 1.5 ms and 3 ms, at which point, they become almost same before deviating again at about 5.5 ms.

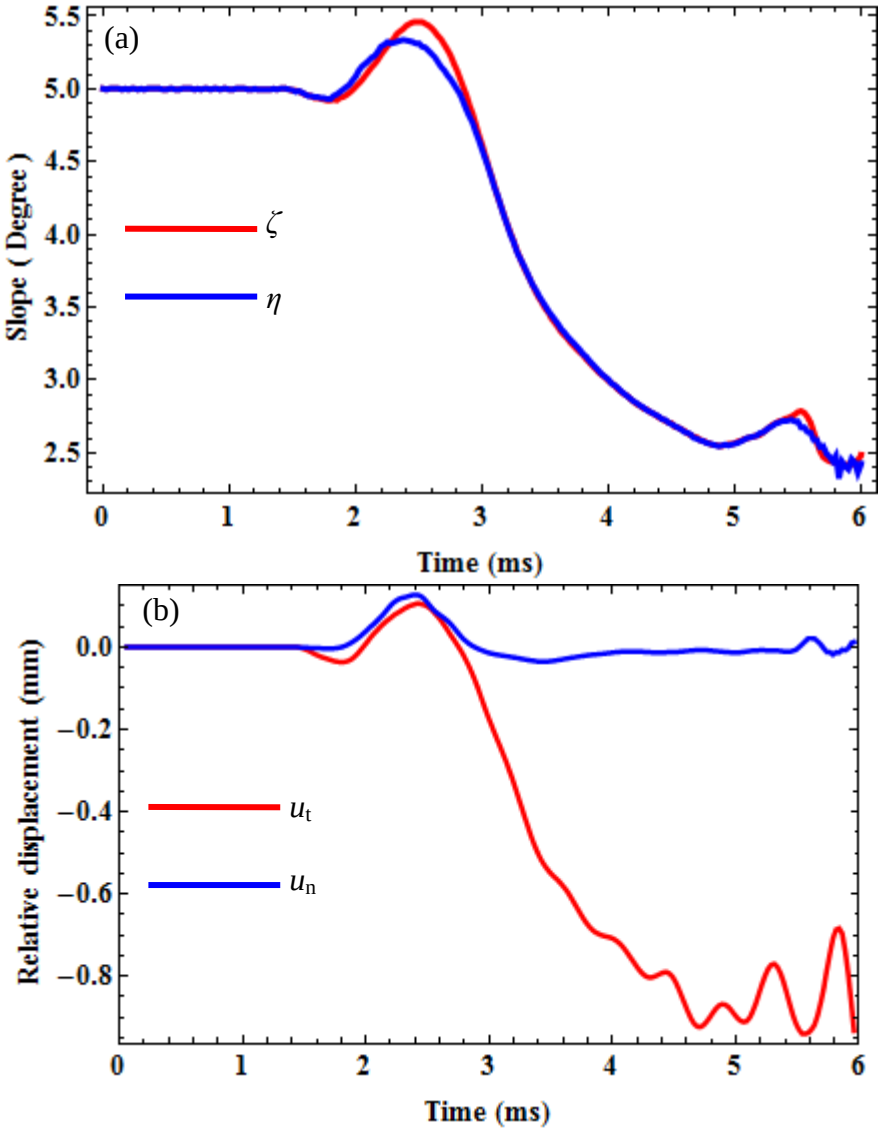
(a)
Slope (Degree)
5.5
5.0
4.5
4.0
3.5
3.0
2.5
ζ
η
0
1
2
3
4
5
6
Time (ms)
(b)
Relative displacement (mm)
0.0
−0.2
−0.4
−0.6
−0.8
u_t
u_n
0
1
2
3
4
5
6
Time (ms)

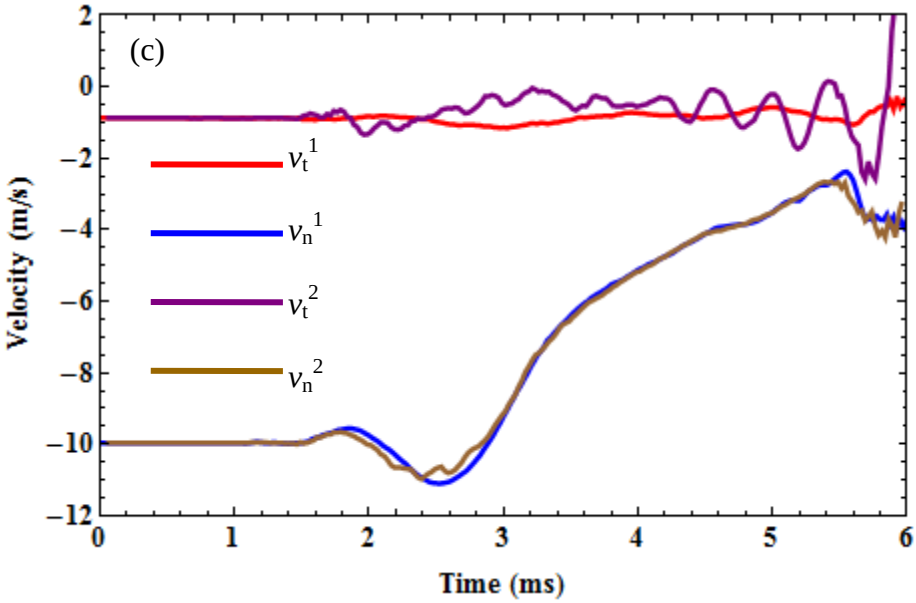

Figure 118 (a) Local slopes ζ and η of the face sheet and the core at two initialy coincident points (x_1,x_2) and (y_1,y_2) at the midspan of the panel; (b) the normal (tangential) relative displacement u_n (u_t); (c) tangential (normal) velocities v_t^1 and v_t^2 (v_n^1 and v_n^2) of points (x_1,x_2) and (y_1,y_2), respectively.

We have plotted in figure 119 variations of the strain energy density in the core and the two face sheets at t = 2.735 ms both with and without the consideration of delamination; results for the latter case are from subsection 2.3.4. The comparison of these two sets of results shows that the energy due to core deformations is insignificant after delamination, and the work done by external forces is used to deform the face sheets. After delamination the core is either separated from the face sheets or slides between them and there is no load transfer between the core and the face sheets except when the two are in contact when only the normal traction can be transferred from a face sheet to the core. The strain energy due to the transverse shear and the transverse normal strains in the core is negligible, whereas, without the consideration of the delamination, only the strain energy in the core due to the transverse shear strain is negligible but that due to transverse normal strain is significant.

Figure 120 exhibits fringe plots of the transverse normal strain in the core and face sheets at t = 2.735 ms with consideration of delamination, and figure 96(a) shows the similar result without considering delamination. When the face sheets are allowed to separate from the core the transverse normal strain in the core is significantly lower than that in the core when delamination is not allowed.

Figures 121 and 122 exhibit fringe plots of strains at t = 4.7 ms with and without the consideration of the delamination, respectively. Table 16 lists the maximum and the minimum values of strains in the core and the two face sheets at t = 4.7 ms. It is observed that the transverse normal strain in the core is significantly higher when delamination is not allowed than that when delamination is allowed.

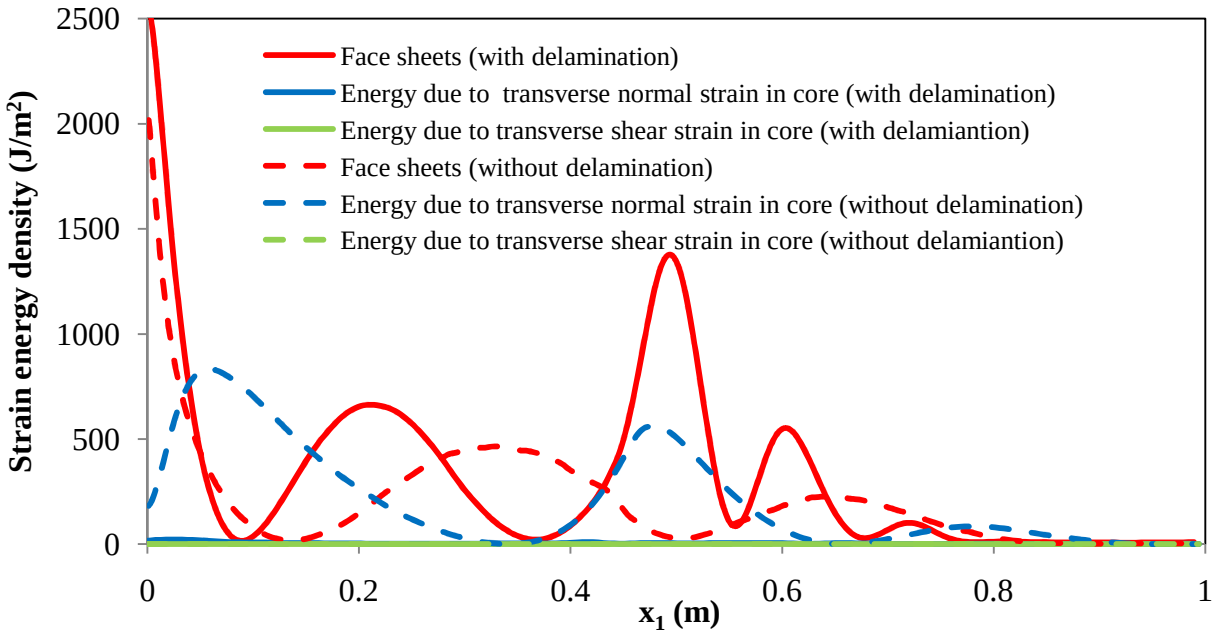

Figure 119. Strain energy density in the core and face sheets at t = 2.735 ms.

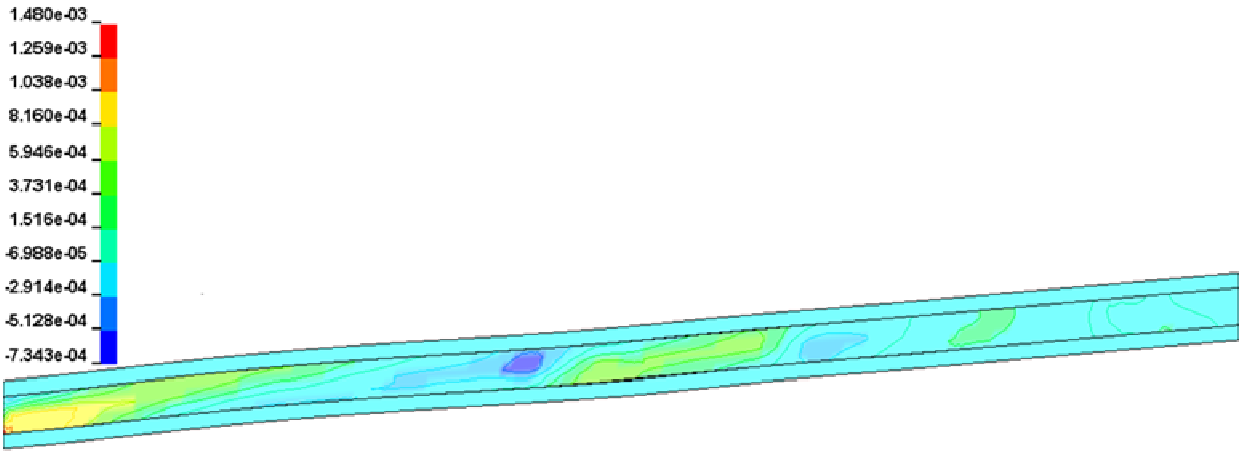

Figure 120. Fringe plots of the transverse normal strain in the core and the face sheets at t = 2.735 ms.

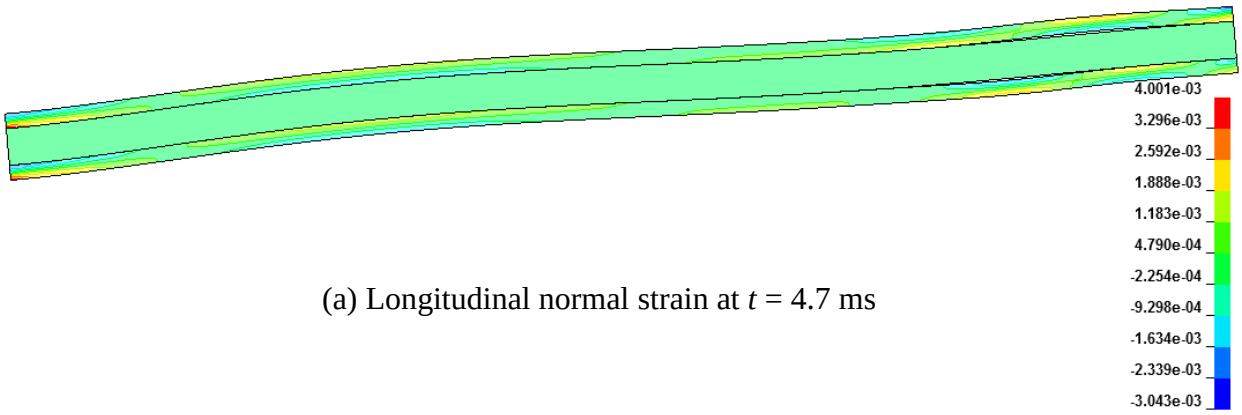

(a) Longitudinal normal strain at t = 4.7 ms

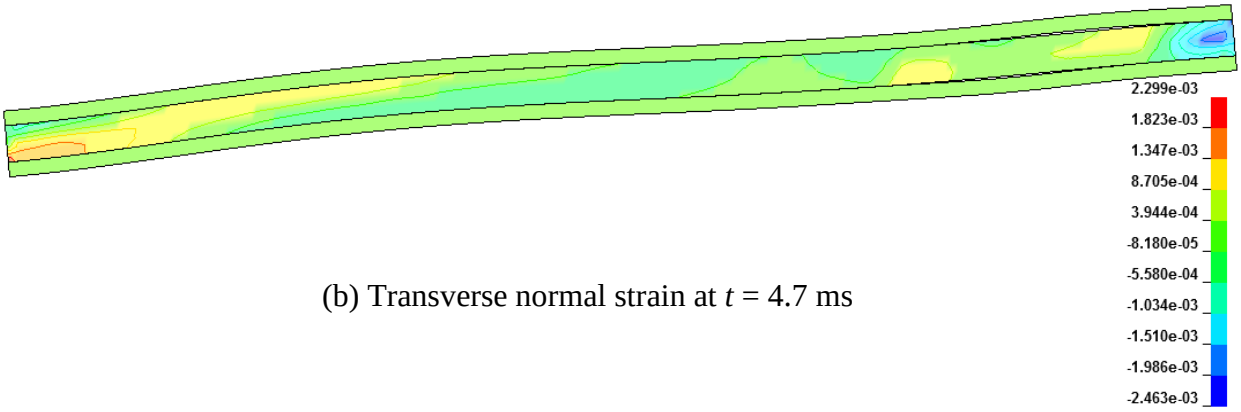

(b) Transverse normal strain at t = 4.7 ms

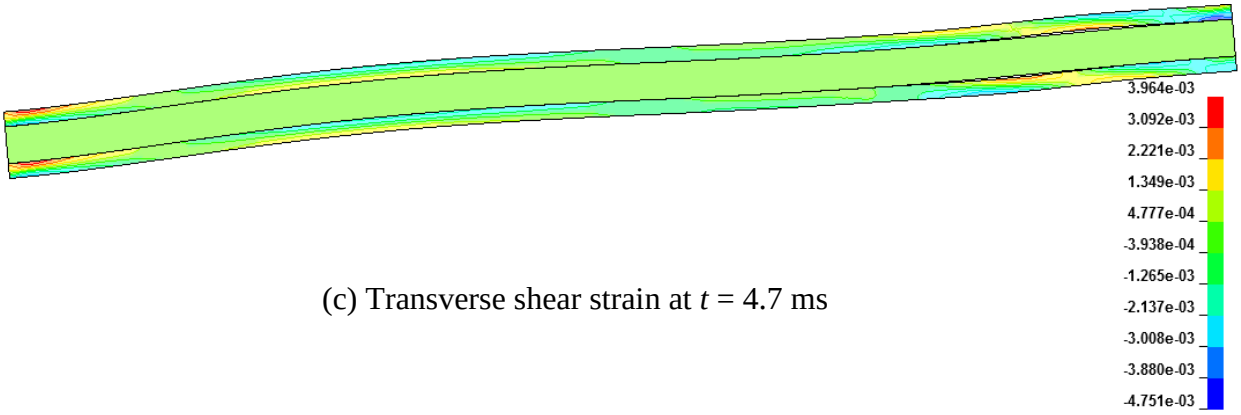

(c) Transverse shear strain at t = 4.7 ms

Figure 121. Fringe plots of the strain in the core and the face sheets at t = 4.7 ms with the consideration of the delamination.

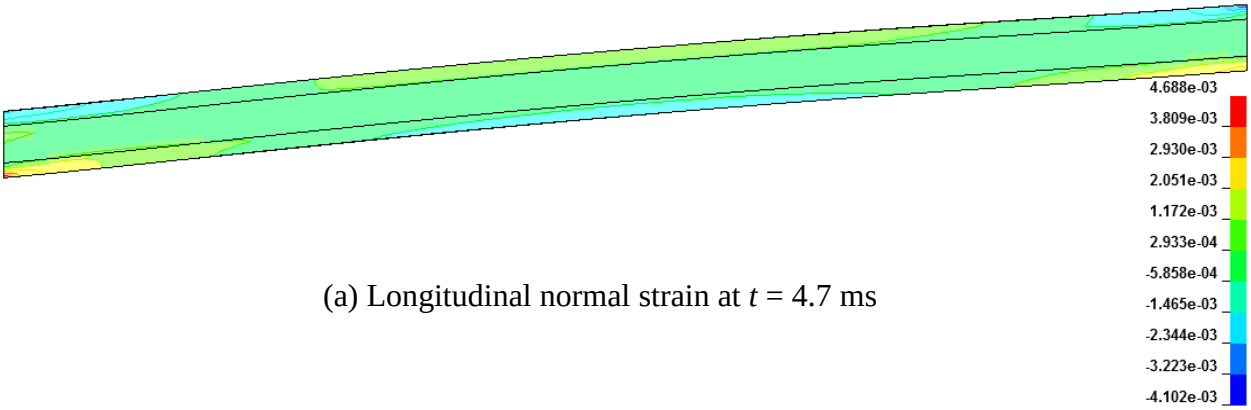

(a) Longitudinal normal strain at t = 4.7 ms

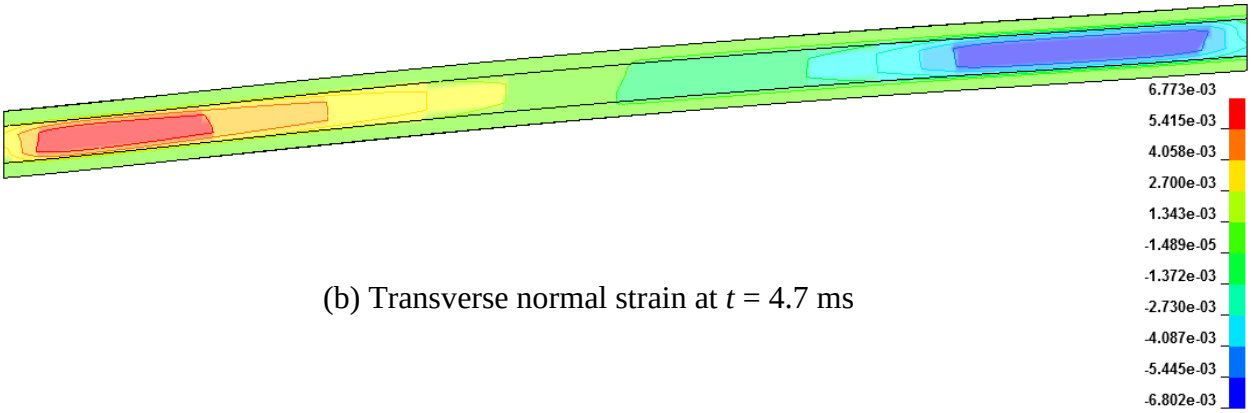

(b) Transverse normal strain at t = 4.7 ms

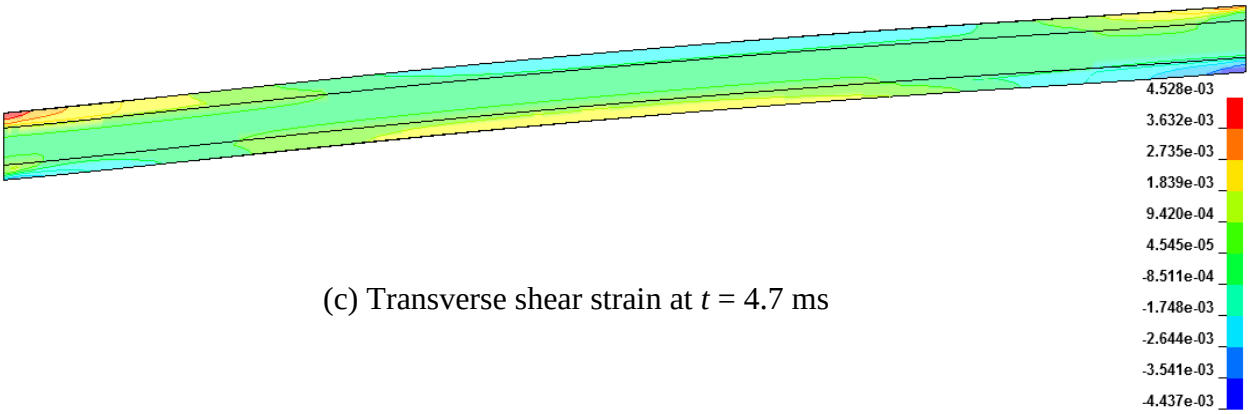

(c) Transverse shear strain at t = 4.7 ms

Figure 122. Fringe plots of the strain in the core and the face sheets at t = 4.7 ms without the consideration of the delamination.

Table 16: Maximum and minimum strains in the core and the two face sheets of the sandwich composite panel at *t* = 4.7 ms.

Strain		Delamination allowed		Delamination not allowed	
		Face sheets	Core	Face sheets	Core
Longitudinal normal strain	Min	-0.003	0.0000	-0.004	-0.0004
	Max	+0.004	0.0000	+0.005	+0.0005
Transverse normal strain	Min	0.0000	-0.0025	0.000	-0.007
	Max	0.0000	0.0023	0.0001	+0.007
Transverse shear strain	Min	-0.005	0.0000	-0.004	0.0000
	Max	0.004	0.0000	+0.005	0.0000

2.4. Conclusions

We have simulated the slamming impact of rigid and deformable hulls by using a coupled Lagrangian and Eulerian formulation available in the commercial finite element (FE) code LS-DYNA, and approximating the deformations of the hull and the water as two dimensional (plane strain). The Lagrangian (Eulerian) description of motion is used to describe deformations of the wedge (water), and the penalty method is used to satisfy continuity conditions between the wedge and the water surface. Effects of different values of parameters in the penalty method on the pressure distribution at the interface and the penetration of water into the hull are delineated. It is found that values of these parameters to minimize oscillations in the pressure and reduce water penetration depend upon the deadrise angle, the FE mesh, the initial velocity of the wedge, and whether or not deformations of the hull material are considered. Whenever possible, computed results are compared with those available in the literature. Effects of damage and delamination induced, respectively, in a fiber reinforced composite panel and a sandwich composite panel due to the hydroelastic pressure are studied.

Other conclusions are summarized below:

1. Fluid pressure at the solid-fluid interface and the velocity profile near the interface depend significantly on values of parameters in the penalty method, (see Appendix A), the FE mesh used, materials of the hull, and the hull's deadrise angle. We used at least two different FE meshes to ascertain the likely error in the numerical solution.
2. For V-shaped rigid wedges entering initially calm water with a constant downward velocity, and deformations assumed to be symmetric about the vertical axis passing through the apex of the V, computed pressures at the fluid-hull interface are found to agree reasonably well with those reported in the literature (e.g., see figures 81). For deadrise angles of 30^0 and 45^0, the interface pressure variation along the span of the wedge is approximately uniform when the water level reached the chine. For small deadrise angles (e.g. 10^0) the peak pressure occurs at the jet flow, and for relatively large deadrise angles (e.g. 81^0), the peak pressure occurs at the keel.
3. For rigid V-shaped hulls of deadrise angles of 30^0 and 45^0, the length of jet flow near the chine is more than that for other deadrise angles studied here (cf. figures 82).

4. For a rigid V-shaped wedge the tangential component of the water velocity at the wedge-water interface increases from zero at the keel to the maximum value in region A of the jet flow (cf. figure 84(a)).
5. For V-shaped rigid wedges symmetrically falling freely through initially calm water with deformations symmetric about the vertical axis passing through the apex of the V, the time history of the total upward force acting on the hull agreed well with that reported in [103] but the computed pressure distribution on the fluid-wedge interface differed noticeably from that reported in [103].
6. The core material in a sandwich composite panel is effective in absorbing the impact energy due to water slamming. However, delamination between the core and the face sheets significantly reduces the effectiveness of the core material.
7. For the fiber-reinforced composite hull studied here, the damage parameter ω_{11}, which characterizes damage in the longitudinal direction, due to the local water slamming on a fiber reinforced composite panel initiates at the keel and propagates towards the chine. This depends upon the damage evolution laws and the constitutive relations used to degrade material elasticities.

Chapter 3

Conclusions

Nonlinear governing equations (i.e., the continuum balance laws and Maxwell's equations) for an electrically actuated microelectromechanical system (MEMS) have been summarized, and have been numerically solved to study finite transient deformations of a perfectly conductive body by coupling the finite element method and the boundary element method; the former for the structural part of the problem and the latter for the electrical fields. The snap-through and the pull-in instabilities of micro-arches for different potential differences between the two electrodes have been studied. Depending upon how the electrical load is applied a micro-arch may experience either only the pull-in instability or the pull-in and the snap-through instabilities. It has also been found that the pull-in displacement is more for a micro-arch than that for a micro-beam of the same length, width, thickness, and the initial gap as the micro-arch. The pull-in voltage obtained by analyzing the beam problem with the linear strain displacement relation is nearly one-half of that for the same problem studied with the nonlinear strain displacement relation.

The present work is of practical significance and provides results on the nonlinear behavior and instabilities of a micro-arch under transient displacement-dependent electric loads. As a MEM electrode, micro-arches are advantageous over micro-beams because a micro-arch can have a larger operational range without the pull-in instability than a corresponding micro-beam. Moreover, by changing the rate of application of the potential difference between the two electrodes the snap-through instability may be avoided. This provides another means to control the response of a MEMS device. Also, in a micro-arch under an electric load the softening effect may be dominant before it experiences the snap-through instability but the strain-hardening effect may initially exceed the softening due to electric forces subsequent to the snap-through instability. This can be exploited in designing novel MEMS devices.

The present study also investigates the snap-through and the pull-in instabilities in an electrically actuated micro-arch modeled as a damped Euler-Bernoulli beam incorporating the nonlinear mid-plane stretching. The nonlinear time-dependent governing partial differential equation is

solved numerically by using the Galerkin method and an adaptive time integration scheme. For the static problem, the displacement control method (DIPIE algorithm) and the pseudo-arc length continuation method (PALC) are used to derive the bifurcation curve of the peak arch deflection versus the non-dimensional step electric potential difference between the arch and the bottom rigid flat electrode. Two distinct mechanisms, namely the ‘direct’ and the ‘indirect’, snap-through instabilities are found. The relation between the minimum potential energy of the MEMS for a dynamic problem and the total potential energy of the static problem is studied. It is found that the PALC algorithm can compute multiple branches of the bifurcation curve, which correspond to symmetric and asymmetric deformations of the arch. The DIPIE algorithm fails to compute asymmetric solutions.

The phase diagram between the critical load parameter and the arch height showing stable and unstable regions of arch's deformations is provided; it will help in designing arch-shaped MEMS. Effects of damping on the instability parameters have been studied. It is shown that damping suppresses the indirect snap-through instability and permits only the direct snap-through instability.

Results, including the indirect snap through and asymmetric deformations subsequent to the snap through instability, from the reduced-order model agree well with those from the continuum mechanics based approach.

Other conclusions are summarized below:

1. An undamped arch under a step electric load may experience either a direct or an indirect snap-through instability.
2. For relatively small arch heights, the static problem has solutions with deformations symmetric about the mid-span of the arch and the direct snap-through happens when the locus of the maximum deflection of the dynamic problem intersects the unstable branch of the bifurcation curve for the static problem.
3. For relatively large arch heights, the static problem has solutions with deformations symmetric and asymmetric about the mid-span of the arch. The asymmetric solution has lower potential energy than the corresponding symmetric solution.

4. The indirect snap-through happens when the locus of the maximum deflection of the dynamic problem intersects the unstable branch of the bifurcation curve of the asymmetric deformations for the static problem.
5. For a dynamic problem with the electric potential difference increasing linearly in time, whether or not the arch experiences a snap-through instability depends on the rate of application of the electric potential.
6. For a dynamic problem with the electric potential difference applied either as a step function or as a linear function of time, the arch has a stable motion only when its minimum potential energy is $\geq$ the potential energy of the stable deformed shape of the static problem and $<$ the potential energy of the unstable deformed shape of the static problem.
7. A phase diagram between the arch height and the applied electric potential has been constructed to show regions of different instabilities for static and dynamic problems.
8. Responses of sinusoidal and bell-shaped arches are qualitatively similar to each other.

We have simulated plane strain deformations due to the slamming impact of rigid and deformable hulls by using a coupled Lagrangian and Eulerian formulation available in the commercial finite element code LS-DYNA. The Lagrangian (Eulerian) description of motion is used to describe deformations of the wedge (water). A penalty contact algorithm is used to enforce non-interpenetration of the water into the hull and vice versa. Effects of different values of parameters in the penalty method on the satisfaction of the non-interpenetration condition have been delineated, and results for each problem are computed with two different finite element meshes to quantify the error in the numerical solution. Whenever feasible, computed results are compared with those available in the literature. Damage and delamination induced, respectively, in a fiber reinforce composite panel and in a sandwich composite panel due to hydroelastic pressure have been studied. Conclusions of this work are summarized below.

1. Fluid pressure at the solid-fluid interface and the velocity profile near the interface depend significantly on values of parameters in the penalty method, (see Appendix A), the FE mesh used, materials of the hull, and the hull's deadrise angle. We used at least two different FE meshes to ascertain the likely error in the numerical solution.

2. For V-shaped rigid wedges entering initially calm water with a constant downward velocity, and deformations assumed to be symmetric about the vertical axis passing through the apex of the V, computed pressures at the fluid-hull interface are found to agree reasonably well with those reported in the literature (e.g., see figures 81). For deadrise angles of 30^0 and 45^0, the interface pressure variation along the span of the wedge is approximately uniform when the water level reached the chine. For small deadrise angles (e.g. 10^0) the peak pressure occurs at the jet flow; for relatively large deadrise angles (e.g. 81^0), the peak pressure occurs at the keel.
3. For rigid V-shaped hulls of deadrise angles of 30^0 and 45^0, the length of jet flow near the chine is more than that for other deadrise angles studied here (cf. figures 82).
4. For a rigid V-shaped wedge the tangential component of the water velocity at the wedge-water interface increases from zero at the keel to the maximum value in region A of the jet flow (cf. figure 84(a)).
5. For V-shaped rigid wedges symmetrically falling freely through initially calm water with deformations symmetric about the vertical axis passing through the apex of the V, the time history of the total upward force acting on the hull agreed well with found experimentally but the two pressure distributions on the fluid-wedge interface differed.
6. The core material in a sandwich composite panel is effective in absorbing the impact energy due to water slamming. However, delamination between the core and the face sheets significantly reduces the effectiveness of the core material**.**
7. For the fiber-reinforced composite hull studied here, the damage parameter ω_{11}, which characterizes damage in the longitudinal direction, due to the local water slamming on a fiber reinforced composite panel initiates at the keel and propagates towards the chine. This depends upon the damage evolution laws and the constitutive relations used to degrade material elasticities.

References

[1] http://indy.cs.concordia.ca/auto/.

[2] *LS-DYNA Keyword User's Manual*: Livermore Software Technology Corporation)

[3] 2007 *Bio-MEMS : technologies and applications* (Boca Raton: CRC/Taylor & Francis)

[4] Abdel-Rahman E M, Younis M I and Nayfeh A H 2002 Characterization of the mechanical behavior of an electrically actuated microbeam *Journal of Micromechanics and Microengineering* **12** 759-66

[5] Ananthasuresh G K, Gupta R K and Senturia S D 1996 An approach to macromodeling of MEMS for nonlinear dynamic simulation *Proceedings of the ASME International Conference of Mechanical Engineering Congress and Exposition (MEMS). Atlalta, GA.* 401-7

[6] Andrews M, Harris I and Turner G 1993 A comparison of squeeze-film theory with measurements on a microstructure *Sensors and Actuators A: Physical* **36** 79-87

[7] Aquelet N and Souli M 2003 A new ALE formulation for sloshing analysis *Structural Engineering and Mechanics* **16**

[8] Aquelet N, Souli M and Olovsson L 2006 Euler-Lagrange coupling with damping effects: Application to slamming problems *Computer Methods in Applied Mechanics and Engineering* **195** 110-32

[9] Armand J-L and Cointe R 1986 Hydrodynamic impact analysis of a cylinder *Proc. of the Fifth International Offshore Mechanics and Arctic Engineering (OMAE) Symposium* **1** 250-6

[10] Bassous E, Taub H H and Kuhn L 1977 Ink jet printing nozzle arrays etched in silicon *Applied Physics Letters* **31** 135-7

[11] Batra R C, Porfiri M and Spinello D 2004 Treatment of material discontinuity in two meshless local Petrov-Galerkin (MLPG) formulations of axisymmetric transient heat conduction *International Journal for Numerical Methods in Engineering* **61** 2461-79

[12] Batra R C, Porfiri M and Spinello D 2006 Analysis of electrostatic MEMS using meshless local Petrov-Galerkin (MLPG) method *Engineering Analysis with Boundary Elements* **30** 949-62

[13] Batra R C, Porfiri M and Spinello D 2006 Capacitance estimate for electrostatically actuated narrow microbeams *Micro & Nano Letters* **1** 71-3

[14] Batra R C, Porfiri M and Spinello D 2006 Electromechanical Model of Electrically Actuated Narrow Microbeams *Microelectromechanical Systems, Journal of* **15** 1175-89

[15] Batra R C, Porfiri M and Spinello D 2007 Effects of Casimir force on pull-in instability in micromembranes *Europhysics Letters (EPL)* 20010

[16] Batra R C, Porfiri M and Spinello D 2007 Review of modeling electrostatically actuated microelectromechanical systems *Smart Materials and Structures* R23-R31

[17] Batra R C, Porfiri M and Spinello D 2008 Reduced-order models for microelectromechanical rectangular and circular plates incorporating the Casimir force *International Journal of Solids and Structures* **45** 3558-83

[18] Batra R C, Porfiri M and Spinello D 2008 Vibrations and pull-in instabilities of microelectromechanical von Kármán elliptic plates incorporating the Casimir force *Journal of Sound and Vibration* **315** 939-60

[19] Batra R C, Porfiri M and Spinello D 2008 Vibrations of narrow microbeams predeformed by an electric field *Journal of Sound and Vibration* **309** 600-12

[20] Beer G, Smith I M and Duenser C 2008 *The boundary element method with programming: For engineers and scientists.* (New York: Wien: Springer)
[21] Benson D J 1989 An efficient, accurate, simple ale method for nonlinear finite element programs *Computer Methods in Applied Mechanics and Engineering* **72** 305-50
[22] Benson D J 1992 Computational methods in Lagrangian and Eulerian hydrocodes *Computer Methods in Applied Mechanics and Engineering* **99** 235-394
[23] Bereznitski A 2001 Slamming: The role of hydroelasticity *International Shipbuilding Progress* **48** 333-51
[24] Bochobza-Degani O, Elata D and Nemirovsky Y 2002 An efficient DIPIE algorithm for CAD of electrostatically actuated MEMS devices *Microelectromechanical Systems, Journal of* **11** 612-20
[25] Budiansky B and Hutchinson J W 1964 Dynamic buckling of imperfection sensitive structure *TR 18, Contract 1866 (02), Div of Engineering and Applied Physics, Harvard Univ. (June 164) and AIAA J* **4** 525-30
[26] Budiansky B and Roth R S 1962 Axisymmetric dynamic buckling of clamped shallow spherical shells *NASA TN D-1510*
[27] Chao P C-P, Chiu C W and Liu T-H 2008 DC dynamic pull-in predictions for a generalized clamped-clamped micro-beam based on a continuous model and bifurcation analysis *Journal of Micromechanics and Microengineering* **18** 0960-1317
[28] Chao P C P, Chiu C W and Tsai C Y 2006 A novel method to predict the pull-in voltage in a closed form for micro-plates actuated by a distributed electrostatic force *Journal of Micromechanics and Microengineering* 986-98
[29] Christon M A and Jr. G O C 2001 *LS-DYNA's Incompressible Flow Solver User's Manual*: LSTC)
[30] Chu P B, Nelson P R, Tachiki M L and Pister K S J 1996 Dynamics of polysilicon parallel-plate electrostatic actuators *Sensors and Actuators A: Physical* **52** 216-20
[31] Das K and Batra R C Pull-in and snap-through instabilities in transient deformations of microelectromechanical Systems to appear in *the Journal of Micromechanics and Microengineering*
[32] De S K and Aluru N R 2004 Full-Lagrangian schemes for dynamic analysis of electrostatic MEMS *Microelectromechanical Systems, Journal of* **13** 737-58
[33] Doedel E, Keller H B and Kernevez J P 1991 Numerical analysis and control of bifurcation problems *International Journal of Bifurcation and Chaos* **1** 493 - 520
[34] Engelmann B E, Whirley R G and Goudreau G L 1989 *Analytical and Computational Models of Shells,* ed A K Noor*, et al.*: ASME)
[35] Faltinsen O M 1990 *Sea Loads on Ships and Offshore Structures* (Cambridge: Cambridge University Press)
[36] Flores G, Mercado G A and Pelesko J A 2003 Dynamics and touchdown in electrostatic MEMS. In: *MEMS, NANO and Smart Systems, 2003. Proceedings. International Conference on*, pp 182-7
[37] Fujii F 1989 Scheme for elasticas with snap-back and looping *Journal of Engineering Mathematics* **115** 2166-81
[38] Ganapathi M, Gupta S S and Patel B P 2003 Nonlinear axisymmetric dynamic buckling of laminated angle-ply composite spherical caps *Composite Structures* **59** 89-97

[39] Gilbert J R, Legtenberg R and Senturia S D 1995 3D coupled electro-mechanics for MEMS: applications of CoSolve-EM. In: *Micro Electro Mechanical Systems, 1995, Proceedings. IEEE,* p 122
[40] Goll C, Bacher W, Buestgens B, Maas D, Menz W and Schomburg W K 1996 Microvalves with bistable buckled polymer diaphragms *Journal of Micromechanics and Microengineering* 77-9
[41] Gupta S S, Patel B P and Ganapathi M 2003 Nonlinear dynamic buckling of laminated angle-ply composite spherical caps *Journal of Structural Engineering and Mechanics* **15** 463-76
[42] Hallquist J O 1998 *LS-DYNA theoretical manual*: Livermore Software Technology Company)
[43] Herbrt Wagner 1932 Über Stoß- und Gleitvorgänge an der Oberfläche von Flüssigkeiten *ZAMM - Zeitschrift für Angewandte Mathematik und Mechanik* **12** 193-215
[44] Hsu C S 1966 On dynamic stability of elastic bodies with prescribed initial conditions *International Journal of Engineering Science* **4** 1-21
[45] Hsu C S 1968 Equilibrium configurations of a shallow arch of arbitrary shape and their dynamic stability character *International Journal of Non-Linear Mechanics* **3** 113-36
[46] Humphreys J S 1966 On dynamic snap buckling of shallow arches *AIAA Journal* **4** 878-86
[47] Hung E S and Senturia S D 1999 Extending the travel range of analog-tuned electrostatic actuators *Microelectromechanical Systems, Journal of* **8** 497-505
[48] Hung E S and Senturia S D 1999 Generating efficient dynamical models for microelectromechanical systems from a few finite-element simulation runs *Microelectromechanical Systems, Journal of* **8** 280-9
[49] Krylov S, Bojan R I, David S, Shimon S and Harold C 2008 The pull-in behavior of electrostatically actuated bistable microstructures *Journal of Micromechanics and Microengineering* 055026
[50] Krylov S and Maimon R 2004 Pull-in Dynamics of an Elastic Beam Actuated by Continuously Distributed Electrostatic Force *Journal of Vibration and Acoustics* **126** 332-42
[51] Krylov S, Serentensky S and Schreiber D 2007 Pull-in behavior of electrostatically actuated multistable microstructures. In: *ASME 2007 International Design Engineering Technical Conference & Computers and Information in Engineering Conference,* (Las Vegas, Nevada, USA
[52] Krylov S, Seretensky S and Schreiber D 2008 Pull-in behavior and multistability of a curved microbeam actuated by a distributed electrostatic force. In: *Micro Electro Mechanical Systems, 2008. MEMS 2008. IEEE 21st International Conference on,* ed S Seretensky pp 499-502
[53] Kugel V D, Xu B, Zhang Q M and Cross L E 1998 Bimorph-based piezoelectric air acoustic transducer: model *Sensors and Actuators A: Physical* **69** 234-42
[54] Legtenberg R and Tilmans H A C 1994 Electrostatically driven vacuum-encapsulated polysilicon resonators Part I. Design and fabrication *Sensors and Actuators A: Physical* **45** 57-66
[55] Liu Y, Liew K M, Hon Y C and Zhang X 2005 Numerical simulation and analysis of an electroactuated beam using a radial basis function *Smart Materials and Structures* 1163-71

[56] Lock M H 1966 Snapping of a shallow sinusoidal arch under a step pressure load *AIAA Journal* **4** 1249-56
[57] Machauf A, Nemirovsky Y and Dinnar U 2005 A membrane micropump electrostatically actuated across the working fluid *Journal of Micromechanics and Microengineering* 2309-16
[58] Matzenmiller A, Lubliner J and Taylor R L 1995 A constitutive model for anisotropic damage in fiber-composites *Mechanics of Materials* **20** 125-52
[59] Mei X, Liu Y and Yue Dick K P 1999 On the water impact of general two-dimensional sections *Applied Ocean Research* **21** 1-15
[60] Muhkopadhyay S and Majumdar N 2006 Computation of 3D MEMS electrostatics using a nearly exact BEM solver *Engineering Analysis with Boundary Elements* **30** 687-96
[61] Mukherjee S, Bao Z, Roman M and Aubry N 2005 Nonlinear mechanics of MEMS plates with a total Lagrangian approach *Computers & Structures* **83** 758-68
[62] Nathanson H C, Newell W E, Wickstrom R A and Davis J R, Jr. 1967 The resonant gate transistor *Electron Devices, IEEE Transactions on* **14** 117-33
[63] Nayfeh A, Younis M and Abdel-Rahman E 2007 Dynamic pull-in phenomenon in MEMS resonators *Nonlinear Dynamics* **48** 153-63
[64] Nayfeh A and Younis M I 2004 Modeling and simulations of thermoelastic damping in microplates *Journal of Micromechanics and Microengineering* 1711
[65] Nelson D F 1979 *Electric, optic, and acoustic interactions in dielectrics* (New York: John Willey & Sons)
[66] Ng T Y, Jiang T Y, Li H, Lam K Y and Reddy J N 2004 A coupled field study on the non-linear dynamic characteristics of an electrostatic micropump *Journal of Sound and Vibration* **273** 989-1006
[67] Nguyen C T C, Katehi L P B and Rebeiz G M 1998 Micromachined devices for wireless communications *Proceedings of the IEEE* **86** 1756-68
[68] Nishiguchi I and Sasaki M 1994 A large deformation theory of solids subject to electromagnetic loads *Magnetics, IEEE Transactions on* **30** 3272-5
[69] Park S and Hah D 2008 Pre-shaped buckled-beam actuators: Theory and experiments *Sensors and Actuators A: Physical* **148** 186-92
[70] Patricio P, Adda-Bedia M and Ben Amar M 1998 An elastica problem: instabilities of an elastic arch *Physica D: Nonlinear Phenomena* **124** 285-95
[71] Pelesko J A 2001 Mathematical Modeling of Electrostatic MEMS with Tailored Dielectric Properties *SIAM Journal on Applied Mathematics* **62** 888-908
[72] Pelesko J A, Bernstein D H and McCuan J 2003 Symmetry and Symmetry Breaking in Electrostatically Actuated MEMS *Nanotech* **2** 432 - 5
[73] Pippard A B 1990 The elastic arch and its modes of instability *European Journal of Physics* 359-65
[74] Postma H W C, Kozinsky I, Husain A and Roukes M L 2005 Dynamic range of nanotube- and nanowire-based electromechanical systems *Applied Physics Letters* **86** 223105
[75] Pozrikidis C 2002 *A practical guide to boundary element methods with the software library BEMLIB*: Chapman & Hall/CRC)
[76] Qin Z and Batra R C 2009 Local slamming impact of sandwich composite hulls *International Journal of Solids and Structures* **46** 2011-35

[77] Radhakrishnan K and Hindmarsh. A C 1993 *Description and use of LSODE : the Livermore solver for ordinary differential equations* (Springfield, VA: National Aeronautics and Space Administration, Office of Management, Scientific and Technical Information Program)
[78] Rebeiz G M 2003 RF MEMS theory, design, and technology. (Hoboken, NJ: John Wiley & Sons, Inc.)
[79] Roylance L M and Angell J B 1979 A batch-fabricated silicon accelerometer *Electron Devices, IEEE Transactions on* **26** 1911-7
[80] Saif M T A 2000 On a tunable bistable MEMS-theory and experiment *Microelectromechanical Systems, Journal of* **9** 157-70
[81] Schweizerhof K, Weimar K, Muenz T and Rottner T 1995 Crashworthiness Analysis with Enhanced Composite Material Models in LS-DYNA - Merits and Limits. In: *5th International LS-DYNA User's Conference*
[82] Shapoorabadi R J and Andrew G K 2004 Comparison of three finite element models for analysis of MEMS micromirrors. ed C A John, *et al.*: SPIE) pp 849-60
[83] Simitses G J 1962 Dynamic snap-through buckling of low arches and shallow spherical caps. Ph.D. Dissertation. In: *Department of Aeronautics and Astronautics*: Stanford University)
[84] Simitses G J 1990 *Dynamic Stability of Suddenly Loaded Structures* (New York: Springer-Verlag)
[85] Simo J C and Hughes T J R 1986 On the variational foundations of assumed strain methods *Journal of applied mechnics* **53** 1685-95
[86] Stenius I, Ros, eacute, n A and Kuttenkeuler J 2006 Explicit FE-modelling of fluid-structure interaction in hull-water impacts *International Shipbuilding Progress* **53** 103-21
[87] Sun H 2007 A Boundary Element Method Applied to Strongly Nonlinear Wave-Body Interaction Problems. In: *Department of Marine Technology, Faculty of Engineering Science and Technology*, (Trondheim: Norwegian University of Science and Technology)
[88] Sun H and Faltinsen O M 2006 Water impact of horizontal circular cylinders and cylindrical shells *Applied Ocean Research* **28** 299-311
[89] Sun H and Faltinsen O M 2007 The influence of gravity on the performance of planing vessels in calm water *Journal of Engineering Mathematics* **58** 91-107
[90] Sun H and Faltinsen O M 2008 *IUTAM Symposium on Fluid-Structure Interaction in Ocean Engineering*, pp 285-96
[91] Sun H and Faltinsen O M 2009 Water entry of a bow-flare ship section with roll angle *Journal of Marine Science and Technology* **14** 69-79
[92] Taylor G 1968 The Coalescence of Closely Spaced Drops when they are at Different Electric Potentials *Proceedings of the Royal Society of London. Series A, Mathematical and Physical Sciences* **306** 423-34
[93] Telukunta S and Mukherjee S 2006 Fully Lagrangian modeling of MEMS with thin plates *Microelectromechanical Systems, Journal of* **15** 795-810
[94] Tilmans H A and Legtenberg R 1994 Electrostatically driven vacuum-encapsulated polysilicon resonators Part II. Theory and performance *Sensors and Actuators A: Physical* **45** 67-84
[95] V. Rochus D J R J C G 2006 Monolithic modelling of electro-mechanical coupling in micro-structures *International Journal for Numerical Methods in Engineering* **65** 461-93

[96] Van Kessel P F, Hornbeck L J, Meier R E and Douglass M R 1998 A MEMS-based projection display *Proceedings of the IEEE* **86** 1687-704
[97] Vangbo M 1998 An analytical analysis of a compressed bistable buckled beam *Sensors and Actuators A: Physical* **69** 212-6
[98] Vangbo M and Bcklund Y 1998 A lateral symmetrically bistable buckled beam *Journal of Micromechanics and Microengineering* **8** 29-32
[99] Vogl G, W. and Nayfeh A, H. 2005 A reduced-order model for electrically actuated clamped circular plates *Journal of Micromechanics and Microengineering* 684
[100] von Kármán T 1929 The impact of seaplane floats during landing. NACA TN)
[101] Woodward P and Colella P 1984 The numerical simulation of two-dimensional fluid flow with strong shocks *Journal of Computational Physics* **54** 115-73
[102] Xu Z and Mirmiran A 1997 Looping behavior of arches using corotational finite element *Computers & Structures* **62** 1059-71
[103] Yettou E-M, Desrochers A and Champoux Y 2007 A new analytical model for pressure estimation of symmetrical water impact of a rigid wedge at variable velocities *Journal of Fluids and Structures* **23** 501-22
[104] Younis M I, Abdel-Rahman E M and Nayfeh A 2003 A reduced-order model for electrically actuated microbeam-based MEMS *Microelectromechanical Systems, Journal of* **12** 672-80
[105] Zhang Y, Wang Y, Li Z, Huang Y and Li D 2007 Snap-Through and Pull-In Instabilities of an Arch-Shaped Beam Under an Electrostatic Loading *Microelectromechanical Systems, Journal of* **16** 684-93
[106] Zhao R, Faltinsen O M and Aarsnes J 1996 Water entry of arbitrary two-dimensional sections with and without flow separation.: ONR, Norway)
[107] Zhao X, Abdel-Rahman E, M. and Nayfeh A, H. 2004 A reduced-order model for electrically actuated microplates *Journal of Micromechanics and Microengineering* 900-6
[108] Zienkiewicz O C, Taylor R L and Zhu J Z 2005 *Finite element method for solid and structural mechanics* (Oxford: Elsevier Butterworth-Heinemann)
[109] Personal communications between the author and Mr. Allen and Dr. Battely of University of Auckland, New Zealand.
[110] http://ftp.lstc.com/anonymous/outgoing/jday/composites/mat58.

Appendix A. The penalty based contact algorithm

On the interface γ_{12} between the solid and the fluid regions, equations (71) and (72) are satisfied using the penalty method [8, 7]. The contact algorithm computes the pressure at the interface depending upon the relative displacement **d**, where $\mathbf{d} = \mathbf{u}^{s}\text{-}\mathbf{u}^{f}$, and the material time derivative of **d**. These forces are applied to the fluid and the structure nodes in contact to prevent penetration of water inside the solid region.

In the contact algorithm, the surface of the solid body is designated as a slave surface, and the fluid surface in contact with the solid body as a master surface. The forces due to the coupling affect nodes that are on the fluid-structure interface. For each node on slave surface, the increment in **d** is computed at each time step, using the relative velocity $\dot{\mathbf{d}} = \left(\mathbf{v}^{s} - \mathbf{v}^{f}\right)$, where $\mathbf{v}^{s}$ is the velocity of the slave node, and $\mathbf{v}^{f}$ is the velocity of a master particle of the fluid body initially coincident with the slave node on the fluid structure interface (figure A.1.). Note that the master particle is not a FE node, but a particle of the fluid body, which should remain coincident with the slave node, which is a FE node of the solid body. $\mathbf{v}^{f}$ is interpolated from the velocity at FE nodes of the fluid region at the current time.

At time $t = t^{n}$, $\mathbf{d}^{n}$ is updated incrementally by using

$$\mathbf{d}^{n+1} = \mathbf{d}^{n} + \left(\mathbf{v}^{s}{}_{n+1/2} - \mathbf{v}^{f}{}_{n+1/2}\right)\Delta t \qquad \text{(A.1)}$$

where Δt is the time increment. The coupling force acts only if penetration occurs $\left|\mathbf{d}^{n+1}\right| > 0$. For clarity, the superscript of **d** has been omitted; we will use **d** for the relative displacement. Penalty coupling behaves like a spring dashpot system and penalty forces are calculated proportionally to $\mathbf{d}$ and $\dot{\mathbf{d}}$. Figure A.1 illustrates the spring and the dashpot attached to the slave node and the master particle within a fluid element that is intercepted by the structure.

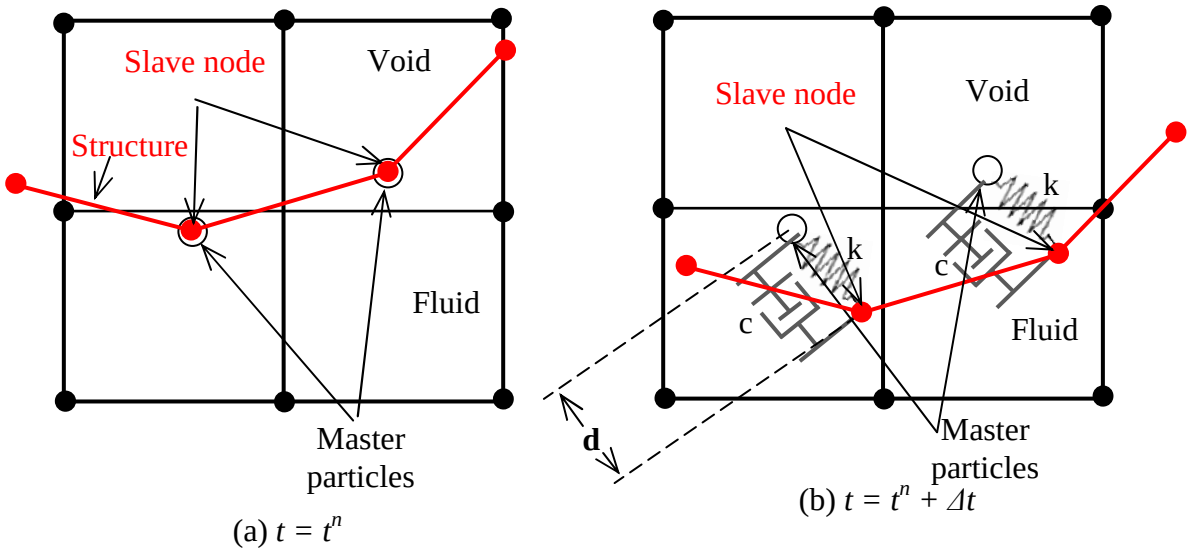

Figure A.1. Penalty coupling between the mesh for the solid region and the mesh for the fluid region.

The coupling force **F** is given by

$$\mathbf{F} = k\mathbf{d} + c\dot{\mathbf{d}} \tag{A.2}$$

where k and c represent the spring stiffness and the damping coefficient respectively. In case of an inviscid fluid, **d** is the displacement between the slave node and the master particle in the direction normal to the surface of the solid body, such that the force **F** = **0** when fluid moves along the tangent to the surface of the solid body. The force **F** is applied to both the master particle and the slave node in opposite directions to satisfy force equilibrium at the interface. At the slave node, force $\mathbf{F}_s = \mathbf{F}$ is applied; whereas for the fluid, the coupling force $\mathbf{F}_f$ is divided among the FE nodes based on the shape functions N_i (i = *1*,..., *8*) of the element on which the master particle is situated.

$$\mathbf{F}_f^i = N_i \mathbf{F} \tag{A.3}$$

As the penalty stiffness k approaches infinity, **d** approaches zero, satisfying the interface condition. However, the penalty method increases the overall stiffness of the system affecting its dynamic behavior. The optimum value of k should be such that it does not alter the dynamics of the problem significantly and prevents relative displacements between the two contacting bodies.

In LS-DYNA the contact stiffness is formulated per unit area as

$$k_d = \frac{k}{A} \tag{A.4}$$

where A is the area of the solid-fluid interface on a structural element. The value of k_d can either be specified through the LS-DYNA input file or can be given in terms of the bulk modulus C_1 of the fluid, and the volume V_{fe} of the fluid element that contains the master fluid particle.

$$k_d = P_f \frac{C_1 A}{V_{fe}} \tag{A.5}$$

The value of P_f , which is a scalar factor, can be specified through the LS-DYNA input file. Its suggested value is between 0.0 and 0.1 [2]. The optimum value of k_d or P_f is problem specific. Stenius et al.[86] have proposed a method to find the optimum values of k_d and P_f for water slamming on a rigid wedge. With an increase in the value of k_d, the interface pressure becomes oscillatory. In this paper, we compute the amount of fluid penetration through the interface and the pressure profile over the interface. For the optimal value of k_d the pressure variation should be smooth over the interface and the amount of fluid penetration should be negligible, e.g., the average value of the component of **d** normal to the interface over the span of the hull should be at least one order of magnitude less than the thickness of the hull.

The viscous dashpot with damping coefficient c damps out high frequency oscillations due to the contact stiffness. Again, to prevent damping force from altering the dynamics of the problem severely an optimal value of damping should be used. The equilibrium equation of the spring-dashpot system can be written as

$$M \frac{d^2}{dt^2} d + c \frac{d}{dt} d + kd = 0 \tag{A.6}$$

where $M = \sqrt{k \frac{m_s + m_f}{m_s m_f}}$, m_s and m_f equal lumped mass at the slave node and the master particle respectively. Equation (A.6) can be rewritten in terms of the damping factor $\xi = \frac{c}{\sqrt{kM}}$ and the frequency $\omega = \sqrt{\frac{k}{M}}$

$$\frac{d^2}{dt^2}d + \xi\omega\frac{d}{dt}d + \omega^2 d = 0 \qquad \text{(A.7)}$$

The damping factor ξ can be specified through the LS-DYNA input file.

Appendix B. LS-DYNA input deck

LS-DYNA input deck for simulation of the local water slamming on a sandwich composite hull of deadrise angle 5^0 and downward velocity of 10 m/s as reported in section 2.3.4

```
*KEYWORD
*TITLE
Water slamming on hull
$
*DATABASE_FORMAT
         0
*CONTROL_ALE
$      DCT      NADV      METH      AFAC      BFAC      CFAC      DFAC      EFAC
         1         1         2      -1.0
$    START       END     AAFAC     VFACT      PRIT       EBC      PREF   NSIDEBC

*SECTION_SOLID
$    SECID    ELFORM       AET
         1        12
*SECTION_SOLID
$    SECID    ELFORM       AET
         2         1
*SET_PART_LIST
$
$  part set for the initial void (1) and the fluid (2) parts
$
$      SID       DA1       DA2       DA3       DA4
         1       0.0       0.0       0.0       0.0
$     PID1      PID2      PID3      PID4      PID5      PID6      PID7      PID8
         1         2
*SET_PART_LIST
$
$  part set for the sandwich composite. Part 3: face sheets; part 4: core
$
$      SID       DA1       DA2       DA3       DA4
         2       0.0       0.0       0.0       0.0
$     PID1      PID2      PID3      PID4      PID5      PID6      PID7      PID8
         3         4
*CONSTRAINED_LAGRANGE_IN_SOLID
$    SLAVE    MASTER     SSTYP     MSTYP     NQUAD     CTYPE     DIREC     MCOUP
         2         1         0         0         3         4         2         1
$    START       END      PFAC      FRIC    FRCMIN      NORM     PNORM      DAMP
                           -2                                             0.9
$       CQ      HMIN      HMAX     ILEAK     PLEAK     LCIDPOR   NVENT     IBLOCK

$    IBOXID    IPENCHK   INTFORC   IALESOF   IALESOF   LAGMUL    PFACMM    THKF
                         1
*DEFINE_CURVE
$
$ curve for the contact stiffness
$
         2         0     1.000     1.000     0.000     0.000
  0.000000000000E+00  0.000000000000E+00
  0.100000000000E-07  0.025000000000E+03
*INITIAL_VELOCITY_GENERATION
$       ID      STYP     OMEGA        VX        VY        VZ
         2         1       0.0       0.0      -10.0       0.0
$       XC        YC        ZC        NX        NY        NZ     PHASE

*INITIAL_VOID_PART
$      PID
```

```
         1
*MAT_NULL
$#     mid        ro        pc        mu     terod     cerod        ym        pr
         1 0.100E+04-0.100E+12  0.00
*EOS_LINEAR_POLYNOMIAL
$    EOSID        C0        C1        C2        C3        C4        C5        C6
         1 0.000E+00 2.500E+09 0.000E+00 0.000E+00  0.000000  0.000000  0.000000
$       E0        V0
 0.000E+00 1.000E+00
$
*MAT_ELASTIC
$#     mid        ro       E     poisson
         2  150.     0.280E+10  0.300000       0.0       0.0       0.0
*MAT_ANISOTROPIC_ELASTIC
$#     mid        ro       c11       c12       c22       c13       c23       c33
         3 31400.000 9.9548E+9 3.0625E+9 9.9548E+9 3.9052E+9 3.9052E+91.4034E+11
$#     c14       c24       c34       c44       c15       c25       c35       c45
     0.000     0.000     0.0001.4200E+10
$#     c55       c16       c26       c36       c46       c56       c66      aopt
1.4200E+10     0.000     0.000     0.000     0.000     0.000 6.8923E+9  2.000000
$#      xp        yp        zp        a1        a2        a3      macf
     0.000     0.000     0.000 -0.241922  0.970296     0.000         1
$#      v1        v2        v3        d1        d2        d3      beta       ref
     0.000     0.000     0.000     0.000     0.000  1.000000
*PART
Initial void region
$#     pid     secid       mid     eosid      hgid      grav    adpopt      tmid
         1         1         1         1         0         0         0
$
*PART
Fluid region
$#     pid     secid       mid     eosid      hgid      grav    adpopt      tmid
         2         1         1         1         0         0         0
$
*PART
Face sheets
$#     pid     secid       mid     eosid      hgid      grav    adpopt      tmid
         3         2         3         0         0         0         0
$
*PART
Core
$#     pid     secid       mid     eosid      hgid      grav    adpopt      tmid
         4         2         2         0         0         0         0
*NODE
       1 0.000000000E+00 0.000000000E+00 0.000000000E+00       0       0
$
$   rest of node definitions are removed
$
*ELEMENT_SOLID
       1       2       1       3     302     153     751     752   23402   23401
$
$   rest of element definitions are removed
$
*CONTROL_TIMESTEP
    0.0000    0.9000         0  0.00      0.00
*CONTROL_TERMINATION
 0.200E-01         0   0.00000   0.00000   0.00000
$
*DATABASE_BINARY_D3PLOT
0.0500E-03
$
*DATABASE_BINARY_FSIFOR
0.0500E-03
```

```
$
*DATABASE_EXTENT_BINARY
$    NEIPH     NEIPS    MAXINT    STRFLG    SIGFLG    EPSFLG    RLTFLG    ENGFLG
         0         0         3         1         1         0         0         0
$   CMPFLG    IEVERP    BEAMIP     DCOMP      SHGE     STSSZ    N3THDT   IALEMAT
         1         0         4         0         0         0         2

*DATABASE_FSI
$       DT
0.0500E-03
$    DBFSI_ID     SID     SIDTYPE    SWID     CONVID
         1         2         0
$
*DEFINE_CURVE
         1         0     1.000     1.000     0.000     0.000
  0.000000000000E+00  0.000000000000E+00
  2.000000000000E-02  0.000000000000E+00
$
*DEFINE_CURVE
         3         0     1.000     1.000     0.000     0.000
  0.000000000000E+00 -1.000000000000E+01
  2.000000000000E-02 -1.000000000000E+01
*SET_NODE_LIST
         1     0.000     0.000     0.000     0.000
     80013     80014     80015     80016     80017     80018     80019     80169
     80170     80469     80619     80620     80919     80920     80921     80922
     80923     80924     81223     81224     81523     81524     81525     81526
     81527     81677     81827     81977
*BOUNDARY_PRESCRIBED_MOTION_SET
         1         1         0         1     1.000         0 0.000     0.000
*BOUNDARY_PRESCRIBED_MOTION_SET
         1         2         0         3     1.000         0 0.000     0.000
*SET_NODE_LIST
         2     0.000     0.000     0.000     0.000
         1         2         3         4         5         6         7         8
$
$ rest of node set definition removed
$
*BOUNDARY_SPC_SET
         2         0         1         0         0         0         0         0
*SET_NODE_LIST
         3     0.000     0.000     0.000     0.000
       303       304       305       306       307       308       309       310
$
$ rest of node set definition removed
$
*BOUNDARY_SPC_SET
         3         0         0         0         1         0         0         0
*SET_NODE_LIST
         4     0.000     0.000     0.000     0.000
     68253     68268     68283     68284     68285     68286     68287     68288
$
$ rest of node set definition removed
$
*BOUNDARY_SPC_SET
         4         0         1         1         1         0         0         0
*END
```

Appendix C. User guide for the coupled FEM-BEM code for simulations of 2D electrostatically actuated MEMS

Linux script files

run	Complies program files to build an executable file for the FEM-BEM code
runpost	Complies program files to build an executable file for the post processor code
runtime	Complies program files to build an executable file for the time history post processor code

Program files

nonlinearfem2d1.f90	Contains the main program code1, the subroutine fex, subroutine gaussb, subroutine constirelation, subroutine prep, subroutine invdet, subroutine solve_spd, and subroutine solve_g
fem2d.f	Contains subroutines to calculate FE shape function and derivatives of the shape function
lsode.f	Contains subroutines for LSODE software
body_2d_fun5.f	Contains subroutine body_2d_fun
gauss_leg.f	Contains subroutine Gauss_Legendre
inversed.f	Contains linpack subroutines

Description of subroutines

fex	Subroutine called by LSODE, sets up FEA and updates accelerations
gaussb	Sets Gauss points and weights for FEA
constirelation	Constitutive relation
prep	Preprocessor, reads input files
invdet	Calculates the inverse of a matrix
solve_spd	Solves a linear system of equations with symmetric positive definite matrix
solve_g	Solves a linear system of equations
body_2d_fun	BEM code

List of input files

Name of the file	Description
input.dat	Inputs number of elements, and number of nodes for FE, etc.
inputbem.dat	Inputs number of elements, and number of nodes for BE, etc.
b2f.in	Lists FE node number and corresponding BE node number on the boundary
bcu.in	Specified x_1 displacement on nodes on the boundary
bcv.in	Specified x_2 displacement on nodes on the boundary
cb1.in	FE element number and node number on the boundary side 1
cb2.in	FE element number and node number on the boundary side 2
cb3.in	FE element number and node number on the boundary side 3
cb4.in	FE element number and node number on the boundary side 4
cntvtbem.in	Element connectivity for BEM code
cntvt.in	Element connectivity for FEM code
coordbem.in	Coordinates of nodes for BEM
coord.in	Coordinates of nodes for FEM
elemat.in	Material number of the element
f2b.in	Lists BE node number and corresponding FE node number on the boundary
b2f.in	Lists FE node number and corresponding BE node number on the boundary
ic.dat	Initial x_1 and x_2 velocity
mat.dat	Material parameters
ne.in	BE numbers attached to a BE node
voltnode.in	Specified electric potential on BE nodes

Simple files:

input.dat

```
  245   ! number of FE nodes
   60   ! number of FE elements
   30   ! number of FE node on the boundary side 1
    2   ! number of FE node on the boundary side 2
   30   ! number of FE node on the boundary side 3
    2   ! number of FE node on the boundary side 4
    8   ! number of nodes in a FE
    3   ! number of nodes in a one side of a FE
```

```
                9 ! number of gauss points in a FE
               10 ! number of boundary nodes with specified values of x1 displacement
               10 ! number of boundary nodes with specified values of x1 displacement
            10000 ! total number of time step
    0.1000000E-01 ! time step in time unit
    0.0000000E+00 ! damping coefficient
               1 ! if set to 1, finite strain is used, if set to 0, infinitesimal stain is used
               1 ! if set to 1, lumped mass is used, if set to 0, consistent mass is used
               3 ! if set to 3, plane-strain problem, if set to 2, plane-stress problem
              32 ! number of a node whose ui and vi are written in fort.28 and fort.29
              32 ! number of a node whose ui and vi are written in fort.30 and fort.31
    0.0000000E+00 ! unused card; set to zero
    0.1010000E-01 ! gap between two electrodes
    0.3000000E-01 ! width of the electrode
    0.2400000E-02 ! height of the electode
    0.0000000E+00 ! ramp time, if the electric potential is increased from zero linearly
    0.1000000E-01 ! time at which electric potential is updated, set a small value or zero
```

inputbem.dat

```
 128                    ! number of BE nodes
 128                    ! number of collocation points (same as above)
 -0.101000000E-01       ! x2 coordinate of the rigid electrode
 12                     !  number of Gauss points in a BE
```

b2f.in

```
  1                     ! Sequentially lists the FE node numbers on the boundary
  2                     ! corresponding to the BE node number. Assume that BE node
  3                     ! numbers are the line number. Add as many lines
  4                     ! as total number of BE nodes
  5
  6
```

f2b.in

```
  1                     ! Sequentially lists the BE node numbers
  2                     ! corresponding to the FE node number on the boundary. Assume that
  3                     ! FE node numbers are line numbers. Add as many lines as total
  4                     ! number of FE nodes , set zero if FE node is an interior node
  5
  6
```

bcu.in

```
 128.  0.0000000E+00    ! list the FE node number and the specified value of
 127.  0.0000000E+00    ! x1 displacement. Add as many line as need
 126.  0.0000000E+00
```

bcv.in is similar to bcu.in, but to specify x_2 displacements.

cb1.in

```
  30  60  2   61      ! first row = number of FE element on side 1
  29  58  60  59      ! 2nd to 4th row = node numbers of whose node of the FE element
  28  56  58  57      ! which are on the side 1
  27  54  56  55      ! Add as many lines as needed
  26  52  54  53
  25  50  52  51
  24  48  50  49
```

cb2.in, cb3.in and cb4.in are similar to cb1.in but for side2, side3 and side4 respectively.

cntvtbem.in

```
   1   3              ! two node numbers of a BE element
   3   4              ! add as many line as many BEs is in the mesh
   4   5
   5   6
   6   7
```

cntvt.in

```
   1    4   131   127    3   130   129   128      ! eight node numbers of a FE element
   4    6   135   131    5   134   133   130      ! add as many line as total number of  FEs
   6    8   139   135    7   138   137   134
   8   10   143   139    9   142   141   138
  10   12   147   143   11   146   145   142
  12   14   151   147   13   150   149   146
  14   16   155   151   15   154   153   150
  16   18   159   155   17   158   157   154
```

coordbem.in and coord.in lists, respectively, the three coordinates of a FE nodes and a BE nodes in a line.

mat.dat

```
1               ! Total number of different materials in the model
8.8419e-15      ! Absolute permittivity
231e-2          ! Density
8.8419e-15      ! Permittivity of the material surrounding electrodes
97.5            ! Elastic constant lambda
65.0            ! Elastic constant mu
                ! Repeat the above four lines as many time as the total number of materials
```

ic.dat

```
0.0d0    0.0d0          ! Initial x1 and x2 velocity at a FE node
```

0.0d0 0.0d0 ! add as many lines as total number of FE nodes

0.0d0 0.0d0

voltnode.in

10.0d0 ! Specified electric potentail at a BE node

10.0d0 ! add as many lines as total number of BE nodes

10.0d0

ne.in

10 1 ! number of BE which attached to a BE node

1 2 ! line number is the BE node number

2 3 ! add as many line as total number of BE node

elemat.in

1 ! Lists the material number of a FE

1 ! line number is the FE number

2 ! add as many line as total number of FEs